Development of an Advanced Battery Thermal Management System for Fast Charging High-Performance Electromobility Application

Eneko Gonzalez Agirre

2023

A thesis submitted for the degree of Doctor of Philosophy

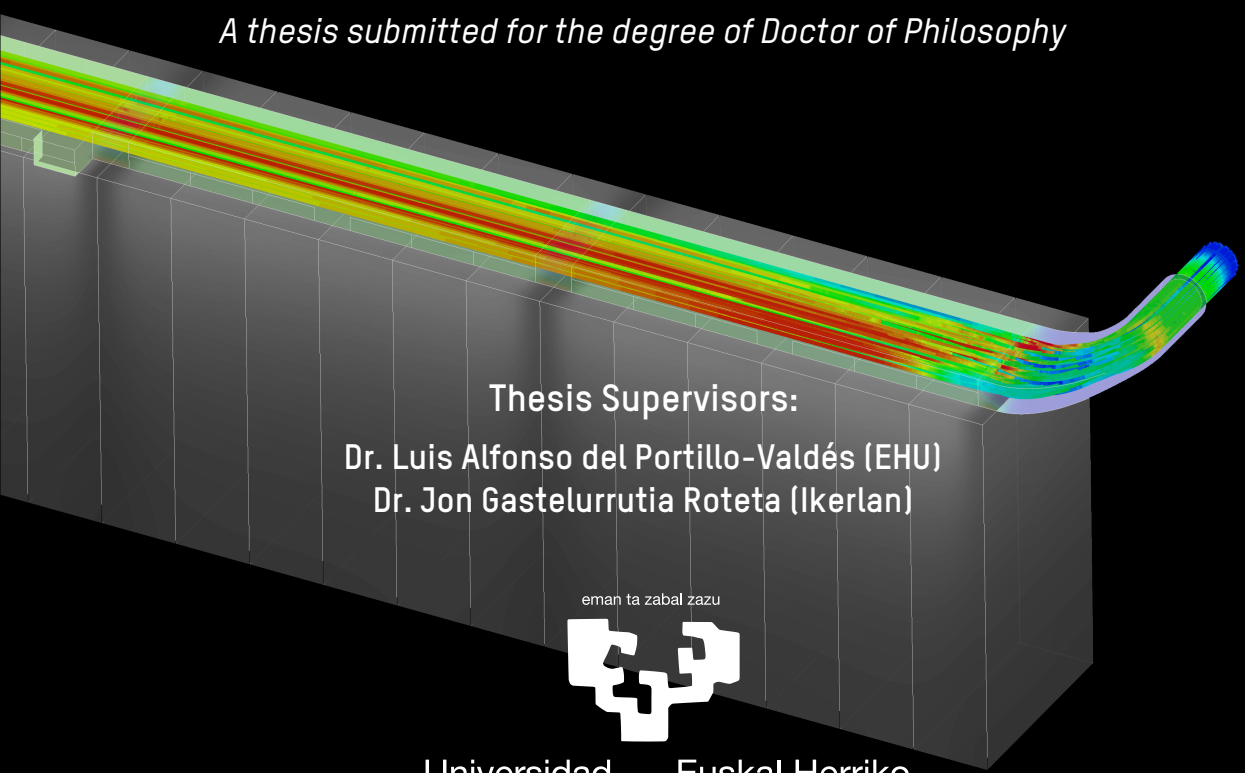

Thesis Supervisors:

Dr. Luis Alfonso del Portillo-Valdés (EHU)
Dr. Jon Gastelurrutia Roteta (Ikerlan)

eman ta zabal zazu

Universidad del País Vasco

Euskal Herriko Unibertsitatea

A thesis submitted for the degree of
Doctor of Philosophy

2023

Doctoral Programme in Energy Efficiency and Sustainability
in Engineering and Architecture

eman ta zabal zazu

Universidad del País Vasco

Euskal Herriko Unibertsitatea

The author would like to extend their sincere gratitude to the Ikerlan Technology Research Centre for funding and hosting this PhD thesis.

ikerlan

MEMBER OF BASQUE RESEARCH
& TECHNOLOGY ALLIANCE

(cc)2023 ENEKO GONZALEZ AGIRRE (cc by-nc 4.0)

Eskerrak

Familiari. *Ama, Aita, Agurtzane*. Dena eman duzuelako nagoen tokira iristearren, ordainetan ezer jasotzeko beharrik erakutsi gabe. Errespetua, esker ona, esfortzua eta maitasuna zer diren erakutsi dizkidazuelako. Nire azken urteetako aldarte on eta batez ere txarrak pazientzia miresgarriz jasan dituzuelako. Nire izaera eraiki duzuelako. Honengatik eta askoz gehiagogatik, ESKERRIK ASKO.

Kuadrilari. Sostengu izateagatik unerik zailenetan. Ohartu gabe, guztia xamurragoa egin izanagatik, deskonektatzen laguntzeagatik. Barre eta momentu on guztiek sortutako poz eta oroitzapenengatik. Momentu txarrekin ikasitakoagatik. Gorabeheraz betetako bidean helduleku izateagatik. Mila esker.

Lankideei. Bidea errazagoa delako lankideak lagun bihurtzean. Une oro laguntzeko prest egoteagatik. Etengabe gauza berriak erakusteagatik. Erakutsitako hurbiltasunagatik, lanik zailena erronka bihurtzeagatik. *Jon*, etengabeko prestutasuna erakusteagatik, esku artekoa utzi eta nire galdera zein arazoei beti arretaz erantzuteagatik. Esker mila.

Leamington and WMG people and friends. For making my stay enjoyable, fruitful and happy. For showing me all the good people out there, wherever you are. For integrating me into the group from the first day. For making me feel at home. Many thanks.

Guztioi. Bidean topatutako guztiei, nire bizitzaren parte izandakoei eta bazaretenoi. Nire sostengu eta pizgarri izateagatik. Nire gaur egungo *nia* eraikitzen laguntzeagatik. ***Bihotzez, mila esker guztioi***.

(C + H) x A

C: Conocimiento
H: Habilidad
A: Actitud

Abstract

The transition to electromobility plays a crucial role in reducing carbon emissions and addressing the impacts of climate change, particularly in the transportation sector. Battery Electric Vehicles (BEVs) powered by Lithium-ion Batteries (LIBs) have emerged as a key solution in this transition. However, the overheating potential of LIBs poses a significant challenge, especially with the increasing demand for high-performance and fast-charging capabilities. Effective thermal management is essential to ensure optimal performance, safety, and reliability while addressing challenges related to energy density, specific energy, and fast-charging requirements.

This research aims to develop a high-performance battery thermal management system (BTMS) for electromobility applications, focusing on designing an optimal system that meets performance standards for demanding use cases. After introducing an improved cell selection methodology for optimising and developing an energy-efficient BTMS to provide an integral system design, two systems are proposed for direct comparison: a Hybrid BTMS with a cold plate and PCM for temperature peak absorptions and a Dielectric Flow- and Tab-Based BTMS that can be adapted to different battery pack designs and cell geometries. After numerical CFD comparison, the research includes the development of a functional prototype of the Dielectric Flow- and Tab-Based BTMS for concept-proof validation.

The results demonstrate that the proposed Dielectric Flow- and Tab-Based system is an effective thermal management solution, improving specific energy and energy density while reducing auxiliary energy consumption. It also enhances safety and overall system efficiency. By addressing these objectives, this research contributes to developing a more sustainable road transport system by advancing the field of high-performance thermal management systems for BEVs.

Laburpena

Elektromugikortasunerako trantsizioak funtsezko eginkizuna du karbono emisioak murriztu eta klima aldaketaren inpaktuak mugatzeko, garraioaren sektorean bereziki. Litio-ioizko bateriez (LIB) elikatutako bateriazko ibilgailu elektrikoak (BEV) trantsizio honen funtsezko irtenbide bilakatu dira. Hala ere, LIBen gainberotze ahalmena erronka garrantzitsua da, errendimendu handiko eta karga azkarreko eskakizunak gero eta handiagoak diren honetan. Kudeaketa termiko eraginkorra funtsezkoa da errendimendu optimoa, segurtasuna eta fidagarritasuna bermatzeko, eta, aldi berean, energia dentsitatearekin, energia espezifikoarekin eta karga azkarreko baldintzekin lotutako desafioei aurre egiteko.

Ikerketa honen helburua elektromugikortasun aplikazioetarako errendimendu handiko baterien kudeaketa termikoko sistema (BTMS) optimo bat garatzean datza, erabilera betekizun zorrotzak jasango dituena. Zeldak hautatzeko metodologia hobetua aztertu ondoren, zeinak BTMS baten diseinu integrala eta sistema energetikoki eraginkorra eta optizatua garatzea ahalbidetuko duen, bi sistema proposatzen dira konparaketa zuzenerako: BTMS Hibrido bat, hotz-plaka eta PCM edo fase aldaketako materialez hornitua, bat bateko tenperatura igoerak xurgatzeko, eta bestalde, fluxu dielektriko eta borne bidezko hozketan oinarritzen den beste sistema bat, baterien diseinu eta geometria ezberdinetara egokitu daitekeena. Jariakin Konputazionalen Dinamikaren (CFD) bidezko konparaketa numerikoaren ondoren, ikerketak fluxu dielektriko eta borne bidezko BTMS prototipo funtzional baten garapena proposatzen du, kontzeptuaren azterketa eta balioztatze experimentalerako.

Emaitzen arabera, proposatutako sistema dielektrikoa kudeaketa termikorako irtenbide eraginkorra da, energia espezifikoa eta energia dentsitatea hobetuz eta albo kontsumoak murriztuz. Sistemaren segurtasuna eta eraginkortasun orokorra ere hobetzen ditu. Helburu horiei ekitean, ikerketa horrek errepide bidezko garraio sistema iraunkorragoa garatzen laguntzen du, bateria bidezko ibilgailu elektrikoetarako errendimendu handiko kudeaketa termikoko sistemen eremuan aurrera eginez.

Resumen

La transición a la electromovilidad desempeña un papel crucial en la reducción de las emisiones de carbono y la lucha contra los efectos del cambio climático, especialmente en el sector del transporte. Los vehículos eléctricos de batería (BEV) propulsados por baterías de iones de litio (LIB) se han revelado como una solución clave en esta transición. Sin embargo, el potencial de sobrecalentamiento de las LIB plantea un reto importante, especialmente con la creciente demanda de prestaciones de alto rendimiento y capacidad de carga rápida. Una gestión térmica eficaz es esencial para garantizar un rendimiento, seguridad y fiabilidad óptimos, al tiempo que se abordan los retos relacionados con la densidad energética, la energía específica y los requisitos de carga rápida.

El objetivo de esta investigación es desarrollar un sistema de gestión térmica de alto rendimiento para aplicaciones de electromovilidad, centrándose en el diseño de un sistema óptimo que cumpla los estándares de rendimiento para casos de uso exigentes. Tras introducir una metodología mejorada de selección de celdas para optimizar y desarrollar un BTMS energéticamente eficiente que proporcione un diseño integral del sistema, se proponen dos sistemas para su comparación directa: un sistema híbrido de gestión térmica de baterías (BTMS) con un cold plate y un PCM para absorber los picos de temperatura y un BTMS basado en flujo dieléctrico y refrigeración por los bornes que puede adaptarse a diferentes diseños de paquetes de baterías y geometrías de celdas. Tras la comparación numérica CFD, la investigación incluye el desarrollo de un prototipo funcional del BTMS basado en flujo dieléctrico para la prueba y validación del concepto.

Los resultados demuestran que el sistema propuesto, basado en flujo dieléctrico y refrigeración por los bornes, es una solución eficaz de gestión térmica que mejora la energía específica y la densidad energética, al tiempo que reduce el consumo de energía auxiliar. También mejora la seguridad y la eficiencia global del sistema. Al abordar estos objetivos, esta investigación contribuye al desarrollo de un sistema de transporte por carretera más sostenible mediante el avance en el campo de los sistemas de gestión térmica de alto rendimiento para BEV.

Contents

List of Figures

List of Tables

Acronyms

ARC	Accelerating Rate Calorimeter
BEV	Battery Electric Vehicle
BM	Battery Module
BMS	Battery Management System
BP	Battery Pack
BTMS	Battery Thermal Management System
C-rate	Current Rate
CAD	Computer-Aided Design
CFD	Computational Fluid Dynamics

CP	Cold Plate
EHC	Entropic Heat Coefficient
eMOV	Electromobility
ESS	Energy Storage System
EU	European Union
EV	Electric Vehicle
FC	Fast Charge
FCEV	Fuel Cell Electric Vehicle
FMI	Functional Mock-up Interface
FMU	Functional Mock-up Unit
GCI	Grid Convergence Index
GHG	Greenhouse Gas
HEV	Hybrid Electric Vehicle
HPPC	Hybrid Power Pulse Characterisation
HVAC	Heating, Ventilation and Air Conditioning
ICE	Internal Combustion Engine
IPCC	Intergovernmental Panel on Climate Change

LFP	Lithium Iron Phosphate
LIB	Lithium-ion Battery
LTO	Lithium Titanate Oxide
n_{cell}	Number of Cells
ND	Normal Drive
NMC	Nickel Manganese Cobalt
PCM	Phase Change Material
R_{in}	Internal Resistance
SLH	Specific Latent Heat
SOC	State of Charge
TEC	Thermoelectric Cooler
TIM	Thermal Interface Material
TMS	Thermal Management System
UDF	User Defined Function
w-e50	water ethylene-glycol 50% mixture

List of Symbols

Symbol	Description	Unit
A_{axial}	Axial Surface of the Cell	[m^2]
C_p	Specific Heat Capacity	[J/kg·K]
C_{bat}	LiB Cell Capacity	[Ah]
$C_{p_{avg}}$	Average Specific Heat Capacity	[J/kg·K]
$C_{thermal}$	Thermal Capacitance	[J/K]
EHC	Entropic Heat Coefficient	[mV/K]
E_{charge}	Electrical Energy Recharged	[Wh]
E_{hyd}	Hydraulic Energy	[Wh]
I_{dch}	Discharge current	[A]
I	Current	[A]
M	Mass	[kg]
P_{hyd}	Hydraulic Power	[W]
$P_{vehicle}$	Vehicle Power Needs	[kW]

Symbol	Description	Unit
Q_{irr}	Irreversible Heat Energy	[Wh]
Q_{rev}	Reversible Heat Energy	[Wh]
R_{in}	Internal Resistance	[mΩ]
R_{th}	Thermal Resistance	[K/W]
Re	Reynolds Number	[–]
SOC	State of Charge	[%]
T_{inlet}	Fluid Inlet Temperature	[°C]
ΔT_{cell}	Maximum thermal gradient inside the cells	[°C]
ΔT_{module}	Maximum thermal dispersion among cells in battery module	[°C]
ΔT_{test}	Thermal jump from test's initial temperature to the test's last cycle averaged temperature	[°C]
ΔT	Temperature Variation	[°C]
Δp	Pressure Drop	[Pa]
Δt	Time Variation	[s]
$\dot{Q}_{cond}$	Heat transfer by conduction	[W]
$\dot{Q}_{conv}$	Heat transfer by convection	[W]
$\dot{Q}_{diss}$	Heat dissipation rate	[W]
$\dot{Q}_{gen}$	Heat generation rate	[W]
$\dot{Q}_{sto_{fluid}}$	Heat stored in the fluid	[W]
$\dot{V}$	Volumetric Flow Rate	[l/min]
$\dot{m}$	Mass Flow Rate	[kg/s]
$\dot{Q}$	Heat generation / consumption rate	[W]
η_{charge}	Efficiency at Charge	[%]
μ	Dynamic Viscosity	[Pa·s]
ν	Kinematic Viscosity	[m^2/s]

Symbol	Description	Unit
ρ	Density	[kg/m^3]
e_{abs}	Absolute error	[°C]
h_{conv}	Convective Heat Transfer Coefficient	[W/m^{2}K]
k	Thermal Conductivity	[W/m·K]
t	Time	[s]

1

General Introduction

Summary

The first chapter of this PhD thesis presents the framework and motivation behind the research, as well as the primary objectives of the study. Additionally, the chapter outlines the structure of the remaining chapters in the thesis

1.1 Framework and Thesis Motivation

The transition to electromobility is a necessary step in reducing the carbon footprint and mitigating the impacts of climate change. The transport sector is responsible for a significant portion of global greenhouse gas emissions, with road transport being a major contributor. In response, the industry has made significant efforts to promote the use of electric vehicles, including e-bikes, electric cars, and electric trucks. These vehicles rely on lithium-ion batteries as an extended energy storage system with high efficiency, reasonable energy density, and significant power storage capacity.

Battery Electric Vehicles (BEVs) have emerged as a critical solution in the automotive industry's transformation to electrification. These vehicles rely on Lithium-ion Batteries (LIBs), an extended energy storage system that offers high efficiency, reasonable energy density, and significant power storage capacity. However, there are several challenges associated with LIBs, including energy density, specific energy, and fast charge requirements. These challenges make thermal management critical to maintaining optimal performance, security, and reliability. Battery thermal management systems, also known as BTMS, have been studied and used extensively in the literature. The current trend is to use cold plates to circulate a water ethylene-glycol mixture inside them. While these systems are thermally efficient, the increased demands for vehicles create the need for a more optimised solution with better specific energy, energy density, and lower auxiliary energy consumption.

This research addresses the need for high-performance thermal management systems for electromobility, where vehicle efficiency and range are paramount for standardising these vehicles. Additionally, battery security and reliability are critical factors that require attention. The rest of the vehicle's thermal needs are beyond the scope of this thesis.

In summary, this thesis aims to provide a novel approach to thermal management that meets the high-performance standards required for high-demanding electromobility applications. By doing so, this work contributes to the transition to a more sustainable road transport system, which is necessary to combat climate change and reduce greenhouse gas emissions.

The following sections outline this work's hypothesis and the main and secondary objectives for achieving this PhD thesis's desired outcomes.

1.2 Hypothesis

On the path to the advanced and energy efficient BTMS, a design and development methodology should be implemented. Therefore, this work's hypothesis is described:

Methodology implementation enhances the selection and development of optimal advanced battery thermal management system for high-performance electromobility application.

The hypothesis suggests that by adopting this structured approach, it will be possible to systematically evaluate various BTMS options, assess their performance, and ultimately improve the overall energy efficiency of the electromobility system under consideration. The comprehensive methodology, which will be presented in Chapter 3, is expected to provide valuable insights into the complex process of designing and developing an advanced BTMS for high-performance electromobility.

The verification of this hypothesis will be carried out following the objectives below described.

1.3 Objectives

The main objective of this PhD Thesis on the path to face the challenges of a more sustainable electromobility based on battery electric vehicles is as follows:

Development of a novel and advanced battery thermal management system for high-performance electromobility application.

The correct achievement of this main objective suggests the definition of other secondary objectives for the advancement of this work:

- Ensure the **proposed system's applicability and adaptability** for different battery pack designs and cell geometries.

- Creation of a **functional prototype** where the proposed technology will be experimentally tested and analysed.
- **CFD thermal model generation** for proposed solution analysis, with experimental validation from functional prototype tests.
- System must counteract fast charges and highway speed discharges on a **high-performance electric cycle**.
- **Numerical comparison** of the proposed system is needed to assess the improvement obtained concerning reference BTMS solutions.

1.4 Thesis Structure

To achieve these objectives, the following lines depict the thesis structure defined.

Chapter 2 introduces the state of the art, focused on the BEV and their lithium-ion battery utilisation and performance. Moreover, the main battery thermal management systems are introduced, presenting the advantages and drawbacks of the literature studies.

Chapter 3 illustrates the overall methodology followed for the thesis objectives achievement. A detailed description of the utilised models, their implementation and the BTMS comparison process are depicted.

Chapter 4 presents the improved cell selection methodology employed in the battery pack cell selection. The cell parameter characterisation tests are explained and the validation case study for the improved cell selection methodology is shown.

Chapter 5 shows the CFD-based comparison analysis of two advanced BTMS solutions for electromobility. The outcomes are discussed with the numerical results of each system, numerically assessing each thermal management solution's main advantages and drawbacks under broad key indicators.

Chapter 6 shows the development of the proposed advanced BTMS technology after the comparison analysis in the previous chapter. Therefore, it gathers the prototype's design, construction and experimental

analysis. CFD model is also developed and validated, with final extra geometry analysis.

Finally, **Chapter 7** summarises the main conclusions of the PhD Thesis, the future research lines and the relevant contributions.

2

State of the Art

Summary

This second chapter provides a comprehensive overview of state of the art in the electro-mobility field, with a specific emphasis on using lithium-ion batteries (LiBs) as energy storage systems. The chapter also introduces the primary battery thermal management systems utilised in existing literature, highlighting the strengths and weaknesses of each.

2.1 Framework and Current Situation

Global warming is an acute and pressing problem that poses significant threats to the planet's sustainability. The changes in climate caused by global warming can lead to a catastrophic loss of biodiversity, ecosystems, and the global economy. There is unequivocally established a strong correlation between the increase in global temperatures and the rise of carbon dioxide emissions in the atmosphere, which are predominantly due to human activities such as burning fossil fuels, deforestation, and industrial processes [1, 2].

The concentration of CO_2 in the atmosphere has risen from about 280 parts per million (ppm) before the Industrial Revolution to over 415 ppm today, surpassing any levels observed in the past 800,000 years [3]. This unprecedented rise in CO_2 levels is the principal driver of the current global warming trend, which is predicted to continue unless immediate and decisive action is taken to reduce greenhouse gas emissions. The fig. 2.1 shows the trend of CO_2 emissions of the last century, along with the temperature changes from the 1951-1980 reference period.

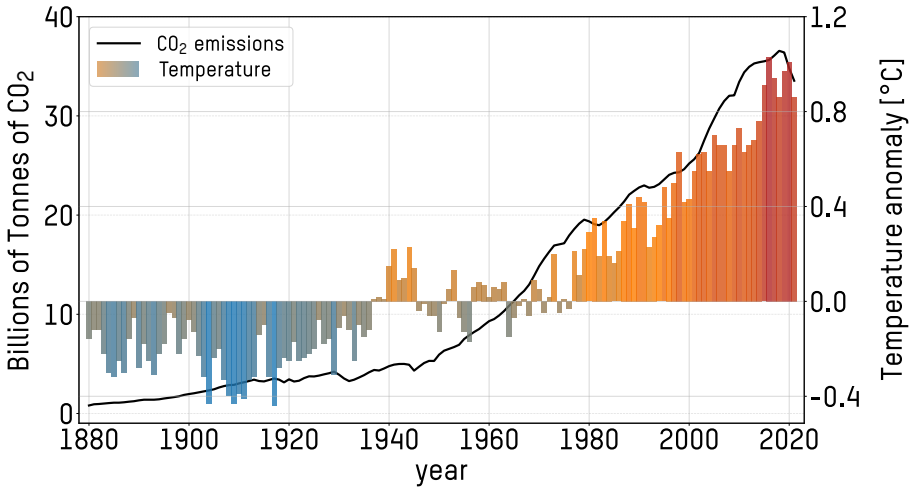

Figure 2.1: *Average global temperature changes (reference period 1951-1980) and world carbon emissions from fossil fuel burning, adapted from [1, 2].*

This unsustainable global warming situation has meant a change in the mindset of society, especially in the last decade. The Intergov-

ernmental Panel on Climate Change Intergovernmental Panel on Climate Change (IPCC) of the United Nations recommended in a special report in October 2018 to limit global warming to 1.5 °C above pre-industrial levels to ensure a more sustainable and equitable society [4]. The European Union (EU) proposed some climate strategies and targets to achieve this and similar objectives, dividing them into deadlines for present and near future decades. Those strategies can be divided into three groups owing to the target year: *2020 climate & energy package*, *2030 climate & energy framework* and *2050 long-term strategy* [5].

This target settled for the year 2020, a 20 % cut in Greenhouse Gas (GHG) emissions (form 1990 levels), the 20 % share of the energy market for renewable energies and 20 % improvement in energy efficiency [6]. In the same way, for the 2030 year, the target percentages are increased to 40 % for GHG emissions reduction, 32 % market share for renewable energies, and 32.5 % in energy efficiency upgrade [7]. Besides, 2050 objectives expect the transition to a climate-neutral society with an economy of net-zero GHG emissions. For all these purposes, the EU wants different sectors such as power, industry, mobility, buildings, agriculture and forestry to play an essential role while leading the way by investigating realistic technological solutions, empowering citizens and aligning action in those areas [8].

Identifying and defining each sector's importance is decisive so that the correct steps are taken to achieve the desired objectives. The GHG emissions of the EU sectors in 2021 can be seen in fig. 2.2, where three main blocks can be defined and connected concerning the climate and energy objectives settled down [9]:

- **Energy Supply:** Represents one-quarter of the total emissions due to the importance of fossil fuels on electricity generation. The increase in renewable energies should counteract this.

- **Industry & Residential and commercial:** This both sectors represents the 33 % of the emissions of EU. with poorly isolated houses and not optimised methodologies and industrial processes as responsible for the problem. Energy efficiency makes a difference in these areas by using new and more efficient technologies, so the total emission will dramatically decrease.

- **Transport:** Transport, together with international aviation and shipping, makes 27 % of the emissions due to using fossil fuel for the traction system of the vehicles. It is worth mentioning the 3 % increase in emissions since 2016 data [9, 10]. This system is based on Internal Combustion Engine (ICE), which is used in almost all the transport ways. With the change in this technology, the decrease in associated direct emissions would be considerable.

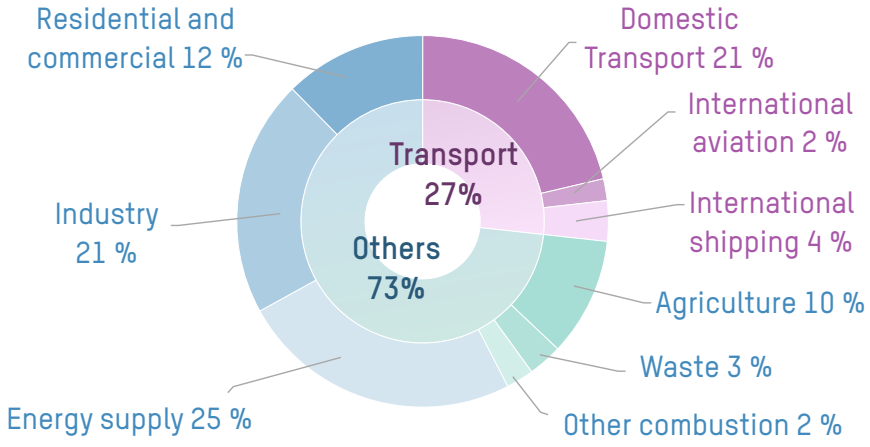

Figure 2.2: *GHG emissions by sector in Europe on the year 2021.*

These three main blocks make 85 % of the total GHG emissions. When it comes to transport, which means mobility for people and goods, the process for the change goes through the innovation of the current predominant technology of ICE. The EU expects by 2030 an emission cut by 30 % (compared to 2005) just in road transportation, which means a significant effort to build the future mobility scenario. Moreover, there is a consensus on the research that the future of energy systems will be dominated by solar photovoltaic and wind power, making 100 % renewable energy systems feasible and cost-effective [11]. This will help on the path to decarbonisation through the electrification of the sector.

For this goal, the sector has started a metamorphosis to electrifying the present transport ways in recent years. This means that Electromobility (eMOV) has been created to replace today's technology and, together with renewable energies as energy suppliers, to reduce or even eliminate the emissions for the sector. Due to the challenges posed by this novelty and the problems to solve, this is the area this PhD thesis will focus on.

2.2 Electromobility

Electromobility could be defined as electricity-powered transport, which means decarbonising a sector based on fossil fuels. For this purpose, today's technology based on fuel combustion has to change to an electricity-powered one without losing the present mobility's characteristics. This means that electric vehicles have some challenges in fulfilling users' expectations:

- **Driving range:** The ICE vehicles have very long driving ranges, allowing them to make long trips without concern. In the case of some public transport and goods transport vehicles, this is critical due to the long distances travelled per day. The new eMOV applications will almost be the same as now, which means that the driving range must be a requirement for the new technology.

  Otherwise, the distance travelled per day by the average car user is not as vast as the goods transport vehicles. The usual urban itinerary is not so challenging; current electric vehicles can face these distances without a problem. However, the charging infrastructure must be available to recharge the cars comfortably.

- **Fast energy recharging:** Refuelling the oil of ICE vehicles takes no more than five minutes. This is another comfort issue directly related to the driving range because fast energy recharging will be essential if electric vehicles have low ranges. Instead, with very high ranges, recharging will become a secondary issue. Nevertheless, refuelling and recharging systems are progressing rapidly to provide the best experience possible.

- **Energy recharging areas:** With petrol stations everywhere, refuelling the oil tank is not a problem with the current vehicles. New technology implementation will suppose the adaptation of all these stations or the creation of new recharging/refuelling areas and stations.

  The usage of electricity opens a broader possibility enabling the charge of fully electric vehicles in any area where the cars are parked. By this, the private garages or even the streets can supply energy to the vehicles, making the process much more comfortable

and easy. Moreover, it brings the possibility of charging the cars whenever they are not needed, at night, for instance, which avoids the charging time issue.

- **Security & reliability:** Although the present vehicles use flammable fuels, they can be considered secure, and due to the maturity of ICE they are also very reliable. The EVs must satisfy both points at least the same way the present technology does.
- **EV prices:** The current ICE vehicles have reached a reasonable market price, whereas as any new technology EVs are much more expensive. This is a clear obstacle and disadvantage for the evolution of the market share and the integration of new vehicles. However, as the technology strengthens and mass production and sale start, the new EV investment cost will decrease gradually.

2.2.1 Electric Vehicle Technologies

To fulfil all these objectives, it is necessary to equip the vehicles with the most suitable technology in Energy Storage System (ESS). Many energy storage systems are available with sufficient reliability to put into effect on eMOV. There are different types, such as mechanical, electrochemical or thermal, but due to each one's characteristics, just a few are appropriate for mobility applications. Moreover, their advantages and disadvantages make only two energy storage systems stand out currently; batteries and fuel cells. Both technologies are being implemented by vehicle manufacturers producing Hybrid Electric Vehicle (HEV) and BEV using batteries, while fuel cells are being used in Fuel Cell Electric Vehicle (FCEV)). The HEV, using the usual ICE together with an electrical power system, were the first step of the fully-battery electric vehicles. Now, BEV and FCEV seem to be the final two configurations of the eMOV. Both systems seem to be the most likely option for reducing emissions from the transport sector.

Other technologies, such as super-capacitors, have been implemented on electric trains. Still, due to their high specific power and considerably low specific energy compared to batteries and fuel cells, they are principally used for power assistance and to take more advantage of regenerative braking [12]. Furthermore, batteries and fuel cells are better choices for electric cars because of their higher specific energy. The fig. 2.3 com-

pares these technologies' energy and power densities.

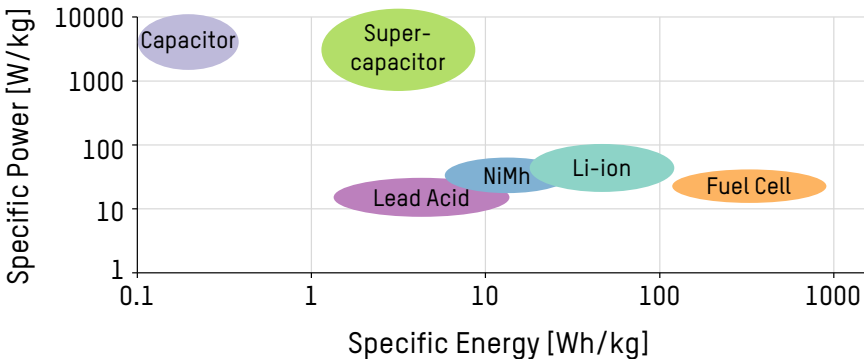

Figure 2.3: *Power and energy density of different ESS Technologies, adapted from [13].*

Nevertheless, both technologies are not at the same development, maturity and usability points. Although batteries' specific energy is considerably lower than fuel cells, it is the best current approach for the EV. FCEVs' have a higher range and refuelling is as fast as in the ICE vehicles. These are key issues analysed before, but current technology prices are not equal to the BEV ones. The price predictions in the following decades (fig. 2.4) show that BEV will lead the electric vehicle market at least on each car's necessary investment. And although the fuel cell will be helpful for specific applications such as long-range transport, it will suffer a slower development and implementation [14].

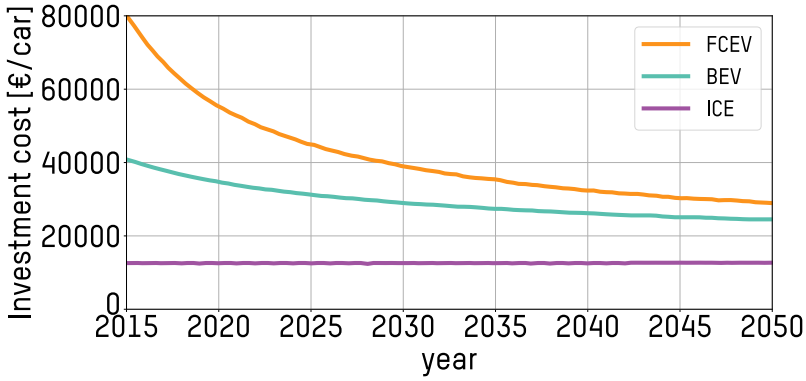

Figure 2.4: *Developments of the investment costs of the vehicles investigated due to technological learning up to 2050, adapted from [14, 15].*

Hydrogen production is also another key issue on FCEV development. Hydrogen must be generated on electrolysis (if non-polluting hydrogen is to be used, avoiding the GHG emissions), compressed or liquefied, transported and stored in that high-pressure condition. Complex facilities are needed to increase before these vehicles gain market share.

Moreover, the whole process decreases the general efficiency of the FCEV considering the well-to-tank and tank-to-wheel process, compared with the simplicity of the BEV. Therefore, the battery technology's overall efficiency is around 77 % whereas the fuel cell reaches 33 %, as shown in fig. 2.5 [16, 17]. Even the efficiency increase in the systems is predicted for the year 2050, the direct electrification is estimated to be around two times more efficient than hydrogen. Moreover, transport decarbonisation based on high electric versus high hydrogen-based scenarios estimates 17.6 % more land needed for renewable energies (based on wind energy estimations), due to increased electricity requirements [18]. Nevertheless, both these technologies are far more efficient than diesel and petrol (carbon neutral, from CO_2 capture) well to wheel efficiencies.

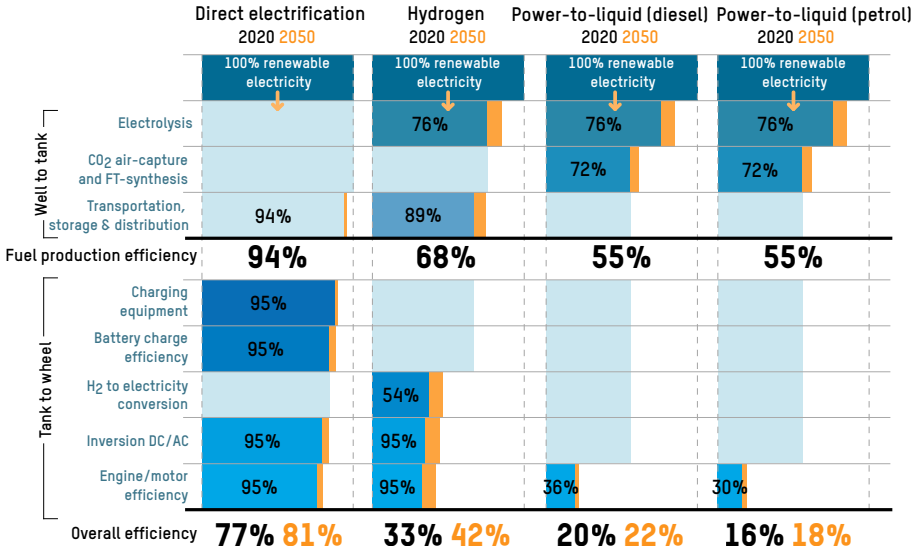

Figure 2.5: *Well to Wheel Efficiency of Battery, Hydrogen, Diesel and petrol EV [17].*

For these reasons, this research will focus on the batteries as ESS due to the current and near-future prevalence for the BEV. Nevertheless, the

eMOV scenario predictions show that both vehicle types will live together in the future.

Even the presented well-to-wheel efficiency and the cost estimations of BEV, their GHG emissions are questioned, mainly focused on battery pack production. In this regard, *Volvo* vehicle manufacturer presented in 2021 an emission research for one of their vehicles in both ICE and BEV technologies. The study is moreover analysed for diverse electric mix scenarios, over the global mix, EU-28 electricity mix and complete renewable mix under wind energy. As depicted in fig. 2.6, over the vehicle's life (200,000 km), the ICE vehicle is the most contaminant, reducing the emissions by more than half with the full renewable electric mix. Moreover, even though the Lithium-ion Battery (LIB) and material production is the most significant contaminant part of the BEV production, only 49,000 km of use can equal the life emissions of both technologies. Therefore, BEV show to be efficient in reducing the GHG emissions. Nevertheless, battery recycling is determinant to reduce the production emissions of this new vehicle technology [19].

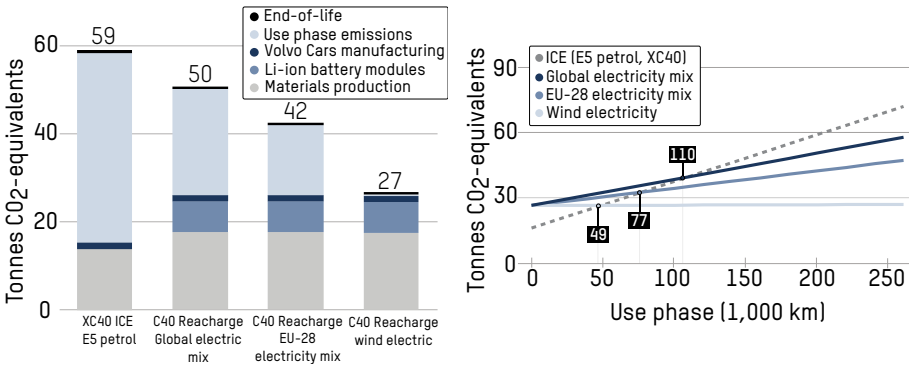

(a) *Carbon footprint for C40 Recharge and XC40 ICE, with different electricity mixes (200,000 km total distance).*

(b) *Total amount of GHG emissions, depending on total kilometres driven, from XC40 ICE (dashed line) and C40 Recharge (with different electricity mixes in the use phase).*

Figure 2.6: *Tonnes of CO_2-equivalent for Volvo ICE and BEV, under full life estimation and in the function of kilometres for different electricity mixes [19].*

2.2.2 Energy Storage System: Lithium Ion Battery

The battery is an electrochemical ESS where electrical energy is transformed into chemical energy and vice versa through a reversible charging and discharging process. These battery cells comprise a positive electrode (cathode), a negative electrode (anode), an electrolyte, a separator, a current collector and a case. Lithium-ion (Li-ion) is the most extended battery type due to its high cell voltage, high energy density, long shelf and life cycle with no memory effect [12]. Moreover, different electrode materials have been developed to achieve better performances, creating many cell types such as $LiCoO_2$ (LCO), $LiNiO_2$ (LNO), $LiMn_2O_4$ (LMO), $LiFePO_4$ (LFP), $LiMnPO_4$ (LMP) and $Li_4Ti_5O_{12}$ (LTO), being the first one the most used since the Li-ion battery was created [20].

In these Li-ion batteries, the anode material acts as the lithium sink and the cathode material as the lithium source while charging, and the opposite happens during discharge. By this, when charging, Li^+ travels from cathode to anode, forming into a lithium atom by combining with charging electrons and depositing between carbon layers as shown in fig. 2.7. The separator, an electrical insulator, separates the positive and the negative electrodes in case of an internal short circuit, allowing the lithium ions to pass through it and blocking the electrons [21, 22].

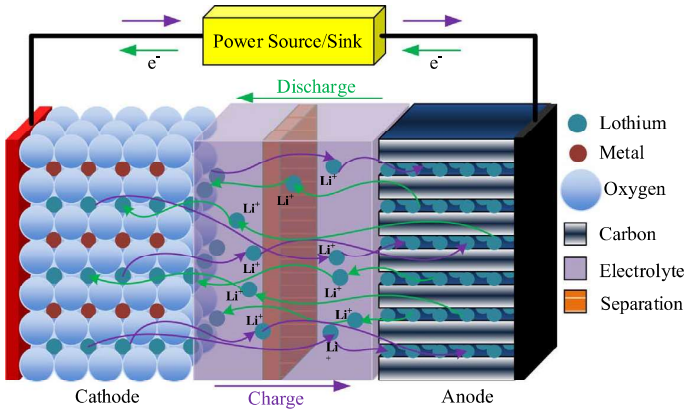

Figure 2.7: *Li-Ion battery operation principle [21].*

Appropriate physical and chemical characteristics of Li-ion batteries made them popular for different applications. As said before, their high voltage, high energy density, long shelf and cycle life, no memory effect,

and relatively small size, lightweight and efficiency of 90-98 %, make them stand out compared with other alternatives [21, 23]. The fig. 2.8 shows the specific energy and the specific power of different types of batteries, where Li-ion prevails. In this way, this technology dominates portable electronic devices with small format batteries. Beyond this, it has also been successfully implemented as the technology of choice for eMOV in hybrid, plug-in hybrid, or fully electric vehicles and for stationary energy storage [24]. This makes this ESS technology the selected one to continue with the analysis in this work.

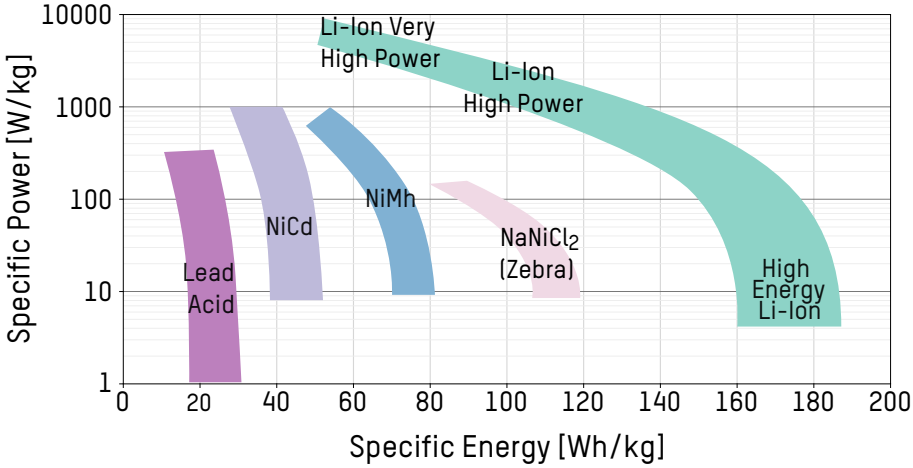

Figure 2.8: *Ragone Plot of battery technologies specific energy and specific power, adapted from [25].*

However, LIB cells' main downside stands in their great overheating potential, critically exacerbated by the high demanding performances and fast charging. Durability and performance are associated with working temperature and temperature differences between the cells. This means the ageing process speeds up with high temperatures [23, 26]. Moreover, whereas the acceptable operating temperature range for LIB is -20 °C to 60 °C, the recommended working temperature to maintain its optimal performance is between 20 °C and 40 °C, with a maximum difference of 5 °C [27–30].

Battery performance worsens outside this temperature range; lithium plating may arise with cold temperatures, which means the lithium dendrites grow on the negative electrode. This loss of some lithium inserted in

the graphite decreases the charge capacity of the cell. With hot temperatures around 90 °C to 120 °C, internal passivating layers decompose, permitting the uncontrolled reaction between electrode and electrolyte and creating exothermic processes, the so-called thermal runaway. This phenomenon may end up with fire, explosion and generation of harmful gas if no action is taken [20, 31].

Moreover, achieving a fast-enough charging battery system aims to increase the charging currents used. By this, heat generation due to joule heating and internal chemical processes of battery cells is increasing in large amounts. This fast charging and high C-rates accelerate the degradation of LIBs, deteriorating capacity and power capabilities [32–35]

Proper operation and major security are essential to counter this degradation and ensure a longer life span [36]. Therefore, thermal stress is controlled through the BTMS. These systems are in charge of temperature adaption inside the optimal range of operation, using different approaches to avoid fast battery degradation and pursue the best performance possible.

This thermal management system must adjust at each battery pack, module or cell to achieve the best performance possible. This task is difficult due to the different sizes and shapes of cells and the modules. The three cell topologies are cylindrical, prismatic and pouch, as seen in fig. 2.9.

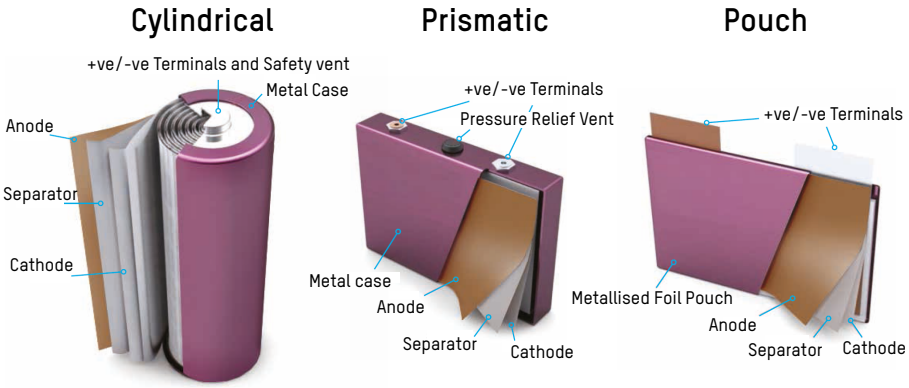

Figure 2.9: *Lithium-ion battery cell topologies [37].*

All shapes are made of repeated layers of anode, cathode and separ-

ator. The current collector connects this anode and cathode to the cell terminal. This means the current will get into and leave the cells from there, going through all the layers [38]. As heat is generated partially by Joule heating, cell terminals are the perfect way to remove the heat from inside the cells. Therefore, focusing the BTMS contact with these terminals will make the difference in cooling ability and efficiency.

2.2.2.1 Heat Generation Mechanisms

The heat generation mechanisms in lithium-ion batteries involve several factors:

Electrochemical reactions: Lithium ions move between the positive (cathode) and negative (anode) electrodes during charge and discharge cycles. Lithium ions are intercalated and deintercalated inside the electrode materials during these processes. Due to the energy generated during the redox processes, heat production can occur in conjunction with electrochemical reactions.

Internal Resistance: As electric current passes through the battery, it encounters resistance, which causes ohmic heating. The electrolyte, current collectors, and electrode-electrolyte interfaces are only a few of the factors that contribute to internal resistance. As the current flows through the battery, the resistance results in energy losses and heat production.

Side Reactions: Side reactions can happen inside the electrolyte itself or at the electrode-electrolyte contacts. For instance, the decomposition of solid-electrolyte interphase (SEI) layers might occur due to interactions between the electrolyte and electrode materials. These side reactions might result in heat production and irreversibly deplete lithium ions.

Heat of Mixing: Heat of mixing refers to the heat released or absorbed when different substances mix. When lithium salts in the electrolyte dissolve or when the electrolyte and electrode materials interact in lithium-ion batteries, the heat of mixing may arise. The heat of mixing can contribute to the overall heat generation within the battery.

Bernardi et al. [39] presented a comprehensive energy balance framework for battery systems, encompassing various thermal aspects such

as reaction-related heat, alterations in heat capacity, phase changes, mixing effects, and electrical work. This framework is captured by eq. (2.1), which provides a concise representation of the interaction between these factors. In this equation, $\dot{Q}$ denotes the heat transfer rate between the battery system and its surroundings, $I{\cdot}V$ represents the electrical work, and the terms on the right-hand side of the equation collectively contribute to the overall change in energy within the system. Notably, these terms account for the influences of mixing, phase changes, and simultaneous electrochemical reactions, with open circuit potentials being composition-dependent.

$$
\begin{aligned}
\dot{Q} - I \cdot V = \\
\sum_{l} \frac{d}{dt}\left(I_l T^2 \frac{d\frac{U_{l,avg}}{dT}}{dT} \right) \text{ enthalpy-of-reaction} \\
- \sum_{j} \frac{d}{dt}\left[\int_{vj} \sum_{i} c_{i,j} R T^2 \frac{\partial}{\partial T} \ln\left(\frac{\gamma_{i,j}}{\gamma_{i,j}^{avg}} \right) dv_j \right] \text{ enthalpy-of-mixing} \\
- \sum_{jj \neq m} \sum_{i} \left[\left(\Delta H_{ij \rightarrow m}^{0} - R T^2 \frac{d}{dT} \ln \frac{\gamma_{i,m}^{avg}}{\gamma_{i,j}^{avg}} \right) \frac{dn_{i,j}}{dt} \right] \text{ phase-change} \\
+ \frac{dT}{dt}\left(\sum_{j} \sum_{i} {n_{i,j}}^{0} \bar{C}_{pi,j}^{avg} + \sum_{l} \frac{\int_0^t I_l dt}{n_l F} \Delta C_{pl} + \sum_{jj \neq m} \sum_{i} \left(\bar{C}_{pi,j}^{avg} - \right. \right. \\
\left. \left. \bar{C}_{pi,m}^{avg} \right) \left(n_{i,j} - n_{i,j}^{0} \right) \right) \text{ heat-capacity}
\end{aligned}
\tag{2.1}
$$

Bernardi et al. [39] also incorporated specific instances and simplifications of the general energy equation in their research. These modifications are particularly relevant when certain assumptions are made. For instance, if an average heat capacity is employed, the enthalpies of mixing and phase changes are not considered. Additionally, the enthalpy-of-reaction is expressed regarding the reversible work contributions and the entropic heat. Furthermore, the electrical work is redefined as an irreversible heat effect, considering the associated losses. These refinements allow for a more streamlined and practical application of the energy equation in battery systems analysis.

Furthermore, it is assumed that only one primary electrochemical reaction occurs. This assumption is deemed valid for the cells in this study, as they exhibit high current efficiency and demonstrate stable resistance over multiple cycles, suggesting the absence of significant side reactions. Consequently, the consideration of side reactions and their associated heat production or consumption is omitted in this work. Forgez et al. [40] similarly assumed that any side reactions contributing to ageing were sufficiently slow to be disregarded, along with the term representing the heat generated or consumed by potential chemical reactions occurring within the cell. In the case of lithium-ion batteries devoid of side reactions, only a single reaction transpires at each electrode, while phase change effects are non-existent [41].

Notably, as indicated by [42, 43], in a well-designed battery system to mitigate concentration overpotential, the heat of mixing is considered negligible. Forgez et al. [40] further asserted that in electrochemical systems with favourable transport properties, concentration gradients are typically limited, thereby allowing for the omission of the heat of mixing term. Considering that the batteries examined in this study are specifically designed for high-power applications, it is reasonable to assume that they adhere to the aforementioned principle. Moreover, neglecting heat in mixing terms is deemed acceptable when the particle size is sufficiently small, characteristic of commercial battery designs [41].

Consequently, the general energy balance is simplified, and the heat generation equation used in this work is determined as follows:

$$\dot{Q} = I(V - U) + IT\frac{dU}{dT} \tag{2.2}$$

2.3 Battery Thermal Management Systems

The thermal management system is pivotal in ensuring the security, reliability, and efficiency of battery packs, electronics, and even fuel cells, considering their operation within specific temperature ranges. However, the subsequent analysis presented in this study narrows its focus to thermal management at the module or battery pack level in electromobility-oriented applications. This deliberate approach aims

to deliver a more concise, precise, and valuable investigation, given that LIBs represents the most widely adopted ESS implementation in electromobility. By concentrating on this particular aspect, the study aims to provide comprehensive insights into the thermal management practices and challenges encountered in this domain.

The specific requirements imposed by mobility applications significantly impact the criteria a well-functioning thermal management system must satisfy. For example, the power and energy density rates relative to the battery's volume and mass units are paramount. Consequently, specific thermal management systems may be more suitable to meet these requirements effectively. Additionally, it is worth noting that various thermal management systems explored in the following sections can leverage the existing Heating, Ventilation and Air Conditioning (HVAC) system in vehicles, regardless of whether they are powered by electricity or combustion engines. The HVAC system is an integral component in every vehicle, maintaining the comfort level of passengers or equipment being transported. As illustrated in fig. 2.10, the HVAC system operates on the principle of heat pumps, comprising two heat exchangers, a compressor, and an expansion valve. The integration between the HVAC system and the thermal management system can vary in complexity depending on the characteristics of each respective TMS. This integration is crucial in achieving a harmonious and efficient overall system, resulting in a simplified, lightweight, and highly efficient electric vehicle or energy storage system.

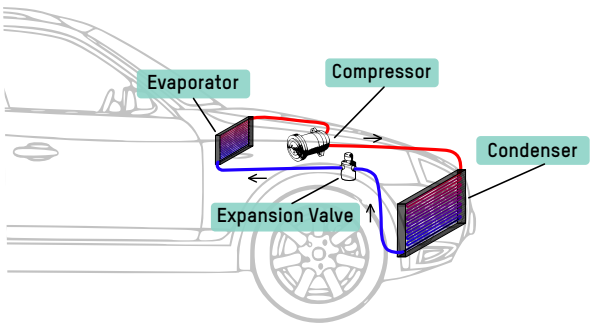

Figure 2.10: *HVAC operation scheme*

A broad classification can be made between conventional BTMS currently implemented in most commercial electric vehicles and novel or ad-

vanced thermal management systems. Conventional BTMS have reached a high level of maturity due to their widespread adoption in the industry. On the other hand, advanced systems are still in the early stages of research and development, lacking consolidated solutions and raising uncertainties regarding their practical implementation. These advanced systems represent a field of ongoing exploration and innovation, aiming to address emerging challenges and improve the thermal management performance of electric vehicles.

The analysis of each thermal management system is structured into four key sections. Firstly, the prevailing physical phenomena underlying the system's operation are described, providing an understanding of its fundamental principles. Secondly, a possible practical implementation of the system in electric vehicles is outlined, highlighting its integration and functionality within an BEV context. Thirdly, the current state of the technology, ongoing research efforts, and advancements made in the field are thoroughly examined, providing insights into the latest developments and potential future directions. Finally, a comprehensive assessment of the system's strengths and weaknesses is conducted, facilitating a general conclusion regarding its overall efficacy and suitability.

2.3.1 Conventional BTMS

Within the first group of thermal management systems, notable examples include those that employ forced air convection and water ethylene-glycol convection for cooling the battery modules. The forced air convection systems, however, are gradually becoming outdated due to their limited capacity for heat extraction. Conversely, the forced water ethylene-glycol convection systems have gained significant traction and are well-established among leading manufacturers of electric passenger cars. These systems typically utilise the vehicle's HVAC system with a heat exchanger to dissipate the generated heat to the surrounding environment. This integrated approach allows for effective temperature regulation of the battery pack, allowing it to cool below ambient temperature during hot weather conditions. Using forced water ethylene-glycol convection systems represents a reliable and widely adopted solution, ensuring proper thermal management and enhancing electric vehicle battery packs' overall performance and longevity.

2.3.1.1 Forced Air Cooling

Physical phenomena & general operation:

This particular system utilises air as the cooling medium. The heat generated within the battery is transferred to the surrounding environment by passing air over the surface of the cells, effectively cooling down the battery pack. The airflow can be initially cooled by routing it through a heat exchanger connected to the HVAC system if necessary. This arrangement enables the batteries' temperature to decrease from ambient levels or, at the very least, approach ambient temperature.

In this cooling process, sensible heat is employed for refrigeration. The heat energy is transferred to the air, increasing its temperature without causing any change in its physical state. When evaluating this type of cooling, it is essential to consider the specific heat capacity (C_p) since the ability of the fluid to absorb heat with temperature change depends on it. The specific heat capacity for air is 1.012 kJ/kg·K (under normal environmental conditions), four times lower than other fluids such as water. The eq. (2.3) emphasises the significance of specific heat capacity in this context,

$$\dot{Q} = \dot{m} \cdot C_p \cdot \Delta T \tag{2.3}$$

where $\dot{Q}$ is the heat energy per time unit absorbed by the air in [J/s], $\dot{m}$ is the air mass flow in [kg/s], C_p is the specific heat in [J/kg·K] and ΔT is the temperature change of the fluid in [K]. This means that a higher flow rate or a fluid with a greater specific heat is needed to increase the heat dissipated from the batteries.

Practical implementation:

The implementation of these cooling systems is relatively straightforward and uncomplicated. It primarily involves using a fan to induce airflow through the spaces between the battery cells [44, 45]. This spatial separation between the cells is crucial to enhance air circulation over the entire cell surface, thereby maximising the contact area and improving heat transfer efficiency [46, 47]. However, it is essential to note that leaving space between the cells increases the overall volume occupied by the battery pack. This increase in volume has implications for the power and en-

ergy density of the battery system [48, 49]. Thus, while this configuration enhances cooling performance, it also introduces a trade-off by affecting the power-to-energy ratio and overall energy storage capacity. Careful consideration must be given to striking a balance between effective cooling and optimising the power and energy density of the battery system.

The air-cooling BTMS is depicted schematically in fig. 2.11. This representation shows the system without any connection to the vehicle's HVAC system. However, a heat exchanger connected to the HVAC system can be employed if lower battery temperatures are required. Passing the incoming air through this heat exchanger can reduce its temperature, resulting in improved cooling capacity. This approach allows for better temperature control of the battery pack but comes at the expense of overall system efficiency and a potential increase in volume and weight ratios.

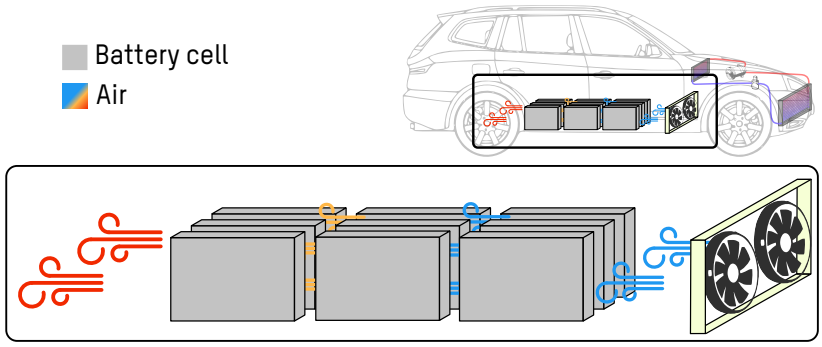

Figure 2.11: *Air cooling implementation scheme.*

Several manufacturers have incorporated this cooling system in their electric or hybrid vehicles, as exemplified by the Kia Soul in fig. 2.12a and the Toyota Prius in fig. 2.12b. With their smaller battery packs, these vehicles can effectively utilise such systems. However, it should be noted that this cooling system may prove insufficient to meet the stringent thermal management requirements for new-generation BEVs equipped with higher-capacity batteries and fast charging capabilities.

Current research:

Various investigations conducted on air cooling systems have highlighted the main challenges associated with this technology. Researchers have observed that due to air's low specific heat capacity, higher airflow

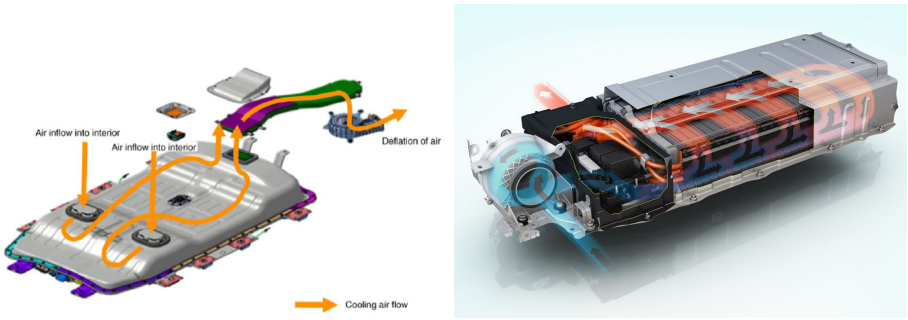

(a) *Kia Soul's cooling system [50].* ***(b)*** *Toyota Prius's cooling system [51].*

Figure 2.12: *Implemented air cooling systems on BEV's*

rates are required to achieve comparable cooling results as liquid-based systems, as depicted in fig. 2.13. The cooling capacity of an air system is up to nine times lower than that of a liquid system [49]. Similarly, other studies have concluded that air cooling systems consume two to three times more energy than alternative technologies to maintain the same temperature levels on the battery cells [48]. This higher energy consumption is attributed to the increased airflow rates, resulting in increased auxiliary power consumption [52, 53].

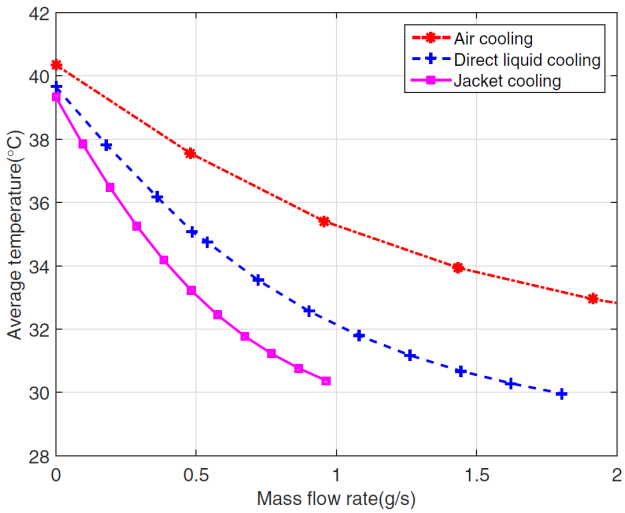

Figure 2.13: *Air vs liquid cooling capacities [48].*

Consequently, this adversely affects the overall efficiency of the batteries and leads to a decrease in the overall performance of the BEV. Additionally, specific configurations of air-cooling BTMS have exhibited a thermal gradient exceeding 5 °C, even when adequately controlling the maximum temperature [54]. These findings highlight the limitations and drawbacks of air cooling systems, necessitating the exploration of more efficient alternatives to meet the evolving requirements of BEVs.

BTMS Conclusions:

Considering the aforementioned factors, air cooling is a simple, lightweight, easy-to-maintain, cost-effective thermal management system. Air, a freely available dielectric fluid, makes it readily accessible for cooling purposes at all times. Some car manufacturers have successfully implemented this solution in their electric vehicles. However, as battery capacities increase, the suitability of air cooling becomes limited in meeting the demands of longer driving ranges and higher charging currents [55, 56].

These limitations pose significant challenges for air cooling systems to meet the minimum requirements of efficiency and effectiveness in battery cooling. Forced air convection systems, which rely on sufficient interspacing between the cells, often incur a penalty in terms of the volumetric ratio of the system. Moreover, these systems tend to exhibit higher thermal dispersion, leading to more significant inefficiencies in the electrical balance of the battery pack.

Considering these factors, it becomes evident that air cooling is not well-suited for the most demanding tasks and fails to meet the increasing requirements of efficiency and effectiveness in battery cooling. Alternative thermal management systems must be explored and implemented to address the evolving needs of electric vehicles with larger battery capacities.

2.3.1.2 Forced Liquid Cooling

Physical phenomena & general operation:

Liquid-based thermal management systems serve as a suitable alternative to air cooling methods, particularly in more demanding applications

and when dealing with abusive conditions of LIBs that require higher heat transfer performance. Although air cooling is relatively easy to design [20, 49, 57, 58], liquid cooling offers superior heat dissipation capabilities. This approach follows the same principle as air cooling, wherein the heat generated by the battery cells is removed through sensible heat transfer, increasing fluid temperature as it flows through the cells.

A cooler, such as a chiller, dissipates the heat from the fluid. The chiller utilises a refrigerant in a closed loop to extract heat from the cooled area and pump it to where it can be transferred to the atmosphere. However, the HVAC system can be utilised to eliminate the need for additional equipment and improve volume and weight ratios, which effectively functions as a chiller. In this configuration, the heat is transferred from the cells to the fluid and ultimately to the air conditioning system through a heat exchanger, removing it from the vehicle entirely.

When using water as the heat transfer fluid, a freezing problem may arise in cold climate conditions. To address this issue, anti-freeze liquids, such as a 50:50 mixture of ethylene glycol and water (w-e50), are commonly employed [59]. It is important to note that water has a significantly higher specific heat capacity compared to air, with values of 4.18 kJ/kg·K for water and 3.3 kJ/kg·K for a water ethylene-glycol 50% mixture (w-e50), under normal environmental conditions. This higher specific heat capacity allows liquids to effectively dissipate heat while raising their temperature to a lesser extent, making them more efficient coolants than air.

Practical implementation:

In liquid-based thermal management systems, the most common configuration in current commercial vehicles involves indirectly cooling the battery cells using a cold plate. Indirect cooling means no direct physical contact between the cooling fluid and the battery cells. Instead, a cold plate is used as an intermediary component. The cold plate is typically a metal plate with channels through which the cooling fluid circulates, as seen in fig. 2.14. It is placed in contact with the surface of the cells to extract heat from them. An electrical insulation layer, Thermal Interface Material (TIM), is placed between the cold plate and the battery cells to prevent short circuits. TIMs provide both electrical insulation and efficient thermal conduction.

Figure 2.14: *Commercial cold plate [60].*

Choosing an appropriate geometric solution that covers the cell surfaces and minimises the volume of the battery pack is crucial in this configuration. For example, in the shown example fig. 2.15, cold plates are positioned among every four cells laterally. Additionally, the BTMS is connected to the HVAC system via a heat exchanger in this configuration.

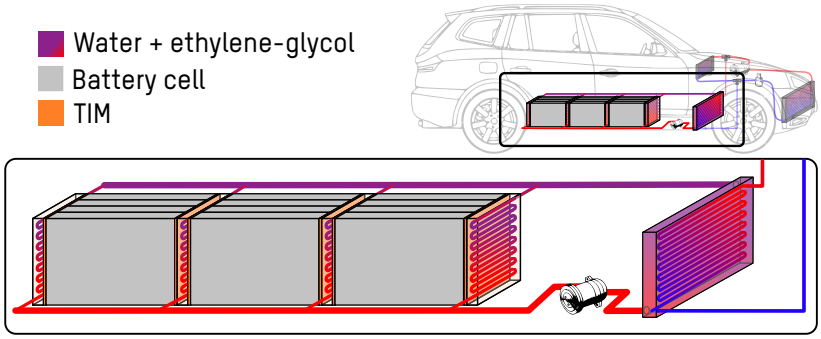

Figure 2.15: *Water + ethylene glycol cooling implementation scheme*

Effective water/glycol systems have been implemented in certain vehicles, such as the Tesla Model S fig. 2.16a, demonstrating good cooling performance in a compact system design. Similarly, the Audi e-Tron fig. 2.16b features a different configuration but employs a similar cooling concept. These examples highlight the utilisation of indirect cooling with cold plates and the integration of water/glycol systems in achieving efficient cooling for battery packs in electric vehicles.

Current research:

The design and structural configuration of batteries play a significant role in the performance of thermal management systems. Several studies have demonstrated the importance of battery design in improving thermal conductivity and reducing maximum temperature differences. By compar-

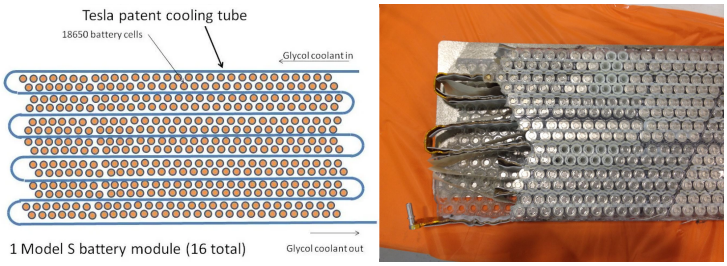

(a) *Tesla Model S's water-glycol cooling system [61, 62].*

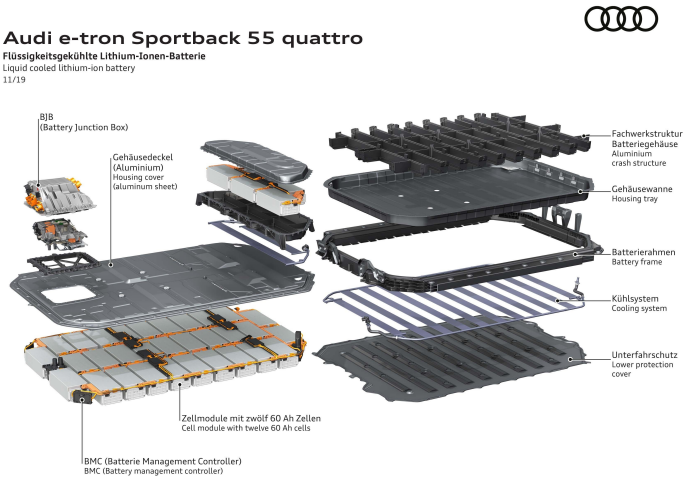

(b) *Audi e-Tron Sportback 55 quattro's water-glycol cooling system [63].*

Figure 2.16: *Implemented water-glycol BTMS systems by Tesla and Audi.*

ing different designs, it has been shown that the equivalent thermal conductivity ratio can be improved by up to 64 %, and the maximum temperature difference can be reduced to below 5 °C [64]. However, it's important to note that there is always a certain amount of thermal resistance between the battery and the heat transfer fluid due to the electrical insulation of the cold plate. This resistance can limit the effectiveness of heat transfer in these systems [20, 65].

Micro-channel heat sinks, primarily used for cooling power electronics with high heat generation, operate similarly to cold plates. In this case, the fluid flows through micro-channels within the heat sink. Studies have demonstrated a reduced thermal resistance of up to 25 % compared to

systems that use standard cold plates [66]. Researchers are continuously optimising the shape of the cold plate, often by narrowing the ducts, to reduce thermal resistance further [67–69]. Nevertheless, the increase in energy consumption due to head losses generated is the greatest obstacle to implementing more and more smaller ducts in the world of batteries [70, 71].

Water ethylene-glycol solutions with cold plates featuring narrow ducts have shown promising results for thermal management, offering more suitable required pumping power [72]. However, attention needs to be given to potential issues such as leakage [73]. Further research and development are required to address these challenges and optimise the performance of such systems.

BTMS Conclusions:

Indeed, liquid-based thermal management systems, such as those using water-glycol solutions with cold plates, offer significant improvements over air cooling systems. Water-glycol solutions' higher heat absorption properties result in increased cooling efficiency and improved thermal management. These liquid systems can maintain battery temperatures even under high work intensities, making them a reliable solution for various applications, including eMOV. They have been implemented in many BEVs and have proven effective in ensuring proper battery temperature control.

However, it is also essential to consider these systems' drawbacks. It adds weight and volume to the system, negatively impacting the specific energy and energy density ratio, a crucial factor in areas like eMOV, where lightweight and efficient systems are desired.

Finding a balance between the effectiveness of thermal management and the weight and volume requirements is challenging in designing liquid-based cooling systems for batteries. Further research and development are necessary to optimise the design and address these challenges, ensuring that the thermal management systems meet the requirements of efficiency, reliability, and lightweight design in the context of electric mobility applications.

2.3.2 Advanced BTMS

In the field of thermal management for electromobility, there are indeed several alternative solutions that have been explored beyond conventional methods. These solutions have been implemented on a small scale and may require further consideration of practical aspects and real limits specific to electromobility.

Several solutions in thermal management systems utilise the phenomenon of phase change, which involves the transition from a solid to a liquid state or from a liquid to a gaseous state. Thermal energy can be stored in the form of sensible heat, as seen in conventional systems, by increasing the temperature of the heat transfer fluid. Alternatively, it can be stored as latent heat by inducing a phase change in the heat transfer fluid. This phase change mechanism offers a greater capacity to extract heat due to the energy required for the physical transformation. The ability of a substance to absorb heat is determined by its Specific Latent Heat (SLH). A higher SLH indicates a greater capacity to absorb or release energy. The eq. (2.4) represents the heat absorption during a phase change process,

$$\dot{Q} = \dot{m} \cdot L \tag{2.4}$$

where $\dot{Q}$ is the amount of power released or absorbed during the change of phase of the substance in [kJ/s], the variable m is the mass flow of the substance in [kg/s] and the L is the specific latent heat for a particular substance in [kJ/kg]. It is important to note that a higher value of specific latent heat indicates a substance's increased capacity to absorb or release heat. Moreover, it should be recognised that the specific latent heat of vaporisation differs from that of fusion, with the former being higher. This implies that vaporisation can absorb greater amounts of heat energy compared to the melting process. For example, water exhibits a specific latent heat of vaporisation of 2260 kJ/kg, whereas its specific latent heat of fusion is only 334 kJ/kg. The table 2.1 compares the specific latent heat of evaporation for various substances, enabling the observation of their differences.

However, this cooling technique often presents practical challenges, including overpressures, hydraulic imbalances, and thermal imbalances

Table 2.1: *Specific Latent Heat of Vaporisation of some substances [74, 75].*

Substance	SLH of vaporisation [kJ/kg]
Water	2260
Acetone	515
Ethanol	844
Novec 7000	142
Novec 7300	102

that are difficult to manage and control. Alternative solutions such as PCM have been investigated in specific environments. However, a comprehensive analysis is required to ascertain their effectiveness across different applications.

There is no clear consensus regarding whether there is a BTMS at the module or battery pack level that is superior to cold plate liquid cooling. Various solutions that have tried to go in this direction are discussed below:

2.3.2.1 Forced Refrigerant Cooling

Physical phenomena & general operation:

The natural evolution of liquid indirect forced convection cooling uses cold plates where refrigerants circulate. This represents a notable difference compared to the w-e50 system, as it involves a phase change and utilises latent heat as a cooling medium. This approach offers a more efficient BTMS by effectively dissipating heat from the cells without significantly altering the fluid temperature.

The concept behind this system is to eliminate the need for an intermediate water circuit that passes through a chiller or heat exchanger in contact with the vehicle's HVAC system. Instead, the cold plate serves as a refrigerant evaporator by incorporating a second loop for the passengers and batteries within the HVAC system. By doing so, it becomes possible to eliminate the heat exchanger used in the w-e50 system, thereby reducing the weight and volume of the thermal management system to some extent.

Practical implementation:

In configuring a cold plate system using refrigerant, the setup is sim-

ilar to the w-e50 system depicted in fig. 2.15. The cold plates must be positioned to ensure good contact with the battery cells, maximising the effective heat transfer area. Just like in the w-e50 system, electrical insulation is still required, and TIM is used, which introduces some thermal inefficiency.

Figure 2.17 illustrates a possible configuration of this system, where a direct connection with the HVAC system eliminates the need for a separate heat exchanger. This improvement contributes to enhancing the overall volume and weight ratio of the battery pack.

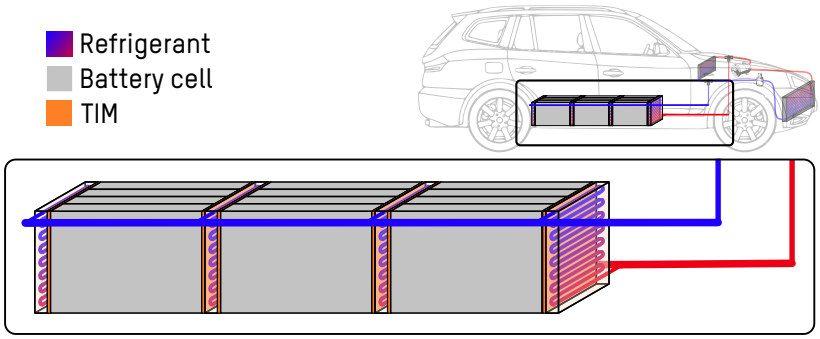

Figure 2.17: *Forced Refrigerant cooling implementation scheme*

Current research:

Studies have shown that refrigerant cooling, particularly in a two-phase configuration, can meet temperature requirements even under harsh environmental conditions more effectively than liquid cooling under normal conditions. In specific investigations, refrigerant cooling outperformed liquid cooling regarding battery capacity and internal resistance during battery ageing under harsh conditions [76–79].

Specifically, the two-phase refrigerant cooling demonstrated a 16.1 % higher battery capacity and a 15 % lower internal resistance than liquid cooling under such harsh environmental conditions [80]. These findings highlight the potential advantages of refrigerant-based cooling systems for maintaining optimal battery performance and longevity, especially in demanding operating conditions.

BTMS Conclusions:

While natural refrigerants like propane or CO_2 possess specific dielectric properties, which could address electrical issues and eliminate the need for TIMs, they also present significant drawbacks that limit their feasibility in electromobility. Propane, for instance, is highly flammable, posing safety concerns. CO_2, on the other hand, requires high operating pressures, which can introduce system design and maintenance challenges.

Although these natural refrigerants may be considered potential candidates for thermal management systems implementation, their drawbacks make them less suitable for widespread adoption in the automotive industry. Nonetheless, some vehicles have already implemented such refrigerants in their cooling systems.

Additionally, when using refrigerants with a phase change, there can be difficulties in achieving hydraulic balance in the refrigerant flow among the various cold plates within the battery pack. Achieving a uniform distribution of refrigerant flow and maintaining consistent cooling performance across all cells can be a technical challenge that needs to be carefully addressed in system design and operation.

2.3.2.2 Heat-Pipe Cooling

Physical phenomena & general operation:

The heat pipe is an alternative passive thermal management system based on a closed-tube casing divided into three sections: the evaporator, adiabatic, and condenser. A working fluid is contained within the heat pipe, and its physical behaviour is similar to that of refrigerants, utilising the latent heat of the working fluid for heat removal. However, the key distinction lies in the fluid choice, with acetone commonly employed in heat pipes.

The operation of heat pipes is straightforward. The fluid within the heat pipe exists in a saturated state. As heat is transferred from the battery cells, the fluid evaporates in the evaporator section. The generated steam moves towards the condenser due to the pressure difference. The condenser section of the heat pipe is in a cooler zone, causing the fluid to condense and release heat, thereby reducing the stored latent heat en-

ergy. The thermal energy is subsequently transferred to other systems, such as HVAC, to dissipate it into the environment. The capillary force, resulting from the heat pipe's structural design, facilitates the fluid's return to the hot zone, completing the thermal cycle [81, 82]. The fig. 2.18 illustrates the fundamental operating principle of a heat pipe.

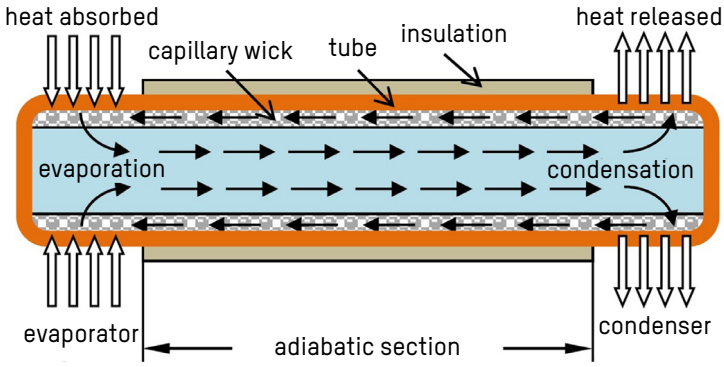

Figure 2.18: *Heat-pipe operation principle [82].*

Practical implementation:

The configuration of these systems encounters similar challenges to those encountered with w-e50 or refrigerant systems when utilising cold plates. Achieving proper contact for enhanced heat transfer and ensuring effective thermal insulation become crucial design considerations. The fig. 2.19 illustrates a potential configuration for this technology, wherein a plate consisting of heat pipes is inserted every four cells, akin to the approach employed with cold plates.

In this configuration, the condenser side of the heat pipes is connected to the HVAC circuit, incorporating a refrigerant loop. As a result, the acetone vapour within the heat pipes condenses, returning to the cell zone and enabling continuous fluid circulation. Another viable option is to expose the condenser zone of the heat pipes to the ambient air, despite a reduction in cooling capacity due to the properties of the air. Consequently, the more suitable choice is connecting the heat pipes to the HVAC system.

Current research:

Heat pipes exhibit a significant heat dissipation capacity relative to

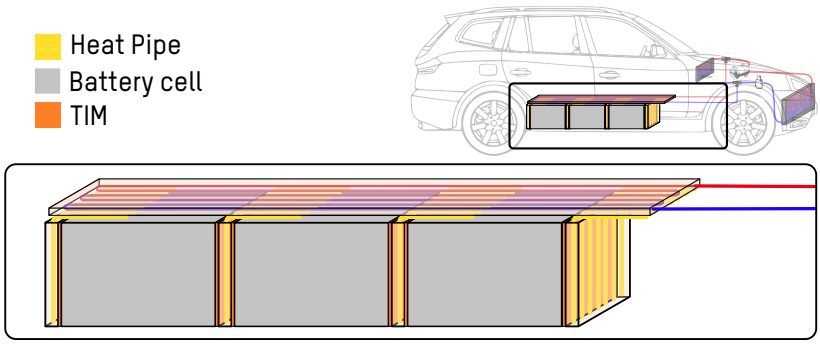

Figure 2.19: *Heat-pipe cooling implementation scheme.*

their compact dimensions. This characteristic makes them highly efficient for cooling small areas that are challenging to access, thus finding widespread application in smartphones and other electronic devices. For example, a heat pipe measuring 2x7x120 mm can achieve heat fluxes of approximately 200 W/cm^2 [83]. Nevertheless, the primary challenge lies in maximising the contact area of the evaporator to enhance heat transfer [84–89].

Several studies have reported positive outcomes when employing heat pipes with batteries. Combined with heat dissipation methods like cold plates, the battery temperature could be effectively maintained below 50 °C, with a maximum temperature difference not exceeding 5 °C [90]. It is crucial to note that these results are highly dependent on the heat generation characteristics of the battery cells and should be interpreted within the context of specific operating conditions.

BTMS Conclusions:

Heat pipes offer an advantageous solution for cooling in areas with limited space and challenging access, as they enable efficient heat extraction and transfer to a separate region where dissipation can occur with fewer constraints. However, similar challenges to cold plate cooling may arise when applied to batteries, such as thermal resistances between the battery and the fluid. The attained temperatures are influenced mainly by the heat generated, posing potential difficulties for high-capacity batteries. While heat pipes provide a compact cooling method, it is essential to note that additional heat exchangers or systems are necessary for the

final dissipation of heat, which is a significant consideration for implementing these systems.

2.3.2.3 Phase Change Material Cooling

Physical phenomena & general operation:

Phase Change Material (PCM) has recently gained considerable attention for passive cooling applications, particularly in stationary settings like regulating building temperatures. PCM consists of solid materials, typically paraffin, that leverage the melting process to maintain a constant battery temperature. When the PCM melts or solidifies at a specific temperature, it can store and release heat to the surrounding system. Like the previously discussed technologies, PCM harnesses latent heat to keep the battery cells within a specified temperature range, at least during the melting process [91–93]. PCM is a cost-effective and non-corrosive thermal management system with a significant latent heat capacity [94]. It is proposed as an effective means to enhance thermal inertia, mitigating temperature peaks or abrupt fluctuations [95]. However, for electromobility applications, the suitability of PCM is less clear. Once the phase change occurs, and with limited time for solidification, the cooling capacity of the batteries may be compromised.

Practical implementation:

To maximise the cooling effect, PCM must have a significant contact area with the battery element. One approach is to apply a coat of PCM directly onto the battery surfaces, creating an encapsulation. This passive configuration enables the PCM to melt and absorb the heat generated by the cells. The system's cooling power is directly influenced by the amount of PCM used, as it determines the quantity of the substance available to absorb heat.

However, in scenarios involving high heat generation over extended periods, the BTMS may need to be complemented with another refrigeration system to ensure sustained effectiveness [96]. For applications like eMOV, where there is limited time for the PCM to solidify passively, the simultaneous use of an additional cooling system becomes necessary. The fig. 2.20 illustrates a schematic representation of this setup, featuring PCM encapsulation alongside a cold plate positioned over on it.

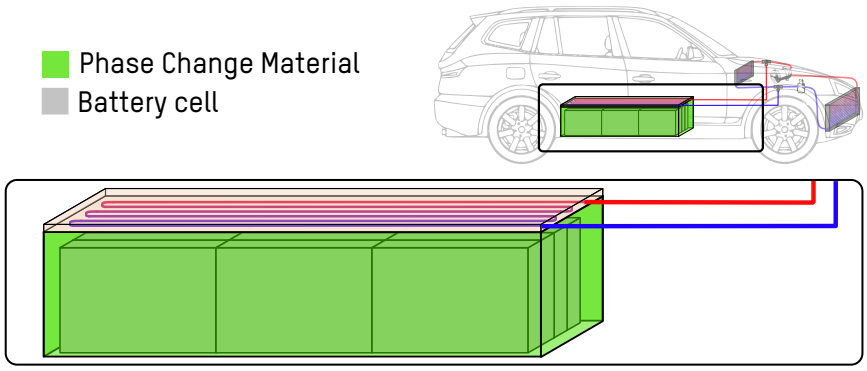

Figure 2.20: *PCM cooling implementation scheme.*

Current research:

Numerous studies have provided evidence of phase change materials' effectiveness in reducing the peak temperatures of batteries. Furthermore, it has been observed that during the relaxation period, when the PCM is in a melted state, and the battery remains below the melting temperature, the latent heat stored in the PCM slightly warms the battery, enhancing its capacity and improving energy efficiency, particularly in colder environmental conditions [95, 97]. The fig. 2.21 illustrates the temperature difference when comparing a heater cooled by air with and without a PCM wrap. The versatility of PCM is also a safety feature, as it can prevent short circuits and facilitate heat dissipation from damaged cells [98].

It is essential to acknowledge that temperature control primarily relies on the material's ability to absorb latent heat. Once in a liquid state, the PCM experiences a significant reduction in its cooling capacity and thermal conductivity. To address these limitations, various materials are incorporated to enhance the effectiveness of paraffin-based compounds. Expanded graphite and copper meshes are commonly utilised elements in these formulations. Graphite prevents paraffin leakage, while the copper mesh enhances heat conduction, thereby improving heat dissipation from the battery. As a result, these modifications lead to enhanced heat dissipation, greater temperature uniformity, and improved performance compared to other PCM formulations [99].

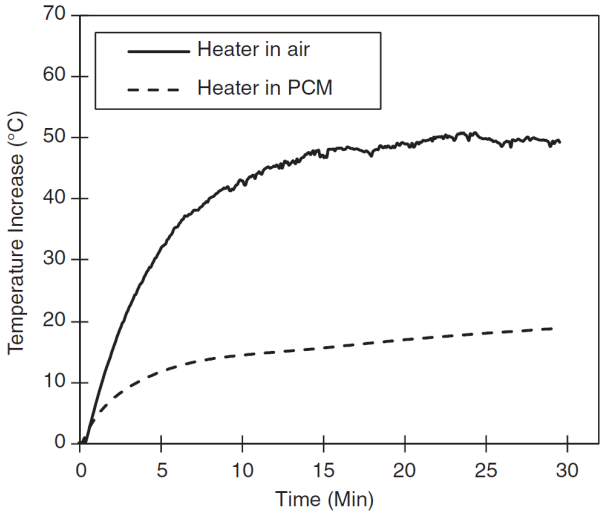

Figure 2.21: *Heater temperature with and without PCM [95].*

BTMS Conclusions:

The phase change material is a passive cooling system that offers compact size, affordability, and the absence of a circulation system. It can remarkably mitigate temperature fluctuations and peaks by leveraging increased thermal inertia. However, it is essential to note that PCM faces challenges such as leakage and limited structural strength. Moreover, the thermal conductivity of PCM is inherently low, necessitating the incorporation of copper meshes and other enhancements to improve heat transfer. Another important consideration is the limitation the PCM poses once it has melted, which often prompts the consideration of using it in conjunction with other refrigeration systems [100].

This combined approach entails reintroducing circulation systems and increasing the weight and volume ratios, which can partially negate the benefits of the PCM system. Therefore, there is a trade-off between the simplicity and passive nature of PCM-based cooling and the potential need for supplementary refrigeration methods to address its limitations.

2.3.2.4 Dielectric Pool Boiling Cooling

Physical phenomena & general operation:

The pool boiling system utilises direct contact and the evaporation effect to achieve enhanced cooling efficiency. In this system, a dielectric liquid harnesses the latent heat through a phase change, similar to the PCM. However, unlike the PCM, the focus here is on evaporation rather than fusion. This is advantageous because, as mentioned earlier, the latent heat of evaporation tends to be higher than fusion. Additionally, a dielectric liquid is essential to prevent short circuits from direct contact between the battery and the cooling fluid.

The pool boiling system submerges the battery in the dielectric liquid, ensuring complete coverage and optimal contact. This arrangement promotes efficient heat convection and minimises thermal resistance. It is important to note that while the pool boiling technique shows promise, its application has thus far been limited to stationary setups involving high-power density electronics.

Practical implementation:

In the context of eMOV, the heat generated by the batteries is absorbed by the evaporating fluid, which then stores it as latent heat until it can be transferred to another part of the system or the HVAC system for dissipation. A schematic representation of this implementation can be seen in fig. 2.22. In this setup, the vapour of the dielectric liquid is directed to a heat exchanger, which is connected to the HVAC system. Alternatively, the vapour can be condensed using forced airflow generated by fans. While this approach may be less effective, it could still meet the cooling requirements depending on the specific needs. It is important to note that implementing this system in a moving vehicle can be relatively challenging due to its size and complexity.

Current research:

The conducted studies have demonstrated the significant thermal potential of the pool boiling system. Using propane [101] and ammonia [102] at high pressures allowed to maintain cell temperatures below 30 °C, even under high current loads of 7C, and this trend continued until approximately half of the discharge too. A direct relationship between the fluid

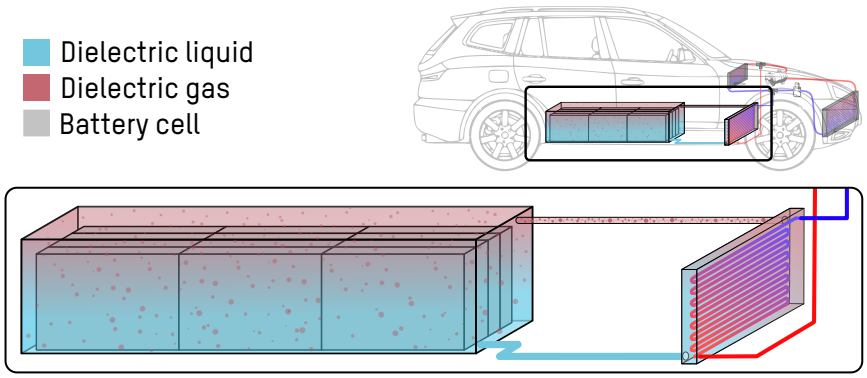

Figure 2.22: *Pool Boiling cooling implementation scheme.*

level and cell temperature dispersion was also observed; higher fluid levels resulted in lower cell temperatures, as depicted in fig. 2.23. Furthermore, when employing a hydrofluoroether liquid with high electric resistance and non-flammability, the cell temperature remained consistently around 35 °C throughout cyclic charging and discharging, even under extremely high-rate discharging and charging conditions (approximately 20C) [103].

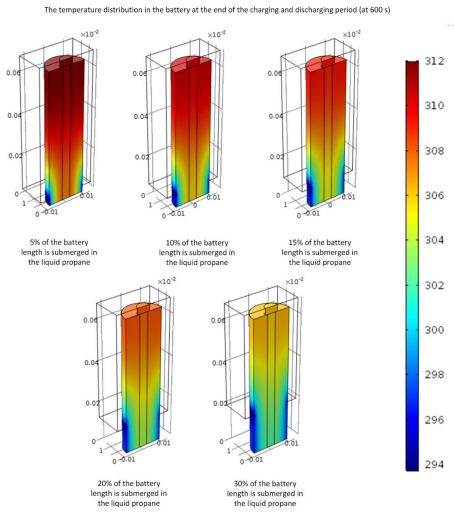

Figure 2.23: *Temperature distribution among the cell depending on the submersion length [101].*

Other tests were conducted using a commercial hydrofluoroether dielectric fluid called Novec 7000, which has a SLH of 142 kJ/kg, as indicated in table 2.1. Although its latent heat is lower than other substances, it was sufficient for meeting the cooling requirements. With Novec 7000, the temperature difference among the cells was maintained below 0.7 °C without the fluid boiling, and the temperature difference completely disappeared when boiling occurred [104]. This BTMS utilising hydrofluoroether demonstrates excellent insulation properties and exhibits good thermal performance, ensuring thermal uniformity within the cells during boiling [105]. Furthermore, the hydrofluoroether dielectric fluid showed no problems interacting with the batteries. However, a significant challenge associated with this technology is the potential interaction between the fluid and the batteries, such as corrosion or electrical conduction.

One of the main challenges in implementing the pool boiling system is managing the pressure increase within the system. This requires working with a pressurised system and necessitates incorporating different control elements. Nonetheless, evaporation simplifies the design by reducing the need for pumps due to the natural movement of vapour. As a result, this approach reduces the required space, maintenance requirements, and costs associated with the system [57, 106].

BTMS Conclusions:

Indeed, the pool boiling system offers effective cooling by establishing direct contact with the battery cells, enabling improved heat dissipation through enhanced heat transfer. However, this system operates under pressure due to evaporation, which introduces control challenges and increased complexity. Another concern is the reluctance of manufacturers to submerge the battery pack and the potential issues that the fluid may pose to the battery system. Furthermore, implementing this technology in a moving vehicle appears impractical. Additionally, the volume and mass rates would be negatively impacted if a large pool of dielectric fluid is required for effective cooling. Therefore, while the pool boiling system demonstrates advantages in terms of heat dissipation, some practical limitations and considerations need to be taken into account for its implementation in real-world applications.

2.3.2.5 Dielectric Flow Cooling

Physical phenomena & general operation:

The use of dielectric liquids for BTMSs has recently gained attention. These systems represent a natural progression from traditional air and cold plate systems, combining the advantages of both approaches. Dielectric liquid-based systems leverage the simplicity and cost-effectiveness of using inexpensive air direct contact flow while also benefiting from the improved heat regulation achieved by employing liquid cooling instead of air cooling. Dielectric fluids enhance heat transfer efficiency by allowing direct contact cooling between the battery cells and the coolant. This direct contact enables more effective heat dissipation, improving the battery pack's thermal management. Additionally, these systems eliminate the need for intermediary elements like cold plates, which can contribute to reducing the energy density and specific energy ratios of battery packs. This means that more energy can be allocated to the battery cells themselves, enhancing the overall performance of the battery system.

The current cooling system employs a dielectric fluid similar to the previous pool boiling method. Nevertheless, a notable distinction exists in performance, as the utilisation of the dielectric fluid's sensible heat replaces its latent heat. As elaborated earlier, this modification results in a reduction of the heat dissipation capacity of the BTMS. However, it retains the primary advantages of pool boiling while circumventing certain implementation challenges and inherent problems.

The battery continues to be immersed completely or partially in the dielectric liquid, just as in the previous configuration. This arrangement guarantees optimal contact between the heat transfer fluid and battery cells, promoting efficient heat convection and minimising thermal resistance. Consequently, the dielectric liquid effectively absorbs all the heat generated by the cells, facilitating superior heat transfer and augmenting the overall cooling efficiency. It is important to note that the evaporating temperature of the dielectric liquid must surpass the battery's typical operational range. In this manner, the heat is stored as sensible heat through temperature elevation rather than latent heat accumulation.

Practical implementation:

To facilitate effective heat dissipation in this sensible heat-based system, it is imperative to establish a flow of the dielectric liquid, allowing heat transfer to another designated location or system for subsequent cooling. This crucial flow mechanism ensures the establishment of a continuous and efficient cooling loop across the batteries. Similar to previous BTMSs, it is feasible to integrate this loop with the HVAC system via a heat exchanger, thereby preventing the requirement for additional cooling equipment such as a chiller, as depicted in fig. 2.24. Unlike pool boiling, the fluid recirculation necessitates incorporating a pump, which includes additional equipment, while the employment of boiling control elements becomes obsolete.

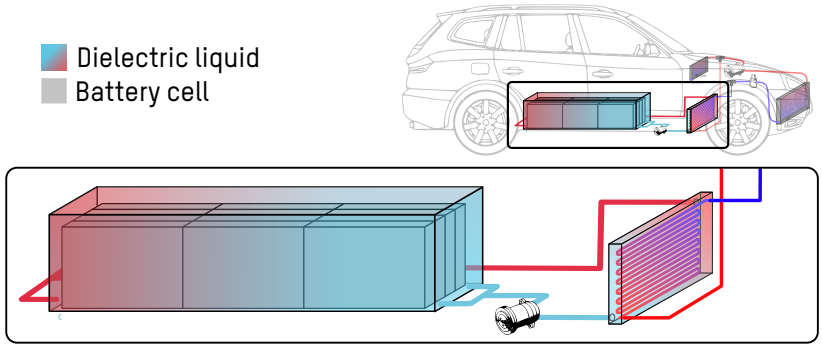

Figure 2.24: *Dielectric flow cooling implementation scheme.*

Current research:

These systems typically adopt a fully immersed approach, submerging the batteries entirely within the dielectric fluid. This immersion has demonstrated the ability to reduce the battery cells' maximum temperature compared to the widely employed cold plate BTMS [107–109]. This temperature reduction proves particularly effective when operating under high C-rates, requiring greater heat dissipation capacity [110]. Furthermore, utilising low-viscosity dielectric fluids in such systems reduces pressure drop, thereby mitigating parasitic power consumption [108, 110]. Notably, the geometry of the Battery Module (BM) significantly influences the temperature of the cells. Decreasing the inter-cell spacing decreases the maximum temperature by augmenting the velocity of the coolant fluid. However, this increase in velocity also results in higher

system pressure drop [52]. The existing literature predominantly focuses on fully immersed concepts for their thermal management strategies. Nevertheless, it is worth considering that partial immersion of the cells can still yield reasonable temperatures for the BM [102]. This distinction becomes vital as the thermal management outcomes diverge depending on the selected BTMS implementation approach.

Similar to the observations made in pool boiling, the direct contact between the dielectric fluid and the battery cells reduces inter-cell spacing, reducing the volume ratios of the power system. Using a liquid in a direct contact configuration also enhances energy efficiency, reducing energy consumption [111]. Furthermore, this cooling system exhibits further advantages in minimising the maximum temperature of the battery module compared to the boiling system [109]. As previously highlighted, using dielectric fluids allows for maintaining a temperature difference among the cells of less than 0.7 °C without fluid boiling [104]. Moreover, this temperature homogenisation due to immersion cooling with dielectric fluids reduces battery pack ageing, with an increase of 3.3 % on capacity retention after 600 cycles compared to air cooling BTMS [112].

It is pertinent to note that similar systems find extensive application in diverse domains, including cooling electrical transformers. In such cases, mineral oil, characterised by higher viscosity, is commonly employed. However, using dielectric fluids offers distinct advantages by reducing viscosity, diminishing pumping consumption, and considerably surpassing cooling requirements [113, 114].

Several commercial solutions have recently emerged that incorporate the BTMS above approach. Xing Mobility, for instance, introduced an automotive-grade and scalable complete immersion-cooled battery pack suitable for a range of applications [115]. Similarly, Kreisel presented their high-voltage battery system equipped with dielectric flow cooling through cell surfaces, which ensures enhanced battery lifespan, improved performance, prevention of thermal propagation, and a modular design for maximum flexibility [116]. Additionally, Exoes developed a dielectric flow immersion thermal management system encapsulating the cells and circulating the fluid on the cell's surface, which facilitates precise temperature control [117, 118]. These systems can be seen in fig. 2.25.

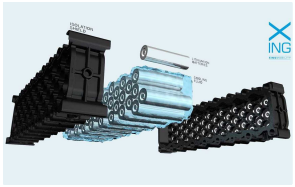

(a) Xing BTMS [115].

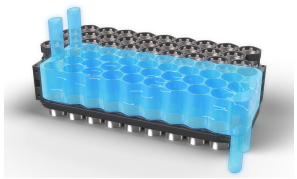

(b) Kreisel BTMS [116].

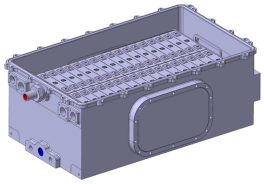

(c) Exoes BTMS [117].

Figure 2.25: *Dielectric flow commercial systems.*

BTMS Conclusions:

Similar to the pool boiling approach, this BTMS design exhibits significant efficiency, simplicity, and a compact structure. Furthermore, it offers the potential for cost savings in manufacturing and maintenance. The cooling performance of this system is commendable, effectively circumventing the over-pressure issues associated with pool boiling. Moreover, using dielectric fluid mitigates concerns regarding leakage and eliminates the risk of short circuits. However, it is essential to acknowledge that the complete immersion of the battery cells introduces undesired weight and volume to the battery pack, which may need to be carefully considered in terms of overall system design and requirements.

2.3.3 BTMS Implementation Topology

The thermal management solutions or concepts presented in the literature often overlook the potential implementation variations that can arise based on cell topology, selected technology, or specific application requirements. It is crucial to consider these factors as they can significantly influence the effectiveness of thermal management strategies.

Traditionally, thermal management is achieved through contact with the battery cell's surface, which maximises the available contact area and enhances heat transfer. However, an alternative approach involves localising the thermal management contact area, specifically on the cells' tabs. Numerous studies have highlighted the advantages of this particular BTMS implementation strategy.

For instance, Hunt et al. [119] conducted a study on the degradation process of pouch cells, comparing tab cooling and surface cooling meth-

ods. The results emphasised the significance of the thermal gradient's nature. It was observed that when the thermal gradient was perpendicular to the cell layers (surface cooling), it led to uneven performance, accelerated degradation, and a more significant decrease in cell capacity. In contrast, when the thermal gradient was along the cell layers (tab cooling), it enabled a more uniform degradation distribution and improved overall performance. Figure 2.26 visually depicts this phenomenon.

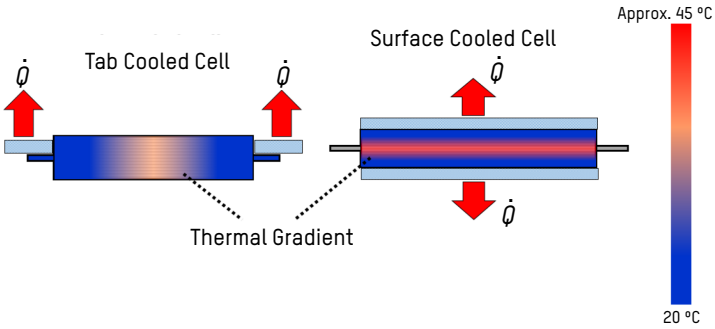

Figure 2.26: *Tab vs surface cooling thermal gradient [119].*

Dondelewski et al. [120] continued comparing both cooling approaches, concluding that surface cooling results in lower usable capacity and energy than tab cooling. However, analysing the cell geometry effect on the cooling configuration determined that tab cooling is not always better in degradation terms. In that regard, increasing the heat-releasing ability (i.e. improving the conductivity through the tab) will make the difference, as analysed by Li et al. [121], showing the importance of the tab and current collector design for proper heat release and internal temperature homogenisation. Tab cooling can therefore gain in importance with new *tabless* cell designs proposed, reducing the electrical and thermal resistance caused by the current collector on today's cylindrical cells [122], and be highly beneficial for the BTMS.

Notably, the new 4680 design cells, under development by companies such as Tesla and Panasonic, exemplify this trend. These cells feature a tabless electrode design, offering intriguing thermal management prospects. As cylindrical cells increase in diameter, heat dissipation at the core becomes more challenging. The tabless design facilitates axial heat transfer through the aluminium and copper current collectors to the

top and bottom of the cell, enabling efficient cooling of the battery pack and ensuring more uniform temperature profiles within individual cells fig. 2.27. Therefore, this enhanced thermal management is expected to support faster charging and discharging capabilities.

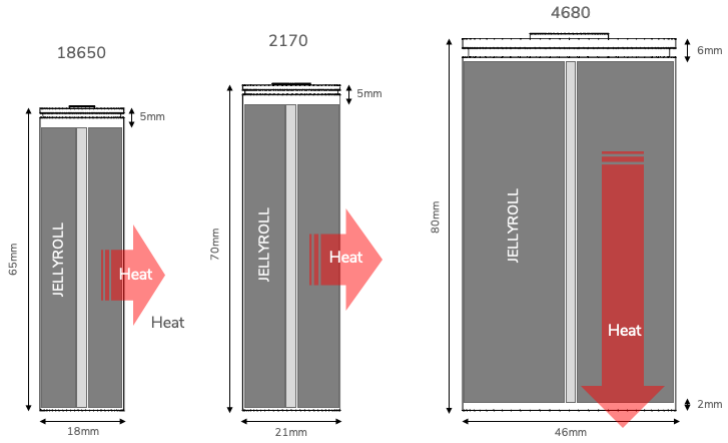

Figure 2.27: *Cells' thermal management opportunities with tabless design [123].*

2.4 Literature Gaps and Proposed BTMS Approaches

Several conclusions can be drawn based on the analysis conducted regarding the state of the art of BTMSs. Firstly, the cold plate approach emerged as the most widely adopted technology. While it possesses sufficient thermal management capabilities, it still encounters challenges in meeting the rapidly increasing demands for fast charging and higher power requirements in current EVs. Additionally, the indirect contact nature of the cold plate approach and the need for electrical isolating elements introduce inefficiencies in the system. Furthermore, it is crucial to consider the leakage issue since the fluid employed in cold plate systems is electrically conducting, posing a security risk.

In this regard, the PCM solution is a highly efficient and energy-saving method for heat absorption. As a passive system, it requires no additional energy input. Utilising latent heat offers excellent temperature peak absorption and ensures long-term temperature stabilisation. Therefore this system can complement a primary active solution (e.g. cold plate system),

enhancing the performance of the BTMS in scenarios such as fast charging or demanding applications. However, the volume and weight implications of the system must be carefully considered.

On the other hand, the novel dielectric fluid systems offer improvements over the limitations of cold plate solutions. These systems enhance thermal efficiency by enabling direct contact between the dielectric fluid and the battery cells. They effectively resolve the short-circuit issue and demonstrate a commendable thermal response even under high-performance requirements and demanding conditions. However, it is noteworthy that both commercial solutions and literature studies predominantly adopt the approach of fully immersing the cells in the dielectric fluid. While this immersion technique provides certain advantages, such as improved heat transfer, it also increases volume and weight. Consequently, this can reduce BEV's efficiency and overall driving range.

As a consequence, the cold plate, PCM and dielectric solutions show the best properties to meet the requirements of an advanced battery thermal management system for high-performance electromobility application.

Furthermore, it has been observed that tab cooling can have a favourable effect on battery thermal management systems. This approach effectively dissipates heat from the tabs, even with a relatively small contact area, owing to the high thermal conduction path established by the connection between the tabs and the internal layers of the battery cells. This localised heat extraction method can also reduce ageing effects and improve overall performance. By creating an even thermal gradient along the cell layers, tab cooling enables a uniform distribution of degradation, leading to enhanced performance and longevity.

This study compares and evaluates two thermal management systems based on the existing literature and the gaps found, being the objective to identify the optimal advanced BTMS solution. Through this comparison, the study will contribute to developing an effective and efficient thermal management system for batteries.

The first system incorporates a cold plate solution with a PCM buffer, which utilises a passive approach to mitigate sudden temperature in-

creases during fast charging. This system referred to as the **Cold Plate and PCM Based BTMS**, aims to enhance the security and efficiency of the battery pack.

The second system, known as the **Dielectric Flow- and Tab-Based BTMS**, explores the promising approach of dielectric flow cooling along with the benefits of tab cooling. Both approaches have shown considerable potential for enhancing BEV systems. This system aims to provide effective thermal management while prioritising the highest possible efficiency while also improving energy density and specific energy.

A numerical comparison between these two systems aims to identify the optimal advanced solution to effectively manage thermal performance, ensuring the battery pack operates efficiently and securely. Additionally, this research aims to contribute to advancements in energy density and specific energy for improved overall battery performance.

3

Methodology for Advanced BTMS Development

Summary

The third chapter of this thesis outlines the comprehensive methodology employed for the development and selection analysis of the advanced BTMS. This chapter explains all the necessary methods and models utilised in the research, including the heat generation model applied to the battery cells and the CFD tool adopted for BTMS analysis. Additionally, the chapter presents the methodology followed for comparing various BTMS options to facilitate the selection process.

3.1 Methodology Description

This PhD thesis aims to develop an advanced BTMS, analysing different solutions for a battery module. Therefore, the methodology proposed in this work focuses on optimal solution development and consists of three steps:

- **Cell Selection:** Prior to conducting BTMS thermal analysis, it is essential to consider the thermal performance of cells as a crucial selection criterion to prevent thermal issues in these fields, optimise the BTMS, and mitigate risks in new and highly demanding areas, as it is the electromobility. By carefully selecting the appropriate cells, developing an energy-efficient BTMS that meets the required specifications is possible without unnecessary over-dimensioning.

  Thus, a refined methodology for cell selection is introduced, in which thermal analysis of cells is incorporated into the selection process. The case study presented in Section 4.3 serves as a demonstration of the effectiveness of this approach, leading to the identification of the cell utilised in the case studies for advanced BTMS solution development (Chapter 5).

- **CFD Based Comparison:** This step in the methodology involves the comprehensive design and development of BTMS solutions, which will subsequently undergo analysis and comparison over the same battery module. The comparison process will be conducted in CFD software to obtain detailed data and insights for evaluation.

  Regarding this work, in Chapter 5, a CFD-based comparison will be conducted between two case studies with two advanced BTMSs over the same battery module: a Cold Plate and PCM based BTMS and a Dielectric Flow- and Tab-based BTMS. Both thermal management systems will be subjected to a comprehensive comparison analysis, considering specific parameters outlined in Section 3.4. The aim is to evaluate and contrast the performance of these BTMSs under well-defined conditions to gain valuable insights into their thermal capabilities.

- **Concept-Proof Validation:** Final step of the methodology consists of the experimental validation of the BTMS solution chosen after the

CFD comparison on the previous step. Therefore, a prototype needs to be developed and tested, ensuring the technology's viability and validating the CFD model in the preceding step.

Consequently, in this work, after the comparative results give an advantage to the latter solution, Chapter 6 will present the design and development process of a functional prototype of dielectric flow- and tab-based BTMS with the following experimental tests. The developed battery module will be based on a previous air-based BTMS for electric elevation application to simplify the design process. Hence, an easy-to-handle battery module for laboratory testing and CFD model validation will be created in Chapter 6. The process will extend dielectric technology's knowledge and design concepts, including a geometry optimisation analysis.

The followed methodology scheme is depicted in fig. 3.1.

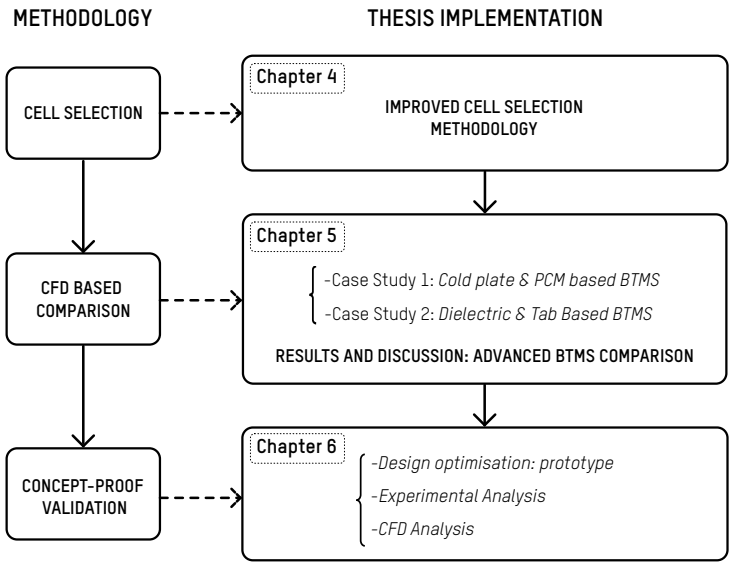

Figure 3.1: *Thesis methodology and its implementation scheme.*

The methodology presented in this work serves as a framework for the development of an optimal BTMS solution. Through the final comparison presented in Chapter 5, this methodology will validate or challenge the ideas supporting the superiority of both technologies highlighted in Section 2.4 of Chapter 2: the PCM and the dielectric flow technology, with the

latter one particularly emphasising the tab-based solution.

- The utilisation of Phase Change Materials holds significant potential in absorbing heat peaks and serving as a reliable safety element, effectively equalising the temperature distribution within the battery pack. By leveraging the latent heat absorption characteristics of PCMs, the maximum active cooling power requirement can be reduced, leading to an optimised sizing of the BTMS.
- Dielectric flow concept enhances the efficiency of battery thermal management by allowing direct contact of the coolant fluid with the battery cells, eliminating the need for intermediary elements such as cold plates and thermal interface materials.
- Tab-based thermal management concept is an efficient solution for high-performance thermal management, even if the heat transfer area is limited, as the usage of the cell's high thermal conductivity path is enhanced.
- Combination of Dielectric Flow and Tab-Based thermal management represents an advanced and robust solution for battery thermal management in high-demanding applications. This approach gathers the outcomes of both previous hypotheses and results in a highly efficient battery thermal management system that can effectively regulate the temperature of high-performance electric cycles, offering a reduced specific energy and energy density, enhancing BEV features and performance

The following sections will depict the necessary models and methods for the BTMS thermal analysis methodology.

3.2 Heat Generation Model

This section describes the Lithium-ion Battery heat generation model implemented in this work's thermal analyses. The LIB heat generation phenomenon is presented along with the simplified equation, and its effect on the battery cell's chemistry is studied. Moreover, the equation application on the thermal models is described. Finally, the tests to obtain the electrothermal parameters necessary for the cells' heat generation model are described.

3.2.1 LiB Heat Generation Phenomenon

When characterising the heat generation on a LIB, certain of the processes can be omitted, as mentioned in section 2.2.2.1, simplifying the understanding of the phenomena. Thus, heat generation on a cell was defined by Bernardi et al. [39] as the sum of both irreversible and reversible heat. The first one always denotes exothermic heat generation and refers to joule heating. The latter, however, is known as entropic heat because of entropy changes and behaves asymmetrically during charge and discharge, switching from exothermic to endothermic behaviour depending on the cell's State of Charge (SOC). The main heat source in a cell comprises these heat generation terms, represented by their sum in eq. (3.1).

$$\dot{Q} = I^2 \cdot R_{in} + I \cdot T \cdot \frac{dU^{avg}}{dT} \tag{3.1}$$

I [A] is the cell charging (positive) or discharging (negative) current, R_{in} [Ω] is the internal resistance of the cell, T [°C] is the cell's temperature and dU^{avg}/dT [V/K] is the EHC defined by equilibrium potential changes to temperature.

When analysing both reversible and irreversible heat, there is a lack of homogeneity in the thermal characterisations provided in the literature. Irreversible heat, which behaves as an exothermic process whether the cell is charging or discharging, is the most frequently used term. It is necessary to characterise the battery cell's internal resistance in order to assess this irreversible heat. It can occasionally be calculated solely as a function of temperature [124] or the state of charge [125], but typically both factors are taken into account [42, 126–129].

For each SOC step in the charge and discharge processes, the EHC determines the exothermic or endothermic performance and the amount of reversible heat generated. A cell produces heat when charged (positive current value) at positive EHC values but absorbs heat when discharged (negative current value). With negative EHC values, the contrary applies. Therefore, whether charge and discharge processes are compared for the same Current Rate (C-rate), reversible heat causes asymmetric thermal behaviour. As a result, reversible heat is underestimated because it is frequently less than irreversible. It is sometimes explicitly disregarded for a presumably undetectable effect [124, 125], or it isn't even brought up [130]. Other research [126, 131, 132] either does not examine it or utilises it in their models but with little impact [133–135]. Finally, while some writers are identifying the effects of entropy changes on the heat generation process [127, 129, 136], others emphasise the need for more research due to the high proportion of reversible heat in the overall amount of heat produced [40, 42, 128, 137].

EHC changes are specific to each cell and should be studied for every cell characterisation to determine its significance. Additionally, an EHC comparison across various cell chemistry reveals distinct tendencies for Nickel Manganese Cobalt (NMC), Lithium Iron Phosphate (LFP), and Lithium Titanate Oxide (LTO) cells. As depicted in fig. 3.2, both NMC (fig. 3.2a) and LFP (fig. 3.2b) cells exhibit a positive increase during half of the charge cycle, while LTO (fig. 3.2c) cells display a flatter response with very low or even negative values throughout the SOC. This can minimise reversible heat generation during cell cycling.

3.2.2 Lumped Heat Generation Model

The LIB heat generation model used in this work follows the heat generation phenomena described in eq. (3.1). Therefore, this equation is implemented as a lumped heat generation model on the BTMS analyses presented.

Based on electric current instantaneous solicitations, the model determines the volumetric heat output of each cell. In that regard, at each time step, the model needs to be fed with the electric current, the cell's SOC, and volume-averaged temperature at that particular moment. The electric current solicitation is defined by the application where the bat-

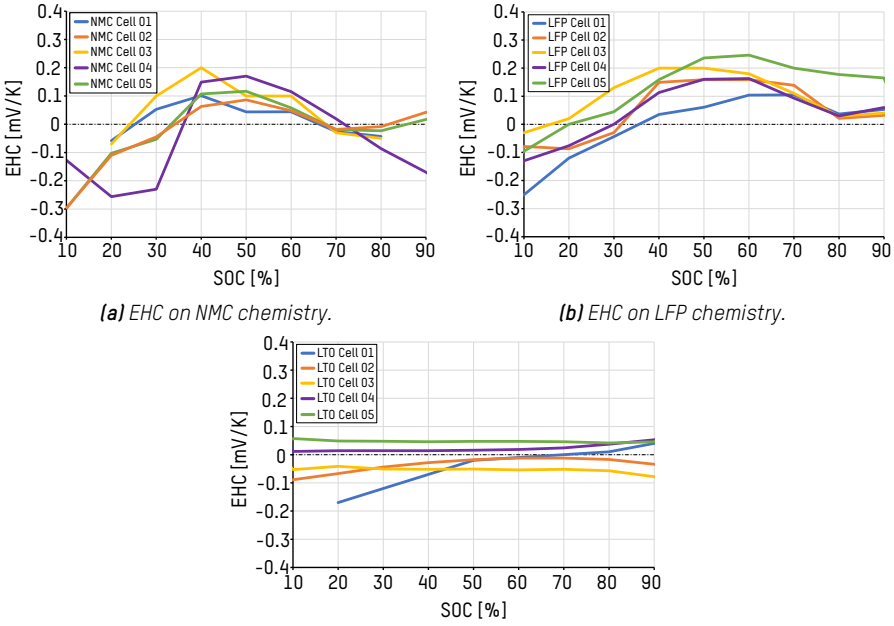

(a) *EHC on NMC chemistry.*

(b) *EHC on LFP chemistry.*

(c) *EHC on LTO chemistry.*

Figure 3.2: *EHC change depending on cell chemistry [40, 128, 129, 133, 137–146].*

tery cell is charged or discharged at a specific C-rate. Moreover, the cell temperature is calculated through CFD, which averages the volumetric cell temperature after balancing the heat transfer and accumulation equations with the heat generated on the cell. Finally, the cell's SOC is estimated following the Coulomb Counting method depicted in eq. (3.2),

$$SOC_{(t)} = SOC_{(t-1)} + \int_{t_0}^{t} \frac{I}{C_{bat}} \cdot dt \tag{3.2}$$

where $SOC_{(t)}$ [%] and $SOC_{(t-1)}$ [%] are the SOC at the desired and previous time step, respectively. I [A] is the electric current, and C_{bat} [Ah] is the cell capacity.

LIB variables used on the lumped heat generation model are the Internal Resistance (R_{in}) and EHC, implemented utilising a look-up table. The first value is double-interpolated to be adjusted to the desired temperature and SOC values, whereas the latter only depends on the cell's SOC level.

These variables specify the entropic and ohmic heat, which establishes the total heat power [W] generated by each cell at that time step. The scheme where the lumped heat generation model's process is explained can be seen in fig. 3.3.

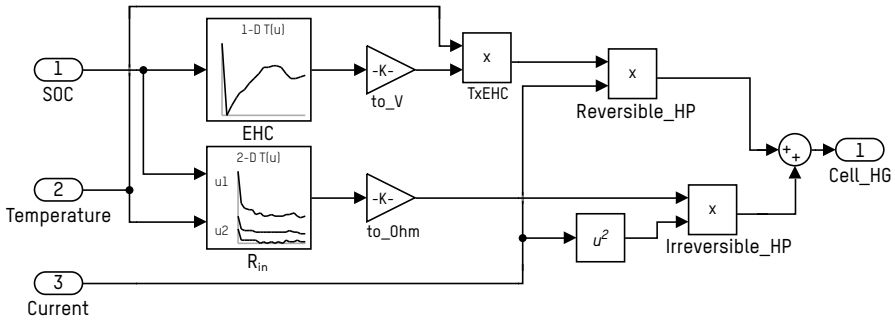

Figure 3.3: *Lumped heat generation model scheme.*

3.2.3 Heat Generation Model Implementation in CFD

Adding the LIBs heat generation to the CFD numerical models is mandatory. This heat should be introduced as volumetric heat on the domain cell zones. However, the LIB heat generation was previously depicted in section 3.2.2 as a simplified model by eq. (3.1). Hence, the simplified model must be introduced externally to the CFD software. Two ways are considered in this work: the User Defined Function subroutine and the co-simulation of heat generation and CFD models through the Functional Mock-up Interface protocol.

3.2.3.1 Heat Generation Subroutine: User Defined Function

The User Defined Function gathers the lumped heat generation model presented in section 3.2.2 using a C language script readable by the CFD. The script is fed with time function electric current and SOC data arrays. As a result, the User Defined Function (UDF) allows performing transient simulations, calculating the volumetric heat generation of each cell every time step. The script code used can be seen in Appendix A.1.

This approach was previously presented and used by Martín-Martín [147]. It is entirely independent of the electric configuration of the cells

in the battery module. Thus, by reducing the resultant volumetric heat generation by half, models or case studies with half cells affected by symmetry planes can be easily studied, with the consequent computational cost reduction. Therefore, this approach is employed for the comparison case studies in Chapter 5, where symmetry planes are introduced along the battery module.

However, a strategy with more possibilities is used when working with entire cells. This makes use of the Functional Mock-up Interface (FMI) protocol.

3.2.3.2 Heat Generation Co-Simulation: Functional Mock-up Interface

The Functional Mock-up Interface is a free standard that defines a container and an interface to exchange dynamic simulation models using a combination of XML files, binaries and C code distributed as a ZIP file. Thus, an FMU is created with the heat generation model, which can be uploaded and co-simulated in Ansys-Fluent.

The FMU used in this work is developed on Matlab-Simulink. Following the co-simulation scheme shown in fig. 3.4, cell temperatures resulting from the CFD model's balance are used as input data, along with the simulation flow time. Hence, with the predefined electrical current value, the SOC can be calculated following eq. (3.2). The model estimates, following the explained procedure in section 3.2.2, the resulting heat generation ratio of each cell, which is then transferred back to the CFD.

The CFD battery model activated for FMU co-simulation allows electrically defining the battery module's configuration and automatically introducing joule heating on passive elements such as the busbar connection between cells. Hence, this model can not be used with half cells when symmetry planes are introduced, in contrast with the UDF approach. Nevertheless, the FMU model offers interesting characteristics and possibilities as it is developed outside the CFD. Therefore, more complex heat generation models or BTMS's active control models could be implementable.

However, in this initial approach of the co-simulation of both simulation tools, it is mandatory to ensure the correct operation of the model developed in Simulink. FMU and UDF approaches are supposed to give similar results during a CFD simulation, as the implemented lumped heat gener-

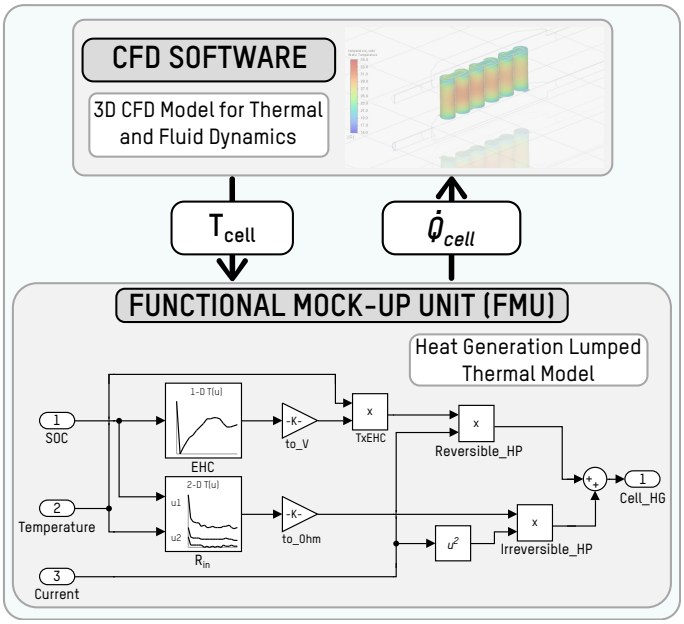

Figure 3.4: *Co-simulation scheme between CFD and FMU lumped heat generation model.*

ation model remains the same. However, to properly validate this statement, a comparison simulation is carried out where the same battery module presented in Chapter 6 is used for simulation. Therefore, CFD simulations carried under FMU and UDF lumped heat generation models are compared, as seen in fig. 3.5.

Temperature evolution of six charge/discharge cycles is shown, with the numerical data results for both FMU and UDF cases. As can be observed, both lumped heat generation models produce identical results. Hence, the FMU co-simulation model is validated and is at least as accurate as the UDF previously employed.

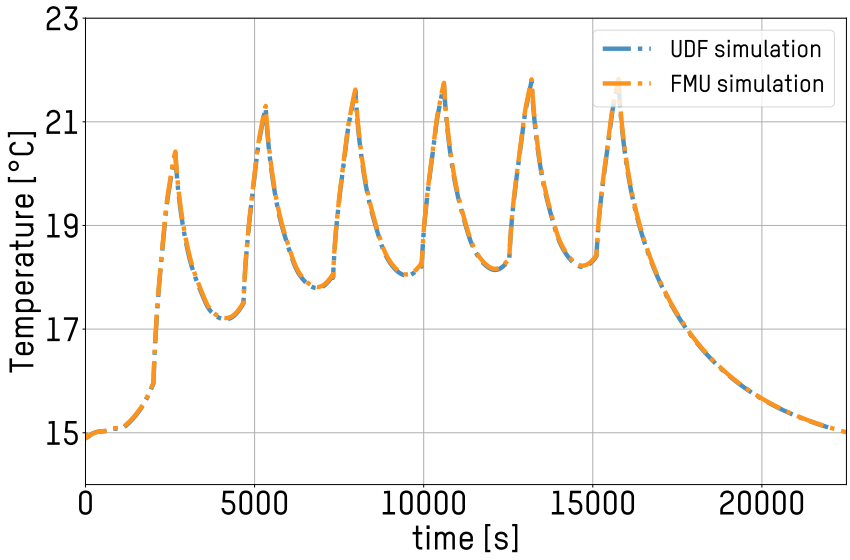

Figure 3.5: *FMU Co-simulation model validation.*

3.3 Numerical Analysis: Computational Fluid Dynamics

The thermal analysis of batteries is of utmost importance as it directly affects their performance and helps prevent potential overheating issues. A detailed model of the battery's thermal behaviour and cooling system is necessary to achieve this. In this study, Computational Fluid Dynamics (CFD) is selected as the method to develop these models, allowing for both constant and transient thermal analysis.

CFD simulations provide a comprehensive understanding of the thermal behaviour in three-dimensional conditions, considering the system's intricate geometric details and precise physical dimensions. While these simulations require more time and effort than straightforward methods, they offer superior accuracy and detailed results that enable a thorough analysis and observation of various system behaviours. Thermal maps can be obtained by simulating the flow of cooling fluids and heat transfer throughout the system, which further enhance the understanding of the results and aid in optimising the thermal management system.

Computational Fluid Dynamics is a commonly applied tool for gener-

ating quantitative predictions for fluid flow phenomena based on mass, momentum and energy conservation laws. To virtually develop a solution for a physical event linked with a fluid flow without sacrificing accuracy, physical parameters such as velocity, pressure, temperature, density, and viscosity must be considered simultaneously in mathematical models.

Different software tools (solvers, pre- and post-processing utilities) can be used to implement such models and obtain the desired simulation solutions restrained by some boundary and initial conditions. The most common CFD simulation programs implement the Eulerian Finite Volume Method. This work employed the *Ansys-Fluent 2022R1* software to implement the models detailed below and hydro-dynamically and thermally analysed the BTMSs presented.

The following explanations resume the information given by Blazek [148] and H K Versteeg [149], who depicts the mathematical model and numerical methods to analyse the fluid flow and thermal transfer used by the *Ansys-Fluent* software tool. The Navier-Stokes equations are specified as the mathematical model of the physical case. This explains how all the physical characteristics affecting heat transmission and fluid movement change. The mathematical model changes according to the issue's nature, including heat transmission, mass transfer, phase change, and chemical reaction. Moreover, partial differential equations are applied describing the essential fluid flow physics (Navier-Stokes), turbulence effects (models of different degrees of closure and complexity) and energy transfer by conduction, convection and radiation in a 3D domain.

The CFD discretises these partial differential equations using the conservation laws in each of the infinitesimal control volumes of the geometry. The equations carry out a methodical count of changes in mass, momentum, and energy brought on by fluid flow around the studied geometry. The following equations are considered in order to accomplish this.

Regardless of the characteristics of the fluid or the forces influencing it, mass conservation is achieved, expressed by eq. (3.3). In its first term, it exhibits variation in density per unit of time and fluctuation in flow's matter in its second term.

$$\frac{\partial \rho}{\partial t} + \frac{\partial}{\partial x_i}(\rho \cdot u_i) = 0 \tag{3.3}$$

The conservation of the moment is expressed in eq. (3.4). This law states the existence of a balance between the momentum change rate in a particle and all acting forces on it. The two terms on the left refer to the conservation of mass and specifically to the term transient and convective, respectively. The terms on the right show the stress tensor.

$$\frac{\partial}{\partial t}(\rho \cdot u_i) + \frac{\partial}{\partial x_i}\left(\rho \cdot u_i \cdot u_j\right) = -\frac{\partial}{\partial x_i} + \frac{\partial x_{ij}}{\partial x_j} + S_{Mi} \tag{3.4}$$

According to the energy conservation law, a particle's energy must change by an amount equal to the total work done and the energy added in the form of heat.

The conservation of energy is described in eq. (3.5). It illustrates, in the first and second terms, how the energy varies and how it is transmitted due to the fluid's movement. On the right side of the equation, four terms are seen. The first two refer to the energy ratio lost in work done by surface forces on the fluid particles. The final two terms represent the particles' overall heat absorption ratio.

$$\frac{\partial(\rho \cdot e)}{\partial t} + \frac{\partial(\rho \cdot E \cdot u_i)}{\partial x_i} = -\frac{\partial(\rho \cdot u_i)}{\partial x_i} + \frac{\partial\left(\tau_{ij} \cdot u_i\right)}{\partial x_j} + \frac{\partial}{\partial x_i}\left(k\frac{\partial T}{\partial x_i}\right) + S_h \tag{3.5}$$

Conversely, the flow may evolve in a turbulent or laminar manner. For the turbulent model considered almost in all cases, Reynolds (Re) and Rayleigh (Ra) numbers have been considered for forced and natural convection, respectively. Reynolds-Averaged Navier-Stokes equations (RANS) and the energy equation have been used to introduce the effects of turbulence on the flow variables. The turbulence model is constructed from these equations to describe the hydrodynamic and convective heat transfer phenomena accurately and is represented using the Realizable k-ε viscous model [150] and a two-layer near-wall treatment [151].

Equation (3.6) describes the transmission of heat on solids. The first left term refers to heat conduction, which considers the solid's orthotropic conductivity (k). The second term, q_g, refers to the solid's heat generation, explicitly considering battery cells' heat generation, which will be introduced in section 3.2. Moreover, the term on the right represents the increase in internal energy per unit of time.

$$k\left(\frac{\partial^2 T}{\partial x^2}+\frac{\partial^2 T}{\partial y^2}+\frac{\partial^2 T}{\partial z^2}\right)+q_G=\rho C\frac{\partial T}{\partial t} \tag{3.6}$$

The Finite Volume Method is applied to discrete the differential equations of the mathematical model described above, using a segregated implicit solver to solve the generated algebraic equation system. Therefore, equations are linearised and then sequentially solved using the Gauss-Seidel algorithm accelerated by an Algebraic Multigrid method [152]. The pressure-velocity coupling is achieved using the SIMPLE algorithm [153]. Diffusive terms of the equations are discretised using a second-order centred scheme, and the convective terms are discretised using a second-order upwind scheme [154]. A body force weighted scheme [155] is chosen to discretise pressure to deal with this buoyancy-driven flow. As mentioned, this numerical procedure has been implemented in *Ansys-Fluent 2022R1*.

Regarding the boundary conditions employed in this work, the mass flow rate has been defined as the specification method at the inlet boundaries, also defining scalar properties of the flow, while pressure-outlet boundary conditions were used to define the static pressure at the flow outlet. Symmetry planes have been employed where possible, reducing the computational domain by half and fastening the simulating time considerably. Finally, an adiabatic environment has been considered on external walls, which creates a rougher environment for the BTMS.

For the specific PCM simulations, the solidification & melting model has been activated, defining as porous zone the PCM buffer material and quantifying the melted and solidified material ratios during the transitory simulation.

Furthermore, on those transitory simulations, all case studies have been initiated at an ambient temperature of 25°C on thermal equilibrium,

and mass flow rate and fluid inlet temperature have been changed depending on the specifications of the simulation performed (detailed later in the corresponding section).

Two main convergence criteria have been applied to determine when the numerical procedure described in the previous paragraph has converged to a solution. The main criterion is to check that the values for the scaled residuals of the equations are below certain magnitudes (10^{-3} for the mass, momentum and turbulent equations and 10^{-6} for the energy equation). Moreover, the balance between the inlet and outlet mass flow rate and the energy balance between the generated and dissipated heat has been checked. For BTMS comparison analysis and data post-processing, the volume average temperature of battery cells and the area weighted-average static pressure in the inlet zone is registered.

3.4 BTMS Comparison Methodology

The results obtained from the diverse BTMSs studied are being compared. This will allow numerically assessing the differences between systems and understanding the pros and cons of each system regarding the application area. Thus, criteria should be established to select each application's most appropriate TMS.

On the comparison methodology definition, it is mandatory to identify the battery and TMS parameters to be evaluated. The battery module used in the comparison will be the same for the TMSs analysed. Moreover, the same electric cycles will be performed.

Based on that standard battery module, the following parameters will be quantitatively evaluated:

- Mass [kg]
- Volume [m^3]
- Energy Density [Wh/m^3]
- Specific Energy [Wh/kg]
- T_{max} [°C]
- ΔT_{module} [°C]
- Δp [Pa]
- P_{hyd} [W]
- E_{hyd} [Wh]

The mass and volume of the entire battery module and the BTMS will be evaluated. Moreover, the energy density and the specific energy of the system will be assessed with the battery module and previously measured mass and volume values. The T_{max} value corresponds to the maximum temperature registered during the simulated electric cycle. On the other hand, ΔT_{module} refers to the maximum thermal dispersion among cells in the battery module. The Δp is the mean pressure drop of the process between the fluid inlet and outlet of the BTMS.

Using the pressure drop, the necessary hydraulic power (P_{hyd} [W]) for TMS's fluid pumping can be estimated following eq. (3.7), which depends on the mass flow rate ($\dot{m}$ [kg/s]) and fluid density (ρ [kg/m^3]) at a specific temperature.

$$P_{hyd} = \frac{\dot{m}}{\rho} \cdot \Delta p \tag{3.7}$$

Finally, the total hydraulic auxiliary energy consumption (E_{hyd} [Wh]) is evaluated by integrating the previously evaluated hydraulic power (P_{hyd}) on the battery module cycling period (t_0 - t), following eq. (3.8).

$$E_{hyd} = \int_{t_0}^{t} P_{hyd} \cdot dt \tag{3.8}$$

In addition to the primary evaluation criteria, there will be an approximate assessment of several other indicators due to limited available data for precise quantification. These additional parameters encompass aspects such as the material and production cost of the system, the safety and reliability of the technology employed, and the potential impact on the overall efficiency of BEVs with the chosen BTMS. While a comprehensive quantitative analysis may not be feasible, these factors will be considered qualitatively to provide a broader perspective on the overall performance and viability of the evaluated thermal management systems.

4

Cell Selection for Efficient BTMS Development

Summary

This thesis chapter delves into the essential process of cell selection, which is a prerequisite before conducting BTMS analysis and comparison. An improved cell selection methodology is introduced, focusing on thermal performance aspects. The chapter also outlines the necessary electrothermal parameter characterisation tests for the cells, which are vital for integrating them into the heat generation and transfer models. A case study exemplifies the cell selection methodology presented, leading to identifying the specific cell utilised in Chapter 5 for developing and analysing the advanced BTMS solution. This comprehensive approach ensures the proper selection of cells to optimise the thermal management system's performance and achieve the study's objectives.

4.1 Improved Cell Selection Methodology

Cell selection based on adequate thermal behaviour could handle potential hazard problems, reduce the energy consumption of TMS and correctly size them to lower the total weight of the Battery Pack (BP). This results in an improvement in overall efficiency and reliability, particularly for fast-charging processes. For that aim, in-depth research on the thermal behaviour of battery cells is required. Accurate characterisation and analysis are required to estimate heat generation, use the data to minimise overheating, correctly size the TMS, and cover cooling requirements. Thus, an improved cell selection methodology is presented below.

As far as it has been seen in the literature, there is no clearly defined approach to cell selection criteria for fast charging coupled with thermal behaviour. The established technique is based on studies to gauge and confirm cell properties, lifespan and ageing, safety, and even cost criteria, but thermal behaviour is rarely considered [156, 157]. In certain studies, the operating temperature is taken into account when choosing a technology or sizing a storage system [158, 159], and even the impact of the charge level, capacity, and ageing on thermal behaviour is taken into account [160]. However, there is a glaring gap in cell selection approaches for thermal behaviour, particularly regarding fast charging problems.

In order to prevent overheating, particularly when fast charging, a deeper thermal behaviour analysis must be incorporated into the cell selection methodology's optimisation. Thus, an enhanced cell selection methodology is described in this work, built from an existing strategy currently in use [157] and is particularly concerned with electrical performance. The following stages make up that base methodology:

Original methodology:

Stage 0: Creation of a comprehensive database of LIB cell market information.

Stage 1: a) Examination of the specific needs of the application and battery pack.
b) Identification and theoretical evaluation of appropriate cell technical specifications.

Stage 2: Focuses on characterising the cells through testing, including validation of nominal capacity, rate capability, internal resistance, and accelerated life cycle tests.

Stage 3: Includes an analysis of calendar and cycle ageing, lifetime, safety, and cost.

The steps outlined above sum up the required process for choosing a cell from a sizeable database. By comparing the application requirements with the characteristics of the available cells chosen from the Stage 0 database, Stage 1 is crucial for obtaining a quick and sufficient reduced cell candidate list. Stage 2 characterises the few candidate cells under application conditions, particularly validating the cell manufacturer's data. Stage 3 is where the chosen cell's durability, cost, and safety examination is completed. Since each level requires significantly more time than the one before it, the number of candidates must be drastically decreased after each stage.

Both irreversible and reversible heat must be considered for implementing an efficient and thorough thermal performance analysis on the new, enhanced approach. As previously explained, the cell's internal resistance is measured at stage 2 of the base methodology, allowing the irreversible heat to be estimated. The EHC is not measured, however. Therefore the reversible heat is not accounted for. Depending on each cell's characteristics, the element's significance will vary in relation to the thermal behaviour, but it is necessary for a thorough thermal analysis. The cell must therefore be electrically and thermally characterised at the second stage.

As a result, EHC must be used for the enhanced methodology. The second stage is the most suited for its measurement, given that characterisation and cell parameter analysis are completed there. Figure 4.1 depicts the updated methodological structure.

For the EHC measurement, it is recommended to start with a 10 % SOC precision approach with the potential to raise accuracy to 5 % on unique and intriguing SOC sites. The accelerated life cycle tests are now included in Ageing and lifespan tests of Stage 3, which is still defined according to the base methodology.

Laying down some standard criteria is fundamental for a faithful

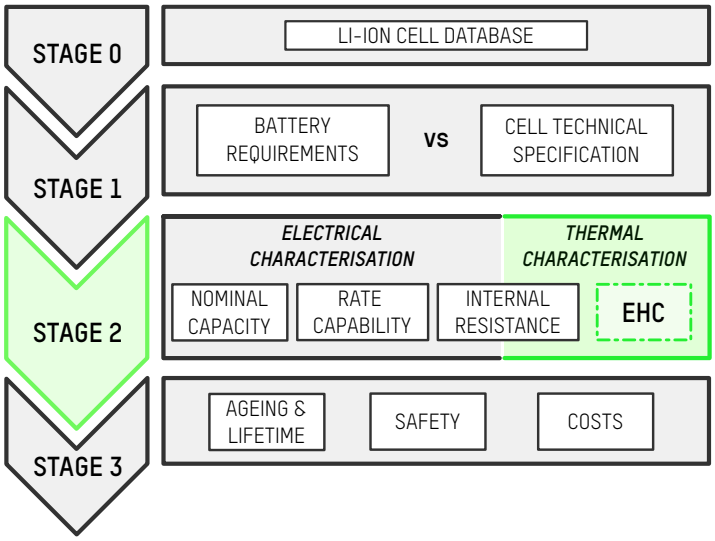

Figure 4.1: *Improved methodology with EHC measurement and thermal characterisation.*

contrast of diverse cells' heat generation. Hence, the comparison is made under specific application requirements. First, a cell series-parallel configuration is suggested, with the cell number to be used dependent on the application BP's minimum necessary energy. The thermal model is then applied to this cell quantity to extrapolate the cell's heat production across the entire battery pack. Additionally, the fast charging need is crucial. In this scenario, time is assumed to be an unchangeable factor; hence all candidate cells are charged at a predetermined C-rate. As a result, the battery pack's recharged energy should be the same, satisfying the application's time and energy needs while allowing for a fair comparison of the various cells.

The thermal behaviour of the cell will be added as a selection parameter using this improved methodology. The comparison for this criterion will favour the lowest heat generation, particularly with fast charging. An endothermic behaviour will also be desired as it will cause the temperature to drop.

4.2 Battery Electrothermal Parameter Characterisation Tests

The cell selection analysis and the heat generation model require the battery cell's R_{in} and EHC electrothermal parameters. The testing procedure for their obtaining is reported, detailing the necessary equipment usage.

Furthermore, the specific heat (C_p) and thermal conductivity (k) testing methods are also depicted. These parameters are not used in the heat generation model or cell selection. Nevertheless, they will be mandatory on heat transfer and accumulation equations on the latter used BTMS thermal models.

4.2.1 Internal Resistance

Internal resistance (R_{in}) [Ω] is one of the essential aspects to consider when doing a thermal characterisation of a cell. The lower the internal resistance, the lower the heat generation in the cell will be. It depends on the thermal and chemical equilibrium levels, meaning it is a function of cell temperature and SOC.

The cell's internal resistance is measured by the Hybrid Power Pulse Characterisation (HPPC) test [161]. This is performed at different SOC and temperature levels by applying a constant current pulse of 18 seconds while voltage change is measured. The cell cycling, as well as the current pulse, is performed with a programmable cycler (Industrial Battery Tester (IBT) with 0.1 % accuracy of full scale, which runs with Digatron/Firing Circuits BTS-600 software for data evaluation) shown in fig. 4.2b. A CTS (Clima Temperatur Systeme) thermal chamber controls the different temperatures at which the cell is tested. This type of chamber provides an excellent testing capacity and significant control due to its wide temperature range, reaching from -70 °C to +180 °C with an accuracy of 0.3 °C. For increased accuracy, cell voltage and temperature are measured using a data acquisition system (DAQ) *Agilent 34970A* shown in fig. 4.2c, along with T-type thermocouples. The DAQ has an accuracy of ±0.0035 % reading and 0.0005 % of range for voltage. Additionally, DAQ's temperature precision is ±0.5 °C of range and 0.2 % of reading, while type-T thermocouples have a ±1.0 °C accuracy.

(a) *Thermal Chamber (CTS).* ***(b)*** *Programmable Cycler.* ***(c)*** *Data Acquisition System (DAQ).*

Figure 4.2: *Equipment used in the experimental tests.*

A 1C current pulse is used for the test, and cell's voltage is measured initially and 18 seconds after the pulse. The relation of the current and voltages is used to determine the internal resistance, following the eq. (4.1).

$$R_{in} = \frac{V_1 - V_2}{I} \tag{4.1}$$

The SOC's usual resolution measured in the test is 10 %, going from 10 % to 90 % of the total capacity of the cell. On the other hand, the temperatures for the tests are at least three: a low, medium and high temperature of around 10 °C, 25 °C, and 40 °C, which are adapted for the specific application.

4.2.2 Entropic Heat Coefficient

The second parameter to be measured is the EHC [V/K] which quantifies the reversible change in the open circuit voltage (OCV) that occurs in response to a temperature change in the cell. The entropic heat coefficient is not a constant factor, and its value varies with SOC levels.

The variable temperature potentiometry is employed to determine the

EHC [162], where thermal chamber temperatures are changed by applying a temperature profile to the LIB at each desired and stable SOC position. The thermal profile used is shown in fig. 4.3, alternating between positive and negative temperature steps of three hours long. This procedure ensures reducing to the minimum the cell relaxation; therefore, EHC results are not affected by the voltage variations derived by this phenomenon. The equipment used is the same as depicted in fig. 4.2, with the thermal chamber for temperature control, the programmable cycler for SOC change, and the DAQ for temperature and voltage measurements.

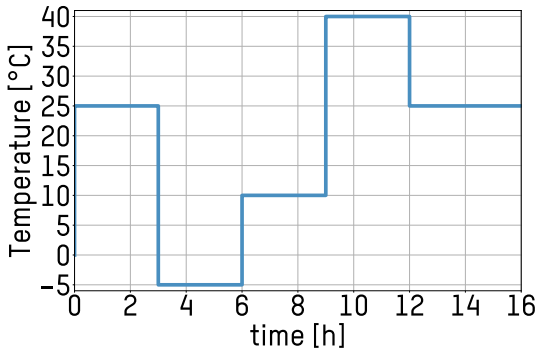

Figure 4.3: *Thermal profile applied for EHC measurement.*

The cell's open circuit voltage is measured for the entire process, obtaining voltage fluctuations at each SOC step, as seen in fig. 4.4a. These SOC steps' voltage profiles are then isolated and fitted to the eq. (4.2).

$$V(t, T) = A + BT + Ct \tag{4.2}$$

T is the cell temperature, whereas t is the test time. A, B, and C are the constants to fit, where B corresponds with the EHC value for that SOC step [40]. As mentioned, due to the minimised cell relaxation effect over time, C constant is almost zero, and EHC can be effectively isolated. The constants are determined by the optimisation procedure function *"curve_fit"* of the scientific computing module Scipy in Python. Figure 4.4b shows the example fitting at 70 % of SOC of the EHC measurements done to a battery. This procedure is repeated for all the SOC interested.

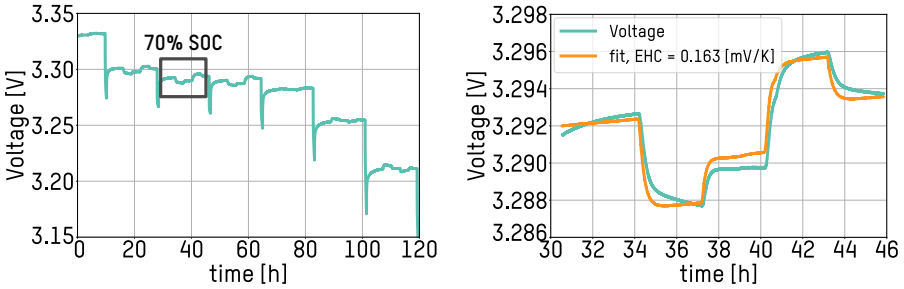

(a) *OCV voltage measurement of the EHC test.*

(b) *OCV variation fitting at 70 % SOC for entropic heat coefficient obtaining.*

Figure 4.4: *EHC measurement procedure with OCV voltage reading and fitting.*

4.2.3 Specific Heat Capacity

The specific heat capacity (C_p) [J/kg·K] of a LIB is not necessary for the heat generation estimation, but it is mandatory for the heat accumulation equation used on the thermal models. Therefore, the experimental measurement procedure utilised for its obtaining is depicted next.

Accelerating Rate Calorimeter (ARC) (THT, EV Standard Calorimeter) shown in fig. 4.5 is used for the calorimetry tests to measure the C_p [163]. In that procedure, the calorimeter walls are heated up following the sample temperature, creating an adiabatic environment where no heat is dissipated outside the cell.

Figure 4.5: *Accelerating Rate Calorimeter (ARC)*

In that adiabatic environment, the analysed cell is heated with a known energy amount through an electric heater. The temperature evolution is measured on the cell, obtaining a ΔT temperature change on a determined period. C_p can then be solved with the measured data from the eq. (4.3):

$$\dot{Q} = M \cdot C_p \cdot \frac{\Delta T}{\Delta t} \tag{4.3}$$

where $\dot{Q}$ [W] is the electric power applied to the heater, M [kg] is the mass of the cell, ΔT [°C] is the temperature change, and Δt [s] is the test time. The test is repeated several times, altering the electric power applied, the temperature range or even the time, and results are averaged, obtaining the cell's $C_{p_{avg}}$.

Two possible arrangements should be used depending on cell geometry. For prismatic or pouch cells, a planar electric heater is sandwiched between two sample cells, ensuring heat conduction to them, as seen in fig. 4.6a. However, with cylindrical cells, cartridge heaters are placed surrounded by 3 to 4 cells, as seen in fig. 4.6b. Necessary thermocouples are added to map the temperature evolution of the cells properly.

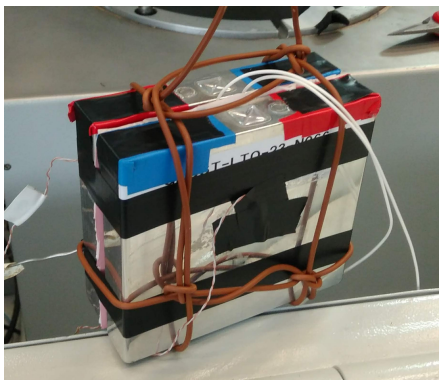

(a) *C_p measurement procedure for prismatic/-pouch cells.*

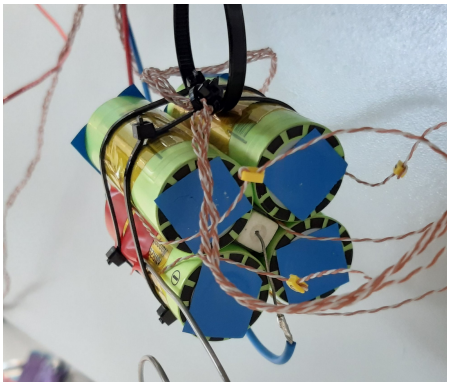

(b) *C_p measurement procedure for cylindrical cells.*

Figure 4.6: *Electric heater arrangement for C_p measurement procedure.*

4.2.4 Thermal Conductivity

A non-destructive technique which required two lithium-ion cells per measurement was used for the determination of both the in-plane and cross-plane thermal conductivities.

The equipment used for thermal conductivity measurements was a hot disk TPS 2500 with anisotropic module (fig. 4.7) with a measurement range from 0.005 to 500 W/m·K. The repeatability of the measurement is 1 to 2% and the equipment has a measurement precision of 2-5%.

Figure 4.7: *Hot disk TPS 2500.*

The hot disk transient plane source (TPS) technique was used, which met ISO Standard (ISO/DIS 22007-2.2 [164]). This method is limited to materials in which the thermal properties along two of the orthogonal and principal axes are the same, but are different from those along the third axis. This was assumed to be the case of the lithium-ion cells tested. The hot disk probe comprised a flat sensor with continuous double spiral of electrically-conducting nickel metal etched out of thin foil and sandwiched between two layers of insulating material. During the experiment, the sensor was placed between the surfaces of two pieces of the sample measured in a sandwich configuration.

During measurement, a current passed through the Nickel spiral and created an increase in temperature. The heat generated is dissipated through the sample on either side at a rate dependent on the thermal transport characteristics of the material. By recording the temperature versus time response in the sensor, the thermal conductivity could accurately be calculated [164].

4.3 Validation Case Study of the Improved Cell Selection Methodology

This section relates how the cell selection procedure is validated after the improved methodology is described in Section 4.1. For this case study, an ICE vehicle electrification project (*SELF-sustained and Smart Battery Thermal Management SolutIon for Battery Electric Vehicles - SELFIE* [165]) is used, where cell selection is the first essential part of the design.

This case study is assessed through a thermal stance. Therefore, this study does not present Stage 3 of the methodology, emphasising the second stage's thermal characterisation and the consequent cells' thermal analysis.

4.3.1 Adequate Cell Identification: Stage 0 and Stage 1

Stage 0

The database is searched for candidate cells at this point. Five examples are found and chosen based on their accessibility for the project, and their technical details are shown in table 4.1. The following stage will determine their appropriateness for the project due to the significant discrepancies in requirements between each other.

Table 4.1: *Stage 0 candidate cells' specifications*

	Sample				
	1	2	3	4	5
Name	Toshiba	Kokam	LG INR21700	ANKA0	Narada
Model	SCiB	SLPB	M50	IFR32135	FE50A
Chemistry	LTO	NMC	NMC	LFP	LFP
Nominal Capacity [Ah]	23	40	5	10	50
Nominal Voltage [V]	2.3	3.7	3.6	3.2	3.2
Nominal Energy [Wh]	52.9	148	18	32	160
Specific Energy [Wh/kg]	96	160	267	128	120
Energy Density [Wh/L]	203	288	186	66.3	227.9
Maximum Charge [C-rate]	8C	3C	0.7C	10C	2C
Mass [kg]	0.55	0.99	0.068	0.25	1.329
Volume [L]	0.260	0.513	0.098	0.483	0.702
Lifetime [Cycles]	15000	3000	4000	2500	2000
Geometry	Prismatic	Pouch	Cylindrical	Cylindrical	Prismatic

Stage 1

In this stage 1, the nominee cells' specifications are compared with the requirements for the battery pack specified for the application. The project is built on three essential requirements for this initial cell selection study: needed energy, maximum volume, and minimum fast-charging capacity. The project's feasibility also depends on a minimal cell lifespan.

In order to attain the needed autonomy, the vehicle must have a battery pack of around 30 kWh of energy capacity, settled as the minimum value for the cell selection study. Furthermore, as this is the electrification of an ICE car, only 220 litres of space is left for the battery pack. The other crucial requirement for the application is fast car charging, with a 3C charge being the standard minimum. Finally, the project must have a minimum lifetime of 1500 cycles.

In light of these references, arrangements for battery packs larger than 30 kWh are evaluated with all potential cell types. Regarding consistency, BP's voltage is likewise made to aim for 400 V. Table 4.2 displays the final cell series-parallel configuration and the total number of cells (Number of Cells (n_{cell})), which also affects the volume of the product. The application requirement is also compared to the charging rate of the cells.

Table 4.2: *Stage 1 cell selection by application requirements comparison.*

	BP	SAMPLE				
	Requisites	**1**	**2**	**3**	**4**	**5**
BP Energy [kWh]	30	30.15	30.19	30.24	30.02	30.72
Voltage [V]	-	437.0	377.4	432.0	428.8	307.2
Cell Configuration	-	190S3P	102S2P	120S14P	134S7P	96S2P
Number of cells [n_{cell}]	-	570	204	1680	938	192
Total Volume [L]	Max. 220L	148.2	104.7	164.6	453.1	134.8
Charge [C-rate]	Min. 3C	8C	3C	0.7C	10C	2C
Lifetime [Cycles]	Min. 1500	15000	3000	4000	2500	2000

Analysing the results, while sample 4 exceeds the maximum volume permitted, samples 3 and 5 falls below the minimum charging C-rate. Every cell has a lifespan higher than the minimum value specified for the application. The candidate cells for stage 2 of the revised approach are thus samples 1 and 2.

The lowest C-rate of Sample 2, with a maximum charge limit of 3C, de-

termines the charging current to be used in this cell selection case study. Furthermore, 570 and 204 cells from samples 1 and 2 are employed, respectively, to achieve the requisite battery pack energy. These data will be integrated into the cell characterisation that comes after stage 1 in order to create a consistent and reasonable comparison of both BP's heat generation.

4.3.2 Proposed Cells' Characterisation: Stage 2

With the two candidate cells selected, electrical and thermal characterisation proceeds for the final cell election. In that way, the cell parameters necessary for the following thermal analysis will be measured.

Measurements include nominal capacity, rate capability, internal resistance, and entropic heat coefficient. The first two parameters describe the cell's electrical behaviour and are measured to check the supplier's data. The two latter components define the thermal properties of the cell. R_{in} defines electrical and thermal behaviours, but it is only assessed from a thermal position to validate the methodology presented. Therefore, EHC and R_{in} values are used at the end of stage 2 to estimate the heat power through reversible and irreversible heat, respectively. Hence, cell selection based on thermal criteria will be performed under a fast charge analysis.

Rate capability assesses the capacity of cells at various current loads, whereas nominal capacity is determined by performing three charge-discharge cycles at varying temperatures and 0.2C in a thermal chamber [157]. For varying SOC and temperature levels, the R_{in} values are determined using constant current discharge pulses lasting 18 seconds [161], whereas the EHC measurements are made using variable temperature potentiometry [162].

(a) Nominal Capacity and Rate Capability:

The capacity of the cells is significantly impacted by temperature and C-rate. However, cells' nominal requirements must be met to recognise the validity of samples. Table 4.1 shows the nominal capacity values for samples 1 and 2 at testing temperatures of 25 °C and 0.5C, respectively, which are 23 Ah and 40 Ah. Nominal capacity testing for the characterisation process is done at 0.2C at 10 °C,

20 °C, 30 °C, and 40 °C. Moreover, rate capability tests are done at 0.5C, 1C, 2C, and 4C at 25 °C. Table 4.3 demonstrates that the cell manufacturer's data is effectively attained and only degrades at low C-rates (>2C for sample 1 and >1C for sample 2) and cold temperatures (10 °C). Consequently, candidate cells are accepted from the nominal capacity and rate capability facets.

Table 4.3: *Nominal Capacity and Rate Capability of Sample 1 and Sample 2 [166].*

Temperature	Nominal Capacity [Ah]		C-Rate	Rate Capability [Ah]	
	Sample 1	Sample 2		Sample 1	Sample 2
10 °C	22.22	39.39	**0.5C**	23.3	40.3
20 °C	23.30	40.43	**1C**	23.1	38.3
30 °C	24.03	41.29	**2C**	23.0	38.0
40 °C	24.57	41.97	**4C**	22.8	37.6

(b) Internal Resistance:

A 10 % resolution is used to quantify the internal resistance on the cell's SOC scale from 10 % to 90 %. On the other hand, the test temperatures are 10 °C, 20 °C, 25 °C, 30 °C, 35 °C, and 40 °C. The internal resistance results for samples 1 and 2 are shown in fig. 4.8a fig. 4.8b, respectively. With significantly greater resistance levels on the second cell, the typical behaviour of R_{in} with its increase at low SOC levels and temperatures is shown.

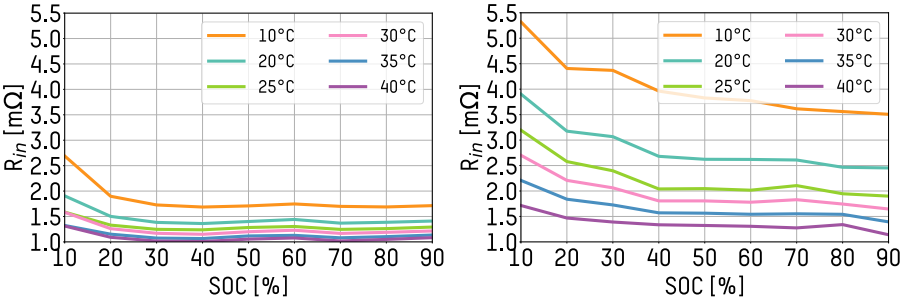

(a) *R_{in} of Sample 1.* ***(b)*** *R_{in} of Sample 2.*

Figure 4.8: *Internal Resistance.*

(c) Entropic Heat Coefficient: With a 10 % resolution of the SOC, from 10 % to 90 %, the entropic heat coefficient of each candidate cell

is determined. For sample 2, data at 55 % of SOC is added, and for sample 1, data steps of 5 % are also introduced from 50 % to 90 % of SOC values, where fast changes in EHC values are detected.

According to fig. 4.9a, sample 1 candidate cell's EHC is highly consistent across all SOC and has a distinct negative peak at -0.46 mV/K at the 65 % charge level. This will imply an increase in heat power when the cell is discharged at that SOC level, but the charging process will result in an endothermic effect and a corresponding decrease in heat power. Sample 2 includes a negative portion with a peak of -0.2 mV/K on the initial SOC level, but this is balanced out by positive EHC values practically throughout the rest of the SOC level with a maximum value of 0.13 mV/K on 55 % of SOC, as seen in fig. 4.9b.

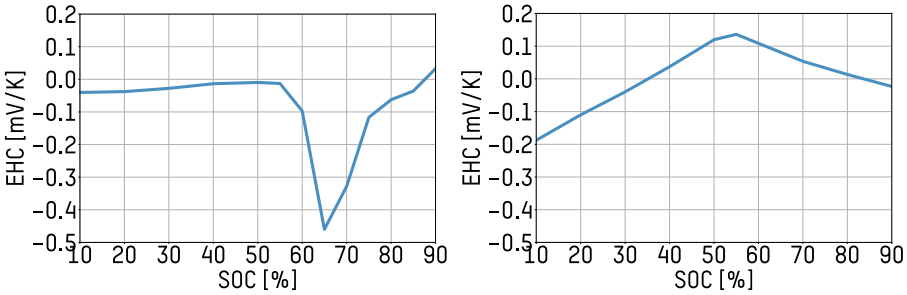

(a) *EHC of Sample 1.* ***(b)*** *EHC of Sample 2.*

Figure 4.9: *Entropic Heat Coefficient.*

The R_{in} and EHC data obtained in the characterisation will be used in the next step of the cell selection methodology to properly estimate the heat generation of each cell sample.

4.3.3 Thermal Analysis: Numerical Assessment

The generated heat estimating model employed in this second stage adheres to the earlier stated eq. (3.1) and follows the guidelines set by Nieto et al. [167]. Several works [167–169] have already verified this cell's heat generation model. However, as illustrated on eq. (4.4), the number of cells is added to extrapolate the heat generation to the battery pack level.

$$\dot{Q} = \left(I^2 \cdot R_{in} + I \cdot T \cdot \frac{dU^{avg}}{dT} \right) \cdot n_{cell} \tag{4.4}$$

The nominal capacity, charging current, and constant cell temperature inputs are used to feed the heat generation model together with the SOC, which is calculated using the coulomb counting method [170]. Utilising those inputs, R_{in} and EHC are interpolated for each time step from the characterisation data presented. For samples with predominately negative EHC values, heat generation will be higher during the discharge process under the same cycling circumstances. The fast-charging procedure is, however, noticeably more intensive due to increased C-rate utilisation, which raises the irreversible heat generation well above the reversible part and, thus, the total heat generation. As a result, the thermal model is run over the charging of the cell to acquire the corresponding heat energy generation of the most demanding operation part.

The heat generation model is fed for a 3C fast charge at four different constant temperatures: 15 °C, 25 °C, 35 °C, and 45 °C. According to fig. 4.10, the amount of reversible, irreversible, and total heat energy for cells from samples 1 (discontinuous line) and 2 (continuous line) are compared. As internal resistance reduces at higher temperatures, irreversible energy also decreases. This effect may be seen more clearly with cell candidate 2, which has significantly higher R_{in} levels at low temperatures.

Reversible energy variations have less impact on temperature changes since they are much smaller than irreversible ones. However, the amount of heat energy in both cells is substantially different. In contrast to Sample 1, which absorbs close to 250 Wh, sample 2 completes the charge with 20 Wh of reversible heat production (Q_{rev}), as seen in table 4.4. Candidate 1 is helped by this phenomenon to reduce its heating capacity, which results in a drop in temperature, as evidenced by the total heat energy generated during the charge. Favourable EHC and, consequently, the reversible heat enable Sample 1 to release less than half the total heat than Sample 2, even at 45 °C where the irreversible generation (Q_{irr}) is at its lowest. This is further corroborated by the charging energy efficiency values (η_{charge}) derived from eq. (4.5), where only the irreversible heat generation is taken into account because the net reversible heat generated during charge and discharge is zero [171].

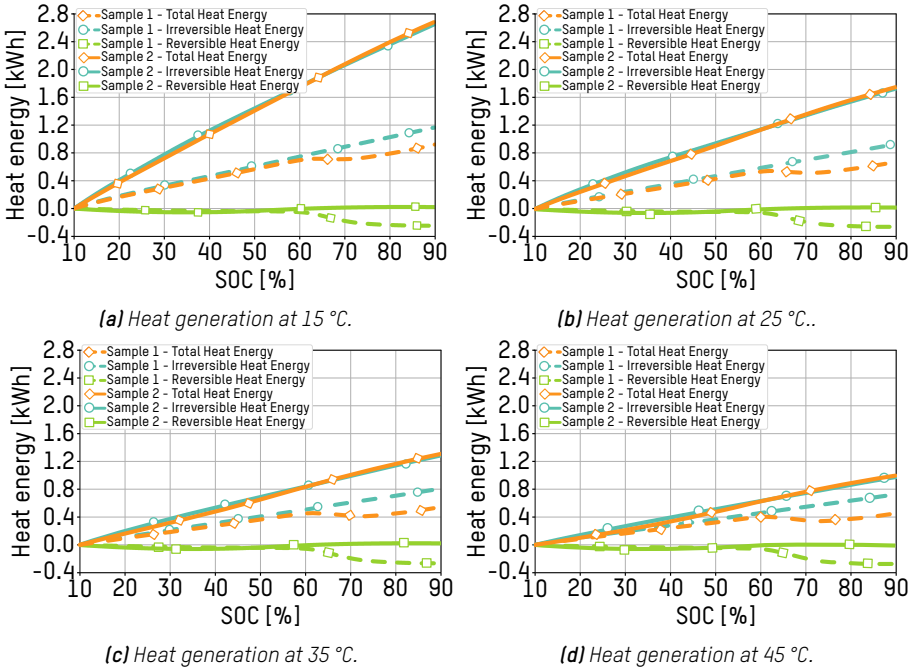

(a) *Heat generation at 15 °C.*

(b) *Heat generation at 25 °C..*

(c) *Heat generation at 35 °C.*

(d) *Heat generation at 45 °C.*

Figure 4.10: *Heat energy generation of sample 1 and 2, at 3C charge*

$$\eta_{charge} = \frac{E_{charge} - Q_{irr}}{E_{charge}} \tag{4.5}$$

E_{charge} [kWh] is the electrical energy charged onto each battery pack configuration between 10 % and 90 % of SOC, and Q_{irr} [kWh] is the process's irreversible heat generation. An endothermic reversible heat is present, along with the increased efficiency seen in Sample 1 for all temperatures considered. Consequently, the TMS will use proportionally less energy than is required for Sample 2 to dissipate that heat.

The cell Sample1 phenomenon will improve performance with lower ultimate temperatures, significantly reducing the need for cooling during fast charging. Additionally, it makes control more accessible and lessens any security issues, making this cell the best choice for this specific application, particularly for quick charging operation.

Table 4.4: *Heat energy generation results at the end of the 3C charge.*

Temperature	Sample 1 [kWh]			η_{charge} [%]	Sample 2 [kWh]			η_{charge} [%]
	Q_{irr}	Q_{rev}	Q_{tot}		Q_{irr}	Q_{rev}	Q_{tot}	
15 °C	1.17	-0.25	0.93	**95.1 %**	2.67	0.02	2.69	**88.9 %**
25 °C	0.94	-0.26	0.68	**96.1 %**	1.74	0.02	1.76	**92.8 %**
35 °C	0.81	-0.26	0.55	**96.6 %**	1.29	0.02	1.31	**94.6 %**
45 °C	0.73	-0.27	0.46	**97.0 %**	0.98	0.02	1.01	**95.9 %**

4.3.4 Thermal Analysis: Experimental Validation

This section ratifies the results of the cell selection numerical analysis to validate the improved methodology presented. First, adiabatic calorimetry is used to identify the heat generation rate ($\dot{Q}$). Finally, a 3C fast charge is performed under three isothermal ambient temperatures. Therefore, temperature measurement during operation can confirm the projected performance of the cell.

(a) Thermal performance during adiabatic ambient discharge:

An Accelerating Rate Calorimeter (ARC) with an accuracy of 0.7 % is used to determine the heat generation rate in an adiabatic environment. Due to the cell's specific EHC property, reversible heat during charging behaves endothermically, absorbing heat at certain C-rate and SOC levels. The endothermic processes cannot be carefully tracked since the calorimeter heats the enclosure walls to create an adiabatic atmosphere and has no cooling capability. Hence, the discharge process, in which net heat is entirely exothermic in this scenario, must be employed for generated heat measurement.

All the heat produced when cycling the cell is deposited on it since the adiabatic atmosphere assures that no heat is transferred to the surrounding air. As a result, this energy balance provides two ways to gauge the pace at which heat is generated: heat accumulation and the heat generation model itself. The energy balance equation is represented by both terms as follows:

$$I^2 \cdot R_{in} + I \cdot T \cdot \frac{dU^{avg}}{dT} = M\, C_{p_{avg}} \frac{dT}{dt} \tag{4.6}$$

The heat generation model shown on eq. (3.1) is represented by the term on the left of the energy balance equation. The new term describes the heat that is stored on the cell on the right side of the energy balance, where M [kg] is the mass of the cell, $C_{p_{avg}}$ [J/kg·K] is the average specific heat capacity, and dT/dt [K/s] is the measured temperature change over time.

Calorimetry measurements were conducted to determine the C_p [163]. The values of C_p were determined by measuring the temperature gradient over time while altering the heat power that the cell received from a planar resistance. The results of the tests are averaged, giving 1163 J/kg·K for the selected cell, as given in table 4.5.

Table 4.5: *$C_{p_{avg}}$ values and test data for cell sample 1.*

	P [W]	ΔT_{avg} [°C]	C_p [J/kg·K]	$C_{p_{avg}}$ [J/kg·K]
Sample 1	4.9	22.7	1161	**1163**
	18.7	22.2	1165	

For the determination of $\dot{Q}$, the battery was connected to a programmable cycler (Industrial Battery Tester (IBT) with 0.1 % accuracy of full scale, which runs with Digatron/Firing Circuits BTS-600 software for data evaluation) for discharging the battery at various C-rate during the adiabatic calorimetry test. T-type thermocouples and an Agilent 34970A data-collecting device were also utilised to gauge the temperature of the cell's surface. The Agilent has accuracy requirements of ±0.0035 % of reading and 0.0005 % of range for voltage. Additionally, Agilent's temperature precision is ±0.5 °C of range and 0.2 % of reading, while type-T thermocouples have a ±1.0 °C accuracy. Figure 4.11 depicts the setup for the discharge test inside the calorimeter.

Each test was run at three different discharging currents of 1C, 2C, and 3C, ranging from 90 % SOC to 10 % SOC. The starting temperature for each test was the ambient one, with mean values of 22.5 °C, 25.5 °C, and 22.2 °C, respectively. The cell temperatures after the testing were 31.7 °C, 39.8 °C, and 41.1 °C; therefore, additional ex-

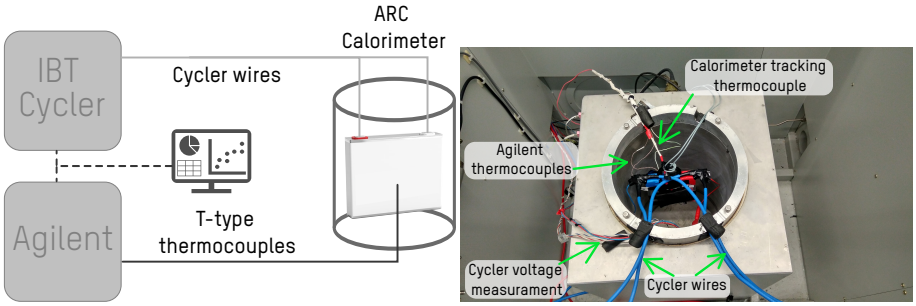

(a) *Scheme of calorimetry test.* ***(b)*** *Setup of calorimetry test.*

Figure 4.11: *Scheme and setup of adiabatic calorimetry test.*

periments with more significant discharge current rates were dismissed to guarantee the cell's functioning within the ideal temperature range. Heat generation was calculated using the accumulation and generation equations in conjunction with the temperature evolution data recorded on the cell's adiabatic calorimetry discharge. Figure 4.12 displays the outcomes of this analysis.

The uncertainty in the heat generation model is negligible due to Agilent's voltage measurement precision on HPPC and potentiometry tests all through cell R_{in} and EHC parameter evaluation. The uncertainty range of the heat accumulation estimation of three discharge tests from the calorimetry test on $C_{p_{avg}}$ assessment is displayed in fig. 4.12. All of the uncertainties were estimated utilising the Lee [172] technique.

On the three discharge tests, a heat power peak caused by the minimum EHC value of -0.46 mV/K is identified using both accumulation and generation models. At that point, reversible heat increases significantly, raising the heat generated overall. The low EHC value combined with a flat internal resistance keeps the heat generation reasonably constant for the remaining SOC values. Owing to the reversible heat flip, these results demonstrate the unique thermal performance of the chosen sample 1, which will be extremely helpful in the charging process.

(b) Thermal performance during isothermal ambient charge:

At this point, fast charging has been used to analyse further the

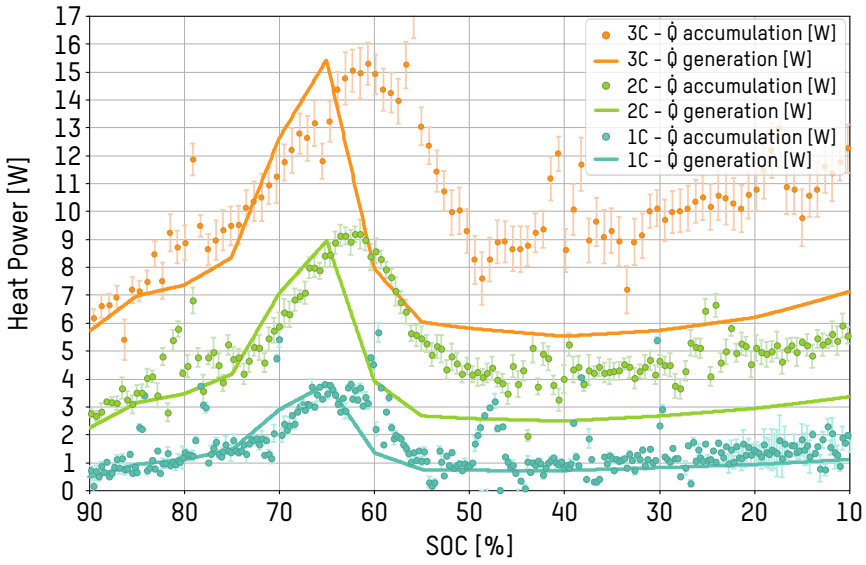

Figure 4.12: *Adiabatic heat power generation analysis by heat accumulation and heat generation methods at 1C, 2C and 3C.*

selected cell's observed favourable thermal behaviour. This allows for the study and real-world validation of the forecasted functioning and optimal thermal response shown during cell selection.

If the theoretical behaviour of EHC is met, the thermal model predicts an optimistic scenario of abrupt heat power drop below zero with a subsequent temperature fall on fast charging. Three different constant ambient temperatures (15 °C, 25 °C, and 35 °C) are settled in a thermal chamber as part of a 3C constant rapid charge to demonstrate this behaviour. The used thermal chamber (CTS, Clima Temperatur Systeme) can maintain the required ambient temperature with an accuracy of 0.3 °C. Agilent was used to map the cell's temperature, and one T-type thermocouple was placed on each cell's surface. The IBT was then used to charge the cells at 3C current, as shown in fig. 4.13's experimental setup.

The three experiments began at slightly higher but stable cell temperatures of 16 °C, 26.5 °C, and 36 °C, respectively, due to the high thermal inertia of the cell and preceding discharging for condition-

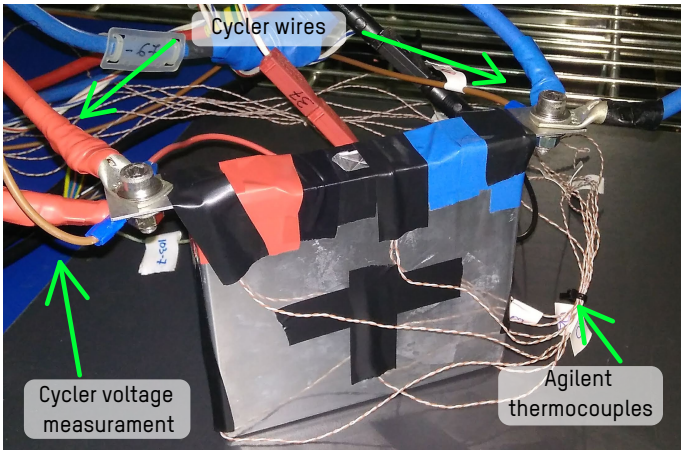

Figure 4.13: *Experimental Setup for fast charge analysis.*

ing. The cell was totally discharged when the charge began and terminated when the maximum cutoff voltage was achieved. Due to the high charging current, the cell's usable capacity was drastically reduced, and the cutoff voltage was reached before the battery was fully charged. The internal resistance is lower and allows for more charging at higher temperatures, which also impacts this behaviour. Thus, at 15 °C, only 77 % of SOC is charged; at 25 °C 88 %, and even at 35 °C test, 92 % of SOC is attained.

After the three tests, the surfaces' mean cell temperatures were 21.8 °C, 32.8 °C, and 40.3 °C, respectively. Therefore, maintaining the ambient temperature assured the cell's performance within the ideal temperature range. Figure 4.14 illustrates the cell's temperature difference evolution with the test beginning temperature and allows for better result comparison between tests, emphasising the significance of ambient temperature. Reversible heat has a noticeable effect, causing a significant temperature change between 60 % and 75 % of SOC. The temperature decreases are relatively insignificant, coming in at 0.21 °C, 0.17 °C, and 0.41 °C, respectively. The temperatures, however, significantly stabilise due to this variance, and the cell's maximum ending temperature is significantly lowered.

To conclude with the presented methodology and its validation case study, the predicted heat generation for the selected cell is much lower,

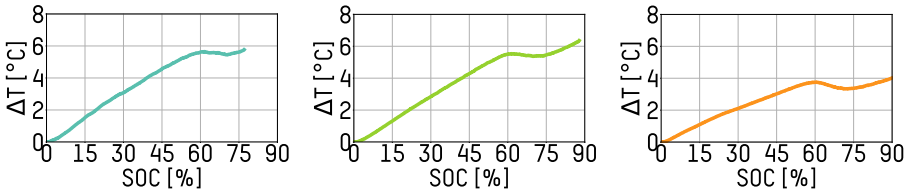

(a) *3C charge at 15 °C.* ***(b)*** *3C charge at 25 °C.* ***(c)*** *3C charge at 35 °C.*

Figure 4.14: *Selected cell's surface mean temperature evolution at 3C charge with 15 °C, 25 °C and 35 °C ambient temperature.*

with the total heat being reduced by at least 550 Wh. The efficiency of the chosen cell is higher than that of the other candidates under all the research settings. The performance in cell sample 1 is primarily driven by the specific EHC coefficient for rapid charging, highlighting the importance of the thermal study and the methods described in this work as critical elements in making the best cell choice.

Therefore, this new methodology aids in identifying a battery's actual performance and provides crucial selection criteria for picking the optimal cell for each activity. After demonstrating the significant impact of the entropic heat coefficient on heat generation efficiency, the significance of accurately characterising the cell is further stressed. Better cell selection for challenging tasks such as fast charging will result from this, increasing battery pack efficiency, decreasing TMS size, and preventing any potential heat problems in the future.

5

CFD Based Comparison:

Case Studies for Advanced BTMS Solutions for Electromobility

Summary

This thesis chapter compares two case studies of advanced BTMS solutions for electromobility. Using the same battery module, both systems will undergo CFD simulations. The first system is a Cold Plate- and PCM-based BTMS, while the second is a Dielectric Flow- and Tab-Based BTMS. The chapter will present the concepts and designs of these systems, along with the corresponding thermal models. The obtained thermal and hydraulic results will be discussed, and a comparative analysis of the BTMS solutions will be conducted. Finally, the chapter will conclude with a comprehensive discussion of the advantages and disadvantages of each system.

5.1 Battery Module Implemented for Electromobility BTMS Comparison

This chapter presents a CFD-based comparison of two advanced BTMSs in two case studies. The thermal management solutions are implemented on a real-case electromobility battery module. This shared battery platform will allow a fair comparison between the two case studies and advanced thermal management systems under the same cycling circumstances.

The electric characteristics of the BEV used in this case study will be defined following the BP needs previously presented in the case study of cell selection methodology in Section 4.3. These guidelines were derived from the *SELFIE* [165] project, which involved converting an ICE vehicle to a BEV based on a Fiat Doblo platform. The BP aims to achieve a target energy capacity of 30 kWh, with an electric structure operating at a nominal voltage of 400 V. In reality, the BP configuration measures 414 V and 28.56 kWh.

The battery pack comprises prismatic LTO Toshiba SCiB™ 23Ah cells [173]. These cells correspond to the previous choice in the cell selection methodology case study presented on Section 4.3 in Chapter 3. Hence their fast charging capability with an endothermic behaviour around 60 % - 70 % of SOC can be enhanced. Their electrical information is depicted in table 5.1.

Table 5.1: *Properties of prismatic Toshiba SCiB 23Ah cell.*

Toshiba SCiB™23Ah	
Chemistry	LTO
V_{nom} [V]	2.3
Cap_{nom} [Ah]	23
Nominal Energy [Wh]	52.9
Specific Energy [Wh/kg]	96
Max CHA Current [A]	200 (8.6C)
Max DCH Current [A]	100 (4.3C)
Temperature Range [°C]	-30 to 55
Dimensions [mm]	H:105 x L:115 x W:21.5
Volume [L]	0.26
Mass [kg]	0.55

Moreover, both thermal parameters R_{in} and EHC, necessary for cell heat generation modelling, are experimentally characterised following the methodology presented in Section 4.2. The EHC is obtained for all the SOC scope of the cell, as well as the R_{in}, which is measured for six different temperatures (10 °C, 20 °C, 25 °C, 30 °C, 35 °C and 40 °C). This data is depicted in fig. 4.8a and fig. 4.9a on the cell selection part.

The 28.56 kWh battery pack is developed under a 414 V infrastructure. It is distributed in 12 modules connected in series. Moreover, these modules are assemblies of 45 cells in a 15S3P electric configuration. Under this configuration, the battery pack has a total amount of 540 cells. The battery module and pack information are depicted in table 5.2.

Table 5.2: *Electric configuration of the battery module and battery pack.*

	Battery Module	**Battery Pack**
Energy [kWh]	2.38	28.56
Voltage [V]	34.5	414
Capacity [Ah]	69	69
Cell/Module Configuration	15S3P	12S1P
Number of modules	-	12
Number of cells [n_{cell}]	45	540

However, the battery pack consists of two entities, as it is adapted to an existing vehicle. On those entities, the battery cells are uniformly distributed in arrays of 30 and electrically connected by copper busbars to form modules. These arrays are modular, designed with an adapted BTMS and stacked to form the complete battery pack. For this study, the minimal representative portion of the battery pack system is defined as this modular array configuration. Figure 5.1 depicts the battery pack and one of the cell arrays with the electric connection busbars.

The battery thermal management system's thermal analysis and comparison will be developed over this battery array. Initially, the cold plate- and PCM based BTMS solution will be presented and analysed, followed by the dielectric flow- and tab-based thermal management system, both adapted for this battery geometry.

Regarding the operation and cycling of the battery, it will face two distinct situations, the combination of which constitutes the entire battery

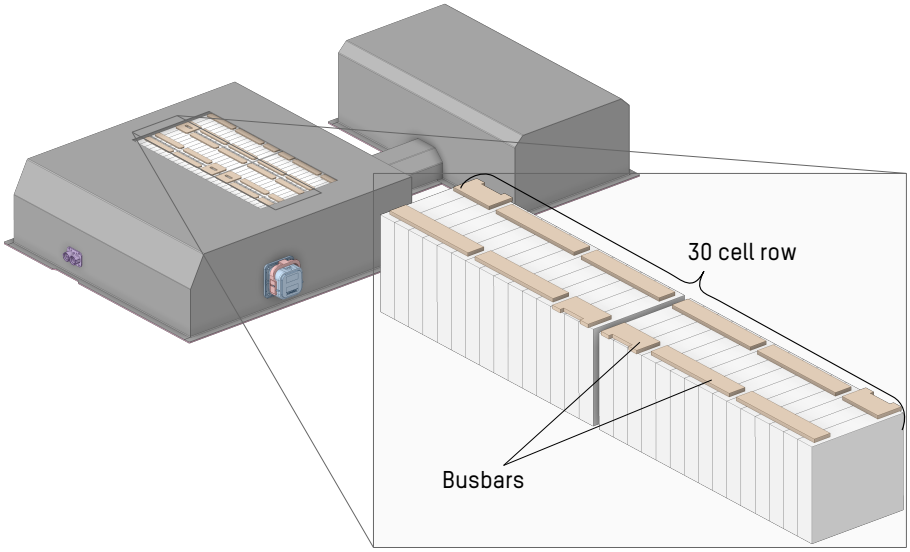

Figure 5.1: *Battery pack and its modular 30-cell array used in the study.*

cycle employed for analysis in this work (fig. 5.2) and is ostensibly the most challenging environment to evaluate the thermal management systems:

- Fast Charge (FC): The battery pack undergoes a predefined constant 6C charge, where in 8 minutes, the SOC recovers from 10 % to 90 %.
- Normal Drive (ND): A demanding discharge application has been defined, which includes a motorway constant driving scenario at 130 km/h. From the vehicle power consumption data shown in fig. 5.3, 47.8 kW is known to be required. Therefore, with the battery pack electric configuration information, the necessary discharging electric current (I_{dch}) of the cells is defined as 38.41 A or 1.67 C-rate, following eq. (5.1). Therefore, the BP is drained in about 28 minutes.

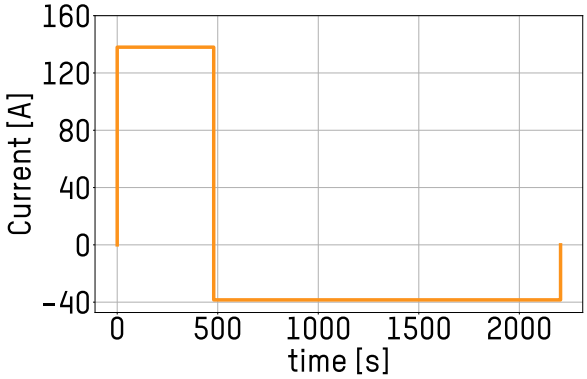

Figure 5.2: *Current profile employed on the battery cycling.*

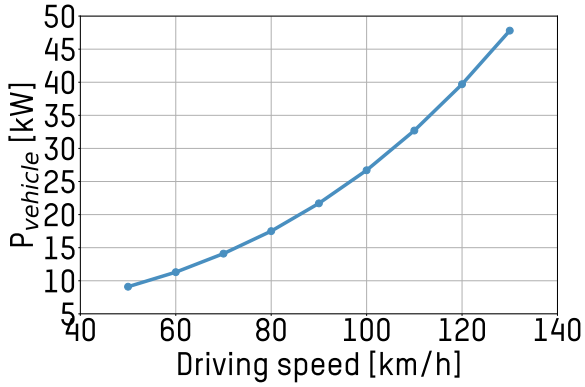

Figure 5.3: *Fiat Doble vehicle power needs.*

$$I_{dch} = \frac{P_{vehicle}}{V_{cell} \cdot n_{cell}} \tag{5.1}$$

The following thermal and hydraulic analysis of compared advanced BTMS solutions will be done under this demanding cycle.

5.2 Case Study 1: Cold Plate- and PCM- Based BTMS

This case study focuses on the first advanced solution of the comparison analysis. Next, this Cold Plate and PCM-based BTMS system will be introduced, and the CFD model will be depicted. Finally, the thermal and hydraulic CFD analysis will be presented.

5.2.1 Hybrid BTMS Concept and Design

The solution in this work corresponds with the one employed for the battery pack of the *SELFIE* project. It focuses on developing a cold plate- and PCM-based BTMS, therefore using passive and active systems, hereafter known as the ***Hybrid BTMS*** for that characteristic. This hybridisation looks to hold both fast charge and vehicle driving efficiently.

The passive approach to thermal management involves a PCM buffer, which consists of a porous aluminium structure filled with paraffin wax at a concentration of 58.55 %. This porosity was defined for manufacturing reasons and to enhance the battery pack's structural strength and thermal conductivity. The PCM buffer is situated underneath the battery cells, acting as a heat storage device that absorbs the heat generated during charging through the latent heat of the wax phase change. The passive system occupies the entire area under the cells, with a total thickness of 13 mm. This is designed following the vehicle's available volume and helps with the battery pack's structural strength. The paraffin wax used is the *Rubitherm RT35HC*, which has a melting temperature of approximately 34 °C to 36 °C and is specifically designed for warm temperatures [174]. In extreme climate conditions, alternative products may be considered for system sizing, as the manufacturer provides products with a melting temperature range between -9 °C and 100 °C. Table 5.3 provides data on the properties of the PCM.

The active system comprises a pair of aluminium cold plates laterally surrounding the 30-cell row, being 664.2 mm long and 100 mm high. The hydraulic equilibrium of the flow is achieved by using a parallel configuration for each cold plate connection. The flow is further separated into three entrance channels in the upper half of the cell and three return channels in the lower half of each cold plate with a 2 mm x 10 mm size each. The cold plate is designed to work with a water ethylene-glycol 50 % mix-

Table 5.3: *RT35HC paraffin wax properties [174].*

RT35HC Paraffin Wax	
Melting Point [°C]	34 - 36
Max. Operating Temperature [°C]	70
Heat Storage Capacity [kJ/kg]	240
Thermal Conductivity [W/m·K]	0.2
Density (Solid-Liquid) [kg/l]	0.88 - 0.77
Specific heat capacity [J/kg·K]]	2000

ture (w-e50), with the necessary thermophysical properties depicted in table 5.4. Moreover, the high thermally conductive TIM *THERM-A-GAP G976* [175] is selected to separate the cold plate and PCM buffer from the cells to prevent electrical short circuits. The 30-cell array used in the analysis can be seen in fig. 5.4, surrounded by two cold plates at each side, and the PCM buffer placed below the cells. The internal duct configuration of the cold plate is also shown.

Table 5.4: *Water Ethylene-glycol 50 % mixure's thermophysical properties.*

T [°C]	ρ [kg/m^3]	C_p [J/kg·K]	k [W/m·K]	ν [m^2/s]	μ [Pa·s]
-30	1089	3088	0.328	$4.04e^{-5}$	$4.40e^{-2}$
-20	1087	3126	0.336	$2.03e^{-5}$	$2.21e^{-2}$
-10	1084	3165	0.344	$1.18e^{-5}$	$1.27e^{-2}$
0	1081	3203	0.352	$7.48e^{-6}$	$8.09e^{-3}$
10	1077	3242	0.360	$5.10e^{-6}$	$5.50e^{-3}$
20	1073	3281	0.366	$3.67e^{-6}$	$3.94e^{-3}$
30	1069	3319	0.373	$2.75e^{-6}$	$2.94e^{-3}$
40	1064	3358	0.378	$2.12e^{-6}$	$2.26e^{-3}$
50	1058	3396	0.383	$1.68e^{-6}$	$1.78e^{-3}$

The Hybrid BTMS is designed to operate using a fixed thermal management strategy, which involves using the active cooling system during ND and relying on the passive PCM system during fast charge. During fast charging, the active cooling system remains inactive due to the absence of coolant flow. In contrast, the passive PCM system absorbs the heat gen-

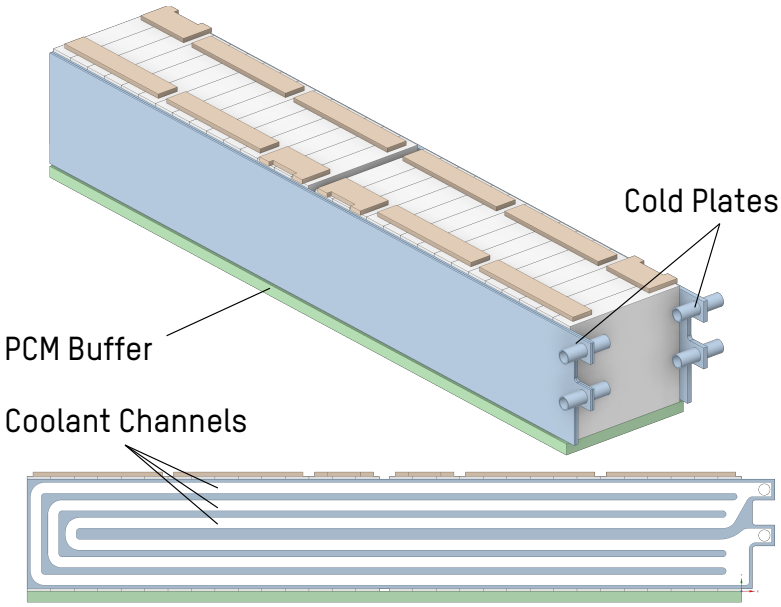

Figure 5.4: *Hybrid BTMS configuration on the 30-cell row.*

erated by the cells through heat accumulation. This is accomplished by heating the paraffin wax until it reaches a melting point, enabling it to absorb heat without affecting its temperature.

During ND performance, the BEV's active cooling system is activated, resulting in the dissipation of heat by the coolant. This process involves cell cooling and PCM solidification, which is necessary for the passive system to operate effectively during subsequent charging cycles. As a result, excess heat energy is transferred from the cells to the cold plate. It is worth mentioning that the cold plate mass flow rate remains constant throughout each ND analysed.

5.2.2 Battery Model and Grid Refinement Study

Using CFD software, a 3D model of the Hybrid BTMS is developed. To reduce computing costs, the system's design is simplified while still providing a clear understanding of how heat is dispersed within the module. A vertical symmetry plane is positioned at the centre of the cell row, so only half of the Hybrid BTMS is included in the computational domain. As a result, the computational domain consists of only one cold plate, thirty-half battery cells, and half of the PCM buffer beneath them.

The heat generation subroutine model through a UDF is used for the cells' heat generation on the CFD (see methodology Section 3.2.3.1). This method is employed instead of the FMU approach because a symmetry plane cuts across the cells. This makes it impossible to establish the co-simulation process on the software. The battery cells are modelled as homogeneous volumes because the heat generation model substitutes the heating processes dependent on the internal geometric design of the cell. Nevertheless, orthotropic thermal conductivity values are employed. Average specific heat capacity is also used, experimentally obtained following test methodology in Section 4.2.3, with the resultant data depicted in table 4.5. Moreover, an electric potential is defined in the busbars; therefore, the joule heat generation dependent on the electric current of the charge or discharge can be defined. Materials and their properties used on the models are defined in table 5.5. Furthermore, an adiabatic environment is defined for all the external walls. The final geometry employed in the CFD model can be seen in fig. 5.5.

Table 5.5: *Material and element properties used on the CFD model.*

	Material	Dimensions (x, y, z) [mm]	ρ [kg/m^3]	C_p [J/kg·K]	k [W/m·K]
Cell	-	21.5 x 105 x 115	2118.5	1163.95	k_x = 0.4 $k_{y,z}$ = 31
CP	Aluminium	664.2 x 100 x 4	2719	871	202.4
PCM	RT35HC	13 (width)	825	2000	0.2
	Aluminium		2719	871	202.4
TIM	G974	0.5 (width)	1400	900	6
Busbar	Copper	118.4 x 4 x 20	8978	381	387.6

With the created model, a grid refinement study is conducted to examine the grid independence from the outcomes of the mathematical model

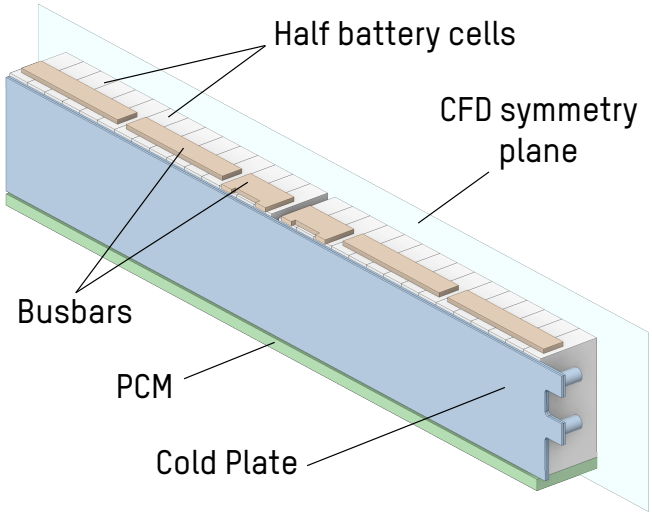

Figure 5.5: *CFD final geometry for analysis simulations.*

to avoid any inaccurate or imprecise simulation and to verify the model. For that objective, the Grid Convergence Index (GCI) method, based on the Richardson Extrapolation [176] approach, is adopted as done in the previous chapter.

Three different meshes are produced, depicted in fig. 5.7. The discretisation error is evaluated while comparing the outputs for the pressure drop (Δp) and the convective heat transfer coefficient (h_{conv}) on the cold plate. Results for the coarse mesh (N_1: 771,272 elements), the medium mesh (N_2: 5,068,480 elements), and the fine mesh (N_3: 34,735,296 elements) can be found in fig. 5.6, with refinement factors of r_{21} = 1.87 and r_{32} = 1.89.

All GCI factors are low enough for results acceptance. For the heat transfer coefficient, the $GCI_{21\_h_{conv}}$ = 1.55 % and $GCI_{32\_h_{conv}}$ = 0.65 % results are achieved. Moreover, the pressure drop results showed $GCI_{21\_\Delta p}$ = 0.03 % and $GCI_{32\_\Delta p}$ = 0.0013 % results. The results show a convergence tendency where changes between meshes reduce one after the other. With the discretisation error low enough and due to agreement between mesh components and outcomes, the medium N_2 mesh is chosen.

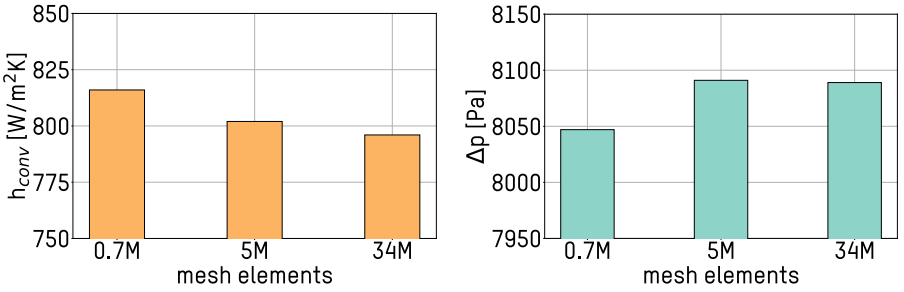

(a) *Convective heat transfer coefficient results.* ***(b)*** *Pressure drop results.*

Figure 5.6: *Grid refinement study's results.*

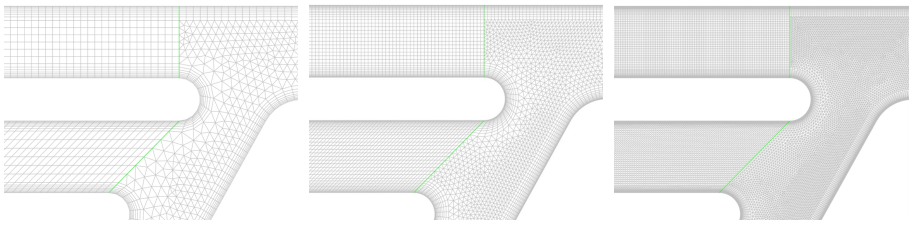

(a) *Mesh N_1.* ***(b)*** *Mesh N_2.* ***(c)*** *Mesh N_3.*

Figure 5.7: *Different mesh levels in the cooling channels of the cold plate.*

5.2.3 CFD Thermal and Hydraulic Results Analysis

This section presents a numerical parametric analysis of the hybrid BTMS under realistic and demanding performance conditions. The module undergoes a cycling process whereby the cells' average temperature evolution over time is obtained. This process is achieved using the previously described electric cycle, consisting of a 6C fast charge from 10 % to 90 % SOC, followed by a 1.67C discharge until the SOC returns to 10 % while simulating a driving speed of 130 km/h (fig. 5.2). Furthermore, all case studies are initiated at an ambient temperature of 25 °C, and w-e50 is utilised as a coolant, following a real-use scenario. A total of seven case studies are performed using this complete cycle, whereby various parameters of the hybrid BTMS are altered, as outlined in table 5.6. It is noteworthy that the presented mass flow rate ($\dot{m}$) corresponds to both cold plates of the 30-cell assembly.

Table 5.6: *Hybrid BTMS Case studies description.*

Case Study	Thermal management CHA	DCH	Coolant	T_{inlet} [°C]	$\dot{m}$ [kg/s]
[1]**Case00**	No thermal management		-	-	-
[2]**Hy-Case01**	PCM	PCM + CP	w-e50	25	0.03125
Hy-Case02	PCM	PCM + CP	w-e50	20	0.03125
Hy-Case03	PCM	PCM	-	-	-
Hy-Case04	-	CP	w-e50	25	0.03125
Hy-Case05	CP	CP	w-e50	25	0.03125
Hy-Case06	PCM + CP	PCM + CP	w-e50	25	0.03125

[1] Reference case with no BTMS.
[2] Reference case with the hybrid BTMS.

The following are the specific cases and their purposes. "Hy-" prefix is used to indicate the studied case represents the Hybrid BTMS:

- Case00 is the reference check-up, where no thermal management system is added. Therefore the 30-cell row is studied together with the busbars. The PCM and the cold plate are removed from the geometry to avoid any thermal management or extra thermal capacity on the system.
- Hy-Case01 is the reference case study, where the hybrid BTMS is fully analysed. The PCM is employed during the fast charge, whereas the cold plate is responsible for battery cells' thermal management during discharge along with the PCM solidification. The utilised w-e50 mass flow rate is 0.03125 kg/s, whereas the inlet fluid temperature is 25 °C.
- Hy-Case02 aims to evaluate the coolant inlet temperature effect. Therefore, the T_{inlet} of the w-e50 is reduced to 20 °C whereas maintaining the mass flow rate on the hybrid BTMS with both the PCM and cold plate.
- Hy-Case03 analyses the PCM passive system individually. It is added to the 30-cell geometry to examine its effect without an active thermal management system.
- Hy-Case04 aims to evaluate the PCM's temperature control and

stabilisation capacity by removing it and activating the cold plate system only during the discharge process on the ND. Therefore, a 0.03125 kg/s mass flow rate at 25 °C inlet temperature is only activated during the discharge stage. The idea is to examine the thermal effect of removing the PCM.

- Hy-Case05, on the other hand, uses only the active system during the entire cycle of the BEV. The same w-e50 flow and temperature conditions of the previous case study are used, still, with a longer activation time of the cold plate system.

- Hy-Case06 finally operates with the entire hybrid system on both the fast charge and motorway driving scenario. With the same mass flow rate of 0.03125 kg/s and an inlet temperature of 25 °C, it looks for the performance when the hybrid BTMS fully works.

The CFD thermal analysis shows the average temperature evolution of the cell array for the initial fast charge at the first 480 seconds and the normal drive discharge until reaching back the 10 % of SOC after nearly 37 minutes of the complete cycle. Moreover, each temperature evolution line is accompanied by the same colour band showing the maximum and minimum cell temperature values inside the 30-cell row, thus showing the ΔT_{module} evolution inside the plot. Moreover, the data is also depicted in table 5.7, showing the maximum temperature reached on the cycle (T_{max}), the maximum thermal dispersion among cells in the battery module (ΔT_{module}), the pressure drop on the cold plate (Δp) and the corresponding hydraulic pumping power (P_{hyd}) and energy consumption (E_{hyd}).

The comparison analysis commenced by contrasting the case with no thermal management system (Case00) and the reference case study for the hybrid BTMS (Hy-Case01) at 25 °C inlet temperature with 0.03125 kg/s mass flow rate. The temperature evolution of these two cases is shown in fig. 5.8. An abrupt temperature rise is pronounced due to the high current of the 6C charge, resulting in a charge ending maximum temperature of 39.1 °C for Case00. Otherwise, the Hy-Case01 with the hybrid BTMS reaches 35.2 °C, showing a reduction of 10 % in temperature due to the PCM effect. Moreover, it is worth mentioning that Case00 continues increasing its temperature during the ND part of the cycle until 45.8 °C. In contrast, the cold plate achieves a temperature reduction and certainly reaches back the cycle starting temperature after the complete discharge with an

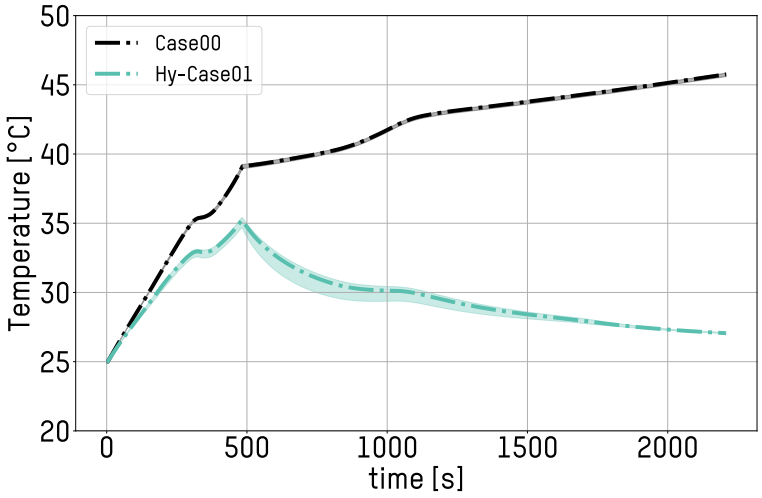

Figure 5.8: *Case00 and Hy-Case01 comparison results, without and with the hybrid BTMS at 25 °C and 0.03125 kg/s, respectively.*

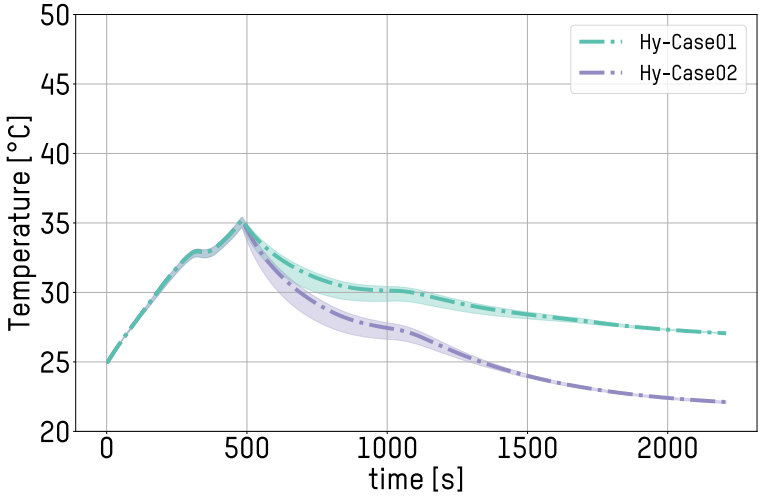

Figure 5.9: *Hy-Case01 and Hy-Case02 comparison results, with T_{inlet} reduction from 25 °C to 20 °C.*

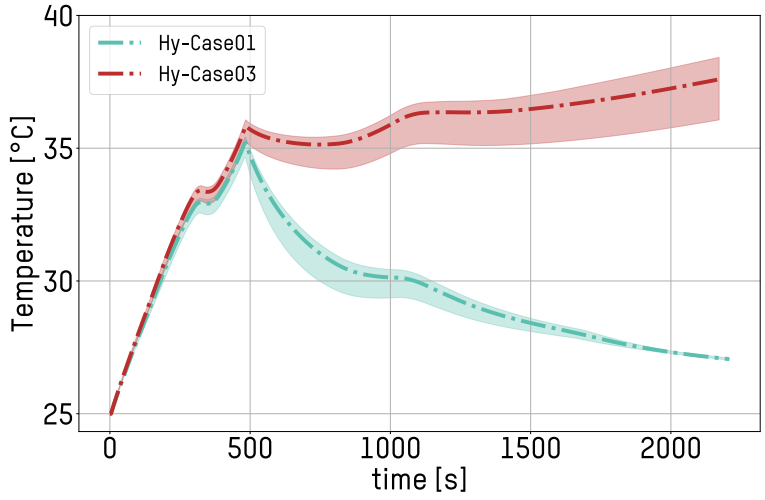

Figure 5.10: *Hy-Case01 and Hy-Case03 comparison results, with only PCM passive system on the latter case study.*

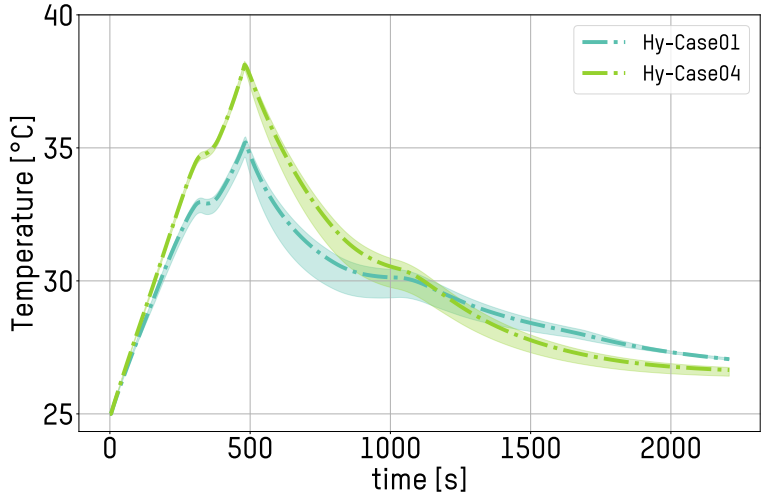

Figure 5.11: *Hy-Case01 and Hy-Case04 comparison results, with only the cold plate active system actuating on the ND on the latter case study, at 0.03125 kg/s and 25°C.*

ending temperature of 27.1 °C. The thermal dispersion of the module is negligible on Case00 due to an inexistent thermal management system. In contrast, the Hy-Case01 increases to a maximum of 1.4 °C as a response to the cold plate effect, still being a very reasonable value.

The hybrid thermal management system is intended to reach back to the initial temperature once the cycle ends, in case another fast charging is required or the complete cycle is repeated in the real use scenario of the BEV. Therefore, Hy-Case02 with a lower inlet temperature of 20 °C is introduced in fig. 5.9, directly comparing with the Hy-Case01 reference case. As expected, the fast charging end temperature remains the same as the active system is not activated at that stage. Nevertheless, the cycle-ending temperature reduces to 22.1 °C, below the initial temperature. This ensures the system's capability to reach the cycle starting temperature easily. The thermal dispersion is slightly increased due to the higher heat dissipation capacity of the fluid until reaching 1.8 °C.

Afterwards, the PCM effect is studied with Hy-Case03 and Hy-Case04, utilising only the PCM and only the cold plate, respectively. Initially, on Hy-Case03, the PCM buffer is utilised without the active system, meaning the battery keeps heating after the fast charge. As seen in fig. 5.10, it contains the temperature during the fast charge reaching to 35.8 °C. However, the discharging process ends at 37.6 °C, increasing the ΔT_{module} until the 2.4 °C. This is the direct consequence of not having an active system with higher thermal management capacity and the ability for PCM solidification.

Conversely, the Hy-Case04 changes the PCM for the cold plate, activating it only during discharge with a mass flow rate of 0.03125 kg/s and inlet temperature of 25°C. The temperature increase with respect to the reference case at the end of the fast charge is considerable, reaching 38.1 °C, 2.9 °C higher, as seen in fig. 5.11. Thus, the passive system usage entails a 7.7 % reduction in the maximum temperature. The normal drive ends at similar temperature conditions, 0.4 °C colder for Hy-Case04. Thermal dispersion is also similar but slightly lower for this last case study with a maximum value of 1.2 °C.

The temperature contour of both cases is shown in fig. 5.12, where the FC ending temperature is displayed. The passive systems, therefore, reduce the average temperature of the module considerably, keeping the module and cell temperature homogeneity properly.

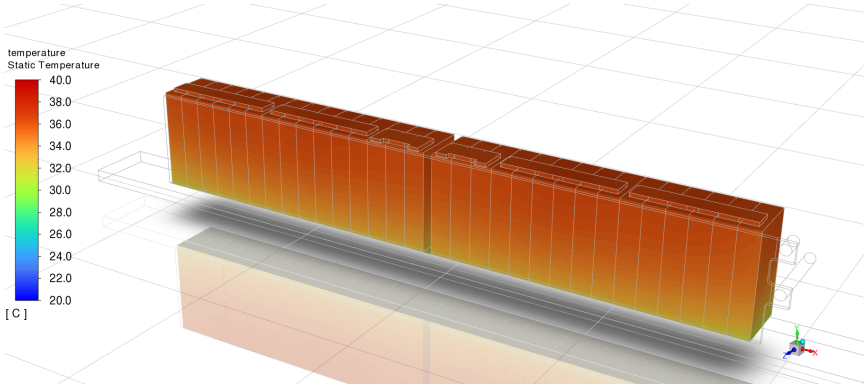

(a) *Hy-Case01 temperature contour at FC end.*

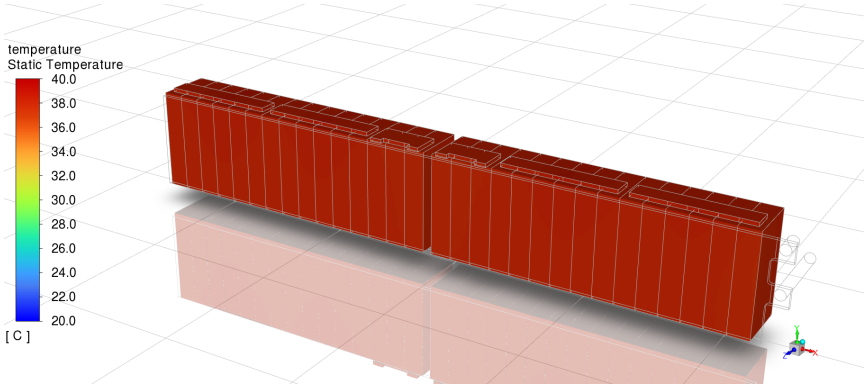

(b) *Hy-Case04 temperature contour at FC end.*

Figure 5.12: *Temperature contour of Hy-Case01 and Hy-Case04 with and without PCM, respectively, at the end of FC.*

Finally, the cold plate effect is studied for the entire cycle, in Hy-Case05 without and in Hy-Case06 with the passive PCM system. The temperature evolution is depicted in fig. 5.13. Both case studies reduce the maximum temperature of the cycle due to cold plate activation. The first one reaches 33.2 °C whereas the latter stays at 32.0 °C, denoting the thermal capacitance increase of the system as the PCM buffer is added. The discharge ending temperature is similar for the three case studies, with less than 0.5 °C difference. Moreover, thermal dispersion is the lowest of the studied cases, with 1.1 °C and 1.2 °C, respectively.

Regarding the hydraulic analysis, the simulation results include the

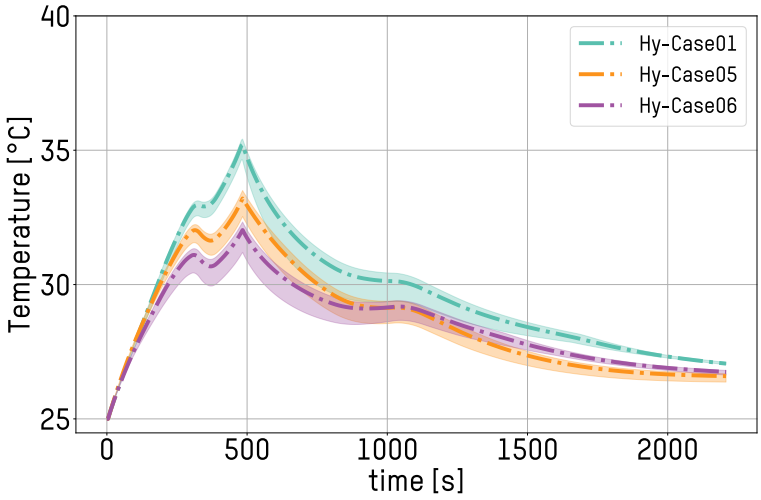

Figure 5.13: *Hy-Case01 reference case, Hy-Case05 and Hy-Case06 comparison results. Hy-Case05 employs only the cold plate for the complete cycle, whereas Hy-Case06 also adds the PCM.*

fluid pressure drop (Δp), which enables comparing the required pumping power and corresponding energy consumption in all the studied cases. Equation (5.2) is used to evaluate the pumping power (P_{hyd}), which is closely related to the pressure loss of the cooling plate and the mass flow rate utilised. Additionally, the density of the coolant used is relevant as it influences the necessary hydraulic power.

$$P_{hyd} = \frac{\dot{m}}{\rho} \cdot \Delta p \tag{5.2}$$

P_{hyd} [W] is the hydraulic power required for the fluid to flow under a specified mass flow rate and temperature conditions. The mass flow rate through the cold plate is represented by $\dot{m}$ [kg/s], ρ [kg/m^3] denotes the fluid density, and Δp [Pa] corresponds to the pressure loss measured on each cold plate. Once the required hydraulic power is calculated, the corresponding energy consumption can be determined by interpolating the hydraulic power over time using eq. (5.3),

$$E_{hyd} = \int_{t_0}^{t} P_{hyd} \cdot dt \tag{5.3}$$

where the hydraulic energy E_{hyd} [Wh] is integrated from the beginning of the active cooling period, t_0 [h], to the end of it, t [h].

For each case study analysed in the present study, table 5.7 presents the values of pressure drop (Δp), cold plate active time, mass flow rate and the resultant P_{hyd} and E_{hyd}. The fluid density (ρ) is evaluated for each case study's inlet temperature following w-e50 fluid data in Appendix B.3.

Table 5.7: *Hybrid BTMS case studies' results. Maximum cycle temperature (T_{max}), maximum thermal dispersion among cells on the module (ΔT_{module}), pressure drop (Δp), hydraulic power (P_{hyd}) and hydraulic energy consumption (E_{hyd}) are shown.*

Case Study	T_{max} [°C]	ΔT_{module} [°C]	CP active time [s]	$\dot{m}$ [kg/s]	Δp [Pa]	P_{hyd} [W]	E_{hyd} [Wh]
Case00	45.8	0.3	0	0	0	0	0
Hy-Case01	35.2	1.4	1725	0.03125	4821.3	0.14	0.067
Hy-Case02	35.2	1.8	1725	0.03125	5127.5	0.15	0.072
Hy-Case03	37.6	2.4	0	0	0	0	0
Hy-Case04	38.1	1.2	1725	0.03125	4821.3	0.14	0.067
Hy-Case05	33.2	1.1	2205	0.03125	4821.3	0.14	0.086
Hy-Case06	32.0	1.2	2205	0.03125	4821.3	0.14	0.086

Pressure drop results are consistent for nearly all the cases as the mass flow rate is not varied. Therefore, the game-changing effect remains on the activation or not of the cold plate active system during the fast charge. The pressure drop is 4821.3 Pa, and thus, the necessary pumping hydraulic power is 0.14 W for all the cases where the cold plate is introduced with the inlet temperature at 25 °C. However, the only variation is in Hy-Case02 with the fluid inlet temperature at 20 °C, which slightly increases the pressure drop to 5127.5 Pa. Nevertheless, cases with the active system operating the entire cycle have 0.086 Wh hydraulic energy consumption. Case studies with the whole hybrid BTMS using the cold plate on the normal drive obtained an energy consumption of 0.067 Wh, except the change registered in Hy-Case02, which slightly increases it to 0.072 Wh. This entails an energy reduction of 22.1 % when using the hybrid system.

With the use of the hybrid BTMS, apart from this energy consumption

reduction, the PCM buffer reduces the maximum temperature peaks in extreme conditions such as a 6C fast charge, reducing it in 7.7 % as seen in fig. 5.11. If compared with Case00, where no thermal management system is used, the use of PCM as seen in Hy-Case03, can reduce the final temperature from 45.8 °C to 37.6 °C, as can be seen comparing those cases in fig. 5.8 and fig. 5.10. As a consequence, PCM buffer demonstrated a powerful system for temperature control and stabilisation or even for safety reasons in case of cold plate malfunctioning; however, the need for the active system is mandatory for the thermal management capability recovery after each cycle.

With the data obtained, a further comparison of thermal management, hydraulic energy requirements and battery pack's specific energy and volumetric energy consequences will be presented in the Section 5.4 and Crefsec:FinalDiscusion against the following Case Study 2 solution, based on dielectric BTMS over the same battery module.

5.3 Case Study 2: Dielectric Flow- and Tab-Based BTMS

This case study focuses on the second advanced solution of the comparison analysis. Next, this Dielectric Flow- and Tab-based BTMS will be introduced. The concept and design of the proposed system are inspired from the prototype development methodology followed in Section 6.1 of Chapter 6, where *Dielectric Fluid Selection Analysis* (section 6.1.2) and *Duct Size Optimisation* (section 6.1.3) are carried out.

Moreover, on this section the CFD model will be depicted. Finally, the thermal and hydraulic CFD analysis will be presented.

5.3.1 Dielectric BTMS Concept and Design

The advanced battery thermal management system proposed in this case study is developed over the same battery module of first case study, shown in fig. 5.1. This strategy will allow a fair comparison of both advanced BTMS solutions. It focuses on developing a Dielectric Flow- and Tab-Based BTMS, gathering the dielectric flow concept along with the tab cooling one. It will hereafter be known as the **Dielectric BTMS** for shortening.

This advanced solution proposes utilising the existing copper busbars to channel the dielectric flow. Therefore, the busbars are perforated, creating a duct inside them. Then, busbars are hydraulically connected via plastic or rubber connectors, thus eluding any short circuit between cells and maintaining the battery module's electrical configuration. In this way, the tab cooling idea is reinforced by avoiding extra structures. In fig. 5.14, this dielectric BTMS is depicted, with the internally holed busbars and plastic hydraulic connector creating two ducts over cell tabs.

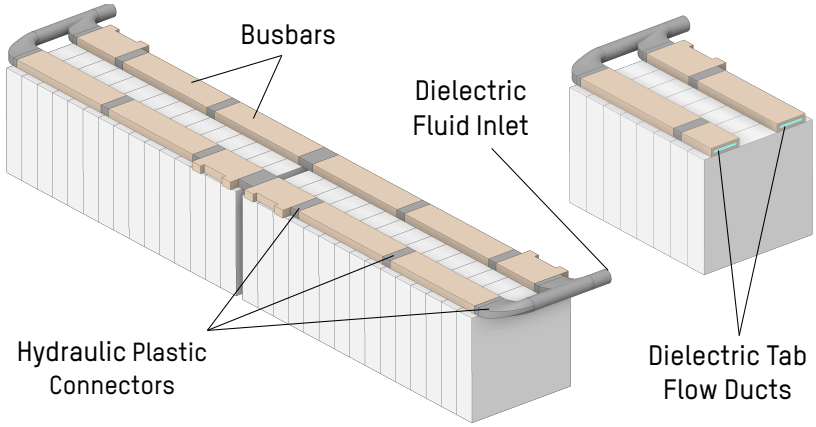

Figure 5.14: *Advanced dielectric BTMS configuration on the 30-cell row.*

The dielectric fluid chosen for this study is Novec7200, manufactured by 3M company, based on its low viscosity. This property can enhance the thermal and hydraulic performance as will be demonstrated on the concept-proof validation in Section 6.1.2. The thermophysical properties of the selected dielectric fluid are provided in table 5.8. To further enhance the thermal transfer capacity of the system, a narrow duct is designed, taking advantage of the low viscosity of the chosen fluid. The analysis of dielectric fluid selection is discussed in detail in Section 6.1.2, and the optimisation of duct sizing is explained in Section 6.1.3. These processes, which are further elaborated upon in Chapter 6 for the concept-proof validation prototype, have greatly contributed to the design of the second case study BTMS.

The busbars are modified in size to properly fulfil the dielectric fluid flow's requirements for optimal thermal management. In that regard, initially, the optimal duct size used in chapter 6 prototype is employed, cor-

Table 5.8: *Novec7200 fluid's thermophysical properties. [177–180]*

T [°C]	ρ [kg/m^3]	C_p [J/kg·K]	k [W/m·K]	ν [m^2/s]	μ [Pa·s]
-30	1550.2	1148.6	$8.48e^{-2}$	$8.76e^{-7}$	$1.36e^{-3}$
-20	1527.2	1192.5	$8.05e^{-2}$	$7.39e^{-7}$	$1.13e^{-3}$
-10	1504.1	1236.3	$7.66e^{-2}$	$6.28e^{-7}$	$9.44e^{-4}$
0	1481.1	1280.2	$7.30e^{-2}$	$5.45e^{-7}$	$8.08e^{-4}$
10	1458.1	1324.1	$6.97e^{-2}$	$4.73e^{-7}$	$6.90e^{-4}$
20	1435.0	1367.9	$6.67e^{-2}$	$4.19e^{-7}$	$6.02e^{-4}$
30	1412.0	1411.8	$6.41e^{-2}$	$3.78e^{-7}$	$5.34e^{-4}$
40	1389.0	1455.7	$6.17e^{-2}$	$3.42e^{-7}$	$4.76e^{-4}$
50	1366.0	1499.5	$5.97e^{-2}$	$3.15e^{-7}$	$4.31e^{-4}$

responding with a 26 x 5 mm cross-area duct. However, the duct size analysis in that chapter disclosed the beneficial effect on heat dissipation of flattening the cross-area of the duct, as seen in fig. 6.6 and fig. 6.7. Therefore, an extra busbar design is developed for simulation comparison to select the most appropriate duct size for optimal thermal management. These designs' dimensions are depicted in fig. 5.15. The original busbar is shown in fig. 5.15a, and the initial design with the mentioned 26 x 5 mm duct size is depicted in fig. 5.15b. Finally, fig. 5.15c shows the improved design to test with a 26 x 3 mm duct.

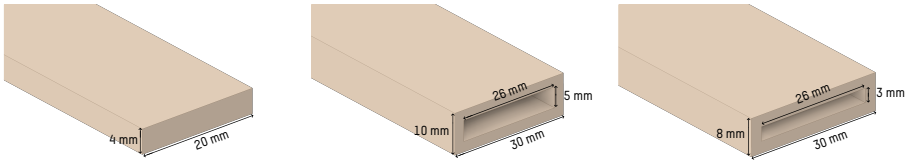

(a) *Original design of busbars.*

(b) *Initial design of dielectric duct busbars.*

(c) *Improved design of dielectric duct busbars.*

Figure 5.15: *Busbar design sizes.*

This advanced dielectric flow- and tab-based BTMS needs to be capable of facing the high-performance cycle previously utilised with this battery pack, composed of the 6C fast charge FC and the normal drive (ND) at equivalent 130 km/h motorway speed. The thermal management strategy for this demanding cycle must be adapted to the characteristics of the

BTMS for optimal equilibrium between the system's performance and efficiency. In contrast with the Hybrid BTMS with a passive solution, this system must operate for the entire cycle. However, due to the low viscosity of the selected dielectric fluid, the hydraulic pumping energy consumption is not expected to rise drastically. The system analysis will be developed in the following sections with a CFD model, where diverse aspects of the operation will be simulated.

5.3.2 Battery Model and Grid Refinement Study

Using CFD software, a 3D model of the Dielectric BTMS is developed. To reduce computing costs, the system's design is simplified while still providing a clear understanding of how heat is dispersed within the module. A vertical symmetry plane is positioned at the centre of the cell row, so only half of the dielectric BTMS is included in the computational domain. As a result, the computational domain consists of only one tab cooling duct and thirty-half battery cells.

As previously done with the Hybrid BTMS, the heat generation subroutine model through a UDF is used for the cells' heat generation on the CFD (see methodology Section 3.2.3.1). This method is employed instead of the FMU approach because a symmetry plane cuts across the cells connected in parallel. This makes it impossible to establish the co-simulation process on the software. The battery cells are modelled as homogeneous volumes because the heat generation model substitutes the heating processes dependent on the internal geometric design of the cell. Nevertheless, orthotropic thermal conductivity values are employed. Average specific heat capacity is also used, experimentally obtained following test methodology in Section 4.2.3, with the resultant data depicted in table 4.5. Moreover, an electric potential is defined in the busbars; therefore, the joule heat generation dependent on the electric current of the charge or discharge can be defined. Materials and their properties used on the models are defined in table 5.9. Furthermore, an adiabatic environment is defined for all the external walls. The final geometry employed in the CFD model can be seen in fig. 5.16.

With the created model, the grid refinement study is conducted to examine the grid independence from the outcomes of the mathematical model to avoid any inaccurate or imprecise simulation and to verify the

Table 5.9: *Material and element properties used on the CFD model.*

	Material	ρ [kg/m^3]	C_p [J/kg·K]	k [W/m·K]
Cell	-	2118.5	1163.95	k_x = 0.4 $k_{y,z}$ = 31
Busbar	Copper	8978	381	387.6
Plastic Connector	Plastic	1250	1950	0.24

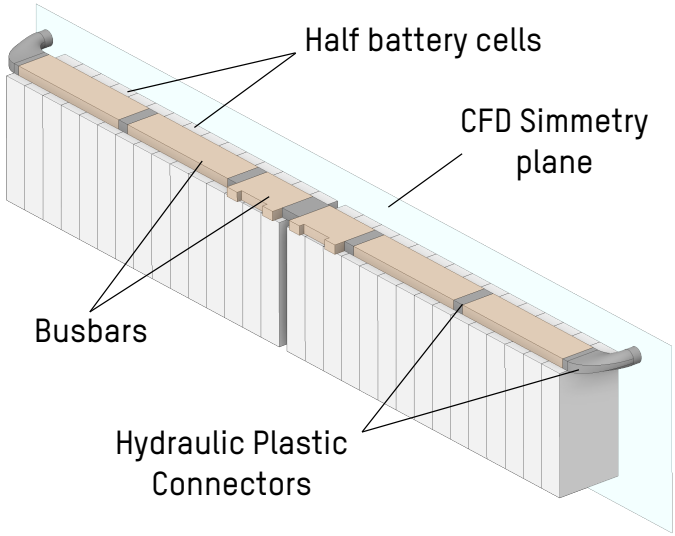

Figure 5.16: *CFD model geometry for Dielectric analysis simulations.*

model. For that objective, the GCI method is adopted as previously done, based on the Richardson Extrapolation approach [176].

Three different meshes are produced. The discretisation error is evaluated while comparing the outputs for the pressure drop (Δp) and the convective heat transfer coefficient (h_{conv}) on the dielectric duct. Results for the coarse mesh (N_1: 3,271,551 elements), the medium mesh (N_2: 4,629,479 elements), and the fine mesh (N_3: 7,232,423 elements) can be found in fig. 5.17, with refinement factors of r_{21} = 1.12 and r_{32} = 1.16. The three meshes are also depicted in fig. 5.18, showing the perpendicular (top) and parallel (bottom) sections of the fluid.

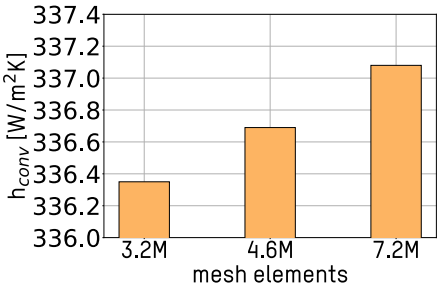

(a) *Convective heat transfer coefficient results.*

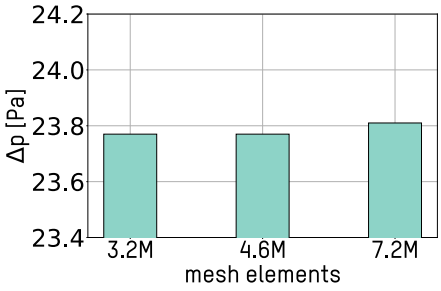

(b) *Pressure drop results.*

Figure 5.17: *Grid refinement study's results.*

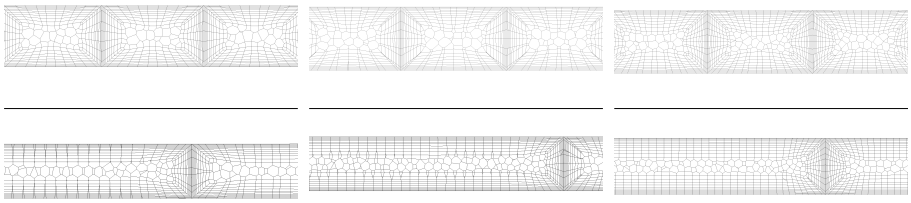

(a) *Mesh N_1. Perpendicular (top) and parallel (bottom) sections of the fluid.*

(b) *Mesh N_2. Perpendicular (top) and parallel (bottom) sections of the fluid.*

(c) *Mesh N_3. Perpendicular (top) and parallel (bottom) sections of the fluid.*

Figure 5.18: *Different mesh levels in the cooling ducts of the tabs.*

All GCI factors are low enough for results acceptance. For the heat transfer coefficient, the $GCI_{21\_h_{conv}}$ = 0.73 % and $GCI_{32\_h_{conv}}$ = 0.62 % results are achieved. Moreover, the pressure drop results showed $GCI_{21\_\Delta p}$ = 0.08 % and $GCI_{32\_\Delta p}$ = 0.035 % results. The results show a convergence tendency where changes between meshes reduce one after the other. With the discretisation error low enough and due to agreement between mesh components and outcomes, the medium N_2 mesh is chosen.

With these grid refinement results, the model can be considered suitable for its use in the following thermal analysis of the dielectric BTMS.

5.3.3 CFD Thermal and Hydraulic Results Analysis

This section presents a numerical parametric analysis of the Dielectric BTMS under realistic and demanding performance conditions. The module undergoes a cycling process whereby the cells' average temperature evolution over time is obtained. This process is achieved using the previously described electric cycle, consisting of a 6C fast charge from 10 % to 90 % SOC, followed by a 1.67C discharge until the SOC returns to 10 % while simulating a driving speed of 130 km/h. Furthermore, all case studies are initiated at an ambient temperature of 25 °C, and Novec7200 dielectric fluid is utilised as a coolant. A total of seven case studies are performed using this complete cycle, whereby various parameters of the dielectric BTMS are altered, as outlined in table 5.10. It is noteworthy that the presented mass flow rate ($\dot{m}$) corresponds to both dielectric ducts of the 30-cell assembly.

Table 5.10: *Dielectric BTMS Case studies description.*

Case Study	Thermal management CHA	DCH	Coolant	T_{inlet} [°C]	$\dot{m}$ [kg/s]
[1]**Case00**	No thermal management		-	-	-
Di-Case01	Dielectric Tab Flow		Novec7200	25	0.03125
[2]**Di-Case02**	Dielectric Tab Flow		Novec7200	25	0.03125
Di-Case03	Dielectric Tab Flow		Novec7200	20	0.03125
Di-Case04	Dielectric Tab Flow		Novec7200	25	0.0625
Di-Case05	Dielectric Tab Flow		Novec7200	20	0.0625

[1] Reference case with no BTMS.
[2] Reference case with the dielectric BTMS.

The followings are the specific cases and their purposes. "Di-" prefix is used to indicate the studied case represents the Dielectric BTMS:

- Case00 is the reference check-up (the same used with the Hybrid BTMS), where no thermal management system is added. Therefore the 30-cell row is studied together with the original busbars. The dielectric ducts are removed from the geometry to avoid any thermal management or extra thermal capacity on the system.
- Di-Case01 is the case study where the initial design of the dielectric duct busbar is tested, with 26 x 5 mm dimension. The case study uses a dielectric fluid inlet temperature of 25 °C and the total mass

flow rate for both ducts is 0.03125 kg/s.

- Di-Case02 is the improved design of the dielectric duct busbars. Therefore, the duct is slightly flattened with a final size of 26 x 3 mm. The mass flow rate and inlet temperature are the same as in the previous case, with 0.03125 kg/s and 25 °C. From the analysis of both dielectric duct busbars, the optimal one will be used as the reference case for comparison with the following case studies.
- Di-Case03 searches for the system response to inlet temperature changes. Therefore, it is reduced to 20 °C. The idea is to analyse the thermal management capability in case more heat dissipation is needed. The mass flow rate is maintained at 0.03125 kg/s.
- Di-Case04 is defined for similar reasons as the previous case study, but this time, the mass flow rate doubles until reaching 0.0625 kg/s, whereas the fluid inlet temperature keeps at 25 °C.
- Di-Case05 increases the system's cooling capacity by joining both the Di-Case03 and Di-Case04. Therefore, 20 °C inlet temperature and 0.0625 kg/s mass flow rate are evaluated to achieve maximum thermal performance.

The CFD thermal analysis shows the average temperature evolution of the cell array for the initial fast charge at the first 480 seconds and the normal drive discharge until reaching back the 10 % of SOC after nearly 37 minutes of the complete cycle. Moreover, each temperature evolution line is accompanied by the same colour band showing the maximum and minimum cell temperature values inside the 30-cell row, thus showing the ΔT_{module} evolution inside the plot. Moreover, the data is also depicted in table 5.11, showing the maximum temperature reached on the cycle (T_{max}), the maximum thermal dispersion among cells in the battery module (ΔT_{module}), the pressure drop on the cold plate (Δp) and the corresponding hydraulic pumping power (P_{hyd}) and energy consumption (E_{hyd}).

The comparison analysis commenced by contrasting the case with no thermal management system (Case00) and the case studies with initial and improved dielectric busbar duct designs, Di-Case01 and Di-Case0, respectively. Both with a mass flow rate of 0.03125 kg/s and an inlet temperature of 25 °C. The temperature evolution of these two cases is shown in fig. 5.19. An abrupt temperature rise is pronounced due to the high current

of the 6C charge, resulting in a charge ending maximum temperature of 39.1 °C for Case00. Otherwise, the Di-Case01 with the initial busbar design of the dielectric BTMS reaches 37.8 °C, showing a reduction of 3.3 % in temperature due to the active cooling effect. Moreover, it is worth mentioning that Case00 continues increasing its temperature during the ND part of the cycle until 45.8 °C. In contrast, the dielectric tab cooling method achieves a slight temperature reduction with an ending temperature of 34.5 °C. The thermal dispersion of the module is negligible on Case00 due to a nonexistent thermal management system. In contrast, the Di-Case01 increases to a maximum of 2.7 °C as a response to the tab cooling effect, still being a reasonable value.

However, Di-Case02 improves these thermal results by optimising the duct's geometry. The FC ends at 36.8 °C, reducing the temperature in contrast with Case00 in 5.9 %. Moreover, the cycle ending temperature is 32.3 °C improving the Di-Case01 results to 2.2 °C. Even that, the thermal dispersion between cells is similar, with a maximum value of 2.8 °C. With these results, it is clear that the improved busbar geometry is beneficial for thermal management, and thus, this duct shape will be used for the following analyses.

The dielectric thermal management system is intended to reach back to the initial temperature once the cycle ends, in case another fast charging is required or the complete cycle is repeated in the real use scenario of the BEV. Therefore, the following case studies attempt to the thermal dissipation ability of the system, by dielectric inlet temperature and mass flow rate parameters change. Di-Case03 with a lower inlet temperature of 20 °C is introduced in fig. 5.20, directly comparing with the Di-Case02 reference case. As expected, both the fast charging and cycle-ending temperatures were reduced due to a higher thermal jump between the dielectric fluid and the cells. As a consequence, the cycle's maximum temperature at the end of FC is 35.6 °C, which implies a 1.2 °C reduction with respect to the reference case. Moreover, the cycle ending temperature is 28.6 °C, reducing the reference case temperature by 11.4 %. However, the temperature stability inside the module is reduced, increasing the ΔT_{module} to 3.5 °C.

Doubling the mass flow rate to 0.0625 kg/s while maintaining the inlet temperature at 25 °C is analysed in Di-Case04 as seen in fig. 5.21. These

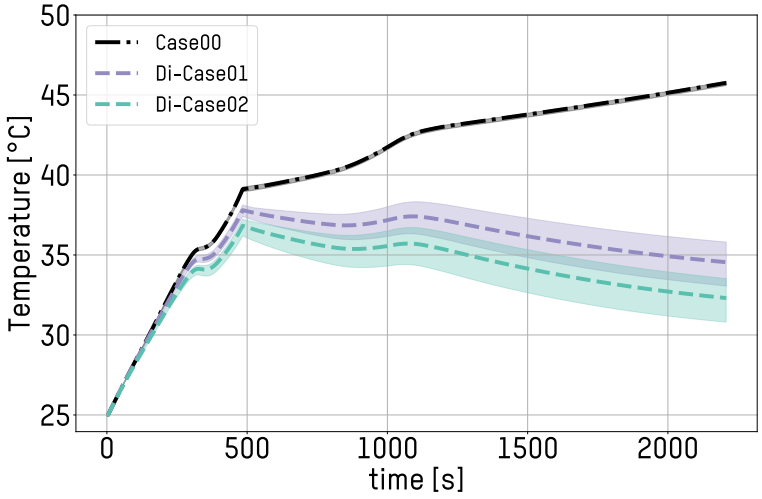

Figure 5.19: *Case00 with no thermal management, and Di-Case01 and Di-Case02 comparison results, with the initial and improved (flattened) busbar duct geometry change, respectively.*

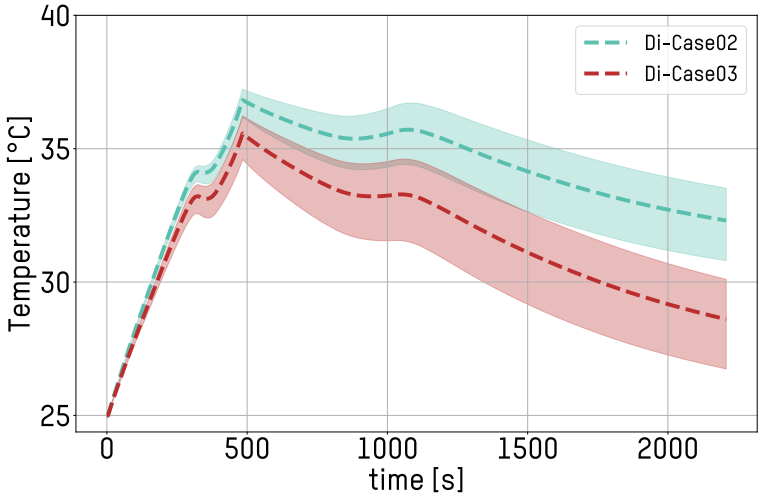

Figure 5.20: *Di-Case02 and Di-Case03 comparison results, reducing the dielectric fluid's inlet temperature to 20 °C.*

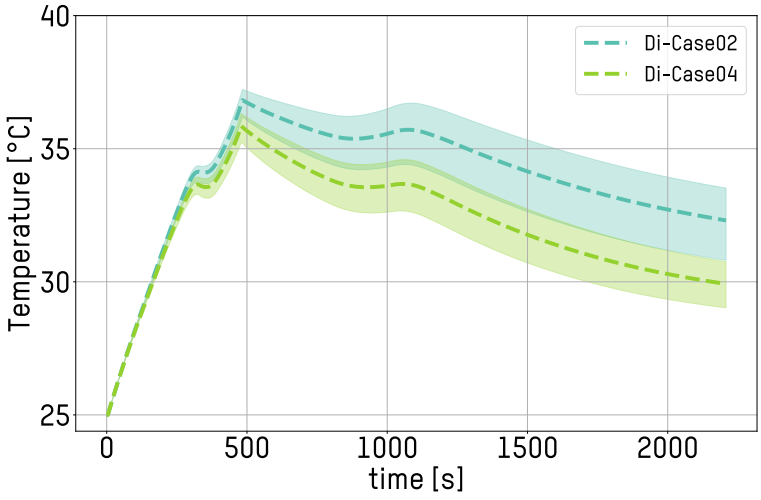

Figure 5.21: *Di-Case02 and Di-Case04 comparison results, doubling the dielectric fluid's mass flow rate to 0.0625 kg/s.*

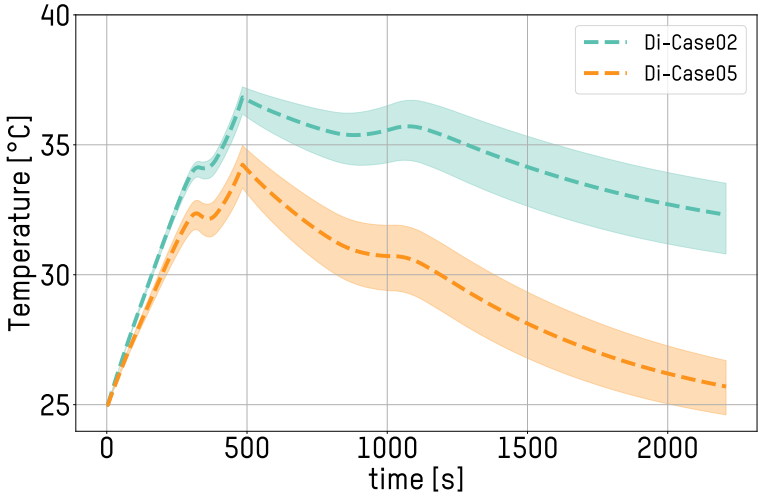

Figure 5.22: *Di-Case02 reference case and Di-Case05 comparison results, with 20 °C inlet temperature and 0.0625 kg/s mass flow rate.*

changes have a lower effect on temperature reduction compared with the previous Di-Case03. Nevertheless, it contributes to temperature reduction from the reference case. The maximum temperature at the end of the fast charge is 35.9 °C, whereas the cycle-ending temperature reduces to 29.9 °C. Additionally, mass flow rate changing benefits over inlet temperature change reducing the thermal dispersion in the module until 2 °C.

Even with the temperature benefits shown by both dielectric inlet temperature and mass flow rate changes, the dielectric BTMS is in trouble for reaching back the test's initial temperature when the cycle ends. Therefore, Di-Case05 gathers both previous cases with the dielectric inlet temperature settled at 20 °C and a mass flow rate of 0.0625 kg/s. The temperature evolution results can be seen in fig. 5.22, with significant temperature reduction over the reference case Di-Case02. The maximum temperature measured after the fast charge is 34.2 °C, resulting in a 7.1 % reduction. Moreover, the cycle-ending temperature is 25.7 °C, with a reduction of 20.4 % from the reference case. Furthermore, this temperature reduction is not conditioned with thermal dispersion on the module, as the maximum ΔT_{module} is 2.6 °C. These results show dielectric BTMS's thermal control and stability ability on the presented demanding performance.

The fig. 5.23 shows the temperature contour of the dielectric BTMS. It can be observed the ability of the system with Di-Case05 to reduce the average temperature of the cells. However, a significant thermal gradient can be seen between the top and bottom sides of the cells. This can be considered the main drawback of the system, even though the cell-to-cell dispersion remains sufficiently homogeneous.

Regarding the hydraulic analysis, the simulation results include the fluid pressure drop (Δp), which enables comparing the required pumping power and corresponding energy consumption in all the studied cases. Following the equations presented in Section 3.4 of methodology, from eq. (3.7) the hydraulic pumping power (P_{hyd}) required for the fluid to flow under a specified mass flow rate and temperature conditions is obtained. Furthermore, the associated hydraulic energy consumption (E_{hyd}) is evaluated by interpolating the hydraulic power over time, following eq. (3.8).

For each case study analysed in the present study, table 5.11 presents the values of pressure drop, dielectric flow active time, mass flow rate and the resultant P_{hyd} and E_{hyd}. The fluid density (ρ) necessary for results

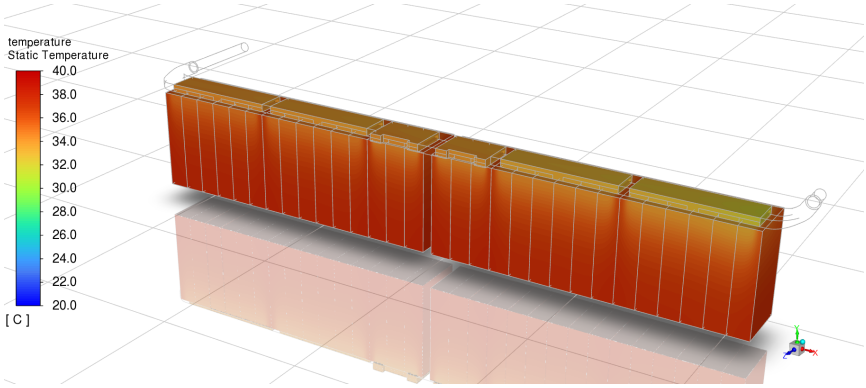

(a) *Di-Case02 temperature contour at FC end.*

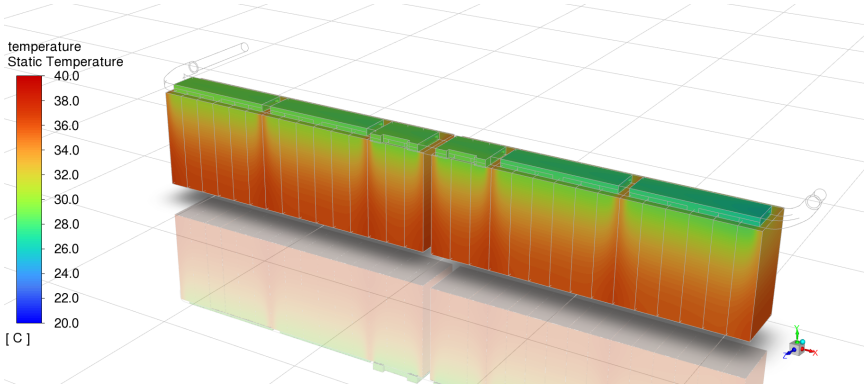

(b) *Di-Case05 temperature contour at FC end.*

Figure 5.23: *Temperature contour of Di-Case02 and Di-Case05, at the end of FC.*

Table 5.11: *Dielectric BTMS case studies' results. Maximum cycle temperature (T_{max}), maximum thermal dispersion among cells on the module (ΔT_{module}), pressure drop (Δp), hydraulic power (P_{hyd}) and hydraulic energy consumption (E_{hyd}) are shown.*

Case Study	T_{max} [°C]	ΔT_{module} [°C]	Dielectric Flow active time [s]	$\dot{m}$ [kg/s]	Δp [Pa]	P_{hyd} [W]	E_{hyd} [Wh]
Case00	45.8	0.3	0	0	0	0	0
Di-Case01	37.8	2.7	2205	0.03125	37.4	0.0008	0.0005
Di-Case02	36.8	2.8	2205	0.03125	160.1	0.0035	0.0022
Di-Case03	35.6	3.5	2205	0.03125	162.7	0.0035	0.0022
Di-Case04	35.9	2.0	2205	0.0625	460.4	0.0202	0.0124
Di-Case05	34.2	2.6	2205	0.0625	467.1	0.0203	0.0125

calculation is evaluated for each case study's inlet temperature following Novec7200 fluid data in table 5.8.

Results show a pressure drop increase as advancing in the thermal dissipation capacity of the dielectric BTMS. Initially, with the dielectric busbar duct geometry improvement from Di-Case01 to Di-Case02, the pressure drop quadruples from 37.4 Pa to 160.1 Pa. This is a direct consequence of the duct's flattening, which creates resistance to the fluid flowing. Therefore, the necessary hydraulic energy consumption increases from 0.0005 Wh to 0.0022 Wh.

Next, Di-Case03 has a minor change in pressure drop due to fluid temperature change from 25 °C to 20 °C. This entails a 2.6 Pa increase, which has an insignificant repercussion on hydraulic energy consumption. However, doubling the mass flow rate in Di-Case04 abruptly increases the pressure drop to 460.4 Pa, considerably increasing the energy consumption to 0.0124 Wh. In comparison, as already seen, changing the inlet temperature on the Di-Case05 has negligible effect again, slightly increasing the pressure drop to 467.1 Pa and, therefore, the energy consumption to 0.0125 Wh.

To further contextualise the obtained data from this proposed advanced dielectric flow- and tab-based BTMS, the comparison with the cold plate and PCM based BTMS will be performed in the next section.

5.4 Results and Discussion: Advanced BTMS Comparison

This chapter presents a detailed comparison between both advanced systems proposed, the Cold Plate and PCM based BTMS, and the Dielectric Flow- and Tab-based BTMS, to assess their fundamental capabilities. This comparative analysis involves a numerical assessment of the differences between the two systems, which provides a comprehensive understanding of the advantages and disadvantages of each system. The outcomes of this analysis are discussed in detail in this and the next sections.

For a more in-depth analysis, two case studies of the Hybrid BTMS will be used for comparison. The Hy-Case01 will represent the Hybrid BTMS, composed of both the PCM passive system and the cold plate active sys-

tem. It employs the PCM for the FC, whereas cold plate is used on ND at a 0.03125 kg/s mass flow rate of w-e50 at an inlet temperature of 25 °C. Moreover, Hy-Case05 uses only the cold plate at the same mass flow rate and temperature as the previous case as the unique thermal management system for the entire cycle. This is the most similar approach utilised in current BEV; therefore, it is added to the comparison process as the reference Cold Plate BTMS.

As a result, three thermal management systems will be compared: the reference **Cold Plate BTMS**, and both the analysed **Hybrid BTMS** and **Dielectric BTMS**. This last system will be based on Di-Case05, with a mass flow rate of 0.0625 kg/s and inlet temperature of 20 °C, characteristics necessary to obtain the desired temperature at the end of the testing cycle. The three systems' geometry is presented in fig. 5.24.

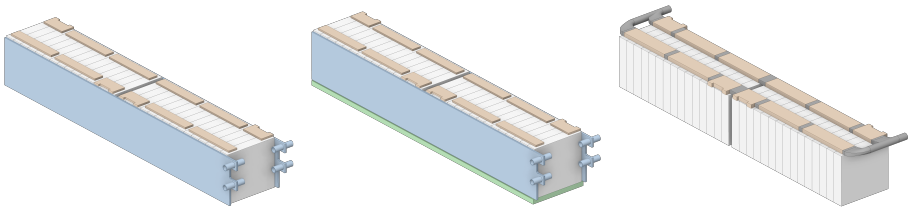

(a) *Cold Plate BTMS.* ***(b)*** *Hybrid BTMS.* ***(c)*** *Dielectric BTMS.*

Figure 5.24: *Battery Thermal Management Systems compared.*

Several aspects of the thermal management systems are evaluated for the intended extensive analysis. Thermal analysis is the leading and most important condition for system evaluation. However, many other features should be analysed to define each system's suitability and the optimal scenarios for each thermal management system. Therefore, the hydraulic energy consumption, each system's mass and volume, specific energy and energy density, cost, safety and reliability, and overall BEV efficiency are evaluated beyond temperature and thermal dispersion evolution.

5.4.1 Thermal Criterion

The thermal perspective is fundamental in studying the three systems under examination. Building upon the findings reported in the preceding case studies, this indicator compares the temperature evolution and maximum cell-to-cell thermal dispersion across the three BTMSs considered in this study.

Figure 5.25a illustrates the average temperature evolution of the module for each of the three BTMSs under analysis. The results demonstrate that all three cases exhibit adequate responses to the high-performance cycle simulated, with the Hybrid BTMS recording a maximum temperature of 35.2 °C at the end of the fast-charging period. Notably, the Dielectric BTMS outperforms the Hybrid solution by reducing the maximum temperature by 1.0 °C, representing a 2.9 % improvement. However, the Cold Plate BTMS stands out as the optimal solution, exhibiting the most significant advancement in thermal performance among the three systems studied.

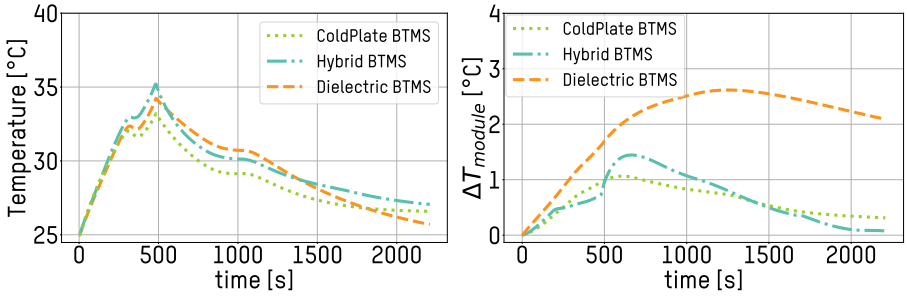

(a) *Temperature evolution results.*

(b) *Maximum cell-to-cell thermal dispersion results.*

Figure 5.25: *Thermal results for the high-performance cycle of reference Cold Plate and Hybrid BTMSs, and proposed advanced Dielectric BTMS.*

Regarding the cell-to-cell thermal dispersion on the module (ΔT_{module}), the Dielectric BTMS exhibits less favourable results than the other two systems, with a maximum ΔT_{module} of 2.6 °C, although still representing a reasonable temperature dispersion. The temperature dispersion evolution over the tested cycle is depicted in fig. 5.25b, with the Cold Plate and Hybrid BTMSs displaying comparable performance, achieving maximum values of 1.1 °C and 1.4 °C, respectively. Comprehensive temperature and thermal dispersion results are tabulated in

table 5.12, facilitating an in-depth analysis of the thermal behaviour of the BTMSs under examination. Moreover, these results are also plotted in fig. 5.27a and fig. 5.27b.

Table 5.12: *Thermal management system thermal comparison results. Maximum cycle temperature (T_{max}), maximum cell-to-cell thermal dispersion on the module (ΔT_{module}), and the resultant improvement concerning the Dielectric BTMS (negative values representing performance deteriorating with the Dielectric BTMS).*

Thermal Management System	T_{max} [°C]	Improvement with Dielectric BTMS [%]	ΔT_{module} [°C]	Improvement with Dielectric BTMS [%]
Cold Plate BTMS	33.2	**-2.9 %**	1.1	**-57.7 %**
Hybrid BTMS	35.2	**2.9 %**	1.4	**-46.1 %**
Dielectric BTMS	34.2	-	2.6	-

Furthermore, the temperature contours of the three systems at the end of the fast charge are presented in fig. 5.26. It is observed that the Cold Plate BTMS exhibits the lowest temperatures and highest homogeneity. In contrast, a comparatively higher thermal dispersion between the top and bottom regions of the cells is evident in the Dielectric BTMS. These findings provide valuable insights into the heat transfer mechanisms and associated thermal behaviour of the different solutions under scrutiny, facilitating an informed evaluation of their thermal performance characteristics.

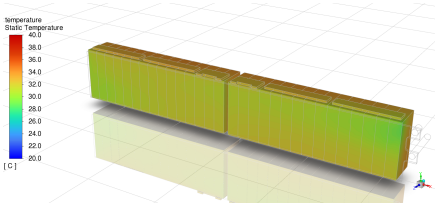

(a) *Cold Plate BTMS at fast charge end.*

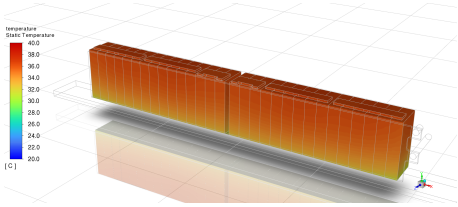

(b) *Hybrid BTMS at fast charge end.*

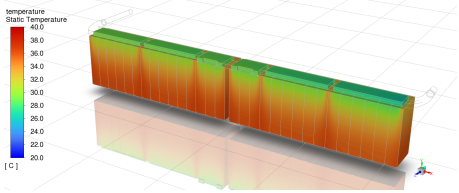

(c) *Dielectric BTMS at fast charge end.*

Figure 5.26: *Temperature contours of the three battery thermal management systems.*

5.4.2 Hydraulic Criterion

Regarding hydraulic pumping energy consumption, the already evaluated data is depicted in table 5.13 for Cold Plate, Hybrid and Dielectric BTMS. The pressure drop (Δp), hydraulic power (P_{hyd}) and hydraulic energy consumption (E_{hyd}) are shown, together with the resultant improvement concerning the Dielectric BTMS. Moreover, these results are also plotted in fig. 5.27e.

Table 5.13: *Hydraulic results of the compared BTMSs. Pressure Drop (Δp), hydraulic power (P_{hyd}) and hydraulic energy consumption (E_{hyd}) are shown, together with the resultant improvement concerning the Dielectric BTMS.*

Thermal Management System	Δp [Pa]	P_{hyd} [W]	E_{hyd} [Wh]	Improvement with Dielectric BTMS [%]
Cold Plate BTMS	4821.3	0.14	0.086	**85.5 %**
Hybrid BTMS	4821.3	0.14	0.067	**81.3 %**
Dielectric BTMS	467.1	0.0203	0.0125	**-**

The selected dielectric fluid's reduced viscosity substantially impacts the BTMS's pressure drop, resulting in more than a ten-fold reduction compared to the other two systems analysed. This improvement enhances the hydraulic performance of the Dielectric BTMS, achieving hydraulic efficiencies of 85.5 % and 81.3 % compared to the Cold Plate and Hybrid BTMSs, respectively. Notably, the energy consumption differences between the latter two systems are attributed to the active system usage time. The Hybrid BTMS utilises the PCM buffer during fast charging, reducing the cold plate operation time, which results in a more energy-efficient system.

Due to the Dielectric BTMS's reduced pressure drop, significant reductions in auxiliary energy consumption are observed, enhancing the system's energy efficiency. Additionally, the reduced pressure drop provides design flexibility for the dielectric system, enabling the incorporation of narrower ducts or higher mass flow rates to improve the system's thermal management ability.

5.4.3 Mass and Volume Criterion

The battery pack's mass and volume characteristics are critical factors in the design of BEVs and significantly impact the vehicle's energy con-

sumption and overall efficiency. Therefore, these fundamental aspects are vital for comparing different battery systems for BEV use.

The 30-cell row battery module studied in this work is the comparison reference. Therefore, the mass and volume increase provided by each BTMS is quantified based on this reference module, with the results depicted in table 5.14.

Table 5.14: *Mass and volume increase associated with each BTMS utilisation.*

	Battery Module	**Cold Plate BTMS**	**Hybrid BTMS**	**Dielectric BTMS**
Mass [kg]	17.39	18.71	20.47	18.59
Increase from base BM [%]	100%	+7.57 %	+17.71 %	+6.88 %
Volume [L]	7.9	8.3	9.4	8.0
Increase from base BM [%]	100%	+5.68 %	+19.57 %	+1.33 %

The reference mass and volume of the battery module are evaluated based on a configuration consisting of 30 cells and their corresponding copper busbars used for electrical connection. Regarding the mass of each BTMS, the reference assembly weighs 17.39 kg. Including the aluminium cold plate and the w-e50 fluid in the Cold Plate solution increases the weight to 18.71 kg, representing an increase of 7.57 %. The Hybrid BTMS yields an even higher weight increase of 17.71 % due to the addition of the PCM buffer, resulting in a weight of 20.47 kg. However, the Dielectric BTMS exhibits the most modest weight increase of 6.88 %, with a final weight of 18.59 kg. In this system, the initial copper busbars are replaced with dielectric duct busbars and the fluid on them. The difference in weight between the Cold Plate and Dielectric BTMS is contained due to the size increase in the duct busbars and the high density of copper.

A similar trend is noticed in the volume data analysis among the compared systems, with a notable improvement observed in the Dielectric BTMS. The reference battery module has a volume of 7.9 L, which increases by 5.68 % when implementing the Cold Plate BTMS. The Hybrid BTMS shows a more significant increase of 19.57 % due to including the PCM buffer. Conversely, the Dielectric system experiences only a slight rise of 1.33 %, bringing its total volume to 8.0 L. Consequently, the Dielectric system's volume improvement is evident as only the busbar size has been modified,

and small plastic connectors have been added to the assembly.

5.4.4 Specific Energy and Energy Density Criterion

The analysis of mass and volume is of direct relevance to the specific energy and energy density of the battery. These properties are evaluated based on the energy of the 30-cell row battery module and the corresponding mass and volume data for each thermal management system.

The energy of each cell is 52.9 Wh, resulting in a total energy of 1587 Wh for the 30-cell module. Based on the corresponding weight of 17.39 kg and volume of 7.9 L, the specific energy and energy density reference values are calculated to be 91.3 Wh/kg and 201.2 Wh/L, respectively, as presented in table 5.15.

Table 5.15: *Specific Energy and Energy Density change associated with each BTMS utilisation.*

	Battery Module	**Cold Plate BTMS**	**Hybrid BTMS**	**Dielectric BTMS**
Specific Energy [Wh/kg]	91.3	84.8	77.5	85.4
Reduction from base BM [%]	100%	-7.04 %	-15.05 %	-6.43 %
Energy Density [Wh/L]	201.2	190.4	168.3	198.6
Reduction from base BM [%]	100%	-5.38 %	-16.37 %	-1.31 %

The specific energy reduction is 7.04 % for Cold Plate BTMS and 15.05 % for Hybrid BTMS. However, the Dielectric system reduces the reference specific energy only by 6.43 %, reaching 85.4 Wh/L.

The energy density is reduced by 5.38 % for Cold Plate BTMS and 16.37 % for Hybrid BTMS. However, the Dielectric system reduces the reference energy density only by 1.31 %, reaching 198.6 Wh/L. These results are also plotted in fig. 5.27c and fig. 5.27d.

The results demonstrate an improvement in both specific energy and energy density for the Dielectric BTMS, with the volume leverage proving superior to the weight leverage. This enhancement is noteworthy compared to the Cold Plate BTMS and offers a distinct advantage compared to the Hybrid BTMS.

5.4.5 Other Criteria

In addition to the quantified metrics presented in this PhD thesis, other criteria must be considered when comparing BTMSs. One of the primary variables that battery pack manufacturers and automobile companies will consider is the manufacturing and material cost. The safety criterion is also of utmost importance for ensuring passenger security and system reliability. Furthermore, overall BEV efficiency is critical for vehicle design and development, particularly in the context of range optimisation.

5.4.5.1 Cost Criterion

Price estimation of the BTMS' components is a complex process for a final product on mass production. However, some key points can be underlined to approximate each system's cost.

- Cold Plate BTMS is a commonly used solution for battery thermal management. Aluminium is affordable, and the manufacturing process for cold plates is standardised, making it a cost-effective solution. The fluid in the cold plate is standard w-e50, which is relatively cheap. However, the cost of this system may vary depending on the size and complexity of the cold plate required for the specific battery application.
- Hybrid BTMS combines the cold plate with a PCM buffer made of paraffin wax inserted into a porous aluminium structure. The cold plate, as already mentioned, should be a cost-effective solution. However, manufacturing a PCM buffer can be challenging and require specialised equipment, leading to a higher cost than the cold plate, considerably increasing the overall cost of the system.
- Dielectric BTMS uses copper busbars expressly manufactured for this system and an expensive dielectric fluid. The busbars can be extruded under a certainly standardised manufacturing process, being reasonably cost-effective. However, dielectric fluid presents a considerable cost increment for the system, as it is not a standard and extended coolant.

In conclusion, the cost estimation for battery thermal management systems depends on several factors, such as the material used, the man-

ufacturing process, and the size and complexity of the system required for the specific battery application. The classical aluminium cold plate system is a cost-effective solution, while the hybrid system may be more expensive due to the specialised manufacturing processes required. The dielectric system's cost may come between both previous systems.

Therefore, it is essential to consider the cost-benefit analysis for different battery thermal management systems to select the most suitable solution for the specific application.

5.4.5.2 Safety and Reliability Criterion

When analysing the safety and reliability of the battery pack system, some characteristics such as leakages, battery cell degradation and lifespan and thermal runaway contention should be considered.

- Cold Plate BTMS can be prone to leakage, especially if not designed and maintained correctly. The w-e50 fluid used is not dielectric, and a leak can cause short circuits in the battery cells. Nevertheless, it can provide good cooling capacity and low thermal dispersion, making it an optimal solution for battery degradation and lifespan.
- Hybrid BTMS also has the same leakage problem on the cold plate and an additional one on the PCM buffer. The PCM buffer is made of a porous structure with paraffin inside, which can leak and contaminate the battery module, leading to reduced battery performance, degradation, or even failure. Nevertheless, the PCM can act as a passive safety mechanism to absorb thermal energy and prevent temperature fluctuations, even preventing thermal runaway in case of cold plate failure.
- Dielectric BTMS is the most effective system in preventing leakage problems, as non-conductive and non-flammable dielectric fluids are used. Moreover, it can be helpful in thermal runaway control if designed to capture thermal runaway gases. The slightly higher thermal dispersion on the battery module can slightly affect the cell unbalance. However, this dispersion is far inside the standardised security limits.

In conclusion, battery thermal management systems' safety and re-

liability estimation depends on several factors. The classical aluminium cold plate system is reliable for temperature control. However, removing leakage-associated problems and thermal runaway control features make the dielectric system stand out from the other two BTMSs. Nevertheless, Cold Plate and Hybrid BTMSs are still competitive solutions.

5.4.5.3 BEV Efficiency Criterion

Battery electric vehicle system efficiency is essential for reducing energy consumption and, thus, range anxiety. This is directly related to the BTMS weight and the auxiliary energy consumption from the required coolant pumping energy. Therefore, the BEV efficiency is directly related to the previously defined specific energy and hydraulic criteria.

- Cold Plate and Hybrid BTMSs require high hydraulic pumping energy for fluid distribution in the thermal management system, especially the cold plate system, which is not supported with a passive system for the fast charge process. However, this PCM buffer increases the system weight far from the single cold plate solution, significantly deteriorating the specific energy. Therefore, both systems deteriorate the vehicle's efficiency and range, especially underlining the Hybrid BTMS.

- Dielectric BTMS is the lightest of the three systems, reducing the required energy for vehicle propulsion. Moreover, the dielectric system has less energy consumption related to fluid pumping due to the reduced viscosity of the selected dielectric fluid.

Both aspects of the analysed BTMS support the dielectric system as the most efficient. It requires less energy to pump the fluid through the battery thermal management system, resulting in less auxiliary energy consumption and more available energy for propulsion. The reduced weight of the system also leads to less energy needed to move the BEV, further increasing efficiency and resulting in the least impact on the BEV's range.

In conclusion, the Dielectric BTMS further increases efficiency and results in the least impact on the BEV's range due to weight reduction and low auxiliary energy consumption.

5.5 Final Discussion

The main variables affecting the performance of the three different BTMS have been presented. Some are numerically assessed, such as the thermal, hydraulic and specific energy and energy density variables. In contrast, some others are theoretically gathered, such as the cost, safety and reliability, and the BEV efficiency.

The exact results and percentage comparisons are already made. Therefore, the five numerically evaluated variables are depicted in fig. 5.27 for a faster resume, visualisation, and comparison. Moreover, arrows indicating the variable's direction for BTMS optimal performance are added on the right side of each plot row.

Figure 5.27a and fig. 5.27b on the first row, shows maximum temperatures and cell-to-cell thermal dispersion on the battery module, respectively. The lower these variables are, the better the thermal management system works. As seen, the Cold Plate BTMS obtains the best results, followed by the Dielectric BTMS on T_{max} variable, and by the Hybrid system on ΔT_{module} variable. However, the three systems present adequate results inside the optimal performance span.

Figure 5.27c and fig. 5.27d on the second row show the specific energy and the energy density, respectively, where higher values represent more onboard energy per mass and volume. Dielectric BTMS presents the best results, followed by the Cold Plate BTMS.

Finally, the fig. 5.27e on the third row presents the auxiliary pumping energy consumption, where lower values represent more efficient BTMSs. Again, the Dielectric solution is the optimal system, far from Hybrid and Cold Plate BTMS.

On the other hand, the theoretically assessed variables' results can be resumed as follows: the cost-optimal solution is the Cold Plate system, whereas Dielectric BTMS presents better performance and potential for safety and reliability. Finally, the overall electric vehicle efficiency can also be boosted with the Dielectric solution.

Therefore, these variables' results are depicted in table 5.16. A colour code is used to reflect the results, where green (best), yellow (intermediate) and red (worst) indicates the optimal solution for each variable ana-

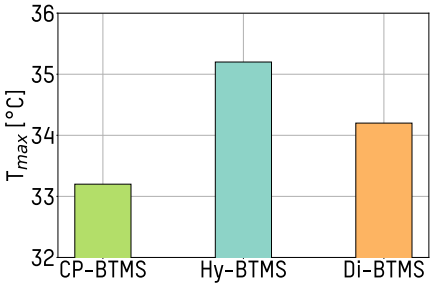

(a) *Maximum temperature results (Lower Best).*

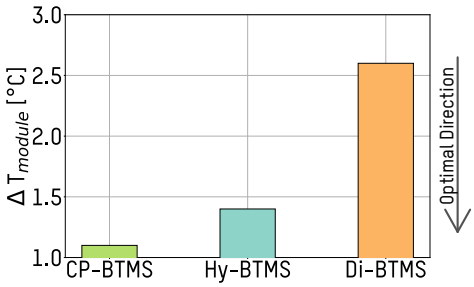

(b) *Maximum cell-to-cell thermal dispersion results (Lower Best).*

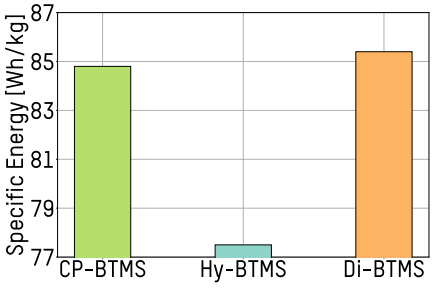

(c) *Specific Energy results (Higher Best).*

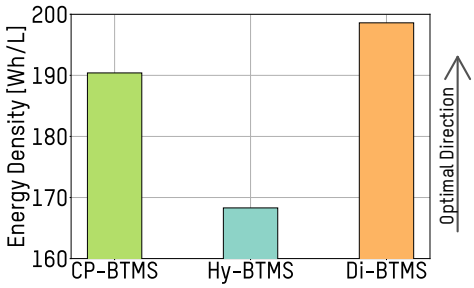

(d) *Energy Density results (Higher Best).*

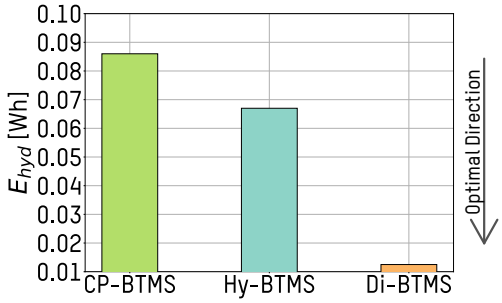

(e) *Hydraulic energy consumption results (Lower Best).*

Figure 5.27: *Results of analysed BTMS comparison variables.*

lysed. An extra symbol code is also added, where ★ is used for the optimal solution, and ✓ and ✗ show the intermediate and worst solution, respectively, for each variable.

Hybrid BTMS presents the least adequate results as it does not stand out in any of the variables. By contrast, the Cold Plate system is outlined in the thermal performance variables and the cost indicator. Finally, Dielec-

Table 5.16: *Compared indicators with colour and symbol code for each BTMS advantage and disadvantage evaluation. The analysed BTMSs are classified as best solution — green colour, ★ —, intermediate solution — yellow colour, ✓ — and worst solution — red colour, ✗ —.*

Thermal Management System	T_{max}	ΔT_{module}	E_{hyd}	Specific Energy	Energy Density	Cost	Safety and Reliability	BEV Efficiency
Cold Plate BTMS	★	★	✗	✓	✓	★	✓	✓
Hybrid BTMS	✗	✓	✓	✗	✗	✗	✓	✗
Dielectric BTMS	✓	✗	★	★	★	✓	★	★

tric BTMS is the optimal solution for the other factors, such as reduced hydraulic energy consumption, higher specific energy and energy density values, increased safety and reliability and better vehicle efficiency.

When selecting the most competitive battery thermal management system, two main conclusions can be drawn based on the results of the comparative analysis:

1. The Dielectric Flow- and Tab-Based Battery Thermal Management System appears promising, with a convincing performance in every indicator analysed. It is outstanding in main indicators for a high performance BEV, highly adaptable for different battery module designs, and with valuable safety and reliability characteristics. Moreover, it offers a competitive thermal performance if compared with the cold plate standard solution, with the battery cells inside the optimal performance temperature zone even in the most demanding tested electric cycle.

   The unique and main drawback is the cost associated with the dielectric fluid's price. However, in specific applications where the cost is not a limiting factor, and outstanding BEV efficiency or reduced weight are pursued, the Dielectric BTMS represents the optimal solution.

2. The standardised Cold Plate Battery Thermal Management System appears to be a reliable and effective solution for electric vehicles when no outstanding performances are required. This technology provides the best possible thermal response over high-performance electric cycles. However, the detriment of specific indicators shows a less efficient performance with an associated range reduction

compared to the advanced dielectric system proposed.

Therefore, this system can comprehend the thermal management of standard BEVs, where overall automobile cost is a limiting factor, and no outstanding range or reduced weight is pursued.

Beyond this, other ideas and concerns emerged after the analysis. This work does not thoroughly evaluate these topics, but their importance should be highlighted.

- It is crucial to evaluate the potential impact of the slightly increased thermal dispersion on battery cell degradation, even if the results are currently within acceptable performance limits. This evaluation should be done through numerical analysis to assess and discard any associated cell degradation.

  Additionally, the temperature gradient observed in fig. 5.26 within the battery cells is not considered significant, provided that the dielectric system is oriented parallel to the cells' layers rather than perpendicular. This effect has been previously noted in literature studies.

- In order to achieve a more competitive solution, exploring the cost of alternative dielectric fluids can be considered. However, it should be noted that many alternative dielectric fluids have a significantly higher viscosity than the base fluid used. This increased viscosity will increase the auxiliary pumping energy consumption, which is one of the key indicators of the proposed system. Therefore, appropriate design considerations must be made to mitigate this issue's impact on the system's overall performance.

- Implementing alternative designs above the cells' venting hole could be a promising solution to mitigate thermal runaway propagation. It is important to note that the use of larger ducts may result in a reduction in the specific energy and energy density of the system. However, the potential benefits of enhanced safety and reliability and improved thermal performance could outweigh this drawback. Further research is necessary to evaluate such designs' feasibility and potential benefits.

- To ensure accurate analysis of the vehicle's efficiency improvement with the dielectric BTMS, it is crucial to measure and numerically assess the range increase achieved through the reduction in weight and pumping auxiliary energy consumption. Such an assessment will better illustrate how much the dielectric BTMS can enhance the vehicle's efficiency.

6

Concept-Proof Validation:

Prototype Development and Experimental Analysis

Summary

This chapter unveils the prototype development of the proposed advanced Dielectric Flow- and Tab-based BTMS, designed for a battery module composed of cylindrical cells. The prototype is constructed and tested through a series of experimental tests, validating the CFD model previously developed. The system's design is studied for optimisation, and comparison simulations are carried out. The primary objective of this study is to gain an in-depth understanding of the proposed technology's capabilities and its potential to enhance the overall performance of the battery module.

6.1 Dielectric BTMS Prototype: Concept, Design and Development

Section 2.3 of Chapter 2 presented a literature review that serves as the foundation for both proposed advanced solutions. Moreover, the comparative analysis in Chapter 5, consolidated one of those solutions as the most promising: the Dielectric Flow- and Tab-based battery thermal management system. This system's concept is developed based on two key ideas:

- The dielectric flow concept reduces thermal resistance by enabling direct contact between the coolant fluid and the battery cells. This design ensures that there are no thermal inefficiencies during heat transfer. By employing a dielectric coolant, the proposed battery thermal management system can achieve a higher thermal conductivity than traditional liquid coolants, thereby playing a critical role in facilitating efficient heat transfer and ensuring the optimal performance of the battery thermal management system.
- Tab-based thermal management concept is an efficient solution for high-performance thermal management, even if the heat transfer area is limited, as the usage of the cell's high thermal conductivity path is enhanced. This contact area reduction can lead to more compact systems with reduced specific energy and energy density.

These ideas have been corroborated under CFD comparison with other BTMSs, and this chapter aims to transfer these results to a functional prototype. In developing this dielectric flow and tab-cooling prototype, the prototype can be considered a testing platform, contemplating possible design aspects, such as several duct sizes or different dielectric fluids. The prototype allows for practical experimentation and assessment of these design parameters.

For a more straightforward implementation, testing ease and to minimise required testing resources, a previously developed battery module for an elevation application [169], with an air-based thermal management system, is utilised to conceptualise the dielectric flow and tab cooling technology. Cylindrical cells are employed in this module, so the design and solution proposed in chapter 5 needs to be adapted, proving technology's flexibility. Figure 6.1a shows this conceptualisation

enclosing a duct on the cell tabs area, where dielectric fluid is intended to flow through. Fluid circulating through cell tabs will extract the heat from the cell core, being the convective heat transfer rate generated on the duct critical. Therefore, thorough work on the design of the duct is crucial.

For the prototype, the battery module configuration comprises twelve cylindrical cells with the exact dimensions and distribution of base air BTMS solution. The design should include two independent ducts, one for the top and another for the bottom tabs. The concept idea is shown in fig. 6.1b, cut in half.

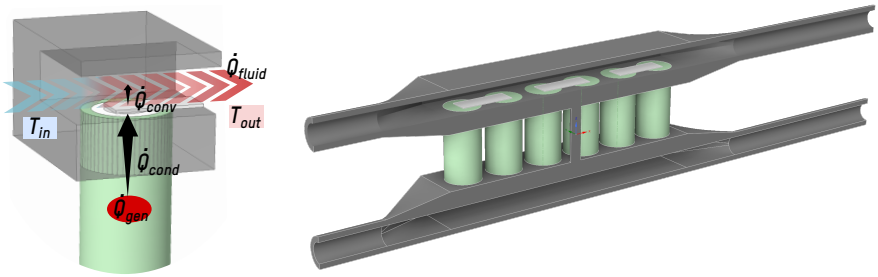

(a) *Dielectric tab flowing thermal concept.* ***(b)*** *Battery module concept idea for dielectric tab flowing TMS.*

Figure 6.1: *Dielectric flow- and tab-based BTMS concept idea.*

During the development of the prototype, two significant difficulties were identified. The first challenge is the need for multiple temperature and voltage sensors on the cells' tab surfaces to conduct accurate experimental measurements. This requirement necessitates a considerable amount of wiring to be routed out of the duct, directly impacting the second difficulty: duct sealing and fluid leakage issues.

To address the challenges of implementing multiple sensors and minimising the risk of fluid leakage, a polythene block structure with necessary holes for the cells is machined to form the duct on the cells' tabs. The created opening dimensions are proportional to the area taken up by the cell tabs, resulting in a big duct of 262.5 x 69.5 mm surface and a 22.5 mm height. This allows testing other duct sizes by adding specifically designed extra polythene pieces on these two openings, as will be seen in section 6.1.3. This initial duct design, called *Geom01*, is enclosed with top

and bottom transparent covers and sealed with a rubber pad to ensure correct sealing.

All sensor connections are added to the prototype sides to facilitate their connections and provide easy access. Voltage readings are obtained from every cell tab, while three thermocouples (positive tab, centre body, and negative tab) are implemented to monitor temperature changes. The prototype's Computer-Aided Design (CAD) is depicted in fig. 6.2.

The proposed design solution provides a robust and reliable platform for testing the advanced BTMS concept. A polythene block structure with necessary holes and a duct on the cells' tabs enables accurate and efficient temperature measurement while minimising the risk of fluid leakage. Incorporating multiple sensors, including thermocouples and voltage sensors, provides valuable data for analysing and validating the proposed BTMS concept.

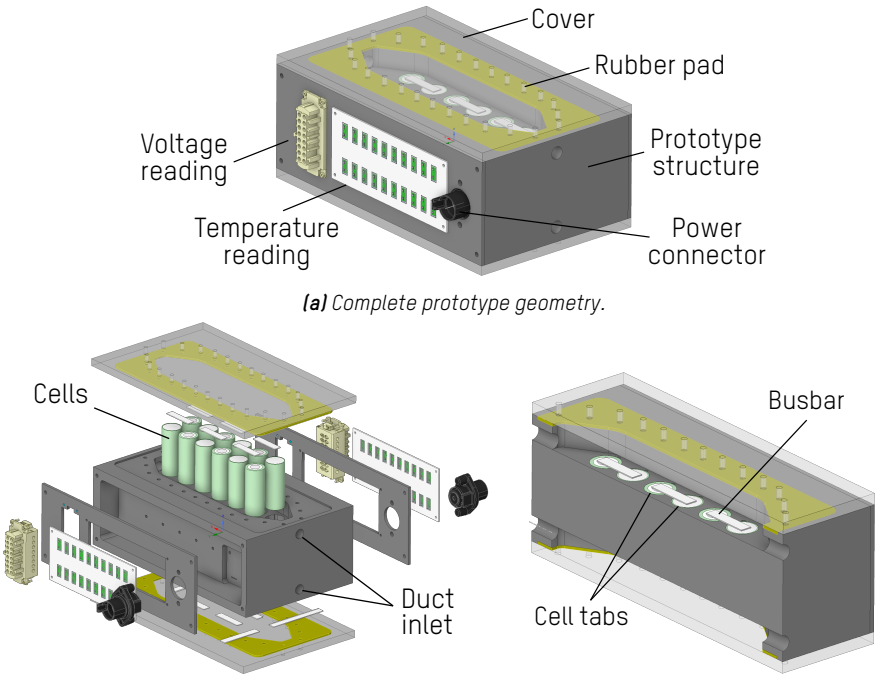

(a) *Complete prototype geometry.*

(b) *Exploded prototype geometry.*

(c) *Half view prototype geometry.*

Figure 6.2: *Geom01 dielectric flow- and tab-based BTMS prototype's design.*

Table 6.1: *Properties of cylindrical LithiumWerks ANR26650m1B cell.*

LithiumWerks ANR26650m1B	
Chemistry	LFP
V_{nom} [V]	3.3
Cap_{nom} [Ah]	2.5
Max CHA Current [A]	10 (4C)
Max DCH Current [A]	50 (20C)
Temperature Range [°C]	0 to 55
Diameter [mm]	26
Length [mm]	65
Mass [kg]	0.076

The battery module under study consists of twelve LithiumWerks ANR26650m1B cylindrical LFP cells [181], each with a capacity of 2.5 Ah. These cells are selected as the commercial evolution of the A123 cells used in the reference case with air BTMS, which justifies their use in this study. The cells' characteristics are identical to those of the previous research and are connected in a 12S1P electric configuration to produce a 39.6 V and 2.5 Ah module. The cell properties are summarised in table 6.1.

In addition, the thermal parameters necessary for modelling the cell heat generation, R_{in} and EHC, are experimentally characterised using the methodology presented in Section 4.2. The EHC is determined for the cell's entire SOC range, while the R_{in} is also measured at three different temperatures (10 °C, 25 °C, and 45 °C). The resulting data is presented graphically in fig. 6.3.

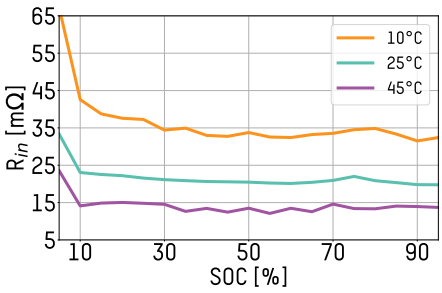

(a) *Internal Resistance.*

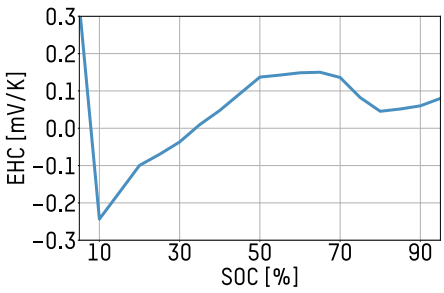

(b) *Entropic Heat Coefficient.*

Figure 6.3: *LithiumWerks ANR26650m1B cell's properties for heat generation model.*

6.1.1 Hypothetical Battery Pack Architecture

The proposed dielectric BTMS prototype is intended for application in electromobility. As such, it is essential to establish the requisite background information and requirements to facilitate proper experimental and numerical analysis. To this end, the concept of a BEV and its associated requirements must be thoroughly considered. A realistic case study can be established by applying these requirements to the developed battery module prototype to obtain results. This will involve determining critical data such as the discharging current (which is directly linked to the electrical configuration of the BP) and the dielectric flow rate (which is associated with the hydraulic connections of the battery modules). With these data points established, BP's hypothetical electric and hydraulic architecture can be defined in detail.

6.1.1.1 Electric Architecture

The electric characteristics of the BEV used in this case study will be defined following the BP needs previously presented in the chapter 5. Therefore the present study utilises the prototype battery module characteristics to develop an approach that aligns with the aforementioned BP requirements.

Therefore with a battery module in a 12S1P electric connection and 39.6 V and 2.5 Ah, the calculated number of battery modules required to meet these requirements is 290, achieving a 396 V and 28.71 kWh battery pack. Each module must be connected in a series of 10 and parallel of 29 to achieve a complete cell configuration of 120S29P, resulting in a battery capacity of 72.5 Ah. A detailed description of these specifications is presented intable 6.2.

Once the electrical configuration of the hypothetical BP is obtained, the discharge current could be calculated knowing the vehicle's driving power needs. The vehicle power related to the constant driving speed curve is shown in fig. 5.3, obtained from *SELFIE* project for the *Fiat Doblo* vehicle.

For the present case study, a demanding discharge application has been defined, which includes a motorway constant driving scenario at 120 km/h, corresponding to the maximum permitted speed and referred to as

Table 6.2: *Electric configuration of the battery module and battery pack.*

	Battery Module	Battery Pack
Energy [kWh]	0.99	28.71
Voltage [V]	39.6	396
Capacity [Ah]	2.5	72.5
Cell/Module Configuration	12S1P	10S29P
Number of modules	-	290
Number of cells [n_{cell}]	12	3480

Normal Drive (ND). The power demand data shows that the vehicle's power needs have been determined to be 39.7 kW. The expression in eq. (5.1) can be utilised to determine each cell's discharging current (I_{dch}).

Consequently, the discharging current corresponding to the ND scenario is determined to be 3.45 A per cell, equivalent to a 1.38 C-rate. Concerning charging current, the Fast Charge (FC) criterion is adopted, and thus, 10 A or 4C C-rate, the maximum current rating of each cell, is used.

6.1.1.2 Hydraulic Architecture

The hydraulic architecture of the hypothetical battery pack is also considered, specifying the flow rate through the ducts of each module. This process involves setting the maximum hydraulic capacity of the vehicle and utilising it to determine the appropriate configuration. The maximum hydraulic capacity of the vehicle is predetermined to be 20 l/min in the *Selfie* project.

Based on the predetermined hydraulic capacity of the vehicle, the 290 battery modules that constitute the BP must be organised into groups with specific numbers of serial and parallel hydraulic connections, as depicted in the schematic diagram in fig. 6.4.

Serial arrangements of 10, 29, 58, 145, and 290 battery modules have been identified to establish different hydraulic configurations for the battery pack. These configurations are named *hyd*-10S29P, *hyd*-29S10P, *hyd*-58S5P, *hyd*-145S2P, *hyd*-290S1P, with the "*hyd*-" prefix added to prevent confusion with the electrical connections described in the preceding section. The hydraulic flow rate on each row increases with the degree

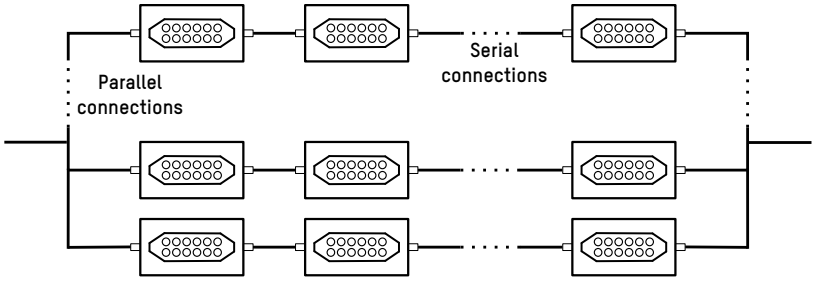

Figure 6.4: *Hydraulic configuration scheme.*

of serial connection among the modules. Consequently, a higher serial connection increases cooling capacity and raises the thermal gradient between the cells.

Considering all the previously mentioned considerations, the hydraulic groups identified above will have a corresponding maximum volumetric flow rate. The following analysis will use these values as the nominal flow rates. However, it should be emphasised that the defined hydraulic groups are solely for logical flow rates utilisation on the dielectric BTMS prototype analysis. The actual volumetric flow rate obtained will depend on the hydraulic configuration and the maximum available volumetric flow rate in each cooling row, which are closely interrelated. The volumetric flow rate used on the analysis, corresponding with each hydraulic configuration, is depicted in table 6.3. The equivalent mass flow rate is also shown.

Table 6.3: *Hydraulic configuration of the modules in the hypothetical battery pack, with the corresponding volumetric flow rates utilised on the prototype case study.*

Hydraulic Configuration	**$\dot{V}$ [l/min]**	**Equivalent $\dot{m}$ [kg/s]**
hyd-10S29P	0.7	0.0165
hyd-29S10P	2	0.0478
hyd-58S5P	4	0.096
hyd-145S2P	10	0.239
hyd-290S1P	20	0.478

6.1.2 Dielectric Fluid Selection Analysis

This section will outline the procedure for analysing the appropriate dielectric fluid for the prototype study. Even though the Novec7200 was selected for its low viscosity in the previous chapter, diverse fluids' thermal and hydraulic effects are analysed to ensure adequate fluid selection. Specifically, the analysis procedure with a lumped thermal model and the results obtained from this analysis will be described.

The analysis involves six different dielectric fluids: two hydrofluoroethers, the Novec7200 and the Fluorinert FC-72 from 3M company; the natural ester Envirotemp FR3, and the synthetic ester M&I Midel-7131; the hydrocarbon PAO (poly-alpha olefin); and a solution of water with ethyleneglycol at 50 % of the mixture (w-e50). However, it should be noted that the latter is a conductive solution currently used in cold plate BTMS solutions. Therefore, it is unsuitable in direct contact with the cells and is only included for comparison reasons. The necessary fluids' data for the analysis are presented in Appendix B.3. The presented parameters include the fluid density (ρ), the specific heat capacity (C_p), the thermal conductivity (k), the kinematic viscosity (ν) and the dynamic viscosity (μ).

6.1.2.1 Lumped Thermal Model

The temperature of the cells in the Geom01 design-based battery pack is determined by calculating it along the hydraulic configurations presented earlier. This is done to identify the most suitable dielectric fluid to effectively maintain the cells within the optimal temperature range. A lumped thermal model of the BTMS is developed in this regard. The model considers the system's energy balance and interrelates the mechanisms of heat transfer and fluid mechanics to understand the system's behaviour comprehensively.

The energy balance on the cells follows the eq. (6.1),

$$M \cdot C_p \cdot \frac{\Delta T}{\Delta t} = \dot{Q}_{gen} - \dot{Q}_{diss} \tag{6.1}$$

where the left term represents the heat stored on the cell, $\dot{Q}_{gen}$ [W] is the cell's generated heat, and $\dot{Q}_{diss}$ [W] is the heat dissipated from the cell

to the fluid by convection.

The energy balance is applied in this study under two main simplifications sufficient to obtain the desired results. Firstly, a stationary calculation is used, where the temperature-dependent average heat generation of the cells during the charge and discharge cycle is considered. In the stationary situation, where the temperatures are stabilised, the heat accumulation on the cells is assumed to be zero, and all the heat generated on the cells is dissipated to the fluid. Secondly, radial heat transfer due to the insulating effect of the prototype structure is eliminated. Therefore, only the axial direction of the cells is considered for heat transfer analysis. By adopting these simplifications, evaluating the cell temperatures with the lumped thermal model becomes feasible.

The average cell heat generation is computed by evaluating the heat generation of the charge and discharge cycles (under the SOC and current scope) at different constant temperatures, following the heat generation depicted in eq. (3.1) and with the heat generation model scheme in fig. 3.3. by following this approach, the results presented in table 6.4 are obtained.

Table 6.4: *Averaged cell heat generation by temperature*

Temperature [°C]	10	15	20	25	30	35	40	45	50
$\dot{Q}_{gen}$ **[W]**	0.94	0.82	0.71	0.60	0.52	0.44	0.36	0.29	0.21

Under the simplifying assumptions outlined above, the lumped thermal model of the system consists of three main blocks: heat generation, heat dissipation, and fluid mechanics. The heat generation block is obtained directly by interpolating the data presented in table 6.4. The heat dissipation block includes heat conduction through the cell and heat convection to the fluid. Finally, the fluid mechanics block evaluates the fluid's heat storage capacity, which depends on its characteristics and the size and shape of the Geom01 duct. This interrelation is illustrated in fig. 6.5. Figure 6.5a shows the energy balance from the cell core heat generation to the fluid heat storage, while fig. 6.5b shows the scheme of the lumped thermal model.

For the model calculation in the stationary situation suggested, the processes are related in the following way: the heat generated by the cell propagates through the cell by conduction ($\dot{Q}_{gen} = \dot{Q}_{cond}$); this heat is, in

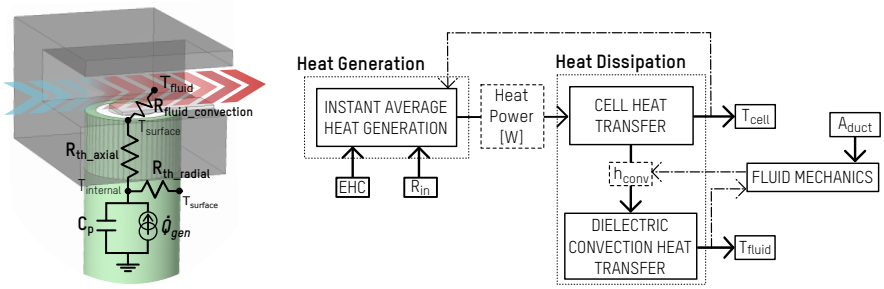

(a) *Heat transfer scheme on the dielectric BTMS.*

(b) *Lumped thermal model's scheme*

Figure 6.5: *Heat transfer and lumped thermal model schemes for Dielectric BTMS design.*

turn, transferred to the fluid by convection ($\dot{Q}_{cond} = \dot{Q}_{conv}$). Finally, it is dissipated, depending on the fluid properties ($\dot{Q}_{conv} = \dot{Q}_{sto_{fluid}}$). With these relations, cells' core and surface temperatures and the fluid's temperature after each cell is calculated. Moreover, the pressure drop (Δp) produced by the duct is also estimated to find the auxiliary energy consumption with each fluid. All the heat transfer and fluid mechanics equation systems are depicted in Appendix B.1.

The lumped model is developed in *Python* code, using the roots finding function "optimize.fsolve" of the scientific computing module Scipy in Python over the equation system suggested.

6.1.2.2 Dielectric Fluid Selection Results

The simulations inlet fluid temperature is imposed at 20 °C, and *hyd*-10S29P, *hyd*-29S10P, *hyd*-58S5P, *hyd*-145S2P and *hyd*-290S1P hydraulic configurations for the modules are simulated. Reynolds number (Re) is evaluated to understand the fluid flow patterns, along with the convective heat transfer coefficient (h_{conv}), which shows the heat dissipation capability from the cell to the fluid. Moreover, the thermal resistance (R_{th}) is calculated following eq. (6.2), where the cell's axial dissipation area is used, which corresponds with the cell tab surface. Maximum registered temperature (T_{max}) from the modules and the thermal dispersion among cells in the modules (ΔT_{module}) is also calculated. Finally, the pressure drop (Δp) is calculated following eq. (B.13) from Appendix B.1 to estimate the auxiliary energy consumption. The results are shown in table 6.5.

Table 6.5: *Dielectric fluid selection analysis results.*

Fluid	Hydraulic configuration	$\dot{V}$ [l/min]	*Re* [-]	h_{conv} [W/m^2·K]	R_{th} [K/W]	T_{max} [°C]	ΔT_{module} [°C]	Δp [Pa]
w-e50	*hyd*-10S29P	0.7	34.99	49.35	38.17	29.52	1.01	4.55
	hyd-29S10P	2	101.48			29.53	1.02	
	hyd-58S5P	4	202.96			29.53	1.02	
	hyd-145S2P	10	507.41			29.53	1.03	
	hyd-290S1P	20	1014.82			29.53	1.03	
Novec7200	*hyd*-10S29P	0.7	306.25	9.00	209.37	45.33	0.57	2.83
	hyd-29S10P	2	888.13			45.33	0.57	
	hyd-58S5P	4	1776.25			45.33	0.57	
	hyd-145S2P	10	4440.63	93.22	20.20	27.15	2.18	
	hyd-290S1P	20	8881.25	188.23	10.01	25.11	2.49	
FC72	*hyd*-10S29P	0.7	351.27	7.79	241.69	46.76	0.51	3.20
	hyd-29S10P	2	1018.70			46.76	0.51	
	hyd-58S5P	4	2037.39			46.76	0.52	
	hyd-145S2P	10	5093.48	90.38	20.84	27.47	2.37	
	hyd-290S1P	20	10186.95	178.93	10.53	25.47	2.73	
Envirotemp FR3	*hyd*-10S29P	0.7	2.00	24.63	76.48	35.58	1.36	68.23
	hyd-29S10P	2	5.80			35.59	1.38	
	hyd-58S5P	4	11.61			35.59	1.38	
	hyd-145S2P	10	29.02			35.59	1.38	
	hyd-290S1P	20	58.04			35.59	1.39	
M&I Midel7131	*hyd*-10S29P	0.7	2.00	21.39	88.04	36.85	1.26	71.68
	hyd-29S10P	2	5.81			36.85	1.27	
	hyd-58S5P	4	11.62			36.86	1.28	
	hyd-145S2P	10	29.05			36.86	1.28	
	hyd-290S1P	20	58.10			36.86	1.28	
PAO	*hyd*-10S29P	0.7	2.03	21.00	89.68	37.08	1.31	58.13
	hyd-29S10P	2	5.88			37.09	1.32	
	hyd-58S5P	4	11.76			37.09	1.33	
	hyd-145S2P	10	29.40			37.09	1.33	
	hyd-290S1P	20	58.79			37.09	1.33	

$$R_{th} = \frac{1}{h_{conv} \cdot A_{axial}} \tag{6.2}$$

In low-viscosity fluids like hydrofluoroethers, achieving a high Reynolds number is much easier than for higher-viscosity esters or hydrocarbons. In fact, results show that the only fluids to obtain turbulent flow are Novec7200 and Fluorinert FC72 (coloured in green) during the highest flow rates (with more modules in series). This has allowed considerably higher convection coefficients to be obtained than in the laminar flow cases.

This phenomenon has been directly transferred to the thermal resist-

ance, lowering it and being the heat transfer capacity of those high flow rates Novec7200 and Fluorinert FC72 configurations better than for the other fluids. This can be appreciated in the maximum temperatures registered on the cells. Whereas on laminar flows, the rest of the fluids show lower temperatures, changing to turbulent flow helps reduce those temperatures drastically.

The temperature difference in these cases, highlighted in green, is somewhat more significant than in the others. This is because of the increased heat transfer capacity of the fluid, which is considerably heated with each cell, thus reducing the thermal gradient and hence the heat transfer on the last cells. However, this difference is still well below the 5°C of the optimal range.

On the other hand, it can be seen that the pressure drop with esters and hydrocarbons is higher due to the higher viscosity. This indicates that the energy consumption needed for pumping will be higher, benefiting the Novec7200 and Fluorinert FC72 also in this respect.

In short, as a result of the analysis, it can be said that the hydrofluoroethers present the most suitable properties for the cooling method to be studied in this work. They show an excellent capability for cooling, especially on turbulent regimens. This was achieved at high flow rates; however, a correct design of the prototype's duct, with a narrow area, will have a similar effect at lower flow rates due to the velocity increase.

According to the manufacturer's recommendations, Novec7200 will be used in this work. Fluorinert FC72 is more suitable for electronics applications, while Novec7200 is more suitable for battery applications. The selected fluid is characterised by having a boiling point of 76°C, zero ozone depletion and low global warming potential beyond the aforementioned low viscosity [177, 182].

6.1.3 Duct Sizing Optimisation

Reducing the number of modules in series and hence the flow rate is desired to minimise possible uneven performances between cells on the hydraulic loop. Moreover, duct shape and size optimisation is enhanced after detecting the turbulence effect's importance on the dielectric flow based BTMS. The initial size can be reduced, obtaining higher fluid speed

at lower volumetric flow rates and thus increasing the turbulence level, maintaining or even improving the heat dissipation capability.

The lumped thermal model employed in fluid selection is adapted and used for the prototype's duct sizing analysis. The lowest three flow rates of the previous research are used — 0.7 l/min, 2.0 l/min and 4.0 l/min —, which should be the most reasonable for smaller ducts and having fewer cells in series. Moreover, the duct is now divided into two narrower channels, each running through the tabs of one row of cells in the module. Diverse duct sizes are studied, with two duct heights — 5 and 10 mm —, and four widths — 10 mm, 15 mm, 20 mm and 26 mm —, being the final width equal to the cell's tab diameter.

As a result, maximum cell temperatures (T_{cell}) on the cooling loop are estimated for each duct size. The maximum thermal dispersion among cells (ΔT_{module}) in the hydraulic loop is also calculated. The resultant data are shown in fig. 6.6, depicted for the three volumetric flow rates and every duct size combination.

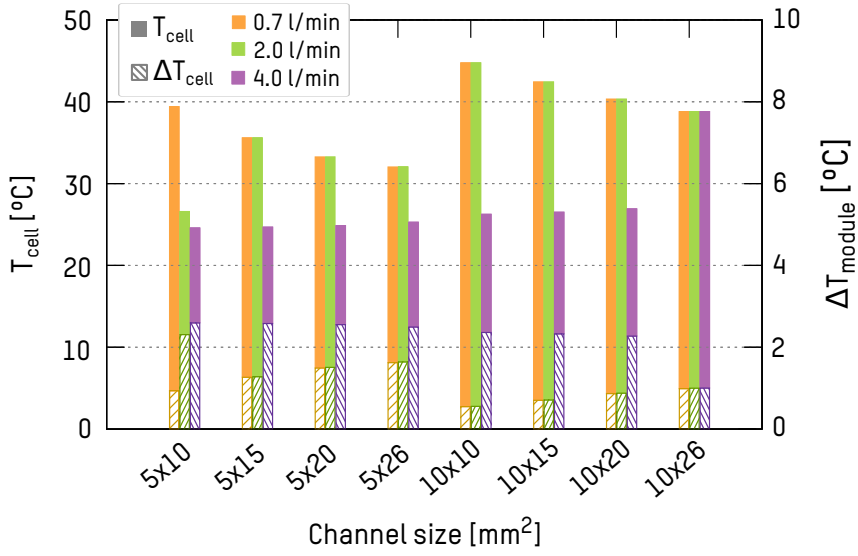

Figure 6.6: *Cell maximum temperatures (T_{cell}) and maximum thermal dispersion among cells (ΔT_{module}) on duct size optimisation analysis.*

The study results indicate that reducing the width of the duct leads to a decrease in temperature. Similarly, the temperature is also lower with

the narrowest height. A clear temperature-lowering tendency can be seen with the duct broadening due to the cell's tab and fluid contact area increase. Regarding the flow rates studied, 0.7 l/min and 2 l/min configurations present similar temperatures related to the laminar characteristic of the flow. However, changing to turbulent fluid flow on the 4 l/min volumetric flow rate entails temperature reduction for every duct size. Related to that turbulence effect, the narrowest configuration (5 mm x 10 mm) has achieved turbulent flow at 2 l/min flow rate as reflected on the temperature. Conversely, the largest duct involves flow becoming laminar, with the temperature increase even for the 4 l/min flow rate case. On the other hand, the ΔT_{module} is increased with narrower duct sizes or higher volumetric flows. This is a direct effect of the increased heat transfer capability under those both conditions. Nevertheless, this thermal dispersion among cells is always below 3 °C, a more than acceptable value.

These results are translated to the duct's thermal resistance point of view through convective heat transfer (h_{conv}) and cell's tab axial area (A_{axial}) relation, following the previously presented eq. (6.2). With the results in fig. 6.7, *Re* number is also displayed, being the green-coloured top zone correspondent to the laminar flow zone and the red area below, the turbulent zone.

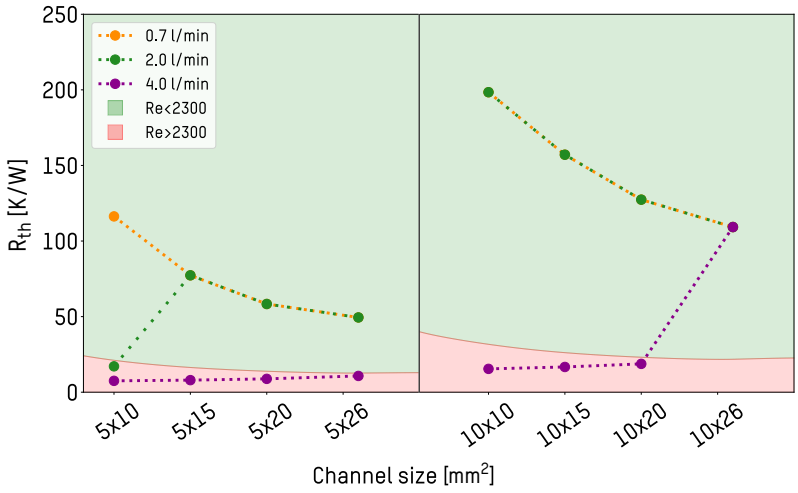

Figure 6.7: *Dielectric flow tab cooling TMS validation.*

The results indicate that at high flow rates, turbulent flow is observed,

resulting in a significant decrease in thermal resistance and improved heat transfer. However, when the volumetric flow rate is insufficient to enter the turbulent zone, the thermal resistance decreases as the duct width approaches the cell diameter size. In this regime, the correlations are mainly dependent on duct size and not flow speed. As a result, the two laminar flows studied (0.7 l/min and 2.0 l/min) exhibit minimal variation.

Based on the results obtained from the study, the duct size of 5 mm x 26 mm was chosen as the most suitable size to improve heat transfer. This duct size can be used with various hydraulic connections and flow rates. The duct should entirely cover the cell tab to enhance the area for heat transmission, and a 5 mm height improves the flow by increasing turbulence. The new design, called *Geom02*, can be seen in fig. 6.8. It can be easily updated from the initial Geom01 design through the usage of an extra piece designed for creating ducts over the cells' tabs, reinforcing the idea of prototype adaptability for many duct sizes and different fluid testing capability.

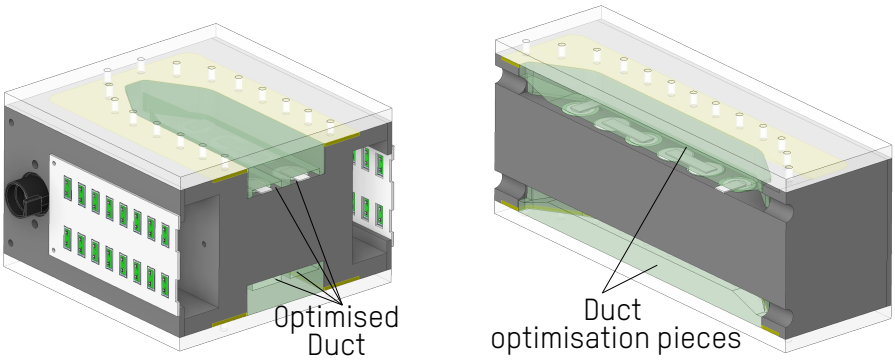

(a) *Widthwise view of Geom02 design.* ***(b)*** *Lengthwise view of Geom02 design.*

Figure 6.8: *Geom02 dielectric flow- and tab-based BTMS prototype's design.*

6.2 Experimental Analysis

The dielectric flow- and tab-based BTMS prototype concept and design is materialised on a functional prototype to perform the technology's experimental analysis. The internal construction of the prototype is shown in fig. 6.9, which depicts the busbar connection, internal thermocouple, and

voltage measurement wiring. As previously mentioned, all these connections are carried to the prototype's side. All the voltage reading wires are directly welded to the cells' tab. Moreover, the thermocouples are stuck to the tabs utilising high thermally conductive Kapton® film, covering up with epoxy adhesive for contact durability. The same epoxy adhesive also seals the wire holes and avoids fluid leakage.

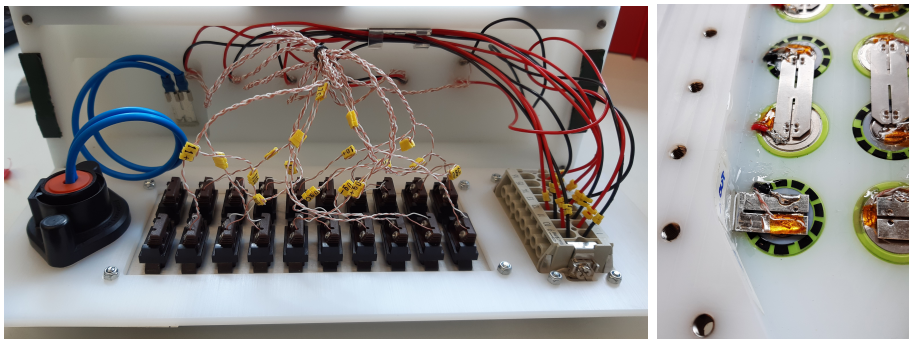

(a) *Wiring connections.* ***(b)*** *Busbar connections.*

Figure 6.9: *Busbar and wiring connections on Geom01 prototype.*

With the prototype in operation, an experimental setup is created to investigate the BTMS's thermal performance over the system's operational range.

The hydraulic circuit of the experimental setup is divided into two separate loops; the former, which serves as the primary loop, includes the prototype and has a separate pump for the dielectric fluid. Moreover, a flow meter and fluid thermocouples are added at the inlet and outlet of the prototype. The latter loop is thermally coupled to the former by a coil heat exchanger. The temperature of the dielectric fluid on the main loop is controlled by this latter loop using chilled water from a chiller. Figure 6.10a depicts the configuration's layout, whereas fig. 6.10b shows the prototype with all the correspondent connections.

According to the details provided in Section 6.1.1, the electrical profile utilised by the battery cycler during the testing is characterised by a cycle of 1.38C discharge and a 4C fast charge, with the SOC range continually oscillating between 10 % and 90 %. To allow for an accurate evaluation of the thermal jump from the initial to the final temperature, the aforementioned cycle is executed six times to ensure prototype temperature stabilisation.

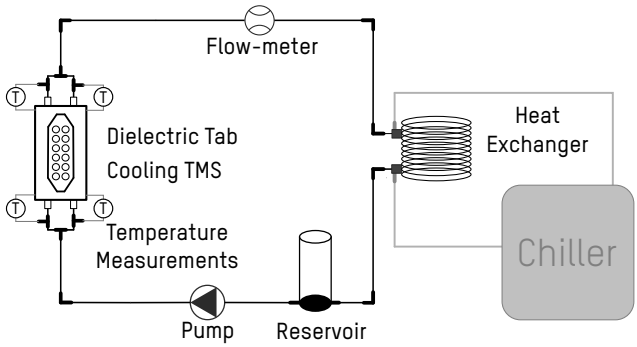

(a) *Experimental setup scheme.*

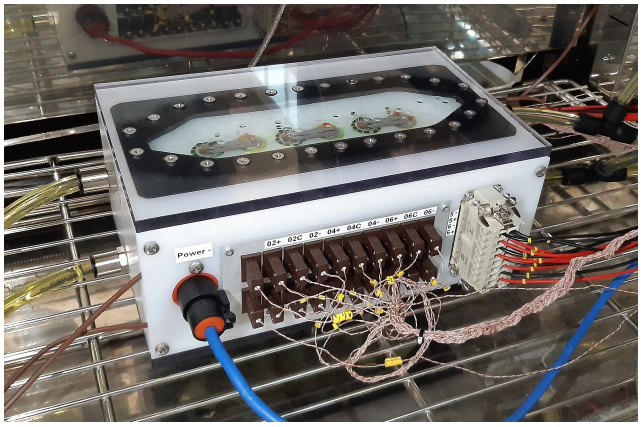

(b) *Dielectric prototype BTMS experimental testing.*

Figure 6.10: *Dielectric flow- and tab-based prototype experimental test setup.*

In addition, the ambient temperature is adjusted as the inlet temperature of the dielectric fluid by performing tests in the CTS thermal chamber.

The experimental test results have been segregated into two distinct blocks. The first block concerns the study of volumetric flow rate change, while the second half deals with modifying the fluid inlet temperature. Accordingly, three tests are carried out in the first block at an ambient temperature of 25 °C, with volumetric flow rates of 0.0 l/min (Test03), 0.7 l/min (Test04), and 3.2 l/min (Test05), with the latter representing the maximum attainable flow rate with the pump in use. Similarly, the study's second section comprises three additional experiments conducted at a flow rate of 0.7 l/min, with fluid input temperatures of 15 °C (Test01), 25 °C (Test04),

and 35 °C (Test06), respectively.

The temperature change of cells during the tests is studied. Figure 6.11a for flow change testing and fig. 6.12a for temperature change tests, respectively, indicate the average temperature during module cycling. In addition, the maximum and minimum cell temperatures for each test are delineated by a coloured band.

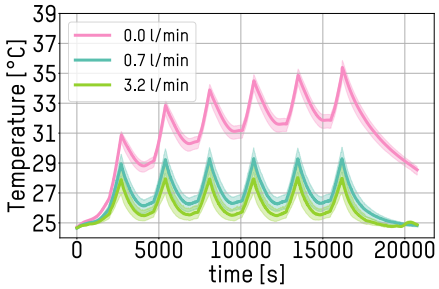

(a) *Volumetric flow rate change under experimental cycle.*

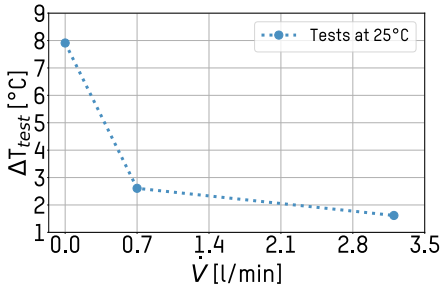

(b) *Tests' thermal jump (ΔT_{test}) from the initial temperature to the last cycle averaged temperature, under volumetric flow rate change.*

Figure 6.11: *Volumetric flow rate change results for 25 °C inlet temperature condition.*

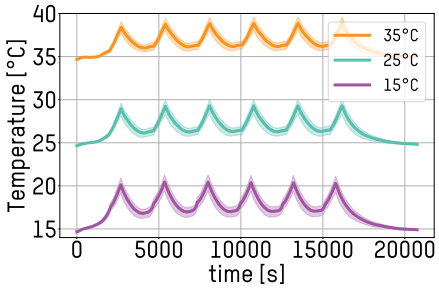

(a) *Fluid inlet temperature change under experimental cycle.*

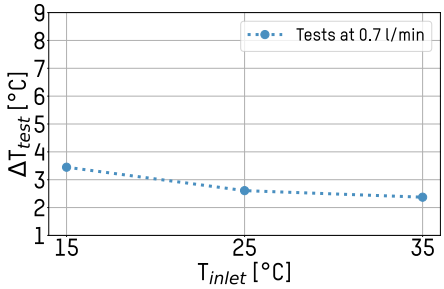

(b) *Tests' thermal jump (ΔT_{test}) from the initial temperature to the last cycle averaged temperature, under fluid inlet temperature change.*

Figure 6.12: *Fluid inlet temperature change results for 0.7 l/min volumetric flow rate condition.*

Figure 6.11b and fig. 6.12b, on the other hand, display the thermal jump for each test (ΔT_{test}). Once the module temperature between test cycles is stabilised, this number is computed by subtracting the beginning test temperature from the average temperature of the last cycle.

Due to the cells' relatively modest heat generation and the system's efficient cooling capacity, all tests demonstrated rapid stabilisation times. The scenario without fluid flow proves this in fig. 6.11a, where the increase in temperature after six electric cycles is 7.9 °C, more significant than the other tests, and even the temperatures are still rising (no stabilisation). The volumetric flow rate increases from 0.7 l/min (Test04) to 3.2 l/min (Test05) for the other two tests in fig. 6.11, decreasing the ΔT_{test} from 2.6 °C to 1.6 °C.

Regarding the outcomes of the intake temperature-changing experiments, fig. 6.12b shows that the ΔT_{test} decreases as the inlet temperature is raised. The primary cause of this phenomenon is the variation in cell heat generation over the temperature spectrum. Low temperatures significantly increase the cell's internal resistance, as depicted in fig. 6.3a. As a result, the heat generated due to the irreversible effect is more significant than at higher temperatures. The heat generation reduction results in a ΔT_{test} drop from 3.4 °C to 2.3 °C at the test scope between 15 °C (Test01) and 35 °C (Test06).

As shown in table 6.6 the temperature dispersion among cells on the module (ΔT_{module}) is also compared. The maximum ΔT_{module} is found to have a value of 2.7 °C at Test02 (15 °C and 2.0 l/min). A value of 2.7 °C on the same test shows a similar result for the maximum thermal gradient inside each cell (ΔT_{cell}).

Table 6.6: *Experimental results: Test ending temperature averaged on the last cycle ($T_{avg\ last-cycle}$), thermal jump of the test (ΔT_{test}), and maximum thermal dispersion among cells on the module (ΔT_{module}) and inside cells (ΔT_{cell}).*

Test	$T_{avg\ last-cycle}$ [°C]	ΔT_{test} [°C]	ΔT_{module} [°C]	ΔT_{cell} [°C]
Test01: 15 °C - 0.7 l/min	18.1	3.4	2.0	2.4
Test02: 15 °C - 2.0 l/min	17.0	2.5	2.7	2.7
Test03: 25 °C - 0.0 l/min	32.6	7.9	1.2	0.9
Test04: 25 °C - 0.7 l/min	27.2	2.6	1.8	2.0
Test05: 25 °C - 3.2 l/min	26.3	1.6	2.2	2.4
Test06: 35 °C - 0.7 l/min	37.1	2.4	1.6	1.6
Test07: 35 °C - 2.0 l/min	36.1	1.7	1.9	1.9

This effect is due to the combination of high cells' heat generation at low operating temperatures and the high flow rate, which results in elev-

ated heat dissipation difference from one cell to another. Regarding the lowest ΔT_{module} and ΔT_{cell}, 1.2 °C and 0.9 °C are identified respectively on the Test03 (0.0 l/min and 25 °C). It is worth mentioning that the thermal dispersion is kept below the advised 5 °C in every test.

These findings show that working at mid-to-high temperatures is desirable to lessen the heat production of the cells. Moreover, low volumetric flow rates are sufficient for effectively operating the dielectric flow and tab based BTMS prototype.

The results show lower temperatures than expected on the lumped thermal model due to its simplifications. The experimental results concord with the need for electromobility and LIB battery correct and secure performance. However, the duct size effect localised on the duct sizing optimisation needs further analysis and hypothesis verification. Therefore, a CFD analysis is conducted, validating the developed 3D model with the experimental results of the Geom01 and making a comparative analysis with the Geom02.

6.3 CFD Analysis

This section explains the models developed and their use for the consequent analysis. 3D CFD models are developed for both Geom01 and Geom02. The mesh independence study is developed for both models, and the former is validated against experimental data. Finally, both duct designs are compared under the same performance conditions.

6.3.1 Model Development and Validation

The prototype's constructional details are simplified to cut down on computation costs, but they nonetheless give a precise representation of the temperature distribution inside the module. The computational domain only contains half of the BM described in section 6.1 with a symmetry plane in the lengthwise direction. Hence, as shown in fig. 6.13, six cells with their corresponding busbars and half of the two top and bottom ducts for the dielectric flow are included.

The co-simulation model through a FMU is used for the cells' heat generation on the CFD (see methodology Section 3.2.3.2), even the

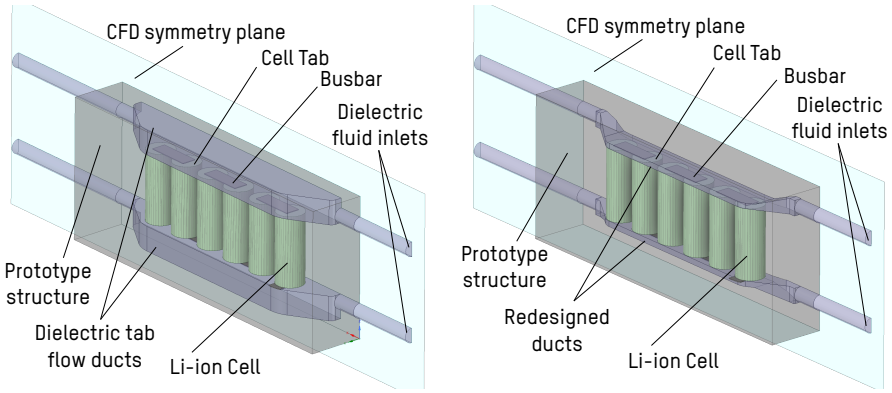

(a) *Geom01 for the CFD model of the BTMS.* ***(b)*** *Geom02 for the CFD model of the BTMS.*

Figure 6.13: *Geom01 and Geom02 designs adaption for CFD models.*

symmetry plane is applied. This is possible due to cells being connected in series, which allows the closing of the electrical circuit on the model. This model replaces the heat generation associated with the processes dependent on the internal geometry construction of the cell, hence representing the battery cells as homogeneous volumes. Nonetheless, cylindrical-orthotropic thermal conductivity is used, with the radial and axial thermal conductivity values, obtained from the hot disk transient plane source experimental technique [183]. Average specific heat capacity is also used, experimentally obtained following test methodology in Section 4.2.3. Those materials and their properties used on the models are defined in table 6.7.

Table 6.7: *Material and element properties used on the CFD model.*

	Material	Dimensions (x, y, z) [mm]	ρ [kg/m^3]	C_p [J/kg·K]	k [W/m·K]
Cell	-	∅=26, l=65	2318.1	1089.6	k_{axial}= 2.17, k_{radial}=0.434
Busbar	Steel	40 x 13 x 0.6	8030	502.5	16.27
Structure	PE1000	312.5 x 51.75 x 130.15	930	1800	0.4

A grid refinement study for the geometry, focusing on the fluid volume, is conducted to guarantee that the model outcomes are independent of the mesh used during the CFD analysis. GCI analysis, based on the Richardson Extrapolation [176] approach is the process used.

Three different meshes are produced, starting with the Geom01. The discretisation error is evaluated while comparing the outputs for the pressure drop Δp and the convective heat transfer coefficient h_{conv} on the dielectric fluid duct. Results for the coarse mesh (N_1: 1,099,821 elements), the medium mesh (N_2: 2,231,507 elements), and the fine mesh (N_3: 9,135,272 elements) can be found in fig. 6.14, with refinement factors of r_{21} = 1.26 and r_{32} =1.6. The three meshes are also depicted in fig. 6.15, showing the fluid on the duct inlet and the first cell.

Both GCI factors are nearly zero for the pressure drop results and heat transfer coefficient. The $e_{relative21}$ = 4.22 % and $e_{relative32}$ = 0.25 % for the pressure drop and $e_{relative21}$ = 2.62 % and $e_{relative32}$ = 0.82 % for the heat transfer coefficient, respectively, are the relative errors between the meshes. These results indicate a clear mesh refinement convergence tendency. Due to the concordance of mesh components and outcomes, the medium N_2 mesh is chosen.

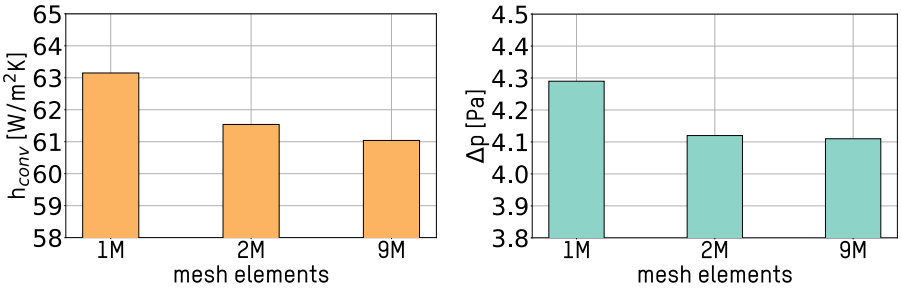

(a) *Convective heat transfer coefficient results.* ***(b)*** *Pressure drop results.*

Figure 6.14: *Geom01 grid refinement study results.*

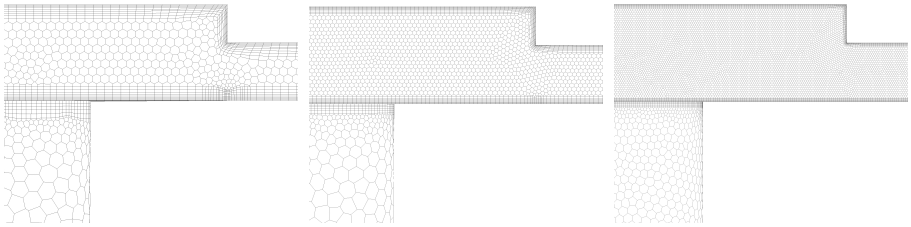

(a) *Mesh N_1.* ***(b)*** *Mesh N_2.* ***(c)*** *Mesh N_3.*

Figure 6.15: *Different mesh levels of the fluid in the inlet part of the duct for Geom01.*

With the duct updating in Geom02, GCI analysis is done again to confirm the results' independence from the geometry alteration.

The Δp and h_{conv} are assessed, and the results are shown in fig. 6.16, for the three meshes used in the study (N_1: 2,037,014; N_2: 4,114,147; N_3: 16,115,061), which have refinement factors of r_{21}=1.26 and r_{32}=1.57. The three meshes are also depicted in fig. 6.17, showing the fluid on the duct inlet and the first cell.

The GCI factor for heat transfer coefficient is nearly zero, whereas, for the pressure drop, low values of $GCI_{21\_\Delta p}$ = 0.46 % and $GCI_{32\_\Delta p}$ =0.17 % are achieved. The medium N_2 mesh is chosen for the following simulations based on the results of the convergence tendency analysis.

With the models arranged with adequate meshes, three of the experimental tests previously presented are selected to perform the dielectric flow- and tab-based BTMS validation process. The model's response to

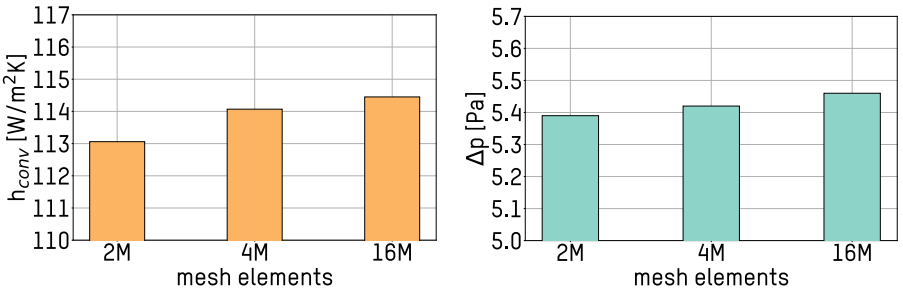

(a) *Convective heat transfer coefficient results.* ***(b)*** *Pressure drop results.*

Figure 6.16: *Geom02 grid refinement study results.*

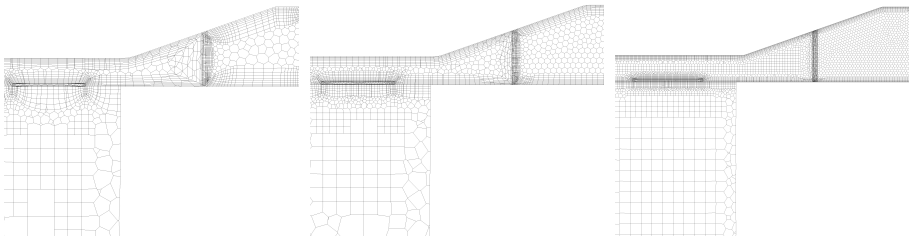

(a) *Mesh N_1.* ***(b)*** *Mesh N_2.* ***(c)*** *Mesh N_3.*

Figure 6.17: *Different mesh levels of the fluid in the inlet part of the duct for Geom02.*

temperature change is tested at 15 °C and 35 °C at 0.7 l/min, while the flow rate change effect is tested at 25 °C at 3.2 l/min. The six cycles used in the experimental testing are reproduced using the model to verify the overall thermal performance seen on the prototype.

In fig. 6.18, the experimental (continuous line) and numerical (discontinuous line) temperature evolutions show the validation results for the three analysed situations. The difference between the experimental and CFD temperature readings is displayed by the absolute error (e_{abs} [°C]), which is placed below them. Consequently, the maximum error is 1.92 °C, while the mean errors for the 15 °C, 25 °C, and 35 °C cases, respectively, are 0.88 °C, 0.39 °C, and 0.34 °C.

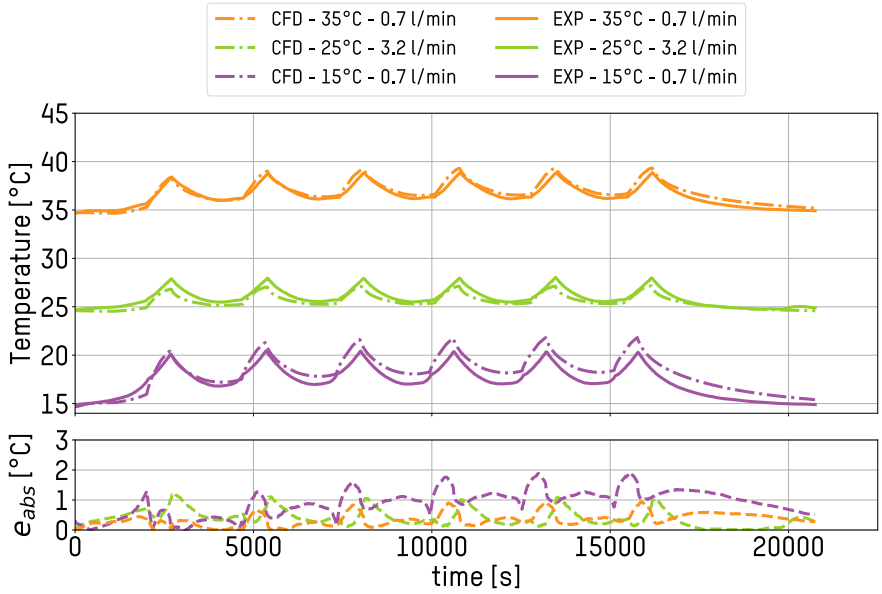

Figure 6.18: *CFD model validation of the dielectric BTMS.*

The results indicate that the dielectric BTMS model faithfully reproduces the phenomena of heat generation and transport on the examined cycles. It accurately depicts the physical effects of the charging and discharging procedures on the battery temperature. Furthermore, it correctly describes the various ΔT_{test} throughout the multiple test scenarios. As a result, the battery module and heat management system are correctly characterised, allowing the use of the CFD model in the subsequent re-

search.

6.3.2 Performance Comparison of Geom01 and Geom02

The validated model is used for Geom01 and Geom02 design's thermal performance comparison. Therefore, the turbulence effect and thermal performance improvement are considered.

Several cases are simulated using CFD. In that sense, experimental tests' charging and discharging conditions are maintained while the cycle number is decreased. As a result, each case simulates a single cycle composed of a 4C charge and a 1.38C discharge.

This analysis studies four cases with quite similar conditions to the experimental ones. Three employed 0.7 l/min volumetric flow rates at 15 °C, 25 °C, and 35 °C, named Case-A, Case-B and Case-C, respectively. Furthermore, Case-D at 4.0 l/min and 25 °C is used to examine the impact of increasing the flow rate. Both geometries are evaluated from the thermal and hydraulic points of view using the resulting data. Figure 6.19 depicts the evolution of cell temperature for the Geom01 and Geom02 samples. Table 6.8 also displays various simulation findings.

Table 6.8: *BTMS geometry optimisation analysis results: maximum cycle temperature (T_{max}), maximum thermal dispersion among cells on the module (ΔT_{module}) and inside cells (ΔT_{cell}), pressure drop (Δp), hydraulic power (P_{hyd}) and hydraulic energy consumption (E_{hyd}).*

Case	T_{max} [°C]		ΔT_{module} [°C]		ΔT_{cell} [°C]		Δp [Pa]		P_{hyd} [W]		E_{hyd} [Wh]	
	Geom		*Geom*		*Geom*		*Geom*		*Geom*		*Geom*	
	01	*02*	*01*	*02*	*01*	*02*	*01*	*02*	*01*	*02*	*01*	*02*
Case-A: 15 °C - 0.7 l/min	20.1	18.8	2.0	1.7	2.7	3.7	8.3	11.0	$9.7e^{-5}$	$12.8e^{-5}$	$5.9e^{-5}$	$7.8e^{-5}$
Case-B: 25 °C - 0.7 l/min	29.0	27.9	1.5	1.3	2.0	2.8	7.8	10.1	$9.1e^{-5}$	$11.8e^{-5}$	$5.6e^{-5}$	$7.2e^{-5}$
Case-C: 35 °C - 0.7 l/min	38.4	37.5	1.3	1.1	1.8	2.4	7.4	9.4	$8.7e^{-5}$	$11.0e^{-5}$	$5.3e^{-5}$	$6.7e^{-5}$
Case-D: 25 °C - 4.0 l/min	26.9	26.2	0.4	0.4	3.2	3.6	163.5	147.8	$10.9e^{-3}$	$9.9e^{-3}$	$6.6e^{-3}$	$6.0e^{-3}$

The maximum temperature of the cycle (T_{max}) and the maximum thermal gradient among cells in the battery module (ΔT_{module}) can be seen, followed by the maximum thermal gradient inside the cells (ΔT_{cell}). Also, the fluid pressure drop (Δp [Pa]) on the duct is used to estimate

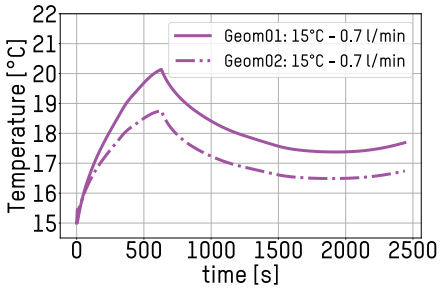

(a) *Temperature evolution at Case-A, 15 °C and 0.7 l/min test.*

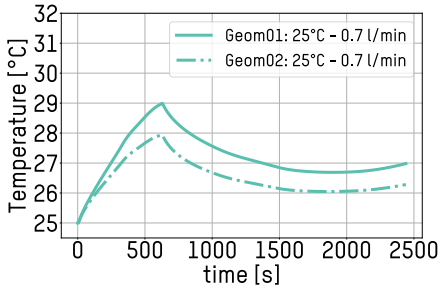

(b) *Temperature evolution at Case-B, 25 °C and 0.7 l/min test.*

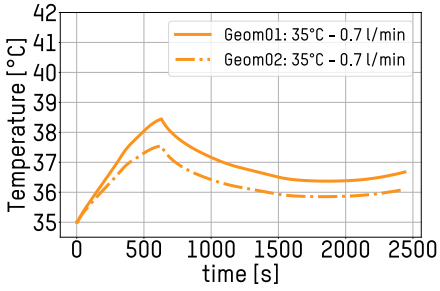

(c) *Temperature evolution at Case-C, 35 °C and 0.7 l/min test.*

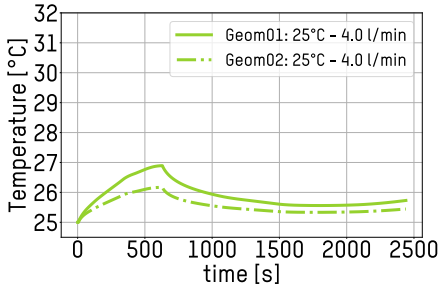

(d) *Temperature evolution at Case-D, 25 °C and 4.0 l/min test.*

Figure 6.19: *Temperature evolution for Geom01 and Geom02 on the duct size optimisation analysis results.*

auxiliary consumption and determine the resulting energy consumption for pumping dielectric fluid (E_{hyd} [Wh]). This is assessed using eq. (5.3) as previously done, which interpolates the power consumption based on the relationship between the pressure drop and volumetric flow rate over the cycle time span (t_0 - t).

With the implementation of Geom02, the temperature experienced throughout the cycle has been consistently lower for each case examined, thereby reducing the highest temperature from 1.4 °C to 0.7 °C. Furthermore, the temperature associated with the highest ΔT_{module} case has been reduced from 2 °C to 1.7 °C. In comparison, the temperature associated with the highest ΔT_{cell} case has increased from 2.7 °C to 3.7 °C. This can be directly attributed to the higher heat transmission capacity of the modified duct geometry. The findings from the four examples analysed align with the experimental results documented in

Section 6.2; specifically, at higher temperatures, there is a decrease in thermal jump (ΔT_{test}), much like with high volumetric flows.

As a result of the reduction in duct size and consequent increase in fluid velocity, there is a notable increase in pressure loss of up to 2.7 Pa in Geom02. Nevertheless, Case-D shows a different behaviour, as Geom02 has a lower pressure drop than Geom01. This phenomenon can be understood by seeing that the pressure loss curves for flow rate in each geometry cross each other from 2.2 l/min onwards, as seen in fig. 6.20. This means that the increase in pressure loss concerning flow rate in Geom02 is slower than in Geom01. Therefore, Geom02 has an advantage over Geom01 when using higher flow rates.

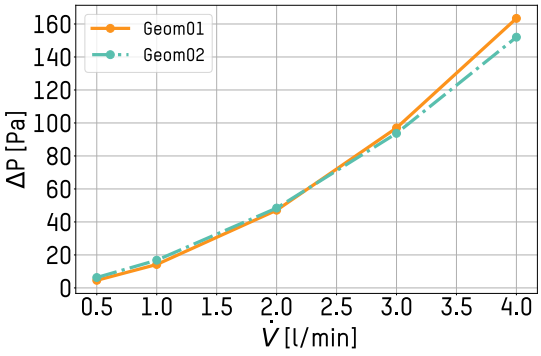

Figure 6.20: *Pressure loss evolution over flow rate for Geom01 and Geom02.*

However, the pressure drop results observed in the dielectric BTMS prototype are low, primarily because of the fluid's low viscosity. This unique fluid characteristic necessitates relatively low pumping energy than the energy consumed by the battery module.

Regarding the duct shape changes, its volume is decreased by 79.8 %, which is particularly significant for the system's energy density reduction compared to more traditional BTMS.

Finally, it should be noted that if the dielectric BTMS's cycle is operated repeatedly, it is necessary to lower the fluid inlet temperature. This would enable safe repetition of the fast charge by bringing the cycle-ending temperature down to at least the initial point temperature.

6.4 Conclusions

This chapter successfully validated the Dielectric Flow- and Tab-based BTMS technology by developing a functional prototype and experimental validation. The design process was effectively carried out, including the analysis of dielectric fluid selection and duct size optimisation. The experimentally validated CFD model compared different duct geometries during the simulation stage.

The developed prototype is a reliable testing platform for evaluating various duct shapes, sizes, and dielectric fluids. The initial design could be easily adapted to accommodate different duct geometries, as demonstrated with the Geom02 duct shape, as shown in fig. 6.8, which can be experimentally validated.

This validation platform is crucial for conducting tests with different ducts and fluids, as the fluid selection analysis revealed significant differences in behaviour among fluids. The selected Novec7200 fluid, with its extremely low viscosity, allowed for exploring very narrow duct sizes. However, it was observed during testing that the Novec7200 fluid experienced challenges with evaporation, particularly at the tested temperatures of 35 °C. Two main factors were identified as the primary causes: insufficient watertight joints and the fluid permeating through certain plastic materials.

Further analysis and testing with alternative fluids are necessary to address these issues. The comparison of different fluids through simulation and experimental testing is essential, considering the unique characteristics and challenges associated with each fluid.

7

Conclusions and Future Lines

Summary

This concluding chapter presents the key findings of the PhD Thesis and provides a comprehensive review of the research objectives and hypotheses. Moreover, future research lines and key contributions are also underlined.

7.1 Conclusions

This PhD Thesis addressed the battery thermal management system improvement investigation for the electromobility application. Focused on the thermal needs of energy-denser battery packs with fast charge requirements, the research objectives were centred on the development of an innovative BTMS that would be capable of improving the performance of electric vehicles by maintaining the temperature of the battery cells within a safe operating range. The proposed research offers essential insights into the development of advanced BTMS to enhance the performance of electric vehicles and expand their viability as a sustainable transportation option.

The work posed a hypothesis, which ensures the possibility of **implementing a methodology to enhance the selection and development of an optimal advanced battery thermal management system for high-performance electromobility applications**. This hypothesis has been corroborated with the process depicted in this document. Cell selection was performed with an improved methodology focusing on the cells' thermal behaviour. Moreover, the research explored various thermal management solutions to develop an advanced BTMS. Dielectric flow and tab cooling technologies denote noteworthy performance characteristics among these solutions after being compared under high-performance conditions against a Cold plate BTMS and a Coldp Plate- and PCM-based BTMS, showing significant improvement potential on the root performance indicators such as auxiliary energy consumption, specific energy and energy density, safety and reliability and overall vehicle range and efficiency. Consequently, a functional prototype was developed to study these technologies further and evaluate their suitability in advanced BTMS designs. The knowledge acquired from this prototype provides valuable design criteria for optimising and developing the novel dielectric flow- and tab-based solution.

Therefore, the procedure carried out in this work has accomplished the main objective proposed; **A novel and advanced battery thermal management system for electromobility application was successfully developed**. Moreover, the secondary objectives were also satisfactorily fulfilled:

- The effectiveness of the proposed thermal management system in

accommodating diverse battery pack designs and cell geometries was evaluated by integrating the solution into two battery modules, each featuring distinct cylindrical and prismatic cell geometries, respectively. The results demonstrate the system's robustness and versatility in maintaining appropriate temperature levels for different battery configurations.

- A functional prototype was developed and tested on a cylindrical cell battery module to study the proposed thermal management solution. In addition, a CFD model was created and validated using the experimental data, enabling further investigation into the system's performance.

- To evaluate the performance of the advanced BTMS, a high-performance electric cycle was employed, featuring a 6C fast charge and a 130 km/h motorway discharge equivalent to 1.67C. The results demonstrate the system's capability to maintain the battery's temperature within the optimal range, enhancing its durability and efficiency during high-demanding applications.

- The advanced dielectric system's improvement over standard solutions was numerically compared and assessed. Two reference systems were incorporated into that process: a standard Cold Plate BTMS and a Hybrid BTMS.

Some key conclusions of the proposed advanced dielectric flow- and tab-based BTMS can be obtained from the thesis objective fulfilment. The first one refers to the results evaluation of the proposed advanced thermal management system. In contrast, the following three main conclusions answer the technology selection supporting ideas generated after the state of the art analysis. The fifth conclusion relates the studied fluid drawbacks and difficulties that came crossed in this work:

1. **Advanced dielectric flow- and tab-based BTMS's** comparison analysis results over the cold plate, and the hybrid reference systems showed that the proposed dielectric system has a compelling performance as a promising advanced thermal management solution. It outperforms the key performance metrics for a high-performance BEV, is extremely adaptable to various battery module designs, and possesses important safety and reliability qualities.

Additionally, compared to the cold plate standard solution, it delivers comparable thermal performance, keeping the battery cells within the ideal performance temperature range even throughout the most difficult tested electric cycle. The expense of the dielectric fluid is the unique and significant downside. However, the Dielectric BTMS is the best option in particular situations when superior BEV efficiency or decreased weight are desired, and the cost is not a limiting factor.

2. **Dielectric flow concept**, enhances the efficiency of battery thermal management by allowing direct contact of the coolant fluid with the battery cells, eliminating the need for intermediary elements such as cold plates and thermal interface materials. This innovation improves heat transfer efficiency and results in a high-performance BTMS that surpasses the performance of standard or more traditional systems.

3. **Tab-based thermal management concept** is an efficient solution for high-performance thermal management, even if the heat transfer area is limited, as the usage of the cell's high thermal conductivity path is enhanced. This innovative approach can effectively regulate the temperature of the battery cells and afford high-performance thermal management.

4. **Combination of Dielectric Flow and Tab-Based thermal management** represents an advanced and robust solution for battery thermal management in high-demanding applications. This approach gathers the outcomes of both previous hypotheses and results in a highly efficient battery thermal management system that can effectively regulate the temperature of high-performance electric cycles. Moreover, the system offers a reduced specific energy and energy density, enhancing BEV features and performance. The combined use of dielectric flow and tab-based thermal management is a promising direction for future research in battery thermal management.

5. **The dielectric fluid** in this study exhibited a high evaporating rate during experimental tests due to its boiling point temperature of 76 °C, highlighting the importance of a hermetic thermal management system design. Additionally, the high cost of the fluid is a critical

aspect that may limit the standardisation of the proposed advanced system. Therefore, alternative fluid selection may be of interest to overcome these drawbacks. However, the lack of suitable low-viscosity fluids identified during the search process may limit the results presented in this study if used in the proposed BTMS.

As a general conclusion, this PhD thesis proposes an important alternative to existing thermal management systems through an advanced dielectric flow- and tab-based BTMS. The proposed system exhibits high-performance standards for high-demanding electromobility applications, making it a promising solution for enhancing the features of electric vehicles and contributing to the development of more sustainable road transport. The results of this study underscore the significance of battery thermal management as a critical aspect of electric vehicle design and pave the way for further research in this field.

7.2 Future Research Lines

The development of the PhD Thesis unveiled some possible future research lines to deepen the study of the proposed advanced dielectric flow- and tab-based battery thermal management system.

- Furthermore, integrating the proposed BTMS with other vehicle systems, such as the battery management system, powertrain, and climate control, should be considered. A holistic approach to vehicle thermal management can lead to better overall vehicle performance and increased range.
- An interesting research line not covered in this work is the degradation analysis of the proposed system. Further research on the quantification of degradation compared to a standard system would provide valuable insights into the long-term performance and durability of the advanced dielectric flow- and tab-based BTMS. Additionally, investigating the potential effect of tab cooling and different dielectric designs (fully or partially immersed) on degradation would be of interest.
- As previously mentioned, the employed dielectric fluid has some drawbacks, including a high evaporation rate and high cost. Future

research should focus on analysing other dielectric fluids under the proposed design or exploring the design requirements for other more viscous dielectric fluids that could be used in the system. The potential impact of different fluids on the overall system's performance should be evaluated, including their effects on heat transfer efficiency, durability, and cost.

- To further advance the proposed BTMS, an implementation of an active control strategy is necessary. This would involve the development of control algorithms and integration with the vehicle's overall control system. The electric profile used in this work was designed to meet high-performance needs, but it may not represent a realistic driving cycle. Therefore, the active control strategy should aim to optimise the auxiliary energy consumption by adapting the BTMS operation to the actual driving conditions. This will help further to improve the system's performance and energy efficiency.

7.3 Scientific Contributions, Publications and Dissemination Activities

Within the presented research work, several scientific publications and contributions were made. The list of these publications is provided below for reference:

EUROPEAN PATENT REQUEST

1. Eneko Gonzalez-Aguirre, Jon Gastelurrutia Roteta and Nerea Nieto Aguirrezabala. "Electric vehicle battery temperature regulation system". 2023.

INTERNATIONAL JOURNAL ARTICLES

1. Eneko Gonzalez-Aguirre, Jon Gastelurrutia, Mahesh Suresh Patil, Luis del Portillo-Valdes. "Avoiding Thermal Issues During Fast Charging Starting with Proper Cell Selection Criteria". In: Journal of The Electrochemical Society 168.11 (Nov. 2021), p. 110523. issn: 1945-7111. doi: 10.1149/1945-7111/ac3348.

2. Eneko Gonzalez-Agirre, Hamidreza Behi, Jon Gastelurrutia, Luis del Portillo-Valdés, Theodoros Kalogiannis, Maitane Berecibar.

"Implementation of Battery Thermal Management System for High-Performance Electromobility Application: A Hybrid Cold Plate and Phase Change Material Approach". In: IEEE Transactions on Vehicular Technology (2023), pp. 1–12. issn: 0018-9545. doi: 10.1109/TVT.2023.3305505.

3. Eneko Gonzalez-Agirre, Jon Gastelurrutia, Laura Oca, Luis del Portillo-Valdés, Leire Erbiti Goienetxe. "Dielectric Flow- and Tab-Based Battery Thermal Management System For EV High Performance Application". In: Journal of Energy Storage. ***Under Review***

INTERNATIONAL CONFERENCE ARTICLES

1. Eneko Gonzalez-Aguirre, Iñigo Aranburu, Jon Gastelurrutia, Luis Diaz, Mahesh Suresh Patil, Luis del Portillo-Valdes. "1D Dynamic Thermal Model Development for a Battery Hybrid Thermal Management System". In: 2021 IEEE Vehicle Power and Propulsion Conference (VPPC). IEEE, Oct. 2022, pp. 1–6. isbn: 978-1-6654-0528-7. doi: 10.1109/vppc53923.2021.9699281.

PRESENTATIONS AND POSTERS

1. Eneko Gonzalez-Aguirre, Leire Erbiti Goienetxe, Jon Gastelurrutia Roteta, Luis del Portillo-Valdes. "Design Optimisation of Advanced Dielectric Battery Thermal Management System". In: 5th International Forum on Progress and Trends in Battery and Capacitor Technologies - Power our Future 2022. 5th - 8th July 2022.

A

Appendix:

Heat Generation Models

A.1 UDF Lumped Heat Generation Script

The entropic heat coefficient and the internal resistance are defined as an array. As can be seen in the following code, the entropic heat generation coefficient is defined as "Coeftxt", whereas the internal resistance as "Data".

```
#include "udf.h"
#include <stdio.h>

#define n_CELL 50
#define n_DATA 100000

real ID[n_CELL]={0};
real HEAT[n_CELL]={0};
int ID_i;
int ID_size;
int ID_value;

real CURR[n_DATA][2]={{0}};
int CURR_i, CURR_j;
int CURR_size_i, CURR_size_j;
float CURR_value;
```

```
real SOC[n_DATA][2]={{0}};
int SOC_i, SOC_j;
int SOC_size_i, SOC_size_j;
float SOC_value;

float Coeftxt[13][2]={
{10.0000,-0.04025},{20.0000,-0.0377},
{30.0000,-0.02770},{40.0000,-0.0135},
{50.0000,-0.00958},{55.0000,-0.0128},
{60.0000,-0.09700},{65.0000,-0.4600},
{70.0000,-0.32800},{75.0000,-0.1166},
{80.0000,-0.06260},{85.0000,-0.03599},
{90.0000, 0.03270}
};
int size_j=13;

float DATA[4][9]={
{1.71,1.69,1.70,1.75,1.71,1.69,1.73,1.90,2.69},
{1.39,1.37,1.36,1.41,1.39,1.36,1.37,1.46,1.77},
{1.21,1.18,1.15,1.21,1.19,1.14,1.15,1.23,1.44},
{1.08,1.05,1.02,1.08,1.06,1.01,1.02,1.09,1.31}
};

float SOCrow[9]={10,20,30,40,50,60,70,80,90};
real Tcolumn[4]={10,20,30,40};
int size_m=4;
int size_n=9;

DEFINE_ADJUST(ID_input,d)
{
        #if !RP_NODE
                FILE *ID_file;
        #endif
        #if !RP_NODE
                ID_file= fopen("ID.txt","r");
                fscanf(ID_file,"%d\n",&ID_size);

                for (ID_i=0; ID_i<ID_size; ID_i++)
                {
                        fscanf(ID_file,"%d\n",&ID_value);

                        ID[ID_i]=ID_value;
                }
                fclose(ID_file);
        #endif
        host_to_node_int_1(ID_size);
        host_to_node_real(ID,n_CELL);
}

DEFINE_ADJUST(input_corriente,d)
{
        #if !RP_NODE
                FILE *CURR_file;
```

```
        #endif
        #if !RP_NODE
                CURR_file= fopen("CURR.txt","r");
                fscanf(CURR_file,"%d\n",&CURR_size_i);

                fscanf(CURR_file,"%d\n",&CURR_size_j);

                for (CURR_i=0; CURR_i<CURR_size_i; CURR_i++)
                {
                        for (CURR_j=0; CURR_j<CURR_size_j; CURR_j++)
                        {
                        fscanf(CURR_file,"%f",&CURR_value);
                        CURR[CURR_i][CURR_j]=CURR_value;
                        }
                }
                fclose(CURR_file);
        #endif
        host_to_node_int_2(CURR_size_i,CURR_size_j);
        host_to_node_real(CURR,(2*n_DATA));
}

DEFINE_ADJUST(input_soc,d)
{
        #if !RP_NODE
                FILE *SOC_file;
        #endif
        #if !RP_NODE
                SOC_file= fopen("SOC.txt","r");
                fscanf(SOC_file,"%d\n",&SOC_size_i);

                fscanf(SOC_file,"%d\n",&SOC_size_j);

                for (SOC_i=0; SOC_i<SOC_size_i; SOC_i++)
                {
                        for (SOC_j=0; SOC_j<SOC_size_j; SOC_j++)
                        {
                        fscanf(SOC_file,"%f",&SOC_value);
                        SOC[SOC_i][SOC_j]=SOC_value;
                        }
                }
                fclose(SOC_file);
        #endif
        host_to_node_int_2(SOC_size_i,SOC_size_j);
        host_to_node_real(SOC,(2*n_DATA));
}

DEFINE_SOURCE(Toshiba_01,c,k,dS,eqn)
{
#if !RP_HOST

        real source1;

                source1 = HEAT[0];
                dS[eqn]=0.0;
```

```
        return sourcel;

#endif
}

DEFINE_SOURCE(Toshiba_02,c,k,dS,eqn)
{
#if !RP_HOST

        real source2;

                source2 = HEAT[1];
                dS[eqn]=0.0;

        return source2;

#endif
}

DEFINE_SOURCE(Toshiba_XX,c,k,dS,eqn)
{
#if !RP_HOST

        real sourceXX;

                sourceXX = HEAT[2];
                dS[eqn]=0.0;

        return sourceXX;

#endif
}

DEFINE_EXECUTE_AT_END(execute_at_end)
{

#if !RP_NODE
    FILE *fp;
#endif

real t;
real CURR_t=0.0;
real SOC_t=0.0;

int CELL_i;
real VOL[n_CELL]={0};
real TEMP_SUM[n_CELL]={0};
real TEMP_AV[n_CELL]={0};
real DUDT[n_CELL]={0};
real RIN[n_CELL]={0};
real QGEN[n_CELL]={0};

for (CELL_i=0; CELL_i<(ID_size); CELL_i++)
```

```
{
    Domain *domain=Get_Domain(1);
    Thread *k=Lookup_Thread(domain,ID[CELL_i]);
    cell_t c;

    int CURR_k;
    int SOC_k;
    real TIME_min=0.0;
    real TIME_max=0.0;
    real CURR_min=0.0;
    real CURR_max=0.0;
    real SOC_min=0.0;
    real SOC_max=0.0;
    real Rin_Tmin_SOCmin=0.0;
    real Rin_Tmin_SOCmax=0.0;
    real Rin_Tmax_SOCmin=0.0;
    real Rin_Tmax_SOCmax=0.0;
    real Rin_T_SOCmin=0.0;
    real Rin_T_SOCmax=0.0;

    int l;
    int yl;
    int xl;
    real SOCmin=0.0;
    real SOCmax=0.0;
    real dUdTmin=0.0;
    real dUdTmax=0.0;
    real Tmin=0.0;
    real Tmax=0.0;

    #if !RP_NODE
        t=CURRENT_TIME;
    #endif
    host_to_node_real_1(t);

    if (t <= CURR[(CURR_size_i - 1)][0])
    {
        if (t <= CURR[0][0])
        {
            CURR_k = 0;
        }
        else
        {
            CURR_k = 1;
            while ((CURR_k < (CURR_size_i - 1))
            & (t >= CURR[CURR_k][0]))
            {
                CURR_k++;
            }
            CURR_k = (CURR_k - 1);
        }
        TIME_min = CURR[CURR_k][0];
        TIME_max = CURR[(CURR_k+1)][0];
        CURR_min = CURR[CURR_k][1];
```

```
        CURR_max = CURR[(CURR_k+1)][1];
        CURR_t = (CURR_min+(CURR_max-CURR_min)*
        (t-TIME_min)/(TIME_max-TIME_min));
    }
    else
    {
        TIME_min = 0.0;
        TIME_max = 0.0;
        CURR_min = 0.0;
        CURR_max = 0.0;
        CURR_t = 0.0;
    }

    if (t <= SOC[(SOC_size_i - 1)][0])
    {
        if (t <= SOC[0][0])
        {
            SOC_k = 0;
        }
        else
        {
            SOC_k = 1;
            while ((SOC_k < (SOC_size_i - 1)) &
            (t >= SOC[SOC_k][0]))
            {
                SOC_k++;
            }
            SOC_k = (SOC_k - 1);
        }
        TIME_min = SOC[SOC_k][0];
        TIME_max = SOC[(SOC_k+1)][0];
        SOC_min = SOC[SOC_k][1];
        SOC_max = SOC[(SOC_k+1)][1];
        SOC_t = (SOC_min+(SOC_max-SOC_min)*
        (t-TIME_min)/(TIME_max-TIME_min));
    }
    else
    {
        SOC_k = (SOC_size_i - 1);
        TIME_min = 0.0;
        TIME_max = 0.0;
        SOC_min = 0.0;
        SOC_max = 0.0;
        SOC_t = SOC[SOC_k][1];
    }

    #if !RP_HOST

        begin_c_loop_int(c,k)
        {
            VOL[CELL_i] += C_VOLUME(c,k);
            TEMP_SUM[CELL_i] +=C_T(c,k)*C_VOLUME(c,k);
        }
        end_c_loop_int(c,k)
```

```
VOL[CELL_i] = PRF_GRSUM1(VOL[CELL_i]);
TEMP_SUM[CELL_i] = PRF_GRSUM1(TEMP_SUM[CELL_i]);

TEMP_AV[CELL_i] = (TEMP_SUM[CELL_i]/VOL[CELL_i]);

if (SOC_t <= Coeftxt[0][0])
{
    l = 0;
}
else
{
    l = 1;
    while ((l < (size_j-1)) & (SOC_t >= Coeftxt[l][0]))
    {
        l++;
    }
    l=l-1;
}
SOCmin=Coeftxt[l][0];
SOCmax=Coeftxt[l+1][0];
dUdTmin=Coeftxt[l][1];
dUdTmax=Coeftxt[l+1][1];

DUDT[CELL_i]=dUdTmin+(dUdTmax-dUdTmin)*
(SOC_t-SOCmin)/(SOCmax-SOCmin);

if (SOC_t <= SOCrow[0])
{
    yl = 0;
}
else
{
    yl = 1;
    while ((yl < (size_n-1)) & (SOC_t >= SOCrow[yl]))
    {
        yl++;
    }
    yl = yl-1;
}

SOCmin=SOCrow[yl];
SOCmax=SOCrow[yl+1];

if ((TEMP_AV[CELL_i]-273) <= Tcolumn[0])
{
    xl = 0;
}
else
{
    xl = 1;
    while ((xl < (size_m-1)) &
    ((TEMP_AV[CELL_i]-273) >= Tcolumn[xl]))
    {
```

```
                xl++;
            }
            xl = xl-1;
        }

        Tmin=Tcolumn[xl];
        Tmax=Tcolumn[xl+1];

        Rin_Tmin_SOCmin=DATA[xl][yl];
        Rin_Tmin_SOCmax=DATA[xl][yl+1];
        Rin_Tmax_SOCmin=DATA[xl+1][yl];
        Rin_Tmax_SOCmax=DATA[xl+1][yl+1];

        Rin_T_SOCmin=(Rin_Tmin_SOCmin-Rin_Tmax_SOCmin)*
        ((TEMP_AV[CELL_i]-273)-Tmax)/(Tmin-Tmax)+Rin_Tmax_SOCmin;

        Rin_T_SOCmax=(Rin_Tmin_SOCmax-Rin_Tmax_SOCmax)*
        ((TEMP_AV[CELL_i]-273)-Tmax)/(Tmin-Tmax)+Rin_Tmax_SOCmax;

        RIN[CELL_i]=(Rin_T_SOCmin-Rin_T_SOCmax)*
        (SOC_t-SOCmax)/(SOCmin-SOCmax)+Rin_T_SOCmax;

        QGEN[CELL_i] = (pow(CURR_t,2))*RIN[CELL_i]/1000+CURR_t*
        TEMP_AV[CELL_i]*DUDT[CELL_i]/1000;

        HEAT[CELL_i]=(QGEN[CELL_i])/VOL[CELL_i];
    #endif

    node_to_host_int_1(CELL_i);
    node_to_host_real_3(t, CURR_t, SOC_t);
    node_to_host_real_6(VOL[CELL_i], TEMP_AV[CELL_i],
    DUDT[CELL_i], RIN[CELL_i], QGEN[CELL_i], HEAT[CELL_i]);

    #if !RP_NODE
        Message("Cell = %d\n",(CELL_i+1));
        Message("Generation = %f\n", QGEN[CELL_i]);
        fp = fopen("GEN.txt", "a");
        fprintf(fp,"%d %f %f %f %f %f %f %f %f %f\n",
        (CELL_i+1), t, CURR_t, SOC_t, VOL[CELL_i], TEMP_AV[CELL_i],
        DUDT[CELL_i], RIN[CELL_i], QGEN[CELL_i], HEAT[CELL_i]);

        fclose(fp);
    #endif

        }
    node_to_host_real(HEAT,n_CELL);

        #if !RP_NODE
                Message("Current = %f\n",CURR_t);
                Message("SOC = %f\n",SOC_t);
        #endif
}
```

B

Appendix:

Dielectric BTMS Lumped Thermal Model

B.1 Lumped Thermal Model for Fluid Selection

The lumped thermal model used on fluid selection analysis follows the scheme in fig. B.1.

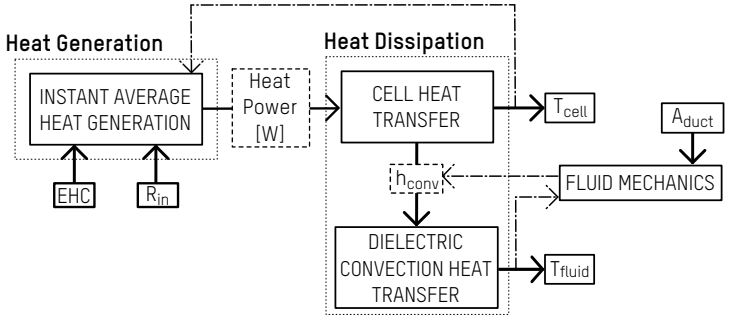

Figure B.1: *Dielectric prototype's lumped thermal model scheme.*

Moreover, the system's energy balance follows eq. (B.1).

$$M \cdot C_p \cdot \frac{\Delta T}{\Delta t} = \dot{Q}_{gen} - \dot{Q}_{diss} \tag{B.1}$$

where the left term represents the heat stored on the cell, $\dot{Q}_{gen}$ [W] is the cell's generated heat, and $\dot{Q}_{diss}$ [W] is the heat dissipated from the cell to the fluid by convection.

The energy balance is applied in the stationary situation, where the temperatures are stabilised, and the heat accumulation on cells is zero, dissipating all the heat generated on the cells to the fluid.

For the model calculation in the stationary situation suggested, the processes are related in the following way: the heat generated by the cell propagates through the cell by conduction ($\dot{Q}_{gen} = \dot{Q}_{cond}$); this heat is, in turn, transferred to the fluid by convection ($\dot{Q}_{cond} = \dot{Q}_{conv}$). Finally, it is dissipated, depending on the heat capacity of the fluid ($\dot{Q}_{conv} = \dot{Q}_{sto_{fluid}}$). With these relations, cells' core and surface temperatures and the fluid's temperature after each cell is calculated.

The following equations and correlations of heat transfer and fluid mechanics are obtained from Incropera et al. [184]. Thus, the heat flux transferred through the cell is expressed by the conduction as follows in eq. (B.2),

$$\dot{Q}_{cond_a} = k_{axial} \cdot A_{axial} \cdot \frac{(T_0 - T_{sa})}{L_a} \tag{B.2}$$

where k_{axial} [W/m °C] is the axial conductivity of the cell, A_{axial} [m^2] the axial surface, T_0 [°C] the temperature at the centre of the cell, T_{sa} [°C] the temperature at the axial surface and L_a [m] the distance between the centre and the top of the cell. Moreover, the convective heat transfer to the fluid is defined in eq. (B.3),

$$\dot{Q}_{conv_a} = h_{fluid} \cdot A_{axial} \cdot (T_{sa} - T_{fm}) \tag{B.3}$$

where h_{fluid} [$W/m^2 \cdot K$] is the fluid convection coefficient and T_{fm} [°C] the average temperature in the fluid, calculated in eq. (B.4), where T_{in} [°C]

and T_{out} [°C] are respectively the temperatures before and after cell's heat transfer to the fluid.

$$T_{fm} = \frac{T_{out} + T_{in}}{2} \tag{B.4}$$

Finally, the heat stored in the fluid can be defined by eq. (B.5),

$$\dot{Q}_{sto_{fluid}} = \dot{m} \cdot C_p \cdot (T_{out} - T_{in}) \tag{B.5}$$

where $\dot{m}$ [kg/s] is the mass flow rate and C_p [J/kg·K] its specific heat value.

These heat transfer calculations allow simulation of the temperature of the cells as well as the maximum dispersion between them. However, it is necessary to obtain the convective heat transfer coefficient (h_{conv}) of the fluid, which will differ according to the temperature, the flow rate and the hydraulic diameter of the channel.

The h_{conv} can be calculated from the hydraulic diameter of the duct (D_h [m]), the Nusselt number (Nu) and the conductivity (k) of the fluid, following eq. (B.6).

$$Nu = \frac{h \cdot D_h}{k} \tag{B.6}$$

The hydraulic diameter in a rectangular channel, such as the one to be used in the prototype follows eq. (B.7), where P [m] is the wet perimeter of the duct.

$$D_h = \frac{4 \cdot A}{P} \tag{B.7}$$

The Nusselt number is a dimensionless ratio of convective to conductive heat transfer at a boundary in a fluid. The way to evaluate that number varies, whether the flow is laminar or turbulent. For this, the Reynolds number must be first calculated as seen in eq. (B.8),

$$Re = \frac{v \cdot D_h}{\nu} = \frac{\rho \cdot v \cdot D_h}{\mu} \tag{B.8}$$

where v [m/s] is the fluid velocity, ρ [kg/m^3] is the fluid density, μ [Pas] is the dynamic viscosity and ν [m^2/s] is the kinematic viscosity of the fluid. In the case of laminar flow (Re < 2300), the Nusselt number is constant for the same shape of the cross-sectional duct area. These values are shown in table B.1, where *a* and *b* represent the height and width of a rectangular area, respectively.

Table B.1: *Nusselt numbers as a function of channel cross-section for laminar flow.*

b/a	*Nu*	$fReD_h$
1.0	2.98	57
1.43	3.08	59
2.0	3.39	62
3.0	3.96	69
4.0	4.44	73
8.0	5.60	82
∞	7.54	96
Triangular	2.49	53
Circular	3.66	64

In the case of turbulent flow (Re ≥ 2300), however, it is calculated by eq. (B.9), where *f* is the friction factor calculated with eq. (B.10) and *Pr* the Prandtl number.

$$Nu = \frac{\left(\frac{f}{8}\right)(Re - 1000)Pr}{1 + 12.7\left(\frac{f}{8}\right)^{1/2}\left(Pr^{2/3} - 1\right)} \tag{B.9}$$

$$f = (0.79 \cdot \ln Re - 1.64)^{-2} \tag{B.10}$$

The Prandlt number evaluated by eq. (B.11) is the ratio of the molecular diffusivity of the quantity of motion to the molecular diffusivity of heat (α), which can be calculated following eq. (B.12).

$$Pr = \frac{\nu}{\alpha} = \frac{\mu \cdot C_p}{k} \tag{B.11}$$

$$\alpha = \frac{k}{\rho \cdot C_p} \tag{B.12}$$

Finally, the pressure drop (Δp) produced by the duct can be calculated to know the energy consumption that would be required to impose each flow rate in the study using eq. (B.13).

$$\Delta p_L = f \frac{L}{D_h} \frac{\rho v^2}{2} \tag{B.13}$$

B.2 Script of the Lumped Thermal Model for Fluid Selection

```
import os
import numpy as np
import pandas as pd
from scipy.optimize import fsolve
import math
import matplotlib.pyplot as plt
from interpolin import interp1
from statistics import mean


dfanalysis=pd.DataFrame(columns=['vf_bp[lpm]', 'vf_loop[lpm]',
    'vf_channel[lpm]', 'mf_channel[kg/s]', 'modules_series[-]',
    'cooling_loops[-]', 'channel_height[m]', 'channel_width[m]',
    'A_channel[m2]', 'Aaxial[m2]', 'Re[-]', 'Nu[-]', 'Pr[-]',
    'h_conv[W/m2K]', 'Tfi[ºC]', 'Tfout[ºC]', 'Tcell_min[ºC]',
    'Tcell_max[ºC]', 'dTcell[ºC]', 'dPa[Pa]'])

##########################
#### PARAMETER INPUT ####
##########################

#%%
vf_bp=20 #[l/min] total flow available.
modules_series_param=[ 290] #10, 29, 58, 145, 290
        # select -> 2,5,10,29,58,145,290 ## number of modules
        (of 12 cells) in series for the cooling loop

Tfi_param=[25] #[ºC] initial (inlet) fluid temperature
channel_height_param=[0.02] #[m] channel height
channel_width_param=[0.0695] #[m] width channel
Amultiplayer=1

def designDF(vf_bp, modules_series, Tfi, channel_height, channel_width,
             Amultiplayer):
    ### IMPORT HFE7200 DATA ###
    def read():
        file= 'HFE7200_data.csv'
        path= (r'C:\Users\eneko.gonzalez\OneDrive - IKERLAN S.COOP\
        TESIA\[03] PROIEKTUAK\[03] DIELECTRIC FLOW\[04] Simulation\
        [01] Predimentsionamendua')
        os.chdir(path)
        N7200=pd.read_csv(file , skiprows=0, header=0, delimiter=',',
        decimal='.')
        return(N7200)

    N7200=read()
    ##########################
```

```
    ############################
    ### HEAT GENERATION DATA ###
    ############################

    # fs_HG=pd.DataFrame(data={'T_C': [10,15,25,35,45,55,65], #[ºC]
    #                          'Heat': [5.23,4.46,2.91,2.45,2.00,1.54,
                                        1.09]})
                                       #[W] False steady Heat generation
                                       at 4C charge and 6.8C discharge

    fs_HG1=pd.DataFrame(data={'T_C': [10,15,20,25,30,35,40,45,50], #[ºC]
                              'Heat': [0.941724138,0.822241379,0.712758621,
                                       0.598448276,0.521551724,
0.442068966,0.362586207,0.285689655,
                                       0.206206897]})
                                      #[W] False steady Heat generation
                                      at 4C charge and 1.38C discharge



    Nu_laminar=pd.DataFrame(data={'b_a': [1.0,1.43,2.0,3.0,4.0,8.0],
                                  # channel width/height relation
                             'Nu': [2.98,3.08,3.39,3.96,4.44,5.6],
                             'fRe': [57, 59, 62, 69, 73, 82]})
                                  #[-] Nusselt number for laminar flow


    ################
    ## CELL DATA ##
    ################
    k_a=2.17 #[W/m·K] cell axial conductivity
    r=0.013 #[m] cell radius
    L=0.065 # [m] cell height
    Aa=math.pi*(r)**2 #[m^2] cell axial surface



    ########################
    ## CHANNEL GEOMETRY ##
    ########################


    A_channel=channel_height*channel_width
    channel_perimeter = (channel_height*2) + (channel_width*2)
    Dh=(4*A_channel)/(channel_perimeter)


    #Aa=math.pi*(r)**2 #[m^2] cell axial surface
    ## Axial surface for heat transfer changes depending on the width
        of the channel.

    if channel_width>= 0.026:
        Aaxial=(math.pi*(r)**2)*Amultiplayer #[m^2] cell axial surface
    else:
```

```
    alpha=(np.degrees(np.arcsin((channel_width/2)/r)))
    Asector=(alpha*2/360)*math.pi*(r)**2
    h_sector= r*np.cos(np.radians(alpha))
    Atriangle_sector=channel_width*h_sector/2
    Aside= (((np.sqrt((r*2)**2-channel_width**2))
           *channel_width/2)-Atriangle_sector)
    Aaxial=(2*Aside+2*Asector)*Amultiplayer


################
## FLUID DATA ##
################

n_cell=3480      #cell number on the BP
cells_module=12      #cells in each module
n_module=n_cell/cells_module     #total number of modules
cells_series=modules_series*cells_module     #cells in series on each
                                                cooling loop
cooling_loops=n_module/modules_series        #cooling loops in
                                             parallel, each one with
                                             "module_series" number
                                             of modules in series.

vf_loop= vf_bp/(cooling_loops)       #[l/min] flow in each cooling
                                     loop
vf_channel=vf_loop/2         #[l/min] flow in each internal channel -
                             one channel for tab+ of one channel,
                             connected in series(thermally) with
                             the next
#########################
#########################


######################################################################
#### h_conv - CONVECTIVE HEAT TRANFER COEFFICIENT CALCULATION ####
######################################################################
def h_fluid(Tfi, Nu_laminar):


####################
##fluid properties ##
####################
    rho = interp1(N720O.T_C, N720O.rho, Tfi)
        #[kg/m3] FLUID DENSITY interpolation in regard
        to fluid temperature

    cp  = interp1(N720O.T_C, N720O.cp, Tfi)
        #[J/kg·K] SPECIFIC HEAT interpolation in regard
        to fluid temperature

    k   = interp1(N720O.T_C, N720O.k, Tfi)
        #[W/m·K] CONDUCTIVITY interpolation in regard
        to fluid temperature
```

```
    nu  = interp1(N7200.T_C, N7200.nu, Tfi)
        #[m2/s] KINEMATIC VISCOSITY interpolation in
        regard to fluid temperature

    alpha = k/(rho*cp)
        #[m2/s] THERMAL DIFFUSIVITY


##################
## flow quantity ##
##################
    # mf_channel=(vf_loop*rho)/(1000*60) #[kg/s] mass flow-rate
    mf_channel=(vf_channel*rho)/(1000*60) #[kg/s] mass flow-rate
    v_fluid = mf_channel/(rho*A_channel) #[m/s] fluid flow speed

##########################################
## Reynolds, Prandtl and Nusselt numbers ##
##########################################

    Re = (v_fluid*Dh)/(nu) #[] Reynolds number calculation
    # Re = 2300

    if Re>=2300:
        f  = (0.79*np.log(Re)-1.64)**(-2)
                ## "f" coefficient estimation ##

        Pr = nu/alpha
                #[] Prandtl number calculation - kinematic
                    viscosity/thermal diffusivity

        Nu = ((f/8)*(Re-1000)*Pr)/(1+(12.7*((f/8)**(1/2)))
            *(Pr**(2/3)-1))

        h_conv = (Nu*k)/Dh
                #[W/m2·K] CONVECTIVE HEAT TRANSFER
                COEFFICIENT estimation

    else:
        b_a= channel_width/channel_height # channel proportions
        Nu = interp1(Nu_laminar.b_a, Nu_laminar.Nu, b_a)
        f=Nu_laminar.fRe/Re
        h_conv = (Nu*k)/Dh #[W/m2·K] CONVECTIVE HEAT TRANSFER
                            COEFFICIENT estimation
        Pr = nu/alpha  #[] Prandtl number calculation - kinematic
                        viscosity/thermal diffusivity

    #     print(b_a)
    # print(mf_channel)
    # print(vf_loop)
    return(Re, mf_channel, cp, h_conv, Nu,f, v_fluid, Pr)

Re, mf_channel, cp, h_conv, Nu, f, v_fluid, Pr =
h_fluid(Tfi, Nu_laminar)
```

```
#### heat functions ####
def HeatTransfer(Tfi, h_conv, mf_channel, cp):
####adiabatical radial area suppossation###
    def axial(p):
        ### variables
        # the cell is divided in 5 slices
        T0  = p[0] #centre temperature
        Tsa = p[1] #Surface Temperature (Temperature Surface Axial)
        Tff = p[2] #Final Fluid Temperature

        Tfm   = (Tff+Tfi)/2 #fluid mean temperature
        Tcell = T0#Tsa #mean([Tsa,T0]) #Cell mean temperature

        ### HEAT GENERATION AND TRANSFER EQUATIONS ###
        qgen    = interp1(fs_HGl.T_C, fs_HGl.Heat, Tcell)
        qconda = (k_a*Aa*(T0-Tsa)/(L/2))      #axial conduction
        qconva  = h_conv*Aaxial*(Tsa-Tfm)     #fluid (channel)
                                                convection
        qstof   = mf_channel/2*cp*(Tff-Tfi)   #fluid storage

        ### HEAT TRANSFER CORRELATIONS ###
        eq1 = qconda - qgen/2
        eq2 = qconva  - qconda
        eq3 = qstof - qconva

        return [eq1,eq2,eq3]

    T0, Tsa, Tff= fsolve(axial,[1]*3)

    return T0, Tsa, Tff

##################


#### ESTIMATING TEMPERATURES ON COOLING ROWS ####
def coolingloop (Tfi,module_number):
    #create three arrays for the temperature results
    Tinternal=[]
    Tsurface=[]
    Tfluidfinal=[]
    Tfluidinlet=[]

    #create three arrays for the temperature results
    Reynolds=[]
    h_convective=[]
    Nusselt=[]
    Prandtl=[]
    massflowchannel=[]

    # create arrays for cell, module and row position identification
    cell_num=[]
    module_num=[]
    row_num=[]
```

```
row=0 #row counter first value
#create results dataframe
dfresults=pd.DataFrame()

# range counter to use on the "FOR" loop
modules=range(module_number)
cells=range(6)

for module in modules:
    for cell in cells:

        Re, mf_channel, cp, h_conv, Nu, f, v_fluid, Pr =
        h_fluid(Tfi, Nu_laminar)

        # run DEF and calculate the heat transfer for
        the specific cell number.

        TO, Tsa, Tff =HeatTransfer(Tfi, h_conv, mf_channel, cp)
        Tfluidinlet.append(Tfi)
        Tfi=Tff

        Tinternal.append(TO)
        Tsurface.append(Tsa)
        Tfluidfinal.append(Tff)
        massflowchannel.append(mf_channel)

        Reynolds.append(Re)
        h_convective.append(h_conv)
        Nusselt.append(Nu)
        Prandtl.append(Pr)

        cell_num.append(cell+1)
        module_num.append(module+1)
        row=row+1
        row_num.append(row)


dfresults['Tinternal']=Tinternal
dfresults['Tsurface']=Tsurface
dfresults['Tfi']=Tfluidinlet
dfresults['Tff']=Tfluidfinal
dfresults['module']=module_num
dfresults['cells']=cell_num
dfresults['row']=row_num
dfresults['Re']=Reynolds
dfresults['Nu']=Nusselt
dfresults['Pr']=Prandtl
dfresults['mf_channel']=massflowchannel
dfresults['h_conv']=h_convective



return (dfresults)
```

```
dfresults  =coolingloop(Tfi,modules_series)


###pressure drop ##
def pressuredrop (Tfi, Nu_laminar, Re, v_fluid):

    l_channel=0.2625
    Tmeanfluid=mean([Tfi,dfresults.Tff[[len(dfresults)-1]]])
    rho = interp1(N7200.T_C, N7200.rho, Tmeanfluid)
        #[kg/m3] FLUID DENSITY interpolation in regard
        to fluid temperature

    if Re>=2300:
        f  = (0.79*np.log(Re)-1.64)**(-2)
            ## "f" coefficient estimation ##
    else:
        b_a= channel_width/channel_height # channel proportions
        fRe = interp1(Nu_laminar.b_a, Nu_laminar.fRe, b_a)
        f=fRe/Re

    dPa=f*(l_channel/Dh)*((rho*v_fluid**2)/2)
    return (dPa)
dPa = pressuredrop(Tfi, Nu_laminar, Re, v_fluid)


data=[]
data.append(float(vf_bp))
data.append(float(vf_loop))
data.append(float(vf_channel))
data.append(float(mean(dfresults.mf_channel)))
data.append(float(modules_series))
data.append(float(cooling_loops))
data.append(float(channel_height))
data.append(float(channel_width))
data.append(float(A_channel))
data.append(float(Aaxial))
data.append(float(Re))
data.append(float(Nu))
data.append(float(Pr))
data.append(float(h_conv))
data.append(float(Tfi))
data.append(float(dfresults.Tff[[len(dfresults)-1]]))
data.append(float(min(dfresults.Tsurface)))
data.append(float(max(dfresults.Tsurface)))
data.append(float((dfresults.Tsurface[[len(dfresults)-1]]-
                                dfresults.Tsurface[0])))
data.append(float(dPa))

dfanalysis.loc[len(dfanalysis)]= data


print('vf_bp[lpm] ='+ str(vf_bp))
print('vf_loop[lpm] ='+ str(vf_loop))
```

```
    print('vf_channel[lpm] ='+ str(vf_channel))
    print('Re[-] ='+ str(mean(dfresults.mf_channel)))
    print('modules_series[-] ='+ str(modules_series))
    print('cooling_loops[-] ='+ str(cooling_loops))
    print('channel_height[m] ='+ str(channel_height))
    print('channel_width[m] ='+ str(channel_width))
    print('A_channel[m2] ='+ str(A_channel))
    print('Aaxial[m2] ='+ str(Aaxial))
    print('Re[-] ='+ str(mean(dfresults.Re)))
    print('Nu[-] ='+ str(Nu))
    print('Pr[-] ='+ str(Pr))
    print('h_conv[W/m2K] ='+ str(h_conv))
    print('Tfi[ºC] ='+ str(Tfi))
    print('Tfout[ºC] ='+ str(dfresults.Tff[[len(dfresults)-1]]))
    print('Tcell_min[ºC] ='+ str(min(dfresults.Tsurface)))
    print('Tcell_max[ºC] ='+ str(max(dfresults.Tsurface)))
    print('dTcell[ºC] ='+ str([dfresults.Tsurface[[len(dfresults)-1]]-
                                dfresults.Tsurface[0]]))
    print('dPa[Pa] ='+ str(dPa))

    return(fs_HG1, N7200, dfresults, dfanalysis)

for modules_series in modules_series_param:
    for Tfi in Tfi_param:
        for channel_height in channel_height_param:
            for channel_width in channel_width_param:
                fs_HG1, N7200, dfresults, dfanalysis=
                designDF(vf_bp, modules_series, Tfi,
                channel_height, channel_width, Amultiplayer)
```

B.3 Fluid Thermophysical Data

The fluid data employed in the analysis can be found in the tables below. Hence, table B.2 shows the data for water ethylene-glycol mixture at 50 %, Novec7200 data is shown in table B.3, Fluorinert FC72 data is shown in table B.4, Envirotemp Ester FR3 data is shown in table B.5, M&I Midel-7131 data is shown in table B.6, and finally, PAO's data is shown in table B.7. Water data is also depicted in table B.8

Table B.2: *Water Ethylene-glycol 50 % mixure's thermophysical properties.*

T [°C]	ρ [kg/m^3]	C_p [J/kg·K]	k [W/m·K]	ν [m^2/s]	μ [Pa·s]
-30	1089	3088	0.328	$4.04e^{-5}$	$4.40e^{-2}$
-20	1087	3126	0.336	$2.03e^{-5}$	$2.21e^{-2}$
-10	1084	3165	0.344	$1.18e^{-5}$	$1.27e^{-2}$
0	1081	3203	0.352	$7.48e^{-6}$	$8.09e^{-3}$
10	1077	3242	0.360	$5.10e^{-6}$	$5.50e^{-3}$
20	1073	3281	0.366	$3.67e^{-6}$	$3.94e^{-3}$
30	1069	3319	0.373	$2.75e^{-6}$	$2.94e^{-3}$
40	1064	3358	0.378	$2.12e^{-6}$	$2.26e^{-3}$
50	1058	3396	0.383	$1.68e^{-6}$	$1.78e^{-3}$

Table B.3: *Novec7200 fluid's thermophysical properties. [177–180]*

T [°C]	ρ [kg/m^3]	C_p [J/kg·K]	k [W/m·K]	ν [m^2/s]	μ [Pa·s]
-30	1550.2	1148.6	$8.48e^{-2}$	$8.76e^{-7}$	$1.36e^{-3}$
-20	1527.2	1192.5	$8.05e^{-2}$	$7.39e^{-7}$	$1.13e^{-3}$
-10	1504.1	1236.3	$7.66e^{-2}$	$6.28e^{-7}$	$9.44e^{-4}$
0	1481.1	1280.2	$7.30e^{-2}$	$5.45e^{-7}$	$8.08e^{-4}$
10	1458.1	1324.1	$6.97e^{-2}$	$4.73e^{-7}$	$6.90e^{-4}$
20	1435.0	1367.9	$6.67e^{-2}$	$4.19e^{-7}$	$6.02e^{-4}$
30	1412.0	1411.8	$6.41e^{-2}$	$3.78e^{-7}$	$5.34e^{-4}$
40	1389.0	1455.7	$6.17e^{-2}$	$3.42e^{-7}$	$4.76e^{-4}$
50	1366.0	1499.5	$5.97e^{-2}$	$3.15e^{-7}$	$4.31e^{-4}$

Table B.4: *Fluorinert FC72 fluid's thermophysical properties.*

T [°C]	ρ [kg/m^3]	C_p [J/kg·K]	k [W/m·K]	ν [m^2/s]	μ [Pa·s]
-30	1818.30	967.38	0.063	9.04e^{-7}	1.64e^{-3}
-20	1792.20	982.92	0.062	7.69e^{-7}	1.38e^{-3}
-10	1766.10	998.46	0.061	6.56e^{-7}	1.16e^{-3}
0	1740.00	1014.00	0.060	5.47e^{-7}	9.53e^{-4}
10	1713.90	1029.54	0.059	4.47e^{-7}	7.66e^{-4}
20	1687.80	1045.08	0.058	3.66e^{-7}	6.17e^{-4}
30	1661.70	1060.62	0.057	3.15e^{-7}	5.23e^{-4}
40	1635.60	1076.16	0.056	2.99e^{-7}	4.90e^{-4}
50	1609.50	1091.70	0.055	2.90e^{-7}	4.67e^{-4}

Table B.5: *Envirotemp Ester FR3 fluid's thermophysical properties.*

T [°C]	ρ [kg/m^3]	C_p [J/kg·K]	k [W/m·K]	ν [m^2/s]	μ [Pa·s]
25	917	2028	0.182	5.63e^{-5}	5.16e^{-2}
40	908	2082	0.180	3.27e^{-5}	2.97e^{-2}
60	892	2166	0.178	1.83e^{-5}	1.63e^{-2}
80	880	2259	0.175	1.15e^{-5}	1.01e^{-2}

Table B.6: *M&I Midel-7131 fluid's thermophysical properties.*

T [°C]	ρ [kg/m^3]	C_p [J/kg·K]	k [W/m·K]	ν [m^2/s]	μ [Pa·s]
25	964	1910	0.158	5.51e^{-5}	5.32e^{-2}
40	953	1964	0.156	2.83e^{-5}	2.69e^{-2}
60	940	2052	0.153	1.40e^{-5}	1.32e^{-2}
80	926	2149	0.151	8.11e^{-6}	7.51e^{-3}

Table B.7: *PAO fluid's thermophysical properties.*

T [°C]	ρ [kg/m^3]	C_p [J/kg·K]	k [W/m·K]	ν [m^2/s]	μ [Pa·s]
-54	863	1926	0.166	$9.63e^{-4}$	$8.31e^{-1}$
-40	851	2009	0.164	$5.43e^{-4}$	$4.62e^{-1}$
0	814	2135	0.159	$1.06e^{-4}$	$8.62e^{-2}$
40	775	2260	0.152	$2.08e^{-5}$	$1.61e^{-2}$
100	719	2470	0.144	$1.81e^{-6}$	$1.30e^{-3}$
135	687	2553	0.140	$4.37e^{-7}$	$3.00e^{-4}$

Table B.8: *Water's thermophysical properties.*

T [°C]	ρ [kg/m^3]	C_p [J/kg·K]	k [W/m·K]	ν [m^2/s]	μ [Pa·s]
0	1000	4220	0.556	$1.79e^{-6}$	$1.79e^{-3}$
10	1000	4200	0.579	$1.31e^{-6}$	$1.31e^{-3}$
20	998	4180	0.598	$1.00e^{-6}$	$1.00e^{-3}$
30	996	4180	0.615	$8.01e^{-7}$	$7.97e^{-4}$
40	992	4180	0.629	$6.58e^{-7}$	$6.53e^{-4}$
50	988	4180	0.641	$5.53e^{-7}$	$5.47e^{-4}$

Table B.9: *Mivolt DF7's thermophysical properties.*

T [°C]	ρ [kg/m^3]	C_p [J/kg·K]	k [W/m·K]	ν [m^2/s]	μ [Pa·s]
-10			confidential		
0			confidential		
10			confidential		
20	916	1907	0.129	$1.64e^{-5}$	$1.50e^{-2}$
30			confidential		
40			confidential		
50			confidential		

Bibliography

[1] NOAA. *National Centers for Environmental information, Climate at a Glance: Global Time Series*. 2023. URL: https://www.ncei.noaa.gov/access/monitoring/climate-at-a-glance/global/time-series/globe/land%7B%5C_%7Docean/ytd/12/1850-2022.

[2] U.S. Global Change Research Program. *Climate science special report: Fourth national climate assessment, volume I*. Tech. rep. U.S. Global Change Research Program, 2018, p. 470. DOI: 10.7930/J0J964J6. URL: http://www.climate.gov/news-features/understanding-climate/climate-change-global-temperature.

[3] NOAA. *Global Monitoring Laboratory, Carbon Cycle Greenhouse Gases: Trends in Atmospheric CO2*. 2022. URL: https://gml.noaa.gov/ccgg/trends/gl%7B%5C_%7Dtrend.html%7B%5C%%7D0Ahttps://gml.noaa.gov/ccgg/trends%7B%5C_%7Dch4/%7B%5C%%7D0Ahttps://gml.noaa.gov/ccgg/trends/.

[4] IPCC. *Global warming of 1.5°C*. Tech. rep. October. IPCC, 2018, pp. 17-20. URL: https://www.ipcc.ch/sr15/.

[5] European Commission. *Climate strategies & targets*. 2017. URL: https://ec.europa.eu/clima/policies/strategies%7B%5C_%7Den.

[6] European Commission. *2020 climate & energy package | Climate Action*. 2009. DOI: 10.1111/pace.12279. URL: https://ec.europa.eu/clima/policies/strategies/2020%7B%5C_%7Den.

[7] European Commission. *2030 climate & energy framework - Climate Action*. 2018. URL: https://ec.europa.eu/clima/policies/strategies/2030%7B%5C_%7Den.

[8] European Commission. *2050 long-term strategy | Climate Action*. 2018. URL: https://ec.europa.eu/clima/policies/strategies/2050%7B%5C_%7Den.

[9] EEA. *EEA greenhouse gases - data viewer*. 2023. URL: https://www.eea.europa.eu/data-and-maps/data/data-viewers/greenhouse-gases-viewer.

[10] EEA. *GHG emissions by sector in the EU-28, 1990-2016 — European Environment Agency*. 2018. URL: https://www.eea.europa.eu/data-and-maps/daviz/ghg-emissions-by-sector-in/%7B%5C#%7Dtab-chart%7B%5C_%7D2.

[11] Christian Breyer et al. 'On the History and Future of 100% Renewable Energy Systems Research'. In: *IEEE Access* 10 (2022), pp. 78176–78218. ISSN: 21693536. DOI: 10.1109/ACCESS.2022.3193402.

[12] Nima Ghaviha et al. 'Review of Application of Energy Storage Devices in Railway Transportation'. In: *Energy Procedia*. Vol. 105. 2017, pp. 4561–4568. DOI: 10.1016/j.egypro.2017.03.980.

[13] M A Hannan, F A Azidin and A Mohamed. *Hybrid electric vehicles and their challenges: A review*. 2014. DOI: 10.1016/j.rser.2013.08.097.

[14] A. Ajanovic and R. Haas. 'Economic and Environmental Prospects for Battery Electric- and Fuel Cell Vehicles: A Review'. In: *Fuel Cells* 19.5 (2019), pp. 515–529. ISSN: 16156854. DOI: 10.1002/fuce.201800171.

[15] Amela Ajanovic. 'The future of electric vehicles: Prospects and impediments'. In: *Wiley Interdisciplinary Reviews: Energy and Environment* 4.6 (2015), pp. 521–536. ISSN: 2041840X. DOI: 10.1002/wene.160.

[16] Alain Le Duigou and Aimen Smatti. 'On the comparison and the complementarity of batteries and fuel cells for electric driving'. In: *International Journal of Hydrogen Energy*. Vol. 39. 31. 2014, pp. 17873–17883. DOI: 10.1016/j.ijhydene.2014.08.077.

[17] Nick Ash, Alec Davies and Claire Newton. *Renewable electricity requirements to decarbonise transport in Europe with electric vehicles, hydrogen and electrofuels*. Tech. rep. 2020.

[18] Transport & Environment. *Electrofuels? Yes, we can … if we're efficient Decarbonising the EU's transport sector with renewable electricity and electrofuels Executive Summary*. Tech. rep. 2020.

[19] Elisabeth Evrard et al. *Carbon footprint report Volvo C40 Recharge*. Tech. rep. 2021. URL: https://unfccc.int/process-and-meetings/the-paris-agreement/the-paris-agreement.

[20] Huaqiang Liu et al. *Thermal issues about Li-ion batteries and recent progress in battery thermal management systems: A review*. 2017. DOI: 10.1016/j.enconman.2017.08.016.

[21] M A Hannan et al. 'Review of energy storage systems for electric vehicle applications: Issues and challenges'. In: *Renewable and Sustainable Energy Reviews* 69 (2017), pp. 771–789. ISSN: 18790690. DOI: 10.1016/j.rser.2016.11.171.

[22] G Benveniste et al. 'Comparison of the state of Lithium-Sulphur and lithium-ion batteries applied to electromobility'. In: *Journal of Environmental Management* 226 (2018), pp. 1–12. ISSN: 10958630. DOI: 10.1016/j.jenvman.2018.08.008.

[23] Sergio Manzetti and Florin Mariasiu. 'Electric vehicle battery technologies: From present state to future systems'. In: *Renewable and Sustainable Energy Reviews* 51 (2015), pp. 1004–1012. ISSN: 18790690. DOI: 10.1016/j.rser.2015.07.010.

[24] Tobias Placke et al. 'Lithium ion, lithium metal, and alternative rechargeable battery technologies: the odyssey for high energy density'. In: *Journal of Solid State Electrochemistry* 21.7 (2017), pp. 1939–1964. ISSN: 14328488. DOI: 10.1007/s10008-017-3610-7.

[25] Heide Budde-Meiwes et al. *A review of current automotive battery technology and future prospects*. 2013. DOI: 10.1177/0954407013485567.

[26] Rui Zhao et al. 'A review of thermal performance improving methods of lithium ion battery: Electrode modification and thermal management system'. In: *Journal of Power Sources* 299 (2015), pp. 557–577. ISSN: 03787753. DOI: 10.1016/j.jpowsour.2015.09.001.

[27] Ahmad A. Pesaran. 'Battery thermal models for hybrid vehicle simulations'. In: *Journal of Power Sources*. Vol. 110. 2. Elsevier, 2002, pp. 377–382. DOI: 10.1016/S0378-7753(02)00200-8.

[28] J Shim et al. 'Electrochemical analysis for cycle performance and capacity fading of a lithium-ion battery cycled at elevated temperature'. In: *Journal of Power Sources* 112.1 (2002), pp. 222–230. ISSN: 03787753. DOI: 10.1016/S0378-7753(02)00363-4.

[29] Noboru Sato. 'Thermal behavior analysis of lithium-ion batteries for electric and hybrid vehicles'. In: *Journal of Power Sources* 99.1-2 (2001), pp. 70–77. ISSN: 03787753. DOI: 10.1016/S0378-7753(01)00478-5.

[30] C. -K. Huang et al. 'The Limits of Low-Temperature Performance of Li-Ion Cells'. In: *Journal of The Electrochemical Society* 147.8 (2000), p. 2893. ISSN: 00134651. DOI: 10.1149/1.1393622.

[31] Languang Lu et al. 'A review on the key issues for lithium-ion battery management in electric vehicles'. In: *Journal of Power Sources* 226 (2013), pp. 272–288. ISSN: 03787753. DOI: 10.1016/j.jpowsour.2012.10.060.

[32] Anna Tomaszewska et al. 'Lithium-ion battery fast charging: A review'. In: *eTransportation* 1 (2019), p. 100011. ISSN: 25901168. DOI: 10.1016/j.etran.2019.100011.

[33] Gang Ning, Bala Haran and Branko N Popov. 'Capacity fade study of lithium-ion batteries cycled at high discharge rates'. In: *Journal of Power Sources* 117.1-2 (2003), pp. 160–169. ISSN: 03787753. DOI: 10.1016/S0378-7753(03)00029-6.

[34] P Ramadass et al. 'Capacity fade of Sony 18650 cells cycled at elevated temperatures: Part II. Capacity fade analysis'. In: *Journal of Power Sources* 112.2 (2002), pp. 614–620. ISSN: 03787753. DOI: 10.1016/S0378-7753(02)00473-1.

[35] M Broussely et al. 'Main aging mechanisms in Li ion batteries'. In: *Journal of Power Sources* 146.1-2 (2005), pp. 90–96. ISSN: 03787753. DOI: 10.1016/j.jpowsour.2005.03.172.

[36] Amrit Kumar Thakur et al. 'A state of art review and future viewpoint on advance cooling techniques for Lithium–ion battery system of electric vehicles'. In: *Journal of Energy Storage* 32 (2020). ISSN: 2352152X. DOI: 10.1016/j.est.2020.101771.

[37] Peter Miller. *Automotive lithium-ion batteries*. 2015. DOI: 10.1595/205651315X685445.

[38] Robert Schröder, Muhammed Aydemir and Günther Seliger. 'Comparatively Assessing different Shapes of Lithium-ion Battery Cells'. In: *Procedia Manufacturing* 8 (2017), pp. 104–111. ISSN: 23519789. DOI: 10.1016/j.promfg.2017.02.013.

[39] Dawn Bernardi, Ellen Pawlikowski and John Newman. 'A General Energy Balance for Battery Systems'. In: *Journal of the Electrochemical Society* 132.1 (1985), pp. 5–12. DOI: 10.1149/1.2113792.

[40] Christophe Forgez et al. 'Thermal modeling of a cylindrical LiFePO4/graphite lithium-ion battery'. In: *Journal of Power Sources* 195.9 (2010), pp. 2961–2968. ISSN: 03787753. DOI: 10.1016/j.jpowsour.2009.10.105.

[41] Todd M. Bandhauer, Srinivas Garimella and Thomas F. Fuller. 'A Critical Review of Thermal Issues in Lithium-Ion Batteries'. In: *Journal of The Electrochemical Society* 158.3 (2011), R1. ISSN: 00134651. DOI: 10.1149/1.3515880.

[42] Karen E. Thomas and John Newman. 'Thermal Modeling of Porous Insertion Electrodes'. In: *Journal of The Electrochemical Society* 150.2 (2003), A176. ISSN: 00134651. DOI: 10.1149/1.1531194.

[43] Karen E Thomas and John Newman. 'Heats of mixing and of entropy in porous insertion electrodes'. In: *Journal of Power Sources*. Vol. 119-121. 2003, pp. 844-849. DOI: 10.1016/S0378-7753(03)00283-0.

[44] Rajib Mahamud and Chanwoo Park. 'Reciprocating air flow for Li-ion battery thermal management to improve temperature uniformity'. In: *Journal of Power Sources* 196.13 (2011), pp. 5685-5696. ISSN: 03787753. DOI: 10.1016/j.jpowsour.2011.02.076.

[45] Xuesong Li, Fan He and Lin Ma. 'Thermal management of cylindrical batteries investigated using wind tunnel testing and computational fluid dynamics simulation'. In: *Journal of Power Sources* 238 (2013), pp. 395-402. ISSN: 03787753. DOI: 10.1016/j.jpowsour.2013.04.073.

[46] X M Xu and R He. 'Research on the heat dissipation performance of battery pack based on forced air cooling'. In: *Journal of Power Sources* 240 (2013), pp. 33-41. ISSN: 03787753. DOI: 10.1016/j.jpowsour.2013.03.004.

[47] Liwu Fan, J M Khodadadi and A A Pesaran. 'A parametric study on thermal management of an air-cooled lithium-ion battery module for plug-in hybrid electric vehicles'. In: *Journal of Power Sources* 238 (2013), pp. 301-312. ISSN: 03787753. DOI: 10.1016/j.jpowsour.2013.03.050.

[48] Dafen Chen et al. 'Comparison of different cooling methods for lithium ion battery cells'. In: *Applied Thermal Engineering* 94 (2016), pp. 846-854. ISSN: 13594311. DOI: 10.1016/j.applthermaleng.2015.10.015.

[49] Taeyoung Han et al. 'Li-ion battery pack thermal management: Liquid versus air cooling'. In: *Journal of Thermal Science and Engineering Applications* 11.2 (2019). ISSN: 19485093. DOI: 10.1115/1.4041595.

[50] *KIA Soul EV vs. Nissan LEAF: An Owner's Comparison – Driving Solar*. URL: https://driving.solar/kia-soul-ev-vs-nissan-leaf-owners-comparison/.

[51] *Toyota - Mantenimiento de la batería de un híbrido Toyota*. URL: https://www.toyota.es/world-of-toyota/articles-news-events/2018/mantenimiento-bateria-coche-hibrido-toyota.

[52] Sungjin Park and Dohoy Jung. 'Battery cell arrangement and heat transfer fluid effects on the parasitic power consumption and the cell temperature distribution in a hybrid electric vehicle'. In: *Journal of Power Sources* 227 (2013), pp. 191–198. ISSN: 03787753. DOI: 10.1016/j.jpowsour.2012.11.039.

[53] Wang Zichen and Du Changqing. 'A comprehensive review on thermal management systems for power lithium-ion batteries'. In: *Renewable and Sustainable Energy Reviews* 139 (2021), p. 110685. ISSN: 18790690. DOI: 10.1016/j.rser.2020.110685.

[54] Y Lou. 'Nickel-metal hydride battery cooling system research for hybrid electric vehicle'. In: *Shanghai Jiao Tong University. Shanghai* (2007).

[55] Mao Sung Wu et al. 'Heat dissipation design for lithium-ion batteries'. In: *Journal of Power Sources* 109.1 (2002), pp. 160–166. ISSN: 03787753. DOI: 10.1016/S0378-7753(02)00048-4.

[56] Paul Nelson et al. 'Modeling thermal management of lithium-ion PNGV batteries'. In: *Journal of Power Sources* 110.1 (2002), pp. 349–356. ISSN: 03787753. DOI: 10.1016/s0378-7753(02)00197-0.

[57] Weixiong Wu et al. *A critical review of battery thermal performance and liquid based battery thermal management*. 2019. DOI: 10.1016/j.enconman.2018.12.051.

[58] Ahmad Pesaran. 'Battery Thermal Management in EVs and HEVs : Issues and Solutions'. In: *Advanced Automotive Battery Conference* (2001), p. 10. ISSN: 0005-6359.

[59] Zirong Lin et al. 'Heat transfer characteristics and LED heat sink application of aluminum plate oscillating heat pipes'. In: *Applied Thermal Engineering* 31.14-15 (2011), pp. 2221–2229. ISSN: 13594311. DOI: 10.1016/j.applthermaleng.2011.03.003.

[60] *Thermo Cool | Cold Plates*. URL: https://thermocoolcorp.com/project/cold-plates/.

[61] Fuad Un-Noor et al. 'A comprehensive study of key electric vehicle (EV) components, technologies, challenges, impacts, and future direction of development'. In: *Energies* 10.8 (2017). ISSN: 19961073. DOI: 10.3390/en10081217.

[62] *Tesla Motors Club*. Tech. rep. 2015. URL: https://teslamotorsclub.com/tmc/threads/tesla-cuts-60kwh-model-s-entry-level-model-s-is-now-70d.45496/page-25.

[63] Audi. *Audi e-tron Sportback 55 quattro*. 2020. URL: https://www.audi-mediacenter.com/en/photos/detail/audi-e-tron-sportback-55-quattro-91138.

[64] Yoong Chung and Min Soo Kim. 'Thermal analysis and pack level design of battery thermal management system with liquid cooling for electric vehicles'. In: *Energy Conversion and Management* 196 (2019), pp. 105–116. ISSN: 01968904. DOI: 10.1016/j.enconman.2019.05.083.

[65] M. G. Cooper, B. B. Mikic and M. M. Yovanovich. 'Thermal contact conductance'. In: *International Journal of Heat and Mass Transfer*. Mechanical Engineering Series 12.3 (1969), pp. 279–300. ISSN: 00179310. DOI: 10.1016/0017-9310(69)90011-8.

[66] Chun Kai Liu et al. 'Direct liquid cooling for IGBT power module'. In: *2014 9th International Microsystems, Packaging, Assembly and Circuits Technology Conference: Challenges of Change - Shaping the Future, IMPACT 2014 - Proceedings* 2.c (2015), pp. 41–44. DOI: 10.1109/IMPACT.2014.7048421.

[67] Anthony Jarrett and Il Yong Kim. 'Design optimization of electric vehicle battery cooling plates for thermal performance'. In: *Journal of Power Sources* 196.23 (2011), pp. 10359–10368. ISSN: 03787753. DOI: 10.1016/j.jpowsour.2011.06.090.

[68] Yutao Huo et al. 'Investigation of power battery thermal management by using mini-channel cold plate'. In: *Energy Conversion and Management* 89 (2015), pp. 387–395. ISSN: 01968904. DOI: 10.1016/j.enconman.2014.10.015.

[69] Zhuangzhuang Shang et al. 'Structural optimization of lithium-ion battery for improving thermal performance based on a liquid cooling system'. In: *International Journal of Heat and*

Mass Transfer 130 (2019), pp. 33–41. ISSN: 00179310. DOI: 10.1016/j.ijheatmasstransfer.2018.10.074.

[70] Cheng Qian et al. 'Thermal Management on IGBT Power Electronic Devices and Modules'. In: *IEEE Access* 6 (2018), pp. 12868–12884. ISSN: 21693536. DOI: 10.1109/ACCESS.2018.2793300.

[71] Ljubisa D. Stevanovic et al. 'Integral micro-channel liquid cooling for power electronics'. In: *Conference Proceedings - IEEE Applied Power Electronics Conference and Exposition - APEC* (2010), pp. 1591–1597. ISSN: 1048-2334. DOI: 10.1109/APEC.2010.5433444.

[72] Jaewan Kim, Jinwoo Oh and Hoseong Lee. *Review on battery thermal management system for electric vehicles*. 2019. DOI: 10.1016/j.applthermaleng.2018.12.020.

[73] Guodong Xia, Lei Cao and Guanglong Bi. *A review on battery thermal management in electric vehicle application*. 2017. DOI: 10.1016/j.jpowsour.2017.09.046.

[74] C. Staszel and A. L. Yarin. 'Exponential vaporization fronts and critical heat flux in pool boiling'. In: *International Communications in Heat and Mass Transfer* 98 (2018), pp. 171–176. ISSN: 07351933. DOI: 10.1016/j.icheatmasstransfer.2018.08.019.

[75] 3M. *Líquidos Novec especiales | 3M España*. URL: https://www.3m.com.es/3M/es%7B%5C_%7DES/empresa-es/todos-productos-3m/%7B~%7D/Todos-los-productos-3M/Novec/Fluidos-especiales/?N=5002385+8711017+8717595+8736412%7B%5C&%7Drt=r3.

[76] Seonggi Park et al. 'Simulation on cooling performance characteristics of a refrigerant-cooled active thermal management system for lithium ion batteries'. In: *International Journal of Heat and Mass Transfer* 135 (2019), pp. 131–141. ISSN: 00179310. DOI: 10.1016/j.ijheatmasstransfer.2019.01.109.

[77] Jiwen Cen, Zhibin Li and Fangming Jiang. 'Experimental investigation on using the electric vehicle air conditioning system for lithium-ion battery thermal management'. In: *Energy for Sustainable Development* 45 (2018), pp. 88–95. ISSN: 23524669. DOI: 10.1016/j.esd.2018.05.005.

[78] Maan Al-Zareer, Ibrahim Dincer and Marc A. Rosen. 'Heat and mass transfer modeling and assessment of a new battery cooling system'. In: *International Journal of Heat and Mass Transfer* 126 (2018), pp. 765–778. ISSN: 00179310. DOI: 10.1016/j.ijheatmasstransfer.2018.04.157.

[79] Imke Lisa Krüger, Dirk Limperich and Gerhard Schmitz. 'Energy Consumption Of Battery Cooling In Hybrid Electric Vehicles'. In: *International Refrigeration and Air Conditioning Conference* (2012), pp. 1–10.

[80] Seong Ho Hong et al. 'Thermal performance of direct two-phase refrigerant cooling for lithium-ion batteries in electric vehicles'. In: *Applied Thermal Engineering* 173.May 2019 (2020), p. 115213. ISSN: 13594311. DOI: 10.1016/j.applthermaleng.2020.115213.

[81] Leonid Vasiliev et al. 'Loop heat pipe for cooling of high-power electronic components'. In: *International Journal of Heat and Mass Transfer* 52.1-2 (2009), pp. 301–308. ISSN: 00179310. DOI: 10.1016/j.ijheatmasstransfer.2008.06.016.

[82] Bambang Ariantara, Nandy Putra and Sugeng Supriadi. 'Battery thermal management system using loop heat pipe with LTP copper capillary wick'. In: *IOP Conference Series: Earth and Environmental Science*. Vol. 105. 1. 2018. DOI: 10.1088/1755-1315/105/1/012045.

[83] D. Khrustalev and A. Faghri. 'Estimation of the maximum heat flux in the inverted meniscus type evaporator of a flat miniature heat pipe'. In: *International Journal of Heat and Mass Transfer* 39.9 (1996), pp. 1899–1909. ISSN: 00179310. DOI: 10.1016/0017-9310(95)00270-7.

[84] Xin Ye, Yaohua Zhao and Zhenhua Quan. 'Thermal management system of lithium-ion battery module based on micro heat pipe array'. In: *International Journal of Energy Research* 42.2 (2018), pp. 648–655. ISSN: 1099114X. DOI: 10.1002/er.3847.

[85] Xiaoming Xu et al. 'Plate flat heat pipe and liquid-cooled coupled multistage heat dissipation system of Li-ion battery'. In: *International Journal of Energy Research* 43.3 (2019), pp. 1133–1141. ISSN: 1099114X. DOI: 10.1002/er.4341.

[86] Joshua Smith et al. 'Battery thermal management system for electric vehicle using heat pipes'. In: *International Journal of Thermal Sciences* 134 (2018), pp. 517–529. ISSN: 12900729. DOI: 10.1016/j.ijthermalsci.2018.08.022.

[87] Jian Qu et al. 'Heat transfer performance of flexible oscillating heat pipes for electric/hybrid-electric vehicle battery thermal management'. In: *Applied Thermal Engineering* 135 (2018), pp. 1–9. ISSN: 13594311. DOI: 10.1016/j.applthermaleng.2018.02.045.

[88] Jialin Liang, Yunhua Gan and Yong Li. 'Investigation on the thermal performance of a battery thermal management system using heat pipe under different ambient temperatures'. In: *Energy Conversion and Management* 155 (2018), pp. 1–9. ISSN: 01968904. DOI: 10.1016/j.enconman.2017.10.063.

[89] Liyuan Feng et al. 'Experimental investigation of thermal and strain management for lithium-ion battery pack in heat pipe cooling'. In: *Journal of Energy Storage* 16 (2018), pp. 84–92. ISSN: 2352152X. DOI: 10.1016/j.est.2018.01.001.

[90] Zhonghao Rao et al. 'Experimental investigation on thermal management of electric vehicle battery with heat pipe'. In: *Energy Conversion and Management* 65 (2013), pp. 92–97. ISSN: 01968904. DOI: 10.1016/j.enconman.2012.08.014.

[91] Abu Raihan Mohammad Siddique, Shohel Mahmud and Bill Van Heyst. *A comprehensive review on a passive (phase change materials) and an active (thermoelectric cooler) battery thermal management system and their limitations*. 2018. DOI: 10.1016/j.jpowsour.2018.08.094.

[92] S. Al Hallaj and J. R. Selman. 'A Novel Thermal Management System for Electric Vehicle Batteries Using Phase-Change Material'. In: *Journal of The Electrochemical Society* 147.9 (2000), p. 3231. ISSN: 00134651. DOI: 10.1149/1.1393888.

[93] Farah Souayfane, Farouk Fardoun and Pascal Henry Biwole. *Phase change materials (PCM) for cooling applications in buildings: A review*. 2016. DOI: 10.1016/j.enbuild.2016.04.006.

[94] Prabhu Bose and Valan Arasu Amirtham. *A review on thermal conductivity enhancement of paraffinwax as latent heat energy storage material*. 2016. DOI: 10.1016/j.rser.2016.06.071.

[95] X. Duan and G. F. Naterer. 'Heat transfer in phase change materials for thermal management of electric vehicle battery modules'. In: *International Journal of Heat and Mass Transfer* 53.23-24 (2010), pp. 5176–5182. ISSN: 00179310. DOI: 10.1016/j.ijheatmasstransfer.2010.07.044.

[96] Mehdi Mehrabi-Kermani, Ehsan Houshfar and Mehdi Ashjaee. 'A novel hybrid thermal management for Li-ion batteries using phase change materials embedded in copper foams combined with forced-air convection'. In: *International Journal of Thermal Sciences* 141 (2019), pp. 47–61. ISSN: 12900729. DOI: 10.1016/j.ijthermalsci.2019.03.026.

[97] S. Al Hallaj and J. R. Selman. 'A Novel Thermal Management System for Electric Vehicle Batteries Using Phase-Change Material'. In: *Journal of The Electrochemical Society* 147.9 (2000), p. 3231. ISSN: 00134651. DOI: 10.1149/1.1393888.

[98] Stephen Wilke et al. 'Preventing thermal runaway propagation in lithium ion battery packs using a phase change composite material: An experimental study'. In: *Journal of Power Sources* 340 (2017), pp. 51–59. ISSN: 03787753. DOI: 10.1016/j.jpowsour.2016.11.018.

[99] Weixiong Wu et al. 'An experimental study of thermal management system using copper mesh-enhanced composite phase change materials for power battery pack'. In: *Energy* 113 (2016), pp. 909–916. ISSN: 03605442. DOI: 10.1016/j.energy.2016.07.119.

[100] Abu Raihan et al. 'A comprehensive review on a passive (phase change materials) and an active (thermoelectric cooler) battery thermal management system and their limitations'. In: (2018). DOI: 10.1016/j.jpowsour.2018.08.094.

[101] Maan Al-Zareer, Ibrahim Dincer and Marc A. Rosen. 'Novel thermal management system using boiling cooling for high-powered lithium-ion battery packs for hybrid electric vehicles'. In: *Journal of Power Sources* 363 (2017), pp. 291–303. ISSN: 03787753. DOI: 10.1016/j.jpowsour.2017.07.067.

[102] Maan Al-Zareer, Ibrahim Dincer and Marc A Rosen. 'Electrochemical modeling and performance evaluation of a new ammonia-based battery thermal management system for electric and hybrid elec-

tric vehicles'. In: *Electrochimica Acta* 247 (2017), pp. 171–182. ISSN: 00134686. DOI: 10.1016/j.electacta.2017.06.162.

[103] Hirokazu Hirano et al. 'Boiling liquid battery cooling for electric vehicle'. In: *IEEE Transportation Electrification Conference and Expo, ITEC Asia-Pacific 2014 - Conference Proceedings*. Institute of Electrical and Electronics Engineers Inc., 2014. ISBN: 9781479942398. DOI: 10.1109/ITEC-AP.2014.6940931.

[104] R. W. Van Gils et al. 'Battery thermal management by boiling heat-transfer'. In: *Energy Conversion and Management* 79 (2014), pp. 9–17. ISSN: 01968904. DOI: 10.1016/j.enconman.2013.12.006.

[105] AN Zhoujian et al. 'Experimental investigation of lithium-ion power battery liquid cooling'. In: *Applied Thermal Engineering* 117.2 (2017), pp. 534–543. ISSN: 2095-6134. DOI: 10.7523/J.ISSN.2095-6134.2018.02.016.

[106] Chayan Nadjahi, Hasna Louahlia and Stéphane Lemasson. 'A review of thermal management and innovative cooling strategies for data center'. In: *Sustainable Computing: Informatics and Systems* 19 (2018), pp. 14–28. ISSN: 22105379. DOI: 10.1016/j.suscom.2018.05.002.

[107] Mahesh Suresh Patil, Jae Hyeong Seo and Moo Yeon Lee. 'A novel dielectric fluid immersion cooling technology for Li-ion battery thermal management'. In: *Energy Conversion and Management* 229 (2021). ISSN: 01968904. DOI: 10.1016/j.enconman.2020.113715.

[108] K V Jithin and P K Rajesh. 'Numerical analysis of single-phase liquid immersion cooling for lithium-ion battery thermal management using different dielectric fluids'. In: *International Journal of Heat and Mass Transfer* 188 (2022), p. 122608. ISSN: 00179310. DOI: 10.1016/j.ijheatmasstransfer.2022.122608.

[109] Yan Feng Wang and Jiang Tao Wu. 'Thermal performance predictions for an HFE-7000 direct flow boiling cooled battery thermal management system for electric vehicles'. In: *Energy Conversion and Management* 207 (2020). ISSN: 01968904. DOI: 10.1016/j.enconman.2020.112569.

[110] Prahit Dubey, Gautam Pulugundla and A. K. Srouji. 'Direct comparison of immersion and cold-plate based cooling for automotive li-ion battery modules'. In: *Energies* 14.5 (2021). ISSN: 19961073. DOI: 10.3390/en14051259.

[111] Sungjin Park and Dohoy Jung. 'Battery cell arrangement and heat transfer fluid effects on the parasitic power consumption and the cell temperature distribution in a hybrid electric vehicle'. In: *Journal of Power Sources* 227 (2013), pp. 191–198. ISSN: 03787753. DOI: 10.1016/j.jpowsour.2012.11.039.

[112] D Koster et al. 'Degradation analysis of 18650 cylindrical cell battery pack with immersion liquid cooling system. Part 1: Aging assessment at pack level'. In: *Journal of Energy Storage* 62 (2023), p. 106839. DOI: 10.1016/j.est.2023.106839.

[113] Yuanwang Deng et al. *Effects of different coolants and cooling strategies on the cooling performance of the power lithium ion battery system: A review*. 2018. DOI: 10.1016/j.applthermaleng.2018.06.043.

[114] Weixiong Wu et al. *A critical review of battery thermal performance and liquid based battery thermal management*. 2019. DOI: 10.1016/j.enconman.2018.12.051.

[115] *Xing Mobility*. URL: https://www.xingmobility.com/en/products/856d7055a67A.

[116] *KREISEL Electric - Battery technology pioneer*. URL: https://www.kreiselelectric.com/.

[117] *Exoes, Avanced thermal system solutions - Experts en solutions Rankine et Management thermique*. URL: https://exoes.com/en/.

[118] Thomas Kraft. 'High performance battery cooling by innovative immersion cooling systems I'. In: January (2021).

[119] Ian A. Hunt et al. 'Surface Cooling Causes Accelerated Degradation Compared to Tab Cooling for Lithium-Ion Pouch Cells'. In: *Journal of The Electrochemical Society* 163.9 (2016), A1846–A1852. ISSN: 0013-4651. DOI: 10.1149/2.0361609jes.

[120] Oskar Dondelewski et al. 'The role of cell geometry when selecting tab or surface cooling to minimise cell degradation'. In: *eTransportation* 5 (2020). ISSN: 25901168. DOI: 10.1016/j.etran.2020.100073.

[121] Shen Li et al. 'Optimal cell tab design and cooling strategy for cylindrical lithium-ion batteries'. In: *Journal of Power Sources* 492 (2021), p. 229594. ISSN: 03787753. DOI: 10.1016/j.jpowsour.2021.229594.

[122] T. G. Tranter et al. 'Communication—Prediction of Thermal Issues for Larger Format 4680 Cylindrical Cells and Their Mitigation with Enhanced Current Collection'. In: *Journal of The Electrochemical Society* 167.16 (2020), p. 160544. ISSN: 0013-4651. DOI: 10.1149/1945-7111/abd44f.

[123] *The difference between 18650, 21700, 30700, 4680 and other Li-ions*. URL: https://www.batterypowertips.com/18650-21700-30700-4680-and-other-li-ions-whats-the-difference-faq/.

[124] Yan Ma et al. 'Core temperature estimation of lithium-ion battery for EVs using Kalman filter'. In: *Applied Thermal Engineering* 168 (2020). ISSN: 13594311. DOI: 10.1016/j.applthermaleng.2019.114816.

[125] Deokhun Kang et al. 'Internal thermal network model-based inner temperature distribution of high-power lithium-ion battery packs with different shapes for thermal management'. In: *Journal of Energy Storage* 27 (2020). ISSN: 2352152X. DOI: 10.1016/j.est.2019.101017.

[126] Yi Xie et al. 'An improved resistance-based thermal model for a pouch lithium-ion battery considering heat generation of posts'. In: *Applied Thermal Engineering* 164 (2020). ISSN: 13594311. DOI: 10.1016/j.applthermaleng.2019.114455.

[127] Florian Geifes et al. 'Determination of the entropic heat coefficient in a simple electro-thermal lithium-ion cell model with pulse relaxation measurements and least squares algorithm'. In: *Journal of Power Sources* 419 (2019), pp. 148–154. ISSN: 03787753. DOI: 10.1016/j.jpowsour.2019.02.072.

[128] C Veth, D Dragicevic and C Merten. 'Thermal characterizations of a large-format lithium ion cell focused on high current discharges'. In: *Journal of Power Sources* 267 (2014), pp. 760–769. ISSN: 03787753. DOI: 10.1016/j.jpowsour.2014.05.139.

[129] G Vertiz et al. 'Thermal characterization of large size lithium-ion pouch cell based on 1d electro-thermal model'. In: *Journal of Power Sources* 272 (2014), pp. 476–484. ISSN: 03787753. DOI: 10.1016/j.jpowsour.2014.08.092.

[130] Yuan Li et al. 'Characteristic investigation of an electrochemical-thermal coupled model for a LiFePO 4 /Graphene hybrid cathode lithium-ion battery'. In: *Case Studies in Thermal Engineering* 13 (2019). ISSN: 2214157X. DOI: 10.1016/j.csite.2018.100387.

[131] Yiwei Tang et al. 'Study of the thermal properties during the cyclic process of lithium ion power batteries using the electrochemical-thermal coupling model'. In: *Applied Thermal Engineering* 137 (2018), pp. 11–22. ISSN: 13594311. DOI: 10.1016/j.applthermaleng.2018.03.067.

[132] Zhoujian An et al. 'Investigation on lithium-ion battery electrochemical and thermal characteristic based on electrochemical-thermal coupled model'. In: *Applied Thermal Engineering* 137 (2018), pp. 792–807. ISSN: 13594311. DOI: 10.1016/j.applthermaleng.2018.04.014.

[133] Wenxin Mei et al. 'Three-dimensional layered electrochemical-thermal model for a lithium-ion pouch cell Part II. The effect of units number on the performance under adiabatic condition during the discharge'. In: *International Journal of Heat and Mass Transfer* 148 (2020). ISSN: 00179310. DOI: 10.1016/j.ijheatmasstransfer.2019.119082.

[134] Peizhao Lyu et al. 'Investigation on the thermal behavior of Ni-rich NMC lithium ion battery for energy storage'. In: *Applied Thermal Engineering* 166 (2020), p. 114749. ISSN: 13594311. DOI: 10.1016/j.applthermaleng.2019.114749.

[135] Bing Wang et al. 'Study of non-uniform temperature and discharging distribution for lithium-ion battery modules in series and parallel connection'. In: *Applied Thermal Engineering* 168 (2020). ISSN: 13594311. DOI: 10.1016/j.applthermaleng.2019.114831.

[136] Meng Xu et al. 'Modeling the effect of two-stage fast charging protocol on thermal behavior and charging energy efficiency of lithium-ion batteries'. In: *Journal of Energy Storage* 20 (2018), pp. 298–309. ISSN: 2352152X. DOI: 10.1016/j.est.2018.09.004.

[137] Akram Eddahech, Olivier Briat and Jean Michel Vinassa. 'Thermal characterization of a high-power lithium-ion battery: Potentiometric and calorimetric measurement of entropy changes'. In: *Energy* 61 (2013), pp. 432–439. ISSN: 03605442. DOI: 10.1016/j.energy.2013.09.028.

[138] K Jalkanen and K Vuorilehto. 'Entropy change characteristics of LiMn0.67Fe0.33PO4 and Li4Ti5O12 electrode materials'. In: *Journal of Power Sources* 273 (2015), pp. 351–359. ISSN: 03787753. DOI: 10.1016/j.jpowsour.2014.09.091.

[139] Seyed Saeed Madani, Erik Schaltz and Søren Knudsen Kær. 'An experimental analysis of entropic coefficient of a lithium titanate oxide battery'. In: *Energies* 12.14 (2019). ISSN: 19961073. DOI: 10.3390/en12142685.

[140] Philipp Schröer et al. 'Challenges in modeling high power lithium titanate oxide cells in battery management systems'. In: *Journal of Energy Storage* 28 (2020). ISSN: 2352152X. DOI: 10.1016/j.est.2019.101189.

[141] Yang Hu, Song Yul Choe and Taylor R Garrick. 'Hybridized time-frequency method for the measurement of entropy coefficient of lithium-ion battery'. In: *Electrochimica Acta* 362 (2020), p. 137124. ISSN: 00134686. DOI: 10.1016/j.electacta.2020.137124.

[142] Manikandan Balasundaram et al. 'Heat loss distribution: Impedance and thermal loss analyses in LiFePO4/graphite 18650 electrochemical cell'. In: *Journal of Power Sources* 328 (2016), pp. 413–421. ISSN: 03787753. DOI: 10.1016/j.jpowsour.2016.08.045.

[143] Vilayanur V Viswanathan et al. 'Effect of entropy change of lithium intercalation in cathodes and anodes on Li-ion battery thermal management'. In: *Journal of Power Sources* 195.11 (2010), pp. 3720–3729. ISSN: 03787753. DOI: 10.1016/j.jpowsour.2009.11.103.

[144] Zeyang Geng, Jens Groot and Torbjorn Thiringer. 'A Time- and Cost-Effective Method for Entropic Coefficient Determination of a Large Commercial Battery Cell'. In: *IEEE Transactions on Transportation Electrification* 6.1 (2020), pp. 257–266. ISSN: 23327782. DOI: 10.1109/TTE.2020.2971454.

[145] Shuanglong Du et al. 'Study on the thermal behaviors of power lithium iron phosphate (LFP) aluminum-laminated battery with different tab configurations'. In: *International Journal of Thermal Sciences* 89 (2015), pp. 327–336. ISSN: 12900729. DOI: 10.1016/j.ijthermalsci.2014.11.018.

[146] Todd M Bandhauer, Srinivas Garimella and Thomas F Fuller. 'Temperature-dependent electrochemical heat generation in a commercial lithium-ion battery'. In: *Journal of Power Sources* 247 (2014), pp. 618–628. ISSN: 03787753. DOI: 10.1016/j.jpowsour.2013.08.015.

[147] Leire Martín-Martín. 'Model Based Optimization of Thermal Management Systems for Electro-Mobility Applications'. PhD thesis. 2017.

[148] Jiri Blazek. *Computational Fluid Dynamics: Principles and Applications: Third Edition*. Elsevier Ltd, 2015, pp. 1–447. ISBN: 9780128011720. DOI: 10.1016/C2013-0-19038-1.

[149] W Malalasekera H K Versteeg. 'An introduction to computational fluid dynamics : the finite volume method'. In: *Finite Volume Method, Essex, Longman Scientific \& ...* Vol. M. Harlow, England ; Pearson-Prentice Hall, 2015, p. 500. ISBN: 9783319168739.

[150] Tsan Hsing Shih et al. 'A new k- eddy viscosity model for high reynolds number turbulent flows'. In: *Computers and Fluids* 24.3 (1995), pp. 227–238. ISSN: 00457930. DOI: 10.1016/0045-7930(94)00032-T.

[151] H. C. Chen and V. C. Patel. 'Near-wall turbulence models for complex flows including separation'. In: *AIAA Journal* 26.6 (1988), pp. 641–648. ISSN: 00011452. DOI: 10.2514/3.9948.

[152] B. R. Hutchinson and G. D. Raithby. 'A multigrid method based on the additive correction strategy'. In: *Numerical Heat Transfer* 9.5 (1986), pp. 511–537. ISSN: 01495720. DOI: 10.1080/10407788608913491.

[153] Suhas V. Patankar. 'Numerical heat transfer and fluid flow.' In: (1980). ISSN: 0029-5639. DOI: 10.13182/nse81-a20112.

[154] S. R. Mathur and J. Y. Murthy. 'A pressure-based method for unstructured meshes'. In: *Numerical Heat Transfer, Part B: Fundamentals* 31.2 (1997), pp. 195–215. ISSN: 15210626. DOI: 10.1080/10407799708915105.

[155] Joel H. Ferziger, Milovan Peric and Anthony Leonard. 'Computational Methods for Fluid Dynamics'. In: *Physics Today* 50.3 (1997), pp. 80–84. ISSN: 0031-9228. DOI: 10.1063/1.881751.

[156] Kangda Chen et al. 'Selection of lithium-ion battery technologies for electric vehicles under China's new energy vehicle credit regulation'. In: *Energy Procedia*. Vol. 158. Elsevier Ltd, 2019, pp. 3038–3044. DOI: 10.1016/j.egypro.2019.01.987.

[157] Elixabet Sarasketa-Zabala. 'A novel approach for Li-ion battery selection and lifetime prediction'. PhD thesis. Goi Eskola Politeknikoa, Mondragon, 2014, p. 281.

[158] Timur Sayfutdinov, Mazhar Ali and Oleg Khamisov. 'Alternating direction method of multipliers for the optimal siting, sizing, and technology selection of Li-ion battery storage'. In: *Electric Power Systems Research* 185 (2020). ISSN: 03787796. DOI: 10.1016/j.epsr.2020.106388.

[159] Victor Vega-Garita et al. 'Selecting a suitable battery technology for the photovoltaic battery integrated module'. In: *Journal of Power Sources* 438 (2019). ISSN: 03787753. DOI: 10.1016/j.jpowsour.2019.227011.

[160] Yi-Fan Wu et al. 'Thermal Behavior of Lithium-Ion Cells by Adiabatic Calorimetry: One of the Selection Criteria for All Applications of Storage'. In: *ECS Transactions* 16.29 (2019), pp. 93–103. ISSN: 19385862. DOI: 10.1149/1.3115311.

[161] Hans Georg Schweiger et al. 'Comparison of several methods for determining the internal resistance of lithium ion cells'. In: *Sensors* 10.6 (2010), pp. 5604–5625. ISSN: 14248220. DOI: 10.3390/s100605604.

[162] Karen E. Thomas, Christian Bogatu and John Newman. 'Measurement of the Entropy of Reaction as a Function of State of Charge in Doped and Undoped Lithium Manganese Oxide'. In: *Journal of The Electrochemical Society* 148.6 (2001), A570. ISSN: 00134651. DOI: 10.1149/1.1369365.

[163] Hossein Maleki et al. 'Thermal Properties of Lithium Ion Battery and Components'. In: *Journal of The Electrochemical Society* 146.3 (1999), pp. 947–954. ISSN: 0013-4651. DOI: 10.1149/1.1391704.

[164] ISO 22007-2. *ISO 22007-2: Plastics — Determination of thermal conductivity and thermal diffusivity — Part 2: Transient plane heat source (hot disc) method*. Vol. 2008. 2008, p. 17.

[165] *SELFIE - SELF-sustained and Smart Battery Thermal Management SolutIon for Battery Electric Vehicles*. URL: https://eu-project-selfie.eu/.

[166] Theodoros Kalogiannis et al. 'Comparative study on parameter identification methods for dual-polarization lithium-ion equivalent circuit model'. In: *Energies* 12.21 (2019), p. 4031. ISSN: 19961073. DOI: 10.3390/en12214031.

[167] Nerea Nieto et al. 'Thermal Modeling of Large Format Lithium-Ion Cells'. In: *Journal of The Electrochemical Society* 160.2 (2013), A212–A217. ISSN: 0013-4651.

[168] Nerea Nieto et al. 'Novel thermal management system design methodology for power lithium-ion battery'. In: *Journal of Power Sources* 272 (2014), pp. 291–302. ISSN: 03787753. DOI: 10.1016/j.jpowsour.2014.07.169.

[169] Leire Martín-Martín et al. 'Modeling based on design of thermal management systems for vertical elevation applications powered by lithium-ion batteries'. In: *Applied Thermal Engineering* 102 (2016), pp. 1081–1094. ISSN: 13594311. DOI: 10.1016/j.applthermaleng.2016.02.127.

[170] Kong Soon Ng et al. 'Enhanced coulomb counting method for estimating state-of-charge and state-of-health of lithium-ion batteries'. In: *Applied Energy* 86.9 (2009), pp. 1506–1511. ISSN: 03062619. DOI: 10.1016/j.apenergy.2008.11.021.

[171] Siamak Farhad and Ashkan Nazari. 'Introducing the energy efficiency map of lithium-ion batteries'. In: *International Journal of Energy Research* 43.2 (2019), pp. 931–944. ISSN: 1099114X. DOI: 10.1002/er.4332.

[172] T.-W. Lee. *Thermal and Flow Measurements*. CRC Press, 2008, p. 390. ISBN: 9780429125171. DOI: 10.1201/b15094.

[173] *High-energy type cells | SCiB™ Rechargeable battery | Toshiba*. URL: https://www.global.toshiba/ww/products-solutions/battery/scib/product/cell/high-energy.html.

[174] Rubitherm Technologies GmbH. *Rubitherm GmbH*. 2016. URL: https://www.rubitherm.eu/en/productcategory/organische-pcm-rt.

[175] Parker. *THERM-A-GAP™ Pads*. URL: https://www.parker.com/content/dam/Parker-com/Literature/Chomerics/THERM-A-GAP%7B%5C_%7DThermally-Conductive-Gap-Filler-Pads.pdf.

[176] P. J. Boache. 'Perspective: A method for uniform reporting of grid refinement studies'. In: *Journal of Fluids Engineering, Transactions of the ASME* 116.3 (1994), pp. 405–413. ISSN: 1528901X. DOI: 10.1115/1.2910291.

[177] 3M. *3M HFE 7200*. 2009. URL: https://multimedia.3m.com/mws/media/1998190/3m-novec-7200-engineered-fluid-en.pdf.

[178] 3M. *3M ™ Thermal Management Fluids*. 2008. URL: https://multimedia.3m.com/mws/media/5698600/3mtm-thermal-management-fluids-for-military-aerospace-apps.pdf.

[179] Yuxin Zheng et al. 'Isobaric heat capacity measurements of liquid HFE-7200 and HFE-7500 from 245 to 353K at pressures up to 15MPa'. In: *Fluid Phase Equilibria* 372 (2014), pp. 56–62. ISSN: 03783812. DOI: 10.1016/j.fluid.2014.03.017.

[180] Pramod Warrier and Amyn S Teja. 'Density, viscosity, and thermal conductivity of mixtures of 1-ethoxy-1,1,2,2,3,3,4,4,4-nonafluorobutane (HFE 7200) with methanol and 1-ethoxybutane'. In: *Journal of Chemical and Engineering Data* 56.12 (2011), pp. 4291–4294. ISSN: 00219568. DOI: 10.1021/je1011828.

[181] *Lithium-ion 26650 Cells | Nanophosphate Batteries | Lithium Werks*. URL: https://lithiumwerks.com/products/lithium-ion-26650-cells/.

[182] *Fluido electrónico 3M™ Fluorinert™ FC-72 | 3M España*. URL: https://www.3m.com.es/3M/es%7B%5C_%7DES/p/d/b00000622/.

[183] ISO. 'ISO 22007-2: Plastics — Determination of thermal conductivity and thermal diffusivity — Part 2: Transient plane heat source (hot disc) method'. In: *Annual Book ofASTM Standards* 2008 (2008), p. 17.

[184] Frank P. Incropera and David P. DeWitt. *Fundamentals of Heat and Mass Transfer*. Danvers (MA) : John Wiley & Sons, 1996, p. 890. ISBN: 0471304603. DOI: 10.1016/j.applthermaleng.2011.03.022. arXiv: 1105-.

From: Steve Jobs, sjobs@apple.com
To: Steve Jobs, sjobs@apple.com
Date: Thursday, September 2, 2010 at 11:08PM

I grow little of the food I eat, and of the little I do grow I did not breed or perfect the seeds.

I do not make any of my own clothing.

I speak a language I did not invent or refine.

I did not discover the mathematics I use.

I am protected by freedoms and laws I did not conceive of or legislate, and do not enforce or adjudicate.

I am moved by music I did not create myself.

When I needed medical attention, I was helpless to help myself survive.

I did not invent the transistor, the microprocessor, object oriented programming, or most of the technology I work with.

I love and admire my species, living and dead, and am totally dependent on them for my life and well being.

Ez dadila haria eten.

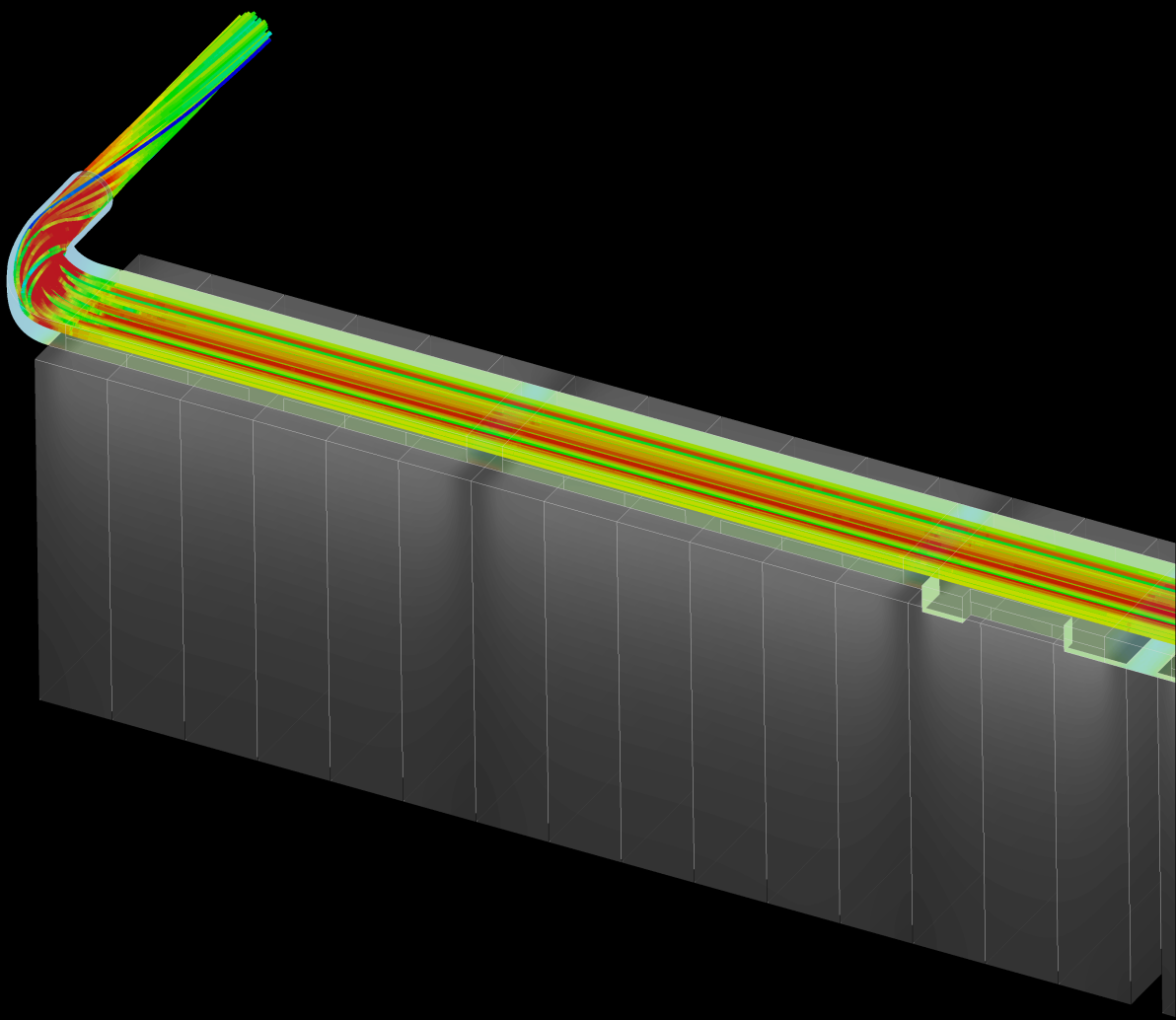

eman ta zabal zazu

Universidad del País Vasco

Euskal Herriko Unibertsitatea

ikerlan

MEMBER OF BASQUE RESEARCH & TECHNOLOGY ALLIANCE